Università degli Studi di Napoli "Federico II"
Dottorato di Ricerca in Fisica - XXXI Ciclo

R&D on the Resistive Plate Chamber for the Phase-II Upgrade of the CMS Muon Detector

Elena Voevodina

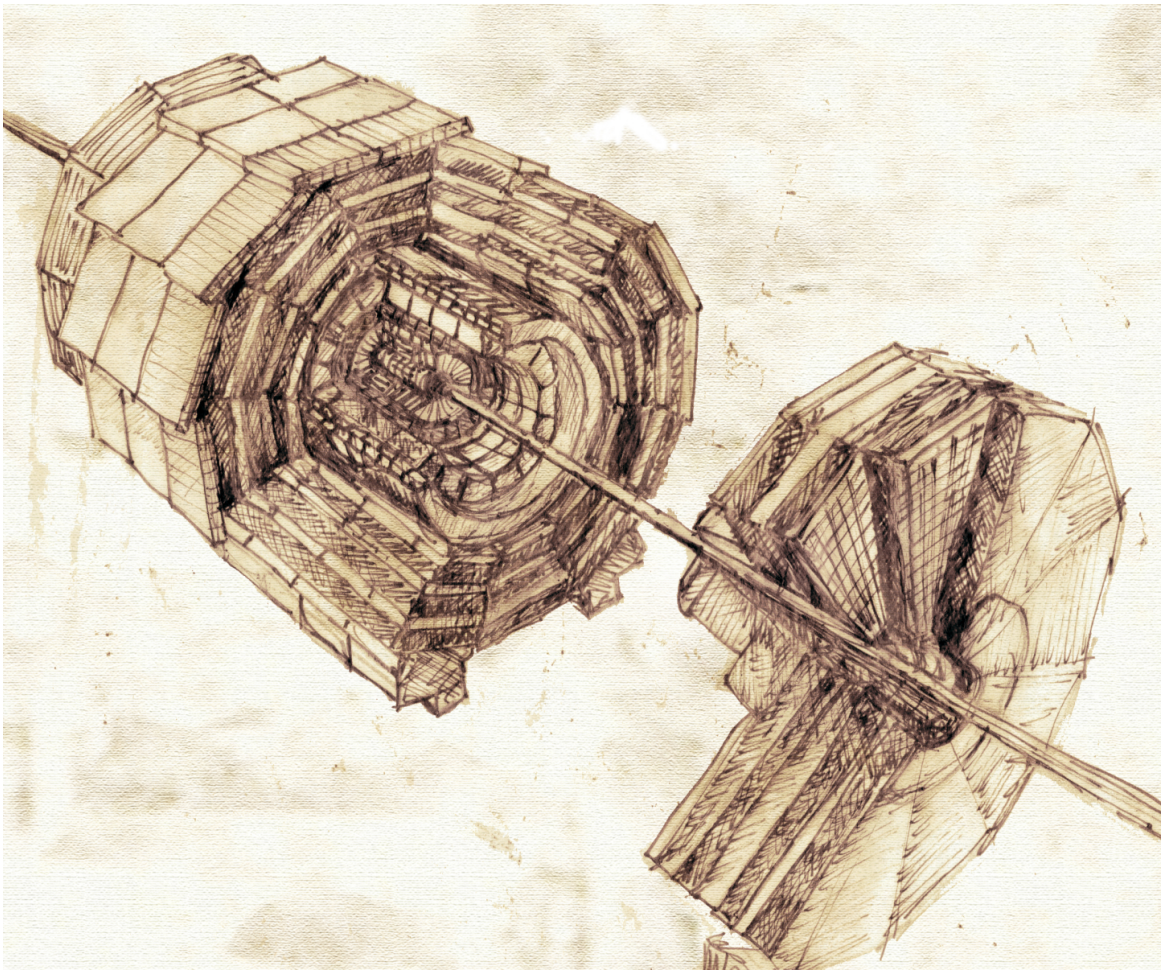

Tesi per il conseguimento del titolo

Università degli Studi di Napoli "Federico II"
Dipartimento di Fisica

Dottorato di Ricerca in Fisica - XXXI Ciclo

Coordinatore: Prof. Salvatore Capozziello

R&D on the Resistive Plate Chamber for the Phase-II Upgrade of the CMS Muon Detector

Elena Voevodina

Submitted to the Graduate School of Physics in partial fulfillment of the requirements for the degree of

DOTTORE DI RICERCA IN FISICA

DOCTOR OF PHILOSOPHY IN PHYSICS

at the

University of Napoli "Federico II"

University Supervisor: Prof. Giovanni De Lellis

CERN Supervisor: Dr. Gabriella Pugliese

R&D on the Resistive Plate Chamber for the Phase-II Upgrade of the CMS Muon Detector

Elena Voevodina

Ph.D. Thesis - University of Napoli "Federico II"

Napoli, Italy, June 2019

To my husband with love

"По-видимому, уже давно существует согласие по поводу роли, которую играют эксперимент и теория в естественных науках. Эксперимент, неотъемлемая основа любого прогресса этих наук, эксперимент, из которого мы всегда исходим и к которому мы всегда возвращаемся, - лишь он один может служить нам источником знаний о реальных фактах, которые стоят выше любой теоретической концепции, любой предвзятой идеи. Но эксперимент не должен сводиться к простому, пассивному наблюдению. Он должен всякий раз, когда это возможно, активно вмешиваться в реальность, изменяя условия возникновения явлений, вопрошая природу строго определенным образом, так, чтобы видеть, каков будет ее ответ. Что касается теории, то ее задача состоит в классификации и синтезе полученных результатов, расположении их в разумную систему, которая не только позволяет истолковывать известное, но также по мере возможности предвидеть еще неизвестное..."

(Louis de Broglie, 1892-1987)

List of Figures

List of Tables

Contents

Chapter 1

Introduction

This Doctoral Thesis takes place in the framework of the Muon System upgrade in the Compact Muon Solenoid (CMS) experiment at CERN and focuses on the extension in the coverage of the small angle (large pseudorapidity, η) region of the CMS Muon Detector. Muon detection in CMS is very important since the signature of events with muons in the final state is very reliable, in terms of its purity. In the next LHC data taking periods, this will be true both in case of discovery of new physics and for precision measurements of bosonic and fermionic Higgs couplings. The importance of the Muon System could even increase in the more difficult operating conditions of the High Luminosity LHC (HL-LHC). The instantaneous luminosity of LHC is expected to exceed the nominal value and reach $2.5 \times 10^{34}\ cm^{-2}s^{-1}$ during Run 3, expected to start in 2021. A further increase is planned during Run 4, starting from 2026, up to $5 \times 10^{34}\ cm^{-2}s^{-1}$, i.e. a yield five times greater than the initial LHC design value. The increase of the energy and luminosity during the future upgrades of the LHC machine will deeply affect the performance of the CMS Muon Detector due to the harsh background environment and the high pile-up. As a consequence, the maintenance of the current performance in the harsher environment will be of primary importance. In view of the next two long shutdown periods, the CMS Muon Collaboration is currently improving the Muon Spectrometer to maintain a high level of performance achieved during the first two periods of operation (Run 1 and Run 2) and also in the challenging environment of the high-luminosity LHC. The CMS Muon System was originally designed as a highly hermetic and redundant system that employs three gas-based detectors. Precision measurements and Level-1 triggering are provided by Drift Tubes (DTs) in the barrel covering acceptances up to $|\eta| < 1.2$, and Cathode Strip Chambers (CSCs) in the endcaps covering $1.0 < |\eta| < 2.4$. Additionally, the Resistive Plate Chambers (RPCs) provide redundant trigger and coarse position measurement in both barrel and endcap regions but were not implemented beyond $|\eta| > 1.8$ due to concerns about their capability to handle the high background particle rate. Operating in the

high background particle rate imposes severe restrictions on the gaseous detection technology that can be used: new detector requirements include high rate capability, good spatial resolution for tracking, good time resolution for triggering, and in addition, radiation hardness.

In order to cope with the very high operation condition, the high pile-up and background environment, in particular in the forward region, the CMS Muon Collaboration is planning to install a new generation of the Resistive Plate Chamber technology, named the improved RPC (iRPC), to upgrade the CMS Muon System, instrumenting the non-redundant high η region with a detector that could withstand the hostile environment and high luminosity rates expected in future runs. The iRPC detector is approved to instrument two inner forward regions of the CMS Muon System at $1.8 < \eta < 2.4$, called RE3/1 and RE4/1 stations, during the annual Year-End Technical Stops 2022 & 2023. The RE3/1 and RE4/1 chambers are wedge-shaped detectors, each contains a double 1.4 mm high-pressure laminates plate, forming of 1.4 mm thick gas gap. They will cover 20° in RE3/1 and RE4/1 stations, respectively, overlapping in φ with the CSC detectors in ME3/1 and ME4/1 stations, complementing them and providing redundancy and enhanced triggering and tracking capabilities in the region which is currently suffering from the highest background rates and a non-uniform magnetic field. The iRPC project will add 18 new chambers per muon disk, and 72 chambers in total for the RE3/1 and RE4/1 stations in both muon endcaps in order to ensure the full azimuthal coverage. Each station will provide one single hit for muon reconstruction with 2 ns time resolution, and a spatial resolution of about 0.6 cm in the transverse direction and 2 cm along the strip.

The Doctoral Thesis subject has been proposed by the CMS RPC Collaboration to demonstrate that iRPC technology is the most suitable choice for the upgrade of the Muon System. The next research activities have been conducted in this context:

The first activity, conducted in the framework of the iRPC RE3/1 and RE4/1 chambers integration and installation in the innermost region of CMS Muon Spectrometer, is focused on survey measurements performed in order to determine the space actually available for future installations during the Yearly Technical Stops at the end of 2022 and 2023. Surface topology and geometry of the Yoke Endcap (YE) ± 2 and YE± 3 iron disks in the region $1.8<|\eta|<2.4$ have been studied in detail by using different methods such as photography, photogrammetry, theodolite and infrared proximity sensor. After analyzing the experimental data obtained during the survey measurements, I developed the very precise 3D-model of the mechanical simulation for the installation of the RE3/1 and RE4/1 detectors in the dedicated η region. I designed the mechanical components to mount chambers here. These results of my work were reported in the CMS Muon Technical Design Report (TDR) which was submitted to the CMS Muon Committee on 12 September 2017.

The second activity has been focused on the developing, commissioning and characterization of the iRPC RE3/1 and RE4/1 detector prototypes. By using the information obtained during the previous activity, in August 2017 at the CERN CMS-RPC QA/QC facility, I organized the development and assembly of the first two real-size RE3/1 and RE4/1 detector prototypes and studied their detection performance with the new version of the PETIROC ASIC Front-end electronics. I was the key person who participated in all production processes on the construction and testing the detecting elements, assembling of the new prototypes and subsequent testing them with the new electronics under muon beam at the CERN Gamma Irradiation Facility (GIF++) in August 2018. By using the unique test area of the CERN GIF++ facility, I studied the iRPC detector performances at the different background conditions which will be similar to the future CMS conditions during the HL-LHC program. By studying the rate capability of the real-size iRPC detector prototypes I have experimentally shown that the new iRPC technology can effectively operate in the harsh background CMS environmental and can fulfill all physics requirements of the CMS experiment.

The third my activity included the testing of the new INFN Rome Front-end electronics together with iRPC detector prototype. The INFN Rome electronics has been proposed as a possible alternative to PETIROC ASIC electronics in time for the CMS-RPC system upgrade project, thus increasing the chance of success for the project. This has been the main strategy adopted by the CMS-RPC community and, consequently, it was necessary to find another available technology in order to develop the Front-end electronics to readout the iRPC detectors. In September 2018, I developed and assembled the second real-size iRPC RE4/1 detector prototype in the INFN Rome Tor Vergata laboratories (Italy) in order to study the performance with the INFN Rome Front-end boards. As in the previous research activity, I organized the subsequent testing of the iRPC detector prototype with the new electronics in the last available muon particle beam in the GIF++ facility at CERN before the starting of the Long Shutdown -2 period at LHC. In order to compare the results obtained from the first two RE3/1 and RE4/1 detector prototypes, I have studied the same number of chamber parameters of second iRPC RE4/1 detector prototype, such as a detection efficiency, cluster size, and rate capability. I experimental shown that this type of new Front-end board can be a great substitute for the PETIROC ASIC electronics.

A majority of the results obtained during the last two years of Ph.D. contributed to the success of the iRPC project and its final approval by CMS Collaboration.

Chapter 2

Large Hadron Collider

By colliding the two oppositely directed beams of charged particles with high-energy in a circular accelerator, it is possible to reconstruct similar conditions which were at the first moments of life of our Universe. The higher the energy, the farther we can see in the past, the more likely, we can observe the exotic interactions and discover the new physics laws. Large Hadron Collider (LHC) and its experiments were built by the European Organization for Nuclear Research (CERN) [1] from 1998 to 2008. They are the unique objects and one of the greatest achievements of human engineering. Since 2008, the development of high-energy physics has been determined by the results obtained in the experiments at the LHC. The LHC and its experiments allowed scientists to verify the predictions of the elementary particles physics theories, by finding the evidence of the existence of the long-theorized Higgs boson and by searching the large family of new particles predicted by the theory of supersymmetry as well.

2.1 Large Hadron Collider

The *Large Hadron Collider* (LHC) [2], [3], [4], [5] is a proton-proton superconducting accelerator and collider installed in the existing 26.7 km tunnel that was constructed between 1984 and 1989 to host the *Large Electron Positron* (LEP) collider [6], [7], [8]. The LEP tunnel has eight straight sections and eight arcs and lies between 45 m and 170 m below the surface. The approval of the LHC project was given by the CERN Council in December 1994. At that time, the plan was to build a machine in two stages starting with a center-of-mass energy of 10 TeV (be upgraded later to 14 TeV), but later it was approved the construction of the 14 TeV machine in a single stage.

The choice of proton beams is mainly dictated by the following considerations [2], [3]:

- hadron allow to explore a wide range of energies with fixed-energy beams:

they are the natural choice for a discovery machine. This is because of the fact that protons are not elementary particles, and in hard collisions, the interaction involves their constituents (quarks and gluons), which carry only a fraction of the proton energy;

- protons due to their higher mass imply a smaller energy loss from synchrotron radiation with respect to electrons, since in a circular collider of radius R, the energy loss per turn is proportional to $(E/m)^4/R$, where E and m are the energy and mass of the particles accelerated, respectively.

Since only a fraction of the proton energy contributes to the hard scattering, the center-of-mass energy of the beam must be much higher than the mass of the particle that has to be produced. It can be noted that the Higgs cross section increases steeply with the center-of-mass energy, while the total cross section remains almost constant. It is clear that the highest center-of-mass energy should be used.

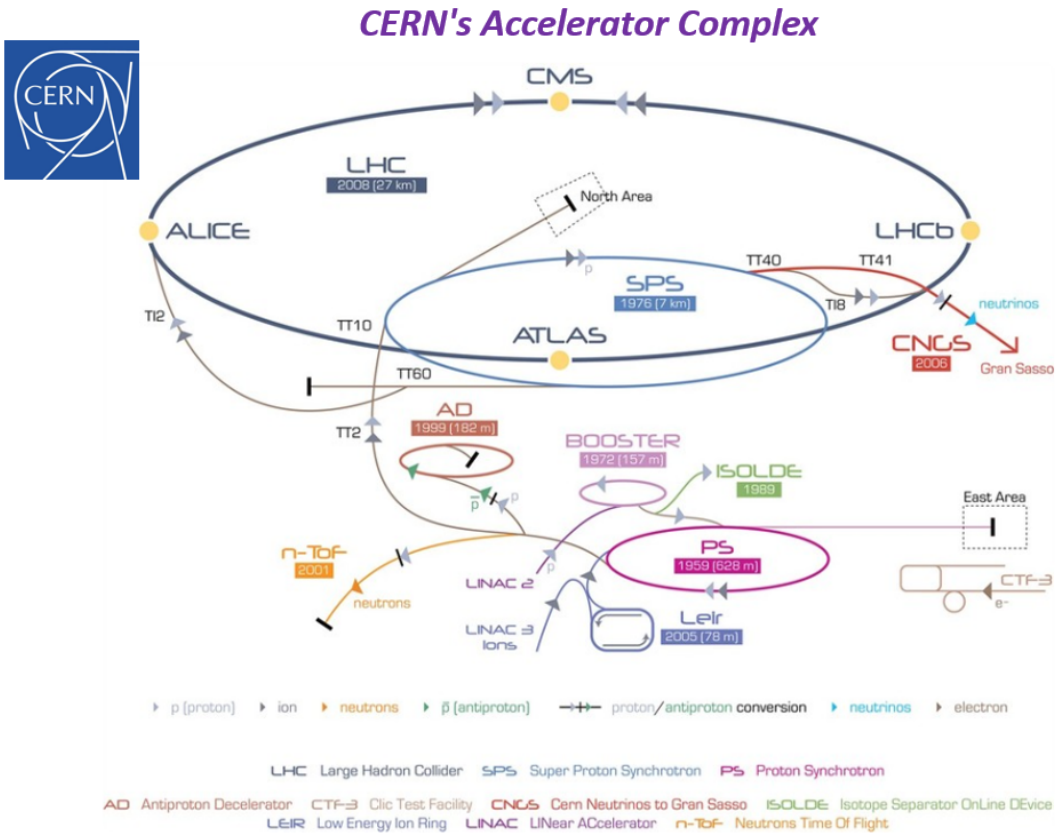

Figure 2.1: General view of the CERN accelerator complex and location of its main experiments [5].

Before begin injected to the LHCs main ring, the charged particles beams are gradually accelerated in the different stages of the CERN accelerating complex

(see Figure 2.1). First of all, protons are extracted from hydrogen stored in a gas cylinder by stripping orbiting electrons from the atoms. At this early stage, the protons have an energy around 100 keV and are pulsed every 100 μs. They enter the 30 m long linear accelerator called LINAC 2, where they acquire an energy of 50 MeV. Protons are then injected into the Proton Synchrotron Booster (PSB), a four ring synchrotron that accelerates single bunches up to 1.4 GeV. Two bunches of protons are transferred to the Proton Synchrotron (PS), the oldest CERN accelerator still in service. In the PS, the large PSB bunches are split into smaller bunches and accelerated to 28 GeV, before being split again to achieve the final 25 ns bunch spacing that will be maintained up to the LHC. The last step of pre-acceleration is made by the 6.9 km Super Proton Synchrotron (SPS), where the beams reach the injection energy of 450 GeV. The SPS is filled with 3 to 4 cycles of the PS (out of the 11 that would fit), as it is not capable of accelerating more than 4×10^{13} protons at a time. After acceleration, the proton bunches are then transferred to the LHC ring for acceleration up to 7 TeV. It takes 12 cycles of the SPS in order to fill the LHC. The LHC rings can contain up to 2808 bunches moving in opposite directions. Every second a proton bunches cross the 27-kilometer ring of 11000 times. Before the particles collide in the four main interaction points (ATLAS [9], CMS [10], ALICE [11], and LHCb [12]), they will circulate around the ring about 5 hr 24 min.

In addition, when LHC operates as a heavy ion accelerator, lead ions are first accelerated by the linear accelerator LINAC 3, and the Low-Energy Ion Ring (LEIR) is used as an ion storage and cooler unit. The ions then are further accelerated by the PS and SPS before being injected into LHC ring, where they will reach an energy of 2.76 TeV per nucleon (or 5.75 TeV per lead ion). The main parameters of the LHC machine and the particle beams are presented in Table 2.1.

Parameters	**p-p collisions**	**Pb-Pb collisions**
Center-of-mass energy (TeV)	14	1148
Number of particles per bunch	1.110^{11}	$\sim 8 \times 10^7$
Number of bunches	2808	608
Design luminosity ($cm^{-2}s^{-1}$)	10^{34}	2×10^{27}
Bunch lenght (mm)	53	75
Beam radius at interaction point (μm)	15	15
Time between collisions (ns)	25	124.75×10^3
Bunch crossing (MHz)	40.08	0.008
Dipole field (T)	8.3	8.3

Table 2.1: Main parameters of the LHC and its beam [3].

To hold and focus the particles inside LHC vacuum tubes, 1632 superconducting magnets were installed (see Figure 2.2a). In order to achieve a center-of-mass energy of $\sqrt{s} = 14\ TeV$ and luminosity of $10^{34}\ cm^{-2}s^{-1}$, these magnets must be cooled up to 1.9 K. It is the temperature at which helium becomes

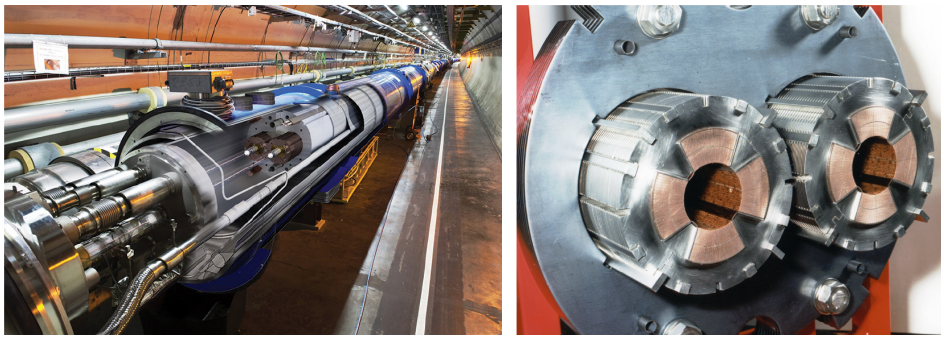

(a) (b)

Figure 2.2: Pictures of the superconducting magnets in the LHC tunnel (left) and its cross-section (right) [3].

superfluid. After that, the magnets can create a magnetic field of 8.3 T. The innovative design of two-in-one magnets allows both transport tubes of beams to be located in a single cryostat (see Figure 2.2b), which significantly reduces the size and cost. The total amount of helium, about 96 tons, allow to cool the LHC accelerator with a mass of 37000 tons. Thus, the LHC is one of the largest cryogenic systems in the World.

2.2 LHC Main Characteristics

The most important performance parameters of LHC are the beam energy and the luminosity.

The energy available for the production of new effects is the most significant feature. It is chosen based on the physical tasks which must be solved during the operation LHC. The range of LHC physics tasks is very wide and a brief description will be given in the Section 2.4, where the main LHC experiments and their main tasks will be presented. In the LHC collides two opposite beams which have the energy depend on the operation phase of the collider. The total energy at the collisions determines as the center-of-mass energy ($\sqrt{s}$) which depends on the energies E_1 and E_2 of the particles of the two beams and of their momenta $\vec{p_1}$ and $\vec{p_2}$. Taking into account that the LHC is a collider, then $\vec{p_1} = -\vec{p_2}$. The center-of-mass energy is given by:

$$\sqrt{s} = \sqrt{(E_1 + E_2)^2 - (\vec{p_1} + \vec{p_1})^2} = \sqrt{(E_1 + E_2)^2} \tag{2.1}$$

The collider's luminosity $\mathcal{L}$ is the second most important parameter. The number of colliding particles increases with increasing luminosity. The instantaneous luminosity is defined as the number of collisions per unit time and cross-sectional area of the beams:

$$\mathcal{L} = \frac{N_1 N_2 n_b f_{rev}}{A} \tag{2.2}$$

where N_1 and N_2 are the number of particles in the two colliding bunches, A is the overlap area of the two bunches transverse to the beam, n_b is the number of bunches in one beam, and f_{rev} is the revolution frequency of one bunch (with a design value of 11245 Hz). At the LHC proton-proton collisions $N_1 = N_2 = N_p$, and, since the area of overlap is difficult to measure directly in an accelerator, for a Gaussian beam distribution $\mathcal{L}$ can be written as:

$$\mathcal{L} = N_p^2 n_b f_{rev} \frac{\gamma}{4\pi\epsilon_n \beta^*} F \tag{2.3}$$

where γ is the relativistic Lorentz factor, ϵ_n is the normalized transverse beam emittance (with a design value of 3.75 μm), β^* is the so-called betatron function at the interaction point [13], and F is the geometric luminosity reduction factor due to the crossing angle at the interaction point.

The luminosity integrated over a time period refers to the number of bunch crossings during this period. It is often expressed in inverse femtobarn fb^{-1}. The integrated luminosity multiplied by the interaction cross-section gives the total number of events produced during a time period. This parameter characterizes the efficiency of obtaining physical information from the LHC.

$$R \equiv \frac{dN}{dt} = \mathcal{L}\sigma \tag{2.4}$$

The first year LHC operated at $\mathcal{L} \sim 6 \times 10^{33}\ cm^{-2}c^{-1}$, center-of-mass energy $\sqrt{s} = 7\ TeV$ and integrated a luminosity of 5.1 fb^{-1}. The gradual increase of the luminosity has led to the fact that by 2017, it reached the value $\mathcal{L} \sim 1 \times 10^{34}\ cm^{-2}s^{-1}$ and nowaday the center-of-mass energy is $\sqrt{s} = 14\ TeV$ with an integrated luminosity of 100 fb^{-1}. Such a high luminosity is necessary to study the extremely rare events with a small cross-section which characterizes the new physics [14].

2.3 The Physics at the LHC

The LHC at CERN is the most powerful particle accelerator in the World at the moment. It operates at 14 TeV center-of-mass energy, and a design luminosity of $10^{34}\ cm^{-2}\ s^{-1}$. This energy and luminosity values are needed in order to investigate a range of energy (mass) never explored before and to confirm or deny the Standard Model theory. The main goal of LHC is to study the physics of elementary particles, such as Higgs boson, at the highest energies accessible to the accelerators.

2.3.1 The Standard Model

The Standard Model (SM) is a theory that describes all the elementary particles actually known and the forces (except for the gravity) between them [15],

[16], [17]. It describes matter as composed by fermions (half-integer spin particles), divided into main groups: leptons including electrons, muons, taus and the related neutrinos, and quarks. In Table 2.2 a classification of SM fermions is given.

Fermions	1^{st} Fam.	2^{st} Fam.	3^{st} Fam.	Charge	Interactions
Quarks	u	c	t	$+2/3$	All
	d	s	b	$-1/3$	
Leptons	e	μ	τ	-1	Weak, E.M.
	ν_e	ν_μ	ν_τ	0	Weak

Table 2.2: Fundamental particles in the Standard Model [15].

In the SM the interactions between particles are described as an exchange of bosons, the mediators of fundamental forces. Bosons are integer spin particles that mediate the fundamental interactions. In particular, the SM describes only three of the four known forces: electromagnetic, weak and strong. Gravitation is not described by SM because is not relevant at the scale of distance common in the particle physics. The fundamental interactions are described in Table 2.3.

	Electromagnetic	**Weak**	**Strong**
Quantum	Photon (γ)	$W^{\pm}$ and Z	Gluons
Mass GeV/c^2	0	80-90	0
Coupling Constant	$\alpha(Q^2 = 0) \approx 1/137$	$G_F \approx 1.2 \times 10^{-5} GeV^{-2}$	$\alpha_s(m_Z) \approx 0.1$
Range (cm)	∞	10^{-6}	10^{-13}

Table 2.3: Fundamental Interactions in the Standard Model [15].

The Standard Model describes these interactions with two gauge theories:

- the theory of the electroweak interaction, or Electroweak Standard Model, that unifies the electromagnetic and the weak interaction;
- the theory of strong interactions or Quantum ChromoDynamics (QCD).

2.3.2 Electroweak Symmetry Breaking in the Standard Model

The Quantum Electrodynamics (QED) is based on the invariance of the QED Lagrangian for local gauge transformation with respect to the $U(1)$ symmetry group [15], [16]. This symmetry leads to the existence of the photon, that is the massless field vector of the electromagnetic interaction. If we extend the symmetry to the group $SU(2) \times U(1)$ we can unified the weak and electromagnetic interactions in a single one, it will be the electroweak interaction. There

are two quantum numbers associated to this interaction: the weak isospin (I) and (Y) that satisfy the relation:

$$Q = I_3 + \frac{Y}{2} \tag{2.5}$$

where I_3 is the third component of the weak isospin and Q is the electric charge. The request of invariance for local gauge transformations with respect to the $SU(2) \times U(1)$ group introduces four massless vector fields $W_\mu^{1,2,3}$ and B_μ that couple to fermions with two coupling constants g and g'. In order to have the physical field, we have to re-organize the four massless fields in a linear combination. This gives us two charged bosons:

$$W_\mu^{1,2,3} = \sqrt{\frac{1}{2}}(W_\mu^1 \pm iW_\mu^2) \tag{2.6}$$

while the neutral bosons γ and Z correspond to

$$A_\mu = B_\mu cos\theta_W + W_\mu^3 sin\theta_W \tag{2.7}$$

$$z_\mu = -B_\mu sin\theta_W + W_\mu^3 cos\theta_W \tag{2.8}$$

The two neutral bosons are obtained by mixing the neutral fields W_μ^3 and B_μ with a rotation defined by Weinberg angle θ_W. In particular, the A_μ field is identified with the electromagnetic field tensor. The unification can be done if the two coupling constants are equal:

$$gsin\theta_W = g'cos\theta_W = e \tag{2.9}$$

that represents the electromagnetic unification.

The four bosons obtained are massless. If we try to introduce a mass term for the gauge bosons in the $SU(2) \times U(1)$ Lagrangian, we will destroy the invariance of local gauge transformations. In order to keep the mass, we have to use the Brout-Englert-Higgs (BEH) mechanism, that permits to have massive fermions, $W^\pm$ and Z leaving the photon γ massless. The BEH mechanism introduces the Higgs field, a doublet of complex scalar field:

$$\phi = \begin{pmatrix} \phi^+ \\ \phi^0 \end{pmatrix} = \sqrt{\frac{1}{2}} \begin{pmatrix} \phi_1 + i\phi_2 \\ \phi_3 + i\phi_4 \end{pmatrix} \tag{2.10}$$

where the ϕ^+ and ϕ^0 are the charged and neutral fields, ϕ_1, ϕ_1, ϕ_3 and ϕ_4 are complex of the scalar fields.

The Lagrangian of this field must be invariant under $SU(2) \times U(1)$ local gauge transformations and include a potential term

$$\mathcal{L}_{Higgs} = (D_\mu \phi)^\dagger (D^\mu \phi) - V(\phi) \tag{2.11}$$

where

$$V(\phi) = -\mu^2\phi^\dagger\phi + \lambda(\phi^\dagger\phi)^2 \tag{2.12}$$

and D_μ is the covariant derivative for local gauge transformations. The potential written above depends on the pure imaginary parameter μ and the real and positive parameter λ. By minimizing $V(\phi)$, the fundamental state of the system is obtained.

At $\lambda > 0$ and $\mu^2 < 0$, we have a lowerly limited Lagrangian density and a minimum of the potential that is not unique, but an infinite set of minimum points dislocated on a circumference on the complex plane, as shown in the Figure 2.3.

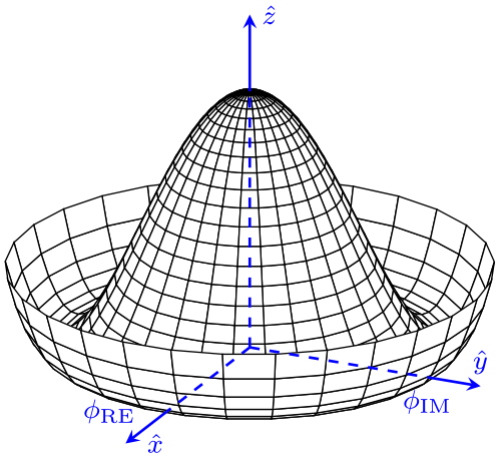

Figure 2.3: Form of potential V as a function of ϕ on the complex plane [16]

Under these condititons ($\lambda > 0$ and $\mu^2 < 0$) the potential has a minimum for

$$\phi^\dagger\phi = \frac{1}{2}(\phi_1^2 + \phi_2^2 + \phi_3^2 + \phi_4^2) = \frac{\mu^2}{2\lambda} \equiv \frac{v^2}{2} \tag{2.13}$$

The minimum is not found for ϕ_i but for a manifold of value: this effect is called *spontaneous symmetry breaking*. The coupling between boson fields and the non-zero vacuum value of the Higgs field gives masses to the bosons. An important result is that the fundamental state of the potential doesn't have the same symmetry properties as the Lagrangian while the minimum of Higgs field is invariant for $U(1)$ transformations. This means that the electromagnetic symmetry remains unbroken and photon remains massless.

Using the Higgs mechanism, we have three massive gauge bosons, corresponding to nine degrees of freedom. Since the initial number of independent fields is ten (three massless bosons $\times$ two polarization states + four real ϕ_i fields), one additional scalar gauge boson should appear as a real particle. This "new"

boson is called Higgs boson and his mass depend on υ and λ. The value is related to the boson masses by the relation:

$$\begin{aligned} m_{W^{\pm}} &= \frac{1}{2} g\upsilon \\ m_Z &= \frac{g\upsilon}{2cos\theta_W} \end{aligned} \tag{2.14}$$

However, the λ parameter is a characteristic of the field ϕ and we cannot determine it from other constrains: this implies that the Higgs mass can not be obtained theoretically. The fermion masses are generated with a similar mechanism, but like free parameters of the theory (6 masses of quarks and 3 for leptons, assuming neutrinos to be massless). This brings the number of free parameters of Standard Model to 17, the others are 4 parameters of Cabibbo-Kobayashi-Maskawa matrix that describes the mixing of quark flavours, the coupling g and g', the parameter of the Higgs vacuum expectation value and the Higgs mass. Nowadays, the parameters have been determined from experimental results and in 2012 the Higgs boson experimental mass close to 125 GeV has been observed by the ATLAS and CMS experiments.

2.3.3 Search for Higgs Boson at LHC

The LHC is providing p-p collisions at high center-of-mass energy. The search for the Standard Model Higgs boson is one of the major physics goals at this collider. But the production of the SM Higgs boson is a very rare process at the LHC, largely dominated by the production of quarks and gluons. The cross-section of the different processes as a function of the center-of-mass energies in proton-(anti) proton collisions are shown in Figure 2.4. Taking into account this, it is clear that the production of $b\bar{b}$-pairs are the dominant process while the production of gauge or Higgs bosons is several orders of magnitude smaller.

2.3.3.1 Phenomenology

The main mechanisms of the Higgs boson production at LHC in the proton-proton collisions are presented below:

- $gluon - gluon\ fusion$ ($gg \rightarrow H$), is a dominant mechanism regulated by strong interaction. The leading order includes a heavy-quark loop with the main contribution given by the top quark, as shown in the Feynman diagram in Figure 2.5a. It also is the main Higgs production mode at the LHC and represents about 87% of the total Higgs production at the center-of-mass energy $\sqrt{s} = 14\ TeV$ and for the Higgs mass around $m_H = 125\ GeV$.

- $vector\ boson\ fusion$ (VBF) ($q\bar{q} \rightarrow qqVV \rightarrow qqH$) is the second most dominant production mode at the LHC. This production mechanism

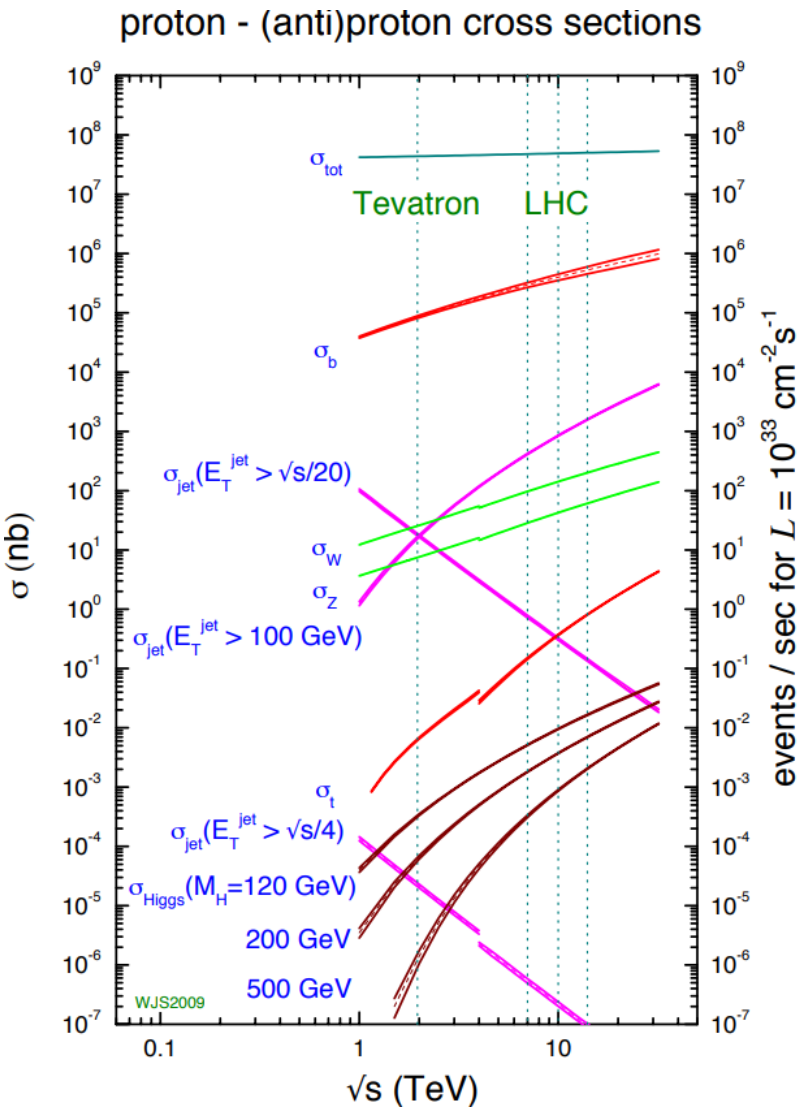

Figure 2.4: Cross section and event rates of several processes as a function of the center-of-mass energy of proton-(anti) proton collisions [18].

occurs as the scattering between two $q\bar{q}$ with weak boson ($W^{\pm}$ and Z) exchange in the t-channel and with the Higgs boson radiated off the weak-boson propagator. The main characteristic of this process, as shown in the corresponding Feynman diagram in Figure 2.5b, is the production of two small angle jets. The Higgs VBF production cross section is somewhat smaller ($\sim 20\%$) than the gluon fusion one.

- *associated with vector boson* ($qq \rightarrow V^* \rightarrow VH$, see in Figure 2.5c) production, called Higgsstrahlung, is the most promising channel (about 5% of the overall Higgs production). This channel is the associate production Higgs with virtual boson decays into a real boson $W^{\pm}$ or Z for $m_H < 135\ GeV$, where the $b\bar{b}$-decay is dominant. This is due to the

possibility to trigger on the leptonic decay of the vector boson.

- *associated with top quarks* ($gg/qq \rightarrow Ht\bar{t}/bbarb$, see in Figure 2.5d). This channel is radiated off one of the two tops in the $q\bar{q}$, gg s-channel or off the top propagator in the gg t-channel. It can be important in the low-mass region at high luminosity LHC condition. In this production mode represents about 1% of the total Higgs production at the center-of-mass energy $\sqrt{s} = 14\ TeV$.

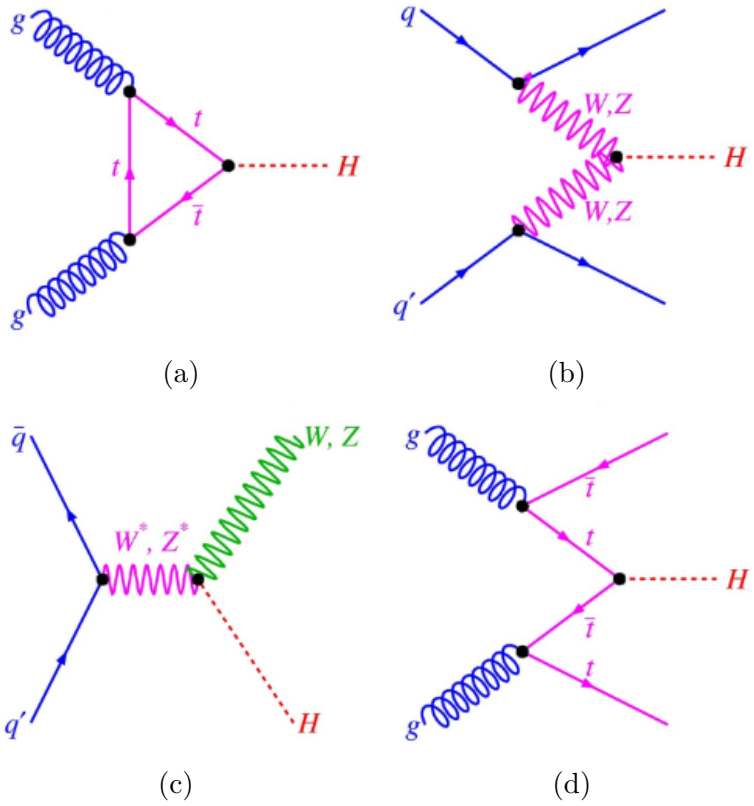

Figure 2.5: The Feynman diagrams for the main production mechanisms of the Higgs boson: (a) *gluon-gluon fusion*; (b) *vector boson fusion* (VBF); (c) *associated with vector boson*; (d) *associated with pairs of top quarks* [18].

The Higgs boson is an unstable particle and therefore can only be revealed through its decay products. The branching ratio is defined for a possible decay channel, such as the probability of decaying in that particular decay channel with respect to the total probability of decay in all permissible channels. The branching ratio and the cross-section at $\sqrt{s} = 14\ TeV$ of the various decay modes of the SM Higgs boson are shown in Figure 2.6. At the leading order, according to the Standard Model, the Higgs boson can decay into: $H \rightarrow \gamma\gamma$; $H \rightarrow WW^*$ or $\rightarrow ZZ^*$; $H \rightarrow 2l$ $(l = \mu, \tau)$; $H \rightarrow b\bar{b}$ or $H \rightarrow gg$ and etc.

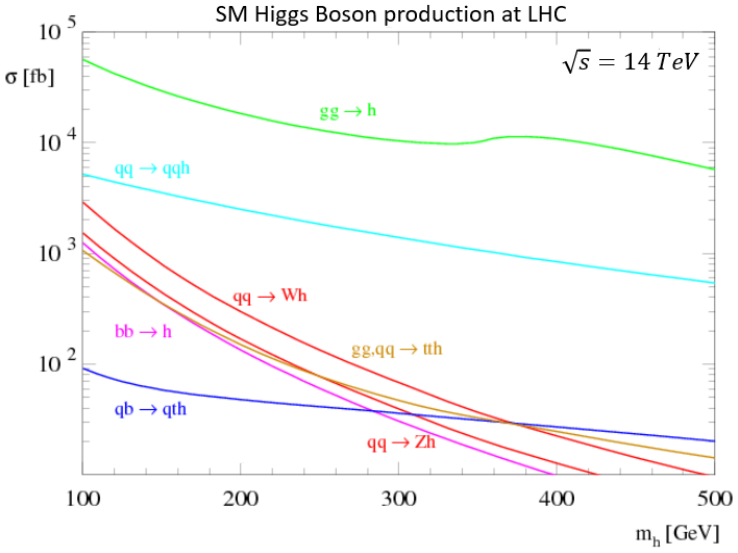

(a)

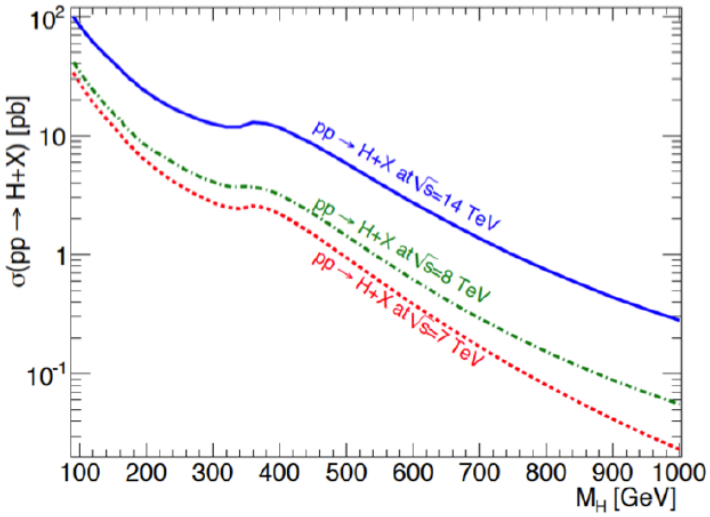

(b)

Figure 2.6: (a) Higgs production cross section and (b) branching ratios as a function of the Higgs mass at the center-of-mass energy $\sqrt{s} = 7,\ 8,\ 14\ TeV$ [19].

2.3.3.2 Discovery of Higgs Boson at LHC

On July 2012 in the 36^{th} Conference on High Energy Physics (ICHEP 2012, Australia) ATLAS and CMS experiments announced the discovery of a new, neutral particle of mass of about 125 GeV. The properties of the new particle were shown to be consistent with those predicted for the SM Higgs boson. Thus, with the discovery of the Higgs boson, the picture appears complete: all fundamental constituents of the Standard Model have been realized in nature, and the major task of the Large Hadron Collider and its detectors was achieved.

Results were received by using data samples collected by the CMS and ATLAS during the first operation of the LHC at the integrated luminosities of 5.1 fb^{-1} and $\sqrt{s}$ = 7 TeV and 19.7 fb^{-1} at $\sqrt{s}$ = 8 TeV. The search was performed in the six different decays: $\gamma\gamma$, ZZ, W^+W^-, $\tau^+\tau^-$, bb and $\mu^+\mu^-$ and the five different production modes, where the boson produced in vector boson constitutes two very distinguishable final states [20] [21]. Each experiment produced an observation compatible with the predictions of production and decay of a SM Higgs boson. ATLAS and CMS each observed a significance of 5.9 and 5.8 standard deviations respectively. Both of these experiments saw the highest contribution to this measurement from the $ZZ^* \rightarrow 4l$ and $\gamma\gamma$ final states, which also correspond to the two final states with the highest resolution on the mass of this newly discovered particle. A combination of ATLAS and CMS results in these channels was performed to provide a combined measured mass of the Higgs boson of $m_H = 125.09 \pm 0.21(stat.) \pm 0.11(syst.)\ GeV$ [21]. The joint ATLAS and CMS results were used to produce observations of the vector boson fusion production process and for the $H \rightarrow \tau^+\tau^-$ decay process of 5.4 and 5.5 standard deviations, respectively.

2.4 LHC Experiments

In June 1995, the LHC Committee approved the construction of two new detectors designed to operate on the accelerator: ATLAS (A Toroidal LHC ApparatuS) and CMS (Compact Muon Solenoid). The general principles of operation of the ATLAS and CMS experiments are the same and aim at detailed studies of the known physics and search for new physics beyond the SM. They maximally cover the space around the interaction point of colliding proton beams (so-called 4π detectors). The decision to build two detectors for physical research was related to the need for the confirmation of each discovery by independent experiments. Independently created experiments should ensure the reliability of the obtained physical results. Each detector has its own area of intersection beams called interaction point (IP). There are four such areas at the LHC. Two of them are designed for ATLAS and CMS detectors (IP1 and IP5). The two remaining ones are intended for other experiments such as ALICE (A Large Ion Collider Experiment) and LHCb (The Large

Hadron Collider beauty experiment), IP2 and IP8 respectively. In the ALICE experiment, a study over lead-ion collisions is done in order to improve the understanding of the quark-gluon plasma, which is postulated to have existed during the early Universe. The LHCb experiment is specialized in studying the bottom-quark physics and CP violation in order to better understand the matter-antimatter asymmetry in the Universe. The schematic views of the LHC main experiments are shown in Figure 2.7.

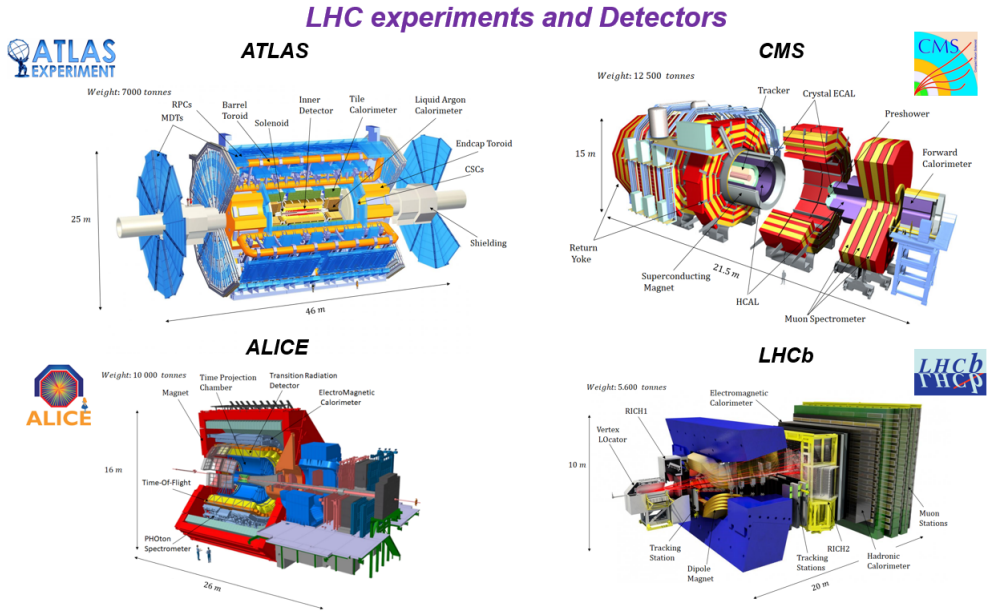

Figure 2.7: The LHC main experiments: ATLAS, CMS, ALICE and LHCb

In addition to the four main experiments, single-purpose experiments such as TOTEM (TOTal Elastic and diffractive cross section Measurement), which is installed near ATLAS and CMS respectively, LHCf (The Large Hadron Collider forward) and MoEDAL (Monopole and Exotic Detector At the LHC) were designed. LHCf aims at studying particle showers close to the beam pipe in order to test models of particle showers as present in astroparticle physics. TOTEM is measuring up to high pseudorapidity in order to study the total cross section of proton collisions. MoEDAL is designed to directly search for magnetic monopoles and other highly ionizing stable or metastable particles arising in various theoretical scenarios beyond the Standard Model. More details about these experiments can be found in [22], [23], [24] and [25].

Chapter 3

The CMS Experiment

The Compact Muon Solenoid (CMS) is one of the four main experiments and a multi-purpose apparatus operating at the Large Hadron Collider. Its scientific goals are to describe the features of all known particles, including the latest discovered Higgs boson, as well as search for new physics beyond the Standard Model at the TeV energy scale. The CMS experiment is a worldwide collaboration that includes more than 4300 scientists and engineers from 186 institutes and 42 countries.

3.1 Overall Design

The CMS detector system, located at the underground cavern (IP 5) near Cessy in France, is in shape of a cylindrical barrel closed by two endcap disks, with a full length of $\sim 21\ m$, a diameter of $\sim 15\ m$ and a total weight of about 14000 tonnes. Its main distinguishing features are a compact solenoid with the high magnetic field of $3.8\ T$.

The CMS detector is designed to follow the traditional scheme of the sub-detectors location: the first layer (close to the interaction point) is an inner tracking detector followed by Electromagnetic and Hadronic Calorimeters and Muon Spectrometer on the outside. All detector components were chosen to meet the LHC physics programme requirements. In Table 3.1 the main characteristics of the CMS sub-detectors and their functions are presented. The overall view of the CMS detector is shown in Figure 3.1 where we can distinguish the barrel region and the endcap stations.

The CMS coordinate frame is a right-handed system where the *x-axis* pointing radially inward that is, toward the center of the LHC ring, the *y-axis* points upwards and the *z-axis* is parallel to the beam and points toward the Jura mountains from LHC Point 5. Reconstruction algorithms, however, use a spherical coordinate system based on the radial distance $R = \sqrt{x^2 + y^2}$ from the *z-axis*, the azimuthal angle ϕ with respect to the *y-axis* and polar angle θ

Sub-detector	Composition	Functions	Main craracteristics
Inner tracker	silicon strip and pixel detectors	the charged particles momentum measuring and reconstruction of their trajectory	isolated track efficiency $\varepsilon > 95\%$ within jets $\varepsilon \sim 90\%$; primary vertex resolution: 10-20μm; p_T resolution: $\Delta p_T/p_T = 1\%$ (0.1 TeV), 10% (TeV); coverage $\eta < 2.5$
Electromagnetic Calorimeter	$PbWO_4$ crystals	high precision measurements of the electrons and photons	energy resolution: $(\frac{\sigma}{E})^2 = (\frac{2.7\%}{\sqrt{E}})^2 + (\frac{245}{E})^2 + 0.55\%$ (barrel); $(\frac{\sigma}{E})^2 = (\frac{5.7\%}{\sqrt{E}})^2 + (\frac{245}{E})^2 + 0.55\%$ (endcap); coverage $\eta < 3$;
Hadron Calorimeter	Cu-Zn scintillators	hadrons energy measurement and the indirect measurement of the presence of non-interacting, uncharged particles such as neutrinos	energy resolution: $(\frac{\sigma}{E})^2 = (\frac{68\%}{\sqrt{E}})^2 + 4.5\%$ (barrel); coverage $\eta < 3$;
Muon Spectrometer	gaseous detectors	precise muon detection and identification	efficiency $\varepsilon \sim 90\%$ $\Delta p_T/p_T$ = 8-15% (0.01 TeV)/20-40% (TeV) coverage $\eta < 2.4$

Table 3.1: The main characteristics of the CMS sub-detectors and their functions [33], [34].

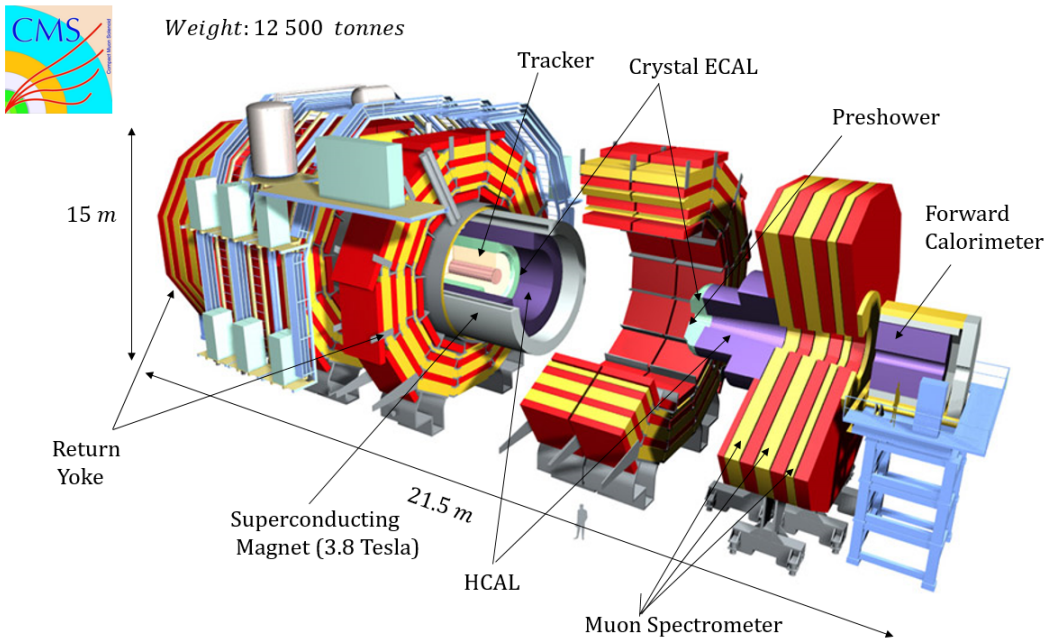

Figure 3.1: Overall view of CMS detector.

with respect to the beam line. However, taking into account that the particles produced by proton collisions are strongly pressed to the collision axis and distributed over the angle θ very unevenly, it is customary to use a different, more convenient, kinematic variable called *pseudorapidity* (η). The η value is determined by the formula [33], [34]:

$$\eta = -ln(tan\frac{\theta}{2}) \tag{3.1}$$

The benefit of this kinematic value is that hadrons generated in proton collisions are much more uniformly distributed in velocity than in angle θ, which makes the analysis of a complex event easier and more clearly. The CMS coordinate system is shown in Figure 3.2.

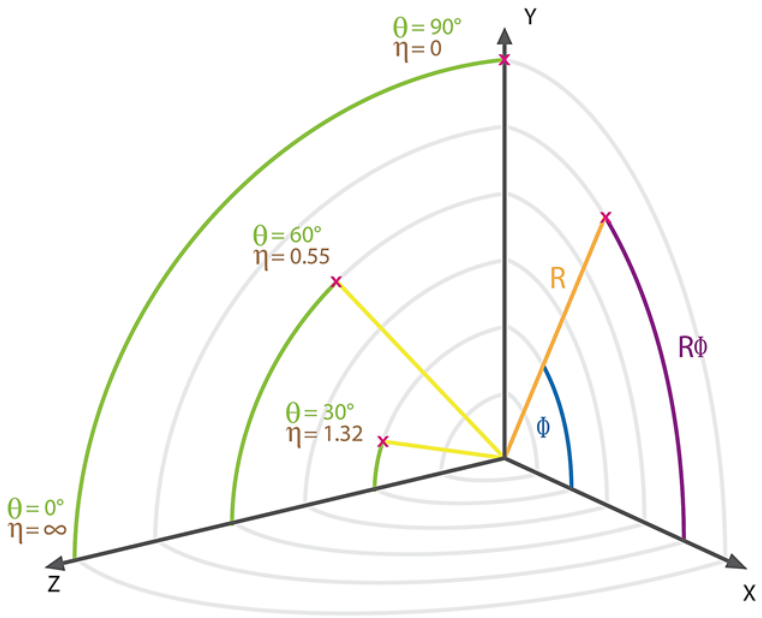

Figure 3.2: The CMS coordinate system.

3.2 The Superconducting Magnet

A magnetic field is essential for identifying the particles emerging from collisions: it curves their trajectory allowing to calculate their momentum and to establish whether they have a positive or negative charge. The stronger the field and the larger the volume on which it acts, the higher the resolution of the detector.

The heart of the CMS detector is the magnet, which consists of a 12.5 m long, 6 m inner diameter, 3.8 T superconducting solenoid and of a 12000 tons, 1.5 m thick iron yoke. Various detectors are located both inside the bore of the magnet coil (inner tracker, calorimetry) and outside the coil into the gaps of the segmented return yoke (muon detection). In Figure 3.3 a schematic view of the CMS solenoid is shown as well as the picture of the steel return yoke and muon chambers around the magnet are presented. Other main parameters of the CMS superconducting magnet are given in Table 3.2 [33], [34].

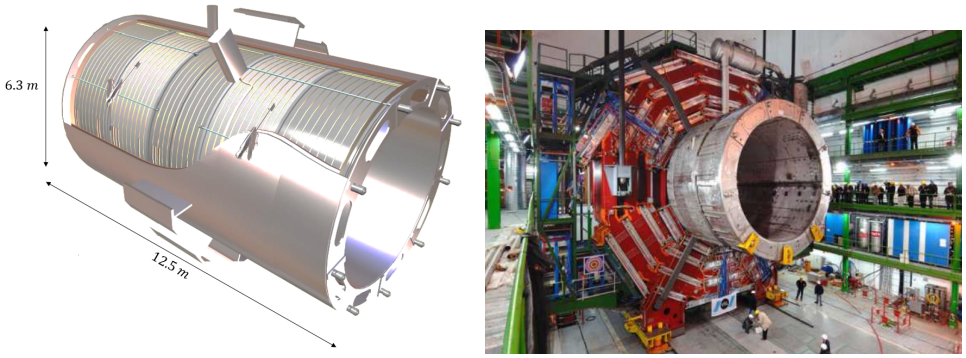

(a) (b)

Figure 3.3: A schematic view of the CMS solenoid (left), and the photograph of the CMS magnet and the return yoke with the barrel muon chambers installed at the Underground Experimental Cavern (right).

Parameter	**Value**
Magnetic length	12.5 m
Free bore diameter	5.9 m
Number of turns	2168
Central magnetic induction	3.8 T
Maximum induction on conductor	4.6 T
Nominal current	19.1 kA
Average inductance	14.2 H
Stored energy	2.6 GJ
Operating temperature	4.5 K

Table 3.2: Parameters of the CMS superconducting solenoid.

3.3 Tracker System

The main goal of the inner tracker is to reconstruct high-p_T charged particles (electrons and muons) tracks in the region $|\eta| < 2.5$ with high efficiency and good momentum resolution, to measure their impact parameter and to reconstruct secondary vertices [26] [27] [28]. It surrounds the interaction point and features high granularity and fast response, as in the LHC design luminosity of $10^{34}\ cm^{-2}s^{-1}$ there will be on average about 1000 particles from more than 20 overlapping proton-proton interactions traversing the tracker for each bunch crossing. The trajectories can, therefore, be identified reliably and attributed to the correct bunch crossing. Tracker has a cylinder shape with 5.4 m long, 2.4 m of the diameter. The magnetic field (3.8 T) is maintained throughout all the volume of the tracker system. The CMS tracker is constructed using the two type of detector technologies: pixel and microstrip. A general overview of the CMS tracker system is given in Figure 3.4, with its subsystems Pixel, Tracker Inner Barrel (TIB) and Tracker Inner Disks (TID), Tracker Outer

Barrel (TOB) and Tracker Endcaps (TEC).

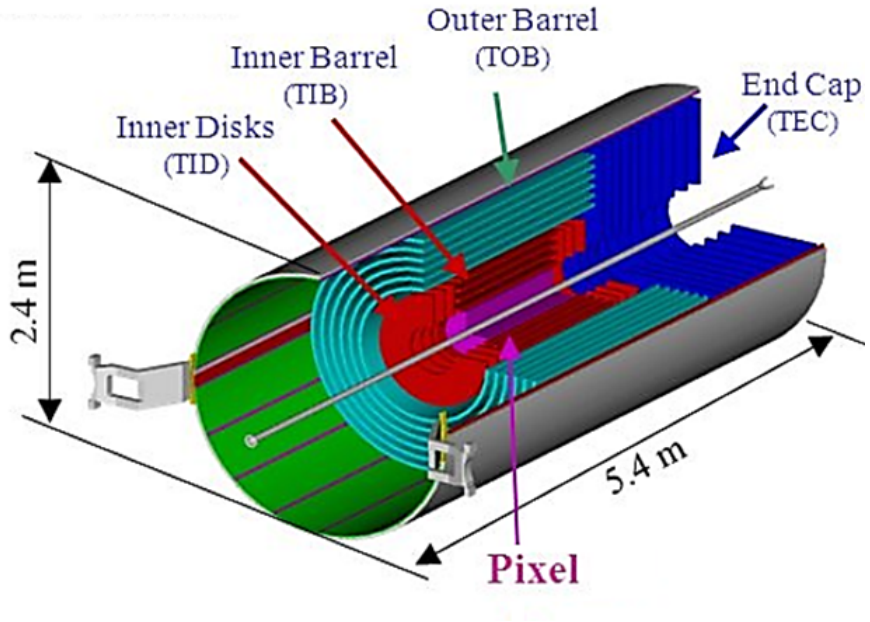

Figure 3.4: Overview of the CMS inner tracking system [26].

Pixel Detector. The inner pixel detector is installed within a distance of 20 *cm* from the beam pipe. It provides high-resolution three-dimensional measurements for the charged track reconstruction. Its excellent resolution allows the measurement of track impact parameter, the identification of *b* and *t-jets* and the reconstruction of vertices in the 3D-dimensions. In overall, the pixel detector consists of three barrel layers (BPix) with two endcap disks (EPix) on each side of the barrel as shown in Figure 3.5a. The 53 *cm* long BPix layers are located at mean radii of 4.4, 7.3, and 10.2 *cm*. The EPix disks extending from 6.1 to 15.0 *cm* in radius are placed on each side at $z = \pm$ 34.5 *cm* and $z = \pm$ 46.5 *cm* [26] [27].

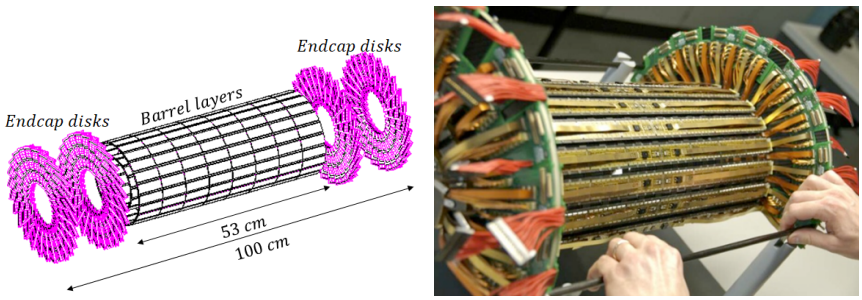

(a) (b)

Figure 3.5: CMS pixel detector: (left) 3D-dimentional view and (right) photo of the detector [26].

It covers an area of about 1 m^2 and consists of 1440 segmented silicon sensor modules with a total of 66 million readout channels with size 100 μm by 150 μm which are implemented into 285 mm thick n-type bulk and p-type backside. They are oriented with the smaller pitch in the azimuthal direction in the barrel and in the radial direction in the disks. The range $-2.5 < |\eta| < 2.5$ covered by the pixel detector matches the acceptance of the central tracker. The spatial resolution of the pixel detector is in the range of 15 - 20 μm [26] [27].

Microstrip Detector. In addition to the pixel detectors, the inner tracker is composed of several layers of silicon microstrip detectors: four-layer Tracker Inner Barrel (TIB), six-layer tracker outer barrel (TOB) and on each side three-disk Tracker Inner Disks (TID) and nine-disk Tracker Endcaps (TEC). The full tracker consists of about 15148 microstrip detectors, with a pitch size ranging from 80 μm to 180 μm. Some of the modules are composed by two detectors mounted back to back with the strips rotated by 100 $mrad$. These double-sided ("stereo") modules also provide a measurement in the coordinate orthogonal to the strips [26] [27].

3.4 Calorimeter System

In accordance with the standard layout, in the CMS detector two types of calorimeters were installed: the internal (electromagnetic) and the external (hadron). In particular, the first one measures the energy of electrons and photons, while the second one measures the energy loss by all the hadrons (i.e. jets formed by the quark hadronization).

Electromagnetic calorimeter. The CMS electromagnetic calorimeter (CMS ECAL) [29] [30] [31] is a hermetic homogeneous calorimeter made of lead tungstate crystals ($PbWO_4$). The ECAL subdetector covers the pseudorapidity range $|\eta| < 3.0$ with 61200 $PbWO_4$ crystals in the barrel, read out by Avalanche Photodiodes (APDs) (see Figure 3.6a (top)), and 7324 crystals in the endcap region, read out by Vacuum Phototriodes (VPTs) (see Figure 3.6a (bottom)).

The use of high-density crystals such as $PbWO_4$ allows the design of a calorimeter which is fast, has fine granularity and is radiation resistant. One of the driving criteria in the design was the capability to detect the decay into two photons of the Higgs boson $H \rightarrow \gamma\gamma$. This capability was enhanced by the good energy resolution provided by a homogeneous crystal calorimeter.

In order to avoid cracks, crystals are mounted slightly turned, so that the crystal axes make a 3° angle with respect to the direction of the nominal interaction point in both the azimuthal ϕ and η projections. The length of the crystals is 230 mm in the barrel and 220 mm in the endcaps, corresponding to 25.8 X_0 and 24.7 X_0 respectively. Crystals are trapezoidal, with a square front

face of $22 \times 22\ mm^2$ in the barrel and $30 \times 30\ mm^2$ in the endcaps, matching the Moliere radius. All crystals are collected in a matrix forming the so-called Super Module and Supercrystal.

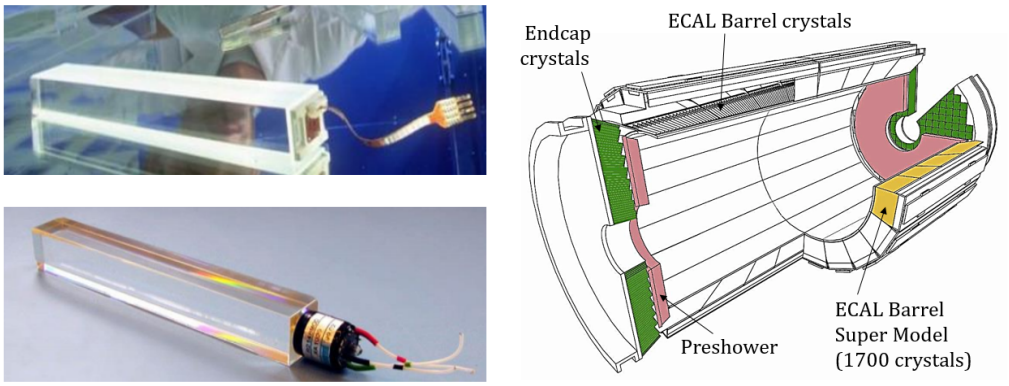

(a) (b)

Figure 3.6: CMS Electromagnetic calorimeter: (left) $PbWO_4$ ECAL crystals with photodetectors attached a barrel crystal with APD capsule (top) and an endcap crystal with a VPT (bottom), and (right) General CMS ECAL layout: Barrel Super Module (yellow), Endcap crystal (green) and Preshower detectors (pink) [29].

In addition to the barrel and endcap crystals, the Preshower detector has been installed, consisting of two lead radiators and two planes of silicon strip detectors, with a total of 3 X_0. The principal aim of the CMS Preshower detector is to identify neutral pions in the endcaps within a fiducial region $1.653 < |\eta| < 2.6$. It also helps the identification of electrons against minimum ionizing particles, and improves the position determination of electrons and photons with high granularity, providing a good measurement of two-photon invariant mass. The CMS ECAL layout is shown in Figure 3.6b.

Hadron calorimeter. The CMS hadron calorimeter (CMS HCAL) [32] measures the energy of the hadrons jets created by the proton-proton interaction. It plays a main role in the identification of neutrinos and exotic particles that do not interact with the detector and whose signature is a non zero transverse energy balance. Due to the fact that the HCAL is placed inside the magnet, materials with short interaction lengths need to be used. Therefore, the main materials, from which the HCAL is made, are the scintillator and the layers of the absorber, mainly brass. The innermost and outermost ones are made of stainless steel whereas the others also consist of brass. A good hermiticity is also requested in order to accurately measure the transverse missing energy.

The HCAL consists of a barrel region up to $|\eta| < 1.3$ (Hadron Barell, 5.4 to 10.6 λ_I), an endcap region up to $|\eta| < 3$ (Hadron Endcap) and a forward region further down the beam pipe at 11.2 m that increases the coverage up to $|\eta| < 5.2$ (Hadron Forward). The limited space for stopping power in the

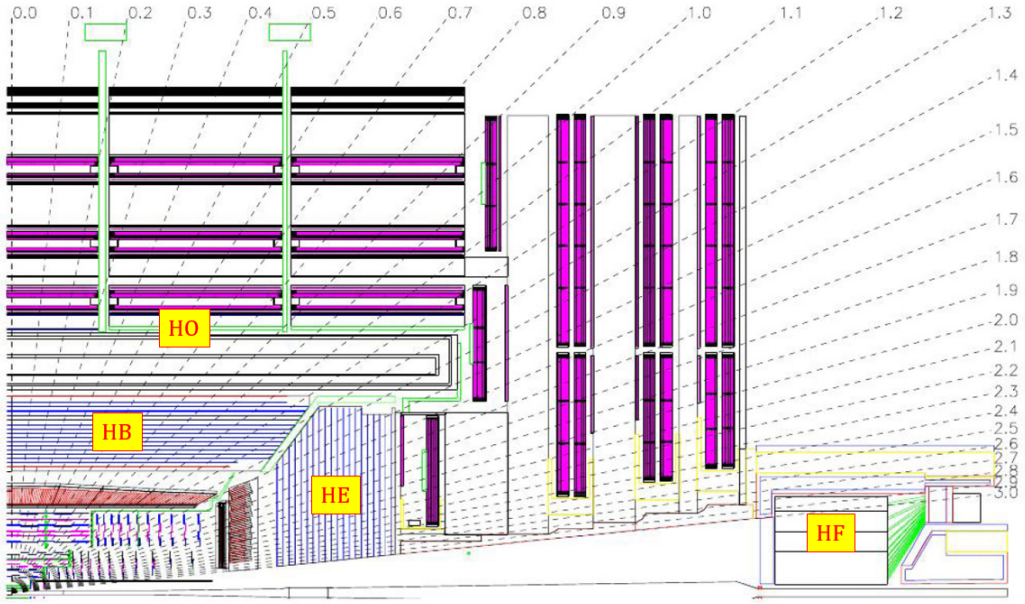

Figure 3.7: A quadrant of the CMS detector with locations of the calorimeters: hadron barrel (HB), endcap (HE), outer (HO) and forward (HF) [32].

barrel region is overcome with an additional calorimeter outside the solenoid up to $|\eta| < 1.3$ (Hadron Outer) that uses the coil and a 19.5 cm layer of steel yoke as the absorber [32]. Figure 3.7 shows the quadrant of the CMS detector with locations of the calorimeters: hadron barrel (HB), endcap (HE), outer (HO) and forward (HF).

In addition, between the brass absorber plates with ≈ 5 cm for HB, ≈ 8 cm for HF, the scintillator tiles with a segmentation depending on η from $\Delta\ \eta \times \Delta\ \phi = 0.087 \times 0.087$ to 0.17×0.17 produce the optical signal that embedded wavelength-shifting fibers take to hybrid photodiodes [32]. The total amount of light summed over the layers of tiles within a given region is a measure for the passing particle energy.

3.5 CMS Muon Spectrometer

Muon detection is a powerful tool for recognizing signatures of interesting processes over the very high background rate expected at the LHC with full and high luminosity. For example, the predicted and confirmed decay of the Standard Model Higgs boson into ZZ or ZZ^*, which in turn decay into 4 leptons, has been called "gold plated" for the case in which all the leptons are muons. This example and others from SUSY models emphasize the discovery potential of muon final states and the necessity for wide angular coverage for muon detection. Therefore, as is implied by the experiment middle name, the detection of muons is of central importance to CMS: precise and robust muon measurement was a central theme from its earliest design stages. The muon

spectrometer has 3 functions: muon identification, momentum measurement, and triggering. Good muon momentum resolution and trigger capability are enabled by the high-field solenoidal magnet and its flux-return yoke. The latter also serves as a hadron absorber for the identification of muons.

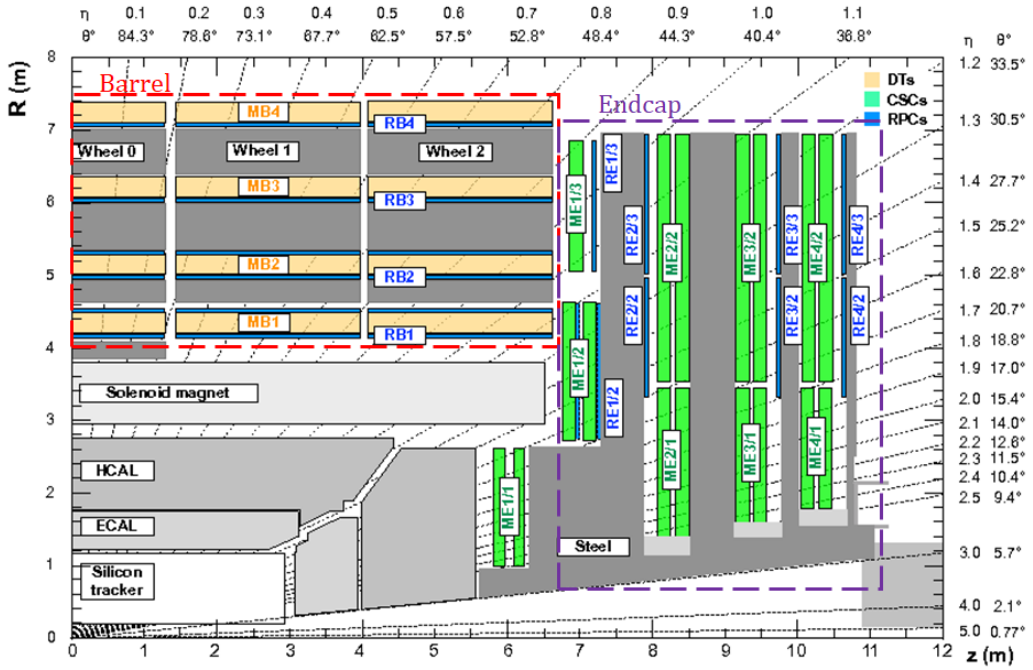

Figure 3.8: Longitudinal view of one quarter of the present CMS Muon Spectrometer [33].

The CMS Muon Spectrometer [33] [34] has been designed to have the capability of reconstructing the momentum and charge of muons over the entire energy range of the LHC. Due to the shape of the solenoid magnet, the muon spectrometer is naturally divided in the cylindrical barrel part and two planar endcap regions. Nowadays, three types of gaseous detector are installed for muon identification, the total surface coverage is around 25000 m^2. The layout of the CMS Muon Spectrometer is presented in Figure 3.8 The gas ionization technology was chosen since the detectors must be relatively inexpensive, reliable and robust.

In the barrel region, where the neutron-induced background is small, the muon rate is low, and the 3.8 T magnetic field is uniform and mostly contained in the steel yoke, drift chambers with standard rectangular drift cells are used. The barrel Drift Tube (DT) chambers cover the pseudorapidity region $|\eta| < 1.2$ and are organized into four stations which are labeled MB1, MB2, MB3, and MB4 in Figure 3.8. In the two endcap regions of CMS, where the muon rates and background levels are high and the magnetic field is large and non-uniform, the muon system uses Cathode Strip Chambers (CSC). With their fast response

time, fine segmentation and radiation resistance, CSC's identify muon in the range $0.9 < |\eta| < 2.4$. There are four stations of CSCs, which are named ME1, ME2, ME3 and ME4 as shown in Figure 3.8, in each endcap, with chambers positioned perpendicular to the beam line and displaced between the flux return plates. In both the barrel and endcap regions ($|\eta| < 1.9$), a third system, composed by Resistive Plate Chamber (RPC) (marked as RB1, RB2, RB3 and RB4 - for barrel and RE1, RE2, RE3 and RE4 - for endcap) is present. This type of detector provides an independent measurement for triggering purposes with a coarser space resolution but a fast time response for unambiguous assignment. All the above muon detectors contribute to the Level-1 Trigger System, providing independent and complementary sources of the information.

3.5.1 Drift Tube

In the barrel the muon detector does not operate in particularly demanding conditions [33] since the occupancy in this region is low and the magnetic field is well contained in the iron plates of the magnet return yoke. For this reason, the Drift Tubes (DT) [33] was chosen. DT system covers the region $|\eta| < 1.2$ and consists of 4 coaxial stations (MB1 to MB4), forming concentric wheels (Wheel 0, $Wheel \pm 1$, $Wheel \pm 2$) which are segmented in 12 sectors around the beam line (total of 250 DT chamber).

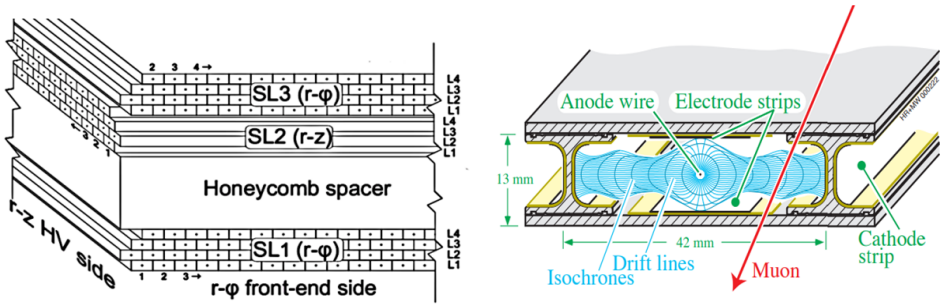

(a) (b)

Figure 3.9: Illustration of the Drift Tube Chamber: (left) schematic view of a DT chamber and (right) the one section of the DT with electric field [33].

The basic detector element is a drift tube cell, whose section is shown in Figure 3.9a. Cells have a size of 42 $mm \times 13$ mm. A layer of cells is obtained by two parallel aluminum planes and by *"I" - shaped* aluminum beams which define the boundary of the cells and serve as cathodes. I-beams are insulated from the planes by a 0.5 mm thick plastic profile. The anode is a 50 μm stainless steel wire placed in the center of the cell. Additional field shaping is obtained with two positively-biased insulated strips, glued on the planes in correspondence to the wire. Typical voltages are $+3.6$ kV, $+1.8$ kV and -1.2 kV for the wires, the strips, and the cathodes, respectively [33].

In addition, the four staggered layers of parallel cells constitute a *Super Layer* (SL), which allows to resolve the left-right ambiguity of a single layer and provides the measurement of a two-dimensional segment (see 3.9a). Also, it measures the bunch crossing time using a generalization of the mean-timer technique: this permit to originate a segment that does not need any external input (trigger). A chamber is composed by two SL measuring the $r - \phi$ coordinates, with the wires parallel to the beam line, and an orthogonal SL measuring the $r - z$ coordinates. The latter is not presented in the outermost MB4 station because MB4 only has the 8 layers measuring the ϕ coordinate [33].

The DT are gaseous detectors and their working principle is based on the produced ionization of the gas volume of the detector caused by the passing of a charged particles (see 3.9b). The used gas mixture is a Ar/CO_2 (85/15) which provides good quenching properties and a saturated drift velocity, of about 5.6 $cm/\mu s$. The maximum drift time is, therefore, $\sim$ 375 ns, i.e. 15 bunch crossing. A single cell has an efficiency of about 99.8% and a resolution of $\sim$ 180 μm [33].

3.5.2 Cathode Strip Chambers

The Cathode Strip Chamber (CSC) [33] is one of a type of the gaseous particle detectors, combining cathode strips running along η, and perpendicular anode wires measuring the η coordinate. These multi-wire proportional chambers have the good spatial and time resolution and can operate at high occupancy levels and in the presence of the large inhomogeneous magnetic field. For this reason, they were adopted for the endcap region. General view and picture of the CSC chambers are shown in Figure 3.10 and Figure 3.11.

CMS CSC system uses of 540 chambers covering the endcap region of $0.9 < |\eta| < 2.4$. CSC chambers are arranged in four disks (stations) placed between the iron disks of the yoke (see Figure 3.8) and directed perpendicular to the beam line. The innermost station consists of three concentric rings (ME1/1, ME1/2 and ME1/3), the first being closer to the interaction point. The other stations are composed by two disks only (ME2/1, ME2/2, ME3/1, and ME3/2). The rings are formed by 18 or 36 trapezoidal chambers with two different sizes covering either 10° or 20° in the azimuthal angle ϕ direction with a small overlap in ϕ (the exception of the outermost ring of ME1/1).

CSC chamber consists of 6 gas gaps 9.5 mm thick (see Figure 3.10), each composed by an array of anode wires between two cathode planes. The wires are held at a potential value from 2.9 kV to 3.6 kV. One of the cathode planes is segmented into strips orthogonal to the wires, disposed in the radial direction to measure the *phi*-coordinate. The strip pitch range is 8.4-16 mm and the distance between wires is 2.5-3.16 mm depending on their location in the chamber. The avalanche produced by crossing particle in the $Ar/CO_2/CF_4$ (40/50/10) gas volume induces a charge in several adjacent strips. A precise

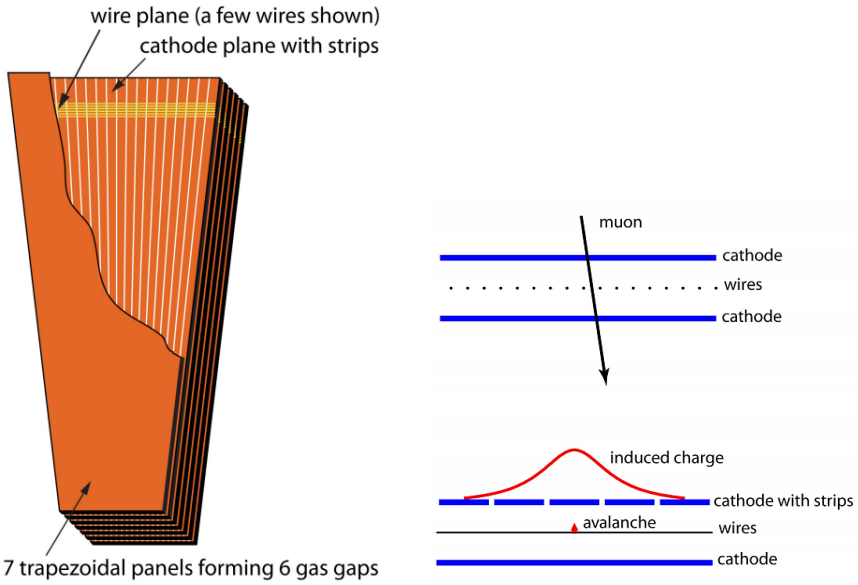

(a) (b)

Figure 3.10: Illustration of the Cathode Strip Chamber: (left) the layout of a CMS CSC with local chamber coordinates and (right) the cross-sectional view of the gas gap in a CSC, with a schematic illustration of the gas ionization avalanche and induced charge distribution on the cathode strips [33].

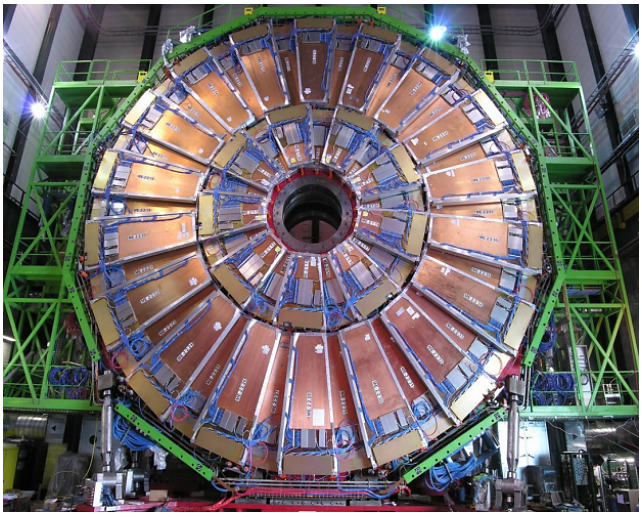

Figure 3.11: Pictures of the CSC chambers installed at CMS detector [33].

spatial measurement is obtained by interpolating the strip signals achieving a resolution of about 50 μm. The r coordinate is measured by the wires which, to reduce the number of channels, are read out in groups of 5 to 16 with a resolution of 0.5 cm [33].

3.5.3 Resistive Plate Chamber

The Resistive Plate Chamber (RPC) [33] is the third type of gaseous detector installed both in the barrel (along with DTs) and endcap regions (along with CSCs), covering $|\eta| < 1.9$ (see Figure 3.8). A total of 1056 RPC detectors with total active area of 3500 m^2 is used in the CMS Muon Spectrometer. The RPC system is complementary to the DT and CSC systems and adds robustness and redundancy to the muon trigger. In the barrel region the RPC system is distributed in five wheels ($Wheel\ 0, Wheel\ \pm 1, Wheel\ \pm 2$) around the beam pipe. Each wheel is divided into 12 sectors, covering the full azimuthal dimension. Each sector consists of four layers of DTs and six layers of RPCs, with a total of 480 RPC stations: the first four are attached to each side of MB1 and MB2, and the other two are attached to MB3 and MB4 DT chambers. Each barrel RPC station is composed of two or three adjacent RPC partitions, called *"rolls"*, making a total of 1020 rolls for the barrel RPC system. This geometry difference is driven by the need to have the adjustable trigger on muons with different transverse momentum p_T. The endcap region has 576 trapezoidal shapes of chambers, covering 10° of the azimuthal angle. RPC chambers are installed in 8 disks (4 for the positive side and 4 for the negative side from the interaction point). Endcap RPCs are divided in 3η-partitions or in the total of 3 rolls.

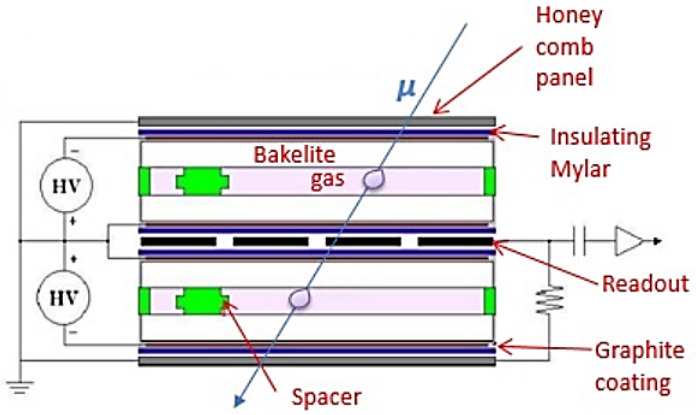

Figure 3.12: Principle scheme of a double-gap RPC chamber [33].

The RPCs used by CMS are double-gap chambers composed by four 2 mm thick HPL (*High Pressure Laminate*) planes externally coated with graphite, as shown in Figure 3.12. Insulated copper strips are placed in the middle, to

collect the signal induced in the gas mixture 95.2% $C_2H_2F_4$ (*tetrafluoroethane*), 4.5% $i - C_4H_{10}$ (*isobutane*) and 0.3% SF_6 (*sulphur hexafluoride*) by crossing particles. The readout strips have different geometry depending on which part of the system they are in: the barrel chambers have rectangular shaped strips, while in the endcap chambers their shape is trapezoidal. The pitch of the strips depends on the distance to the beam pipe varying from 1.5 cm for the innermost stations to 4 cm for the outermost stations.

The two innermost electrodes are kept at -9.6 kV and the RPCs operate in *"avalanche"* mode, rather than in the more common for this technology *"streamer"* mode, obtained with a lower electric field and allowing to sustain higher rates. However, in this case, the gas multiplication is reduced, and improved electronic amplification is required. The two-gap design is adopted to increase the charge induced on the strips. The spatial resolution provided by RPC is limited by the strip pitch but are characterized by an excellent time resolution, of the order of few nanoseconds.

3.6 CMS Trigger Systems

The LHC delivers proton-proton collisions at a rate of 40 MHz and the data produced by the CMS experiment are orders of magnitudes too large to be stored. The typical size of one event recorded by the CMS detector is about 1 MB, and it would be technically impossible to stream about 40 TB/s to disk. However, even if possible, the added scientific value would be questionable since most of the events only contain low-energy glancing collisions rather than inelastic hard scattering processes. The required reduction of the event rate is achieved by the so-called trigger system [35] [36] [37]. The aim of the trigger is the selection of potentially interesting events and the reduction of the rate to a manageable value of a few hundred Hz. While most high energy physics experiments use three trigger levels, the CMS trigger system implements a two-stage (Figure 3.13), rate reduction which provides additional flexibility. The first is the Level-1 (L1) [36] trigger, which is largely based in Field Programmable Gate Arrays (FPGAs) and Application Specific Integrated Circuits (ASICs), and therefore uses the coarse and crude information to reduce the rate from 40 MHz to 100 kHz. The second is the High-Level Trigger (HLT) [37], which is a software-based system, implemented in computing facility with approximately 16000 CPU cores, that reduces the L1 trigger rate to a viable level for storage of about 100 Hz.

3.6.1 Level-1 Trigger

The Level 1 Triggers (L1) are hardware based online triggers, meaning that they decide whether to save the events or not, directly after they have been recorded by the detector. In fact, the decision has to be made within 3-4 μs after each collision, because the data saved in the buffer are overwritten after

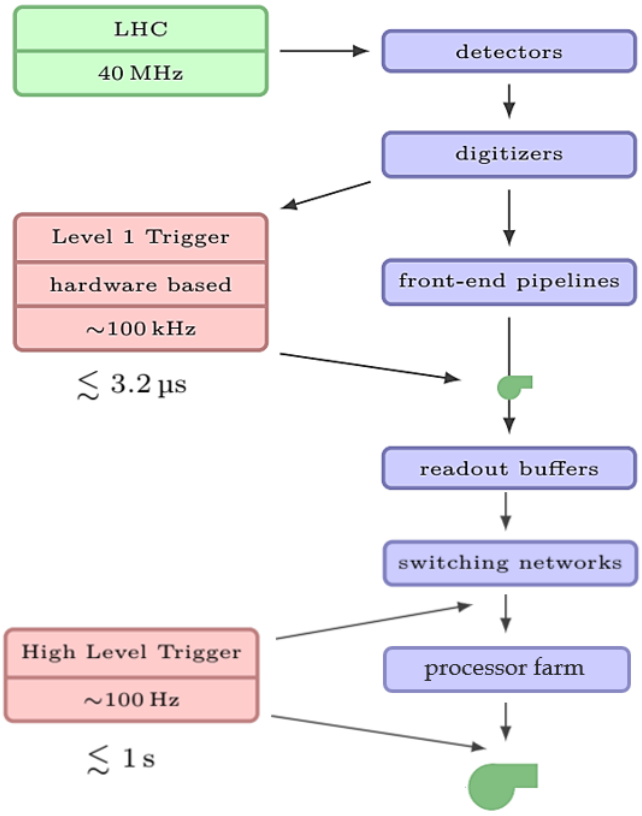

Figure 3.13: The architecture of the CMS Trigger System [35].

this period. The L1 triggers lead to a reduction of the event rate from 40 MHz to 100 kHz, which is low enough to be saved and transferred to a computer facility.

A schematic of the architecture of the Level 1 Trigger is shown in Figure 3.14 and consists of the following components:

- The Calorimeter trigger preserves the local energy sums from the ECAL, HCAL and HF individual readout cells or towers and reconstructed candidates of electrons, photons, taus, and jets. This information is the Trigger Primitive Generator (TPG) which is transferred to the Regional Calorimeter Trigger (RCT), which identifies electrons, γs, τs and hadron jets candidates. The formed trigger primitives with sums of transverse energy from RCT are sent to the Global Calorimeter Trigger (GCT), where the best four candidates from each category go to the last step in the L1 hierarchy, i.e. the L1 Global Trigger.

- The Muon Trigger which is focused on μ preselecting. Information from DT, CSC, and RPC is used to drop events with low-quality muons. The trigger information from the different muon chambers is send to the Global Muon Trigger (GMT). Then the Global Muon Trigger collects,

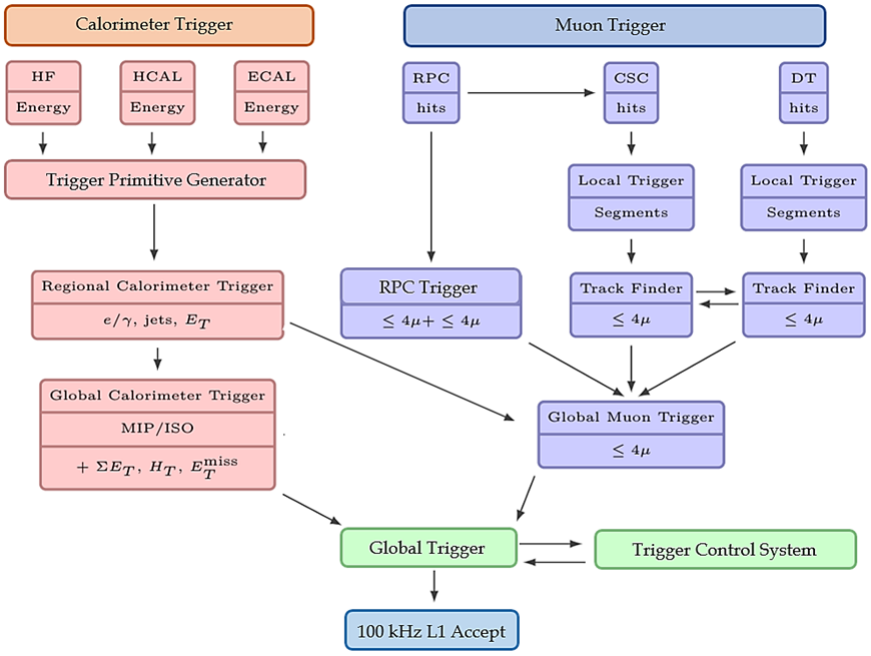

Figure 3.14: Architecture of the Level 1 Trigger [36].

combines and converts the information from all three systems into the same η, ϕ, and p_T scale in order to correlate the muon tracks. Finally, estimates only the four best muon objects and sends them to the L1 Global Trigger.

- The Global Trigger is the last step in the L1 Trigger architecture. It decides whether to reject or accept the event information received from the GCT and GMT to be further analyzed at the HLT. This decision is based on the various algorithms and readiness of the sub-detectors and the DAQ system, which is in turn determined by the Trigger Control System (TCS).

3.6.2 High-Level Trigger

The High-Level Trigger (HLT) is implemented software running on a farm of commercial computers which includes about 16000 CPU cores and reduces the L1 Trigger output rate to the sustainable level of storage and physics analysis of about 100 Hz. The HLT software consists of a streamlined version of the offline reconstruction algorithms.

The HLT menu in CMS has a modular structure, which is graphically depicted in Figure 3.15. The HLT modular design is such that it allows logically independent trigger path, which to a large extent could be run in parallel. Each trigger path is the sequence of software modules and classified based on their function, there are reconstruction modules (*producers*) and filtering modules (*filters*). The latter usually accept or reject events based on the properties

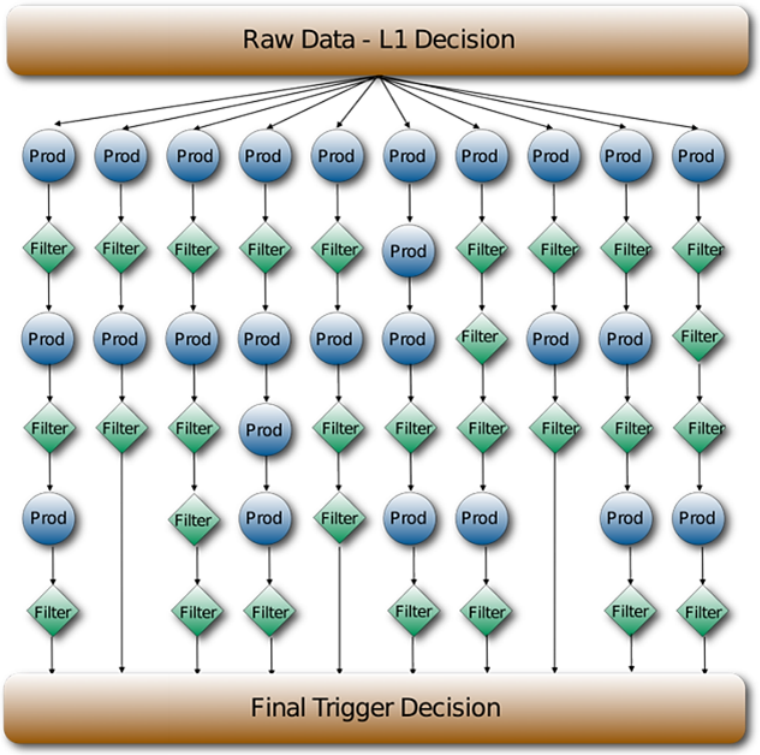

Figure 3.15: Schematic representation of a HLT menu in CMS and of the HLT paths in it [37].

of physics object or kinematic variables. The HLT modules are organized in ascending complexity, such that the faster algorithms are executed first and thus the filters can reject events at an earlier stage.

The reconstruction modules and selection filters of the HLT use the software framework that is also used for offline reconstruction and analyses. Upon completion, accepted events are sent to another software process, called the storage manager, for archival storage. The event data are stored locally on disk and eventually transferred to the CMS Tier-0 computing center for offline processing and permanent storage. Events are grouped into a set of non-exclusive streams according to the HLT decisions.

3.7 Overview of CMS Upgrade Project

The period between 2011 and 2012 was marked as the first major physics run where the LHC collider continuously worked at the peak the luminosity of $7.6 \times 10^{33}\ cm^{-2}s^{-1}$, i.e. more than 75% of its design luminosity, and delivered an integrated luminosity of 30 fb^{-1} to ATLAS and CMS. At the time of the finalization of this Doctoral Thesis, the LHC machine works at luminosity value of $1 \times 10^{34}\ cm^{-2}s^{-1}$ and by 2027 LHC will foreseen to increase this value up to 5-7 $\times\ 10^{34}\ cm^{-2}s^{-1}$ five times more those value for which CMS was

designed. All the system of CMS detector requires upgrades to preserve the efficiency, resolution, and background rejection of the detector at the higher luminosity. The scientific goals now ahead of the LHC experiments concern precision Higgs studies and the search for new physics; both motivations bring indeed a powerful demand for higher luminosities.

3.7.1 Schedule of the Upgrades

In order to open full physics potential, the LHC needs to be upgraded gradually, both the accelerator complex and its experiments. There are two major aspects of the LHC upgrade: the increase of the center-of-mass energy and the increase of the instantaneous luminosity to search very rare physics phenomena. The summary of the present schedule of the LHC upgrade with the various shutdowns and the expected improvements of the beam performance is shown in Figure 3.16 and the projected LHC instantaneous and integrated luminosity as a function of time up to 2037 in Figure 3.17.

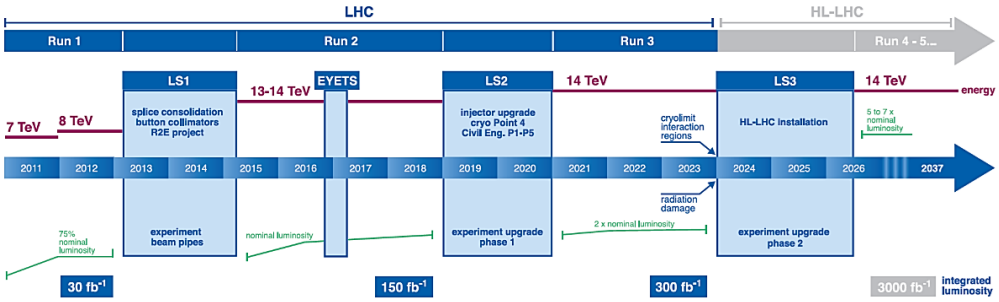

Figure 3.16: The LHC upgrade schedule [39].

The LHC is currently in its first cycle, called Phase-I [39]. The first upgrade was successfully performed during Long Shutdown 1 (LS1) between 2013 and 2014: the magnet interconnections were improved that allowed to increase the center-of-mass energy from 7 TeV to 13 and soon 14 TeV. Moreover, the bunch-spacing has been reduced to 25 ns and luminosity reached the design value of 10^{34} $cm^{-2}s^{-1}$ with 25 pile-up interactions. After LS1, the LHC Run-2 was started and the operation was continued until the integrated luminosity of 150 fb^{-1}. The second long shutdown (LS2) will take place starting from beginning 2019 to the end of 2020. The accelerators will stop again to upgrade the injector chain in order to increase the luminosity up to 2×10^{34} $cm^{-2}s^{-1}$. The LHC is expected to start the Run 3 in 2021 and operate continuously until 300 fb^{-1}. Also, this period will be used to upgrade all detectors for running at this new value of luminosity and at an expected average pile-up of 50. During the LS2, CMS experiment foresees to replace the pixel detector and to upgrade the trigger as well. Finally, the next phase of planned LHC operation called High Luminosity LHC (HL-LHC) or Phase-II [40] will begin with the third Long Shutdown (LS3) in the period from 2024 to middle of 2026,

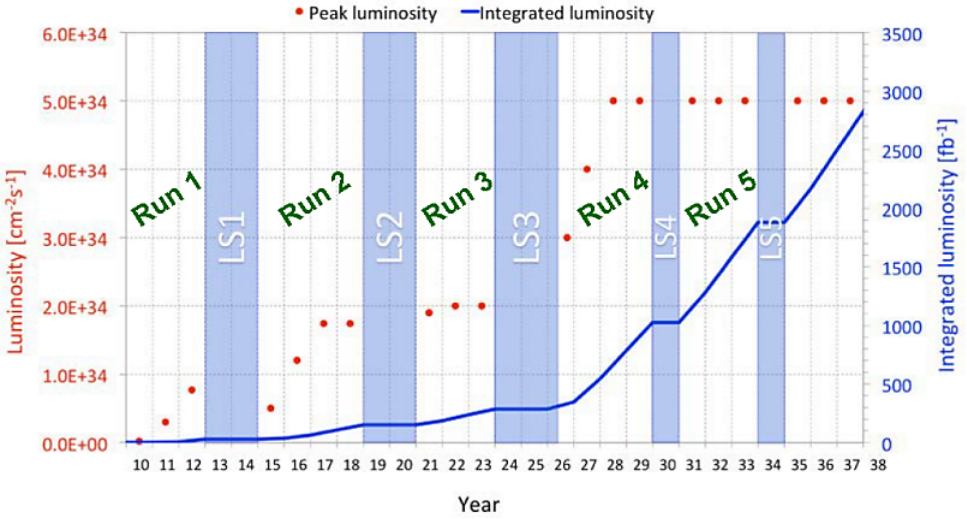

Figure 3.17: Expected LHC instantaneous and integrated luminosity as a function of time up to 2037. Dates for long-shutdowns (LS) periods are also marked [39]

where the machines and detectors will be upgraded to allow for pp running at a luminosity of 5×10^{34} $cm^{-2}s^{-1}$ and the expected average pile-up of 140. In the HL-LHC program, the accelerator machines will continuously operate with the aim of integrating a total luminosity of 3000 fb^{-1}. In particular, the CMS will completely replace the tracking detector and will make many other changes to sub-detectors and the trigger and data acquisition systems.

The upgrades of the LHC and its experiments will be allowed to investigate the properties of the the Higgs boson: it will be measured up to the highest achievable precision, including its self-coupling, while additional Higgs bosons and exotic decays will found or excluded. At the higher luminosity, the search for supersymmetric particles will be intensified and the precision of top and electroweak measurements will continuously improve. All CMS upgrades are designed to enable these physics goals by not only mitigating the effects of radiation damage and higher luminosity but by maintaining the existing performance of the detector in key areas relative to the data taking at 13 TeV. The upgrade activities foreseen involves muon detectors, hadron calorimeters, the pixel detector, the trigger and data acquisition, and the beam radiation monitoring and the luminosity measurement system.

3.7.2 Motivation

During the Phase-I and Phase-II periods, the peak luminosity is expected to exceed the design value by a factor of two and three, respectively. After that, a series of problems must be solved to operate successfully throughout these periods. All these challenges are related to high background environment to which all CMS subsystems will be exposed to. In the CMS detector, the most of

the occurring interactions classify as "soft" because they are dominated by the non-perturbative regime. It means, that they do not make high mass states nor they are considered for the search of the electroweak and Beyond the Standard Model (BSM) physics. High mass states, called "hard" collisions, produce very rarely. For a successful analysis, the CMS detector must distinguish with a sufficient efficiency between "soft" and "hard" collisions. The "pile-up" is the occurrence of many proton-proton interactions in a single crossing corresponding to 25 ns. As an example, in Figure 3.18 a high-pile-up event with some reconstructed vertices is shown. The presence of such pile-up makes the discrimination between types of collisions more difficult. Thus, at the high luminosity, CMS L1 trigger performance will degraded continuously. The Muon Spectrometer and the hadron calorimeters upgrades will be aimed to preserve the L1 trigger capability.

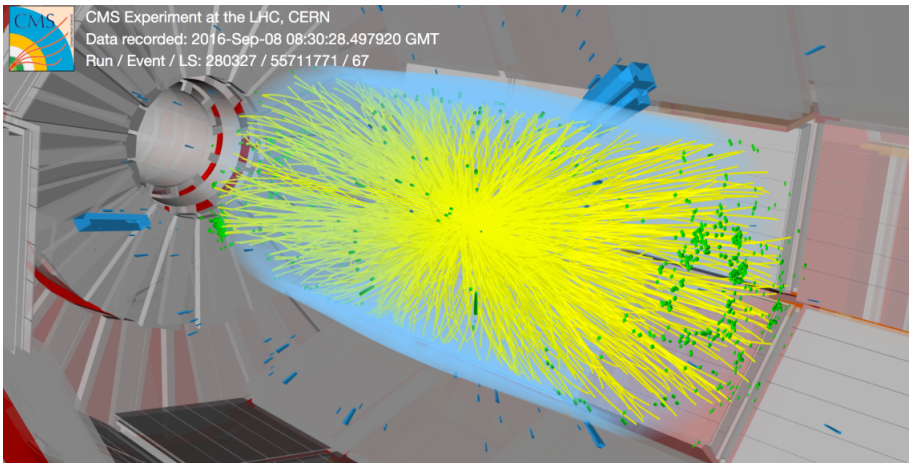

Figure 3.18: A high-pileup events (yellow) with some reconstructed vertices (green) [40]

When the pile-up occurs in the same crossing as the interesting triggered event, it is called "in-time pile-up". On the contrary, when there is signal contamination from preceding or following crossings, we speak of "out-of-time pile-up". This is caused by the intrinsic response of the sensor, or because the electronics takes longer than the 25 ns bunch crossing interval. The contamination is unlikely if the occupancy of a given channel is small: increasing the segmentation of a detector is, therefore, one way to counteract out-of-time pileup.

Also, the integrated luminosity will be affected by the resolution and efficiency of the detector. Ionizing radiations is one of the main sources of detectors damage. The development of radiation hard or radiation tolerant sensors and electronics is a major Research and Development (R&D) effort for experiments installed at LHC. Most CMS detectors can sustain the integrated luminosity of Phase-I with at most slight degradation. But for Phase-II, the replacement of damaged detectors operated during Phase-I will be necessary.

It is also worth noting other effects, not related with pp-collision which can be a motivation for upgrade studies.

- *Cosmic rays:* The cosmic rays are continuously passing through the detector. Occasionally, they will occur in time with a trigger and may be overlaid on the event and be recorded as part of the crossing data. Some may pass through the pixel detector and be close enough to beam spot to mimic genuine tracks from interactions.

- *Beam halo:* Machine-induced secondary particles are produced in showers which are initiated by collisions of the beam with the material of the beam pipe or collimator. In addition to these scattering processes, charged particles are deflected by the magnetic field of the beam optics. These so-called beam halo particles are one of the main sources of beam background at the LHC. These particles are especially troublesome for large area systems such as the muon detectors.

- *Beam-gas interactions:* The protons in one of the beams can hit a residual gas molecule inside the vacuum pipe and interact with them. The collision products may reach the detector a direct path or may strike other material producing more secondaries that eventually reach the detector.

- *The residual radiation:* The particles passing through CMS can activate the elements of the detector producing various radionuclides. Their decay products may cause signals in some detectors.

All these effects also worsen the operation trigger and affect the quality of the identification and reconstruction of the rare events.

3.7.3 Overview of the expected CMS upgrades during the technical stop, LS2, and LS3

The basic goal of the CMS experiment upgrade is to maintain the excellent performance of the detector subsystems in terms of efficiency, resolution, and optimize the reconstruction of the particles at higher luminosities.

Traker. The CMS pixel detector is the innermost sub-detector, located close to the collision point. This detector provides important information to reconstruct the tracks and vertices of charged particles. The present pixel detector was designed to work efficiently at maximum instantaneous luminosity up to1×10^{34} $cm^{-2}s^{-1}$ only and cannot operate for HL-LHC program. The upgrade plan of the pixel systems will be executed during Phase-I and Phase-II. During the Phase-I, the upgrade of the pixel tracker was focused on the replacement of the present pixel detector during the end of year technical stop

of 2016/2017. Due to the fact that the entire tracker will suffer significant radiation damage by LS3, the tracker must be completely replaced for Phase-II. The granularity of both the outer tracker and the pixel systems will be increased by a factor 4. In the outer tracker, the lengths of silicon sensor strips will be shortened without modifying the pitch. Design improvements will lead to a much lighter outer tracker, improving, therefore, the p_T resolution and providing a lower rate of $\gamma-$conversions. Moreover, the module design will provide track-stub information to the L1 trigger at 40 MHz for tracks with $p_T > 2\ GeV/c$, ensuring meaningful power rejection at the earliest stage of the event selection. The pixel system will implement smaller pixels and thinner sensors for improved impact parameter resolution and better two-track separation. The system coverage will be extended to almost $|\eta| = 4$, thanks to the addition of up to 10 additional pixel disks in each of the forward regions [40].

Calorimeters. The hadron calorimeter upgrades for Phase-I was planned to modify the HCAL Barrel (HB), the HCAL Endcap (HE) and the HCAL Forward (HF). HF was designed to measure hadronic energy from jets in the region of $3.0 < |\eta| < 5$. HF calorimeter is a Cherenkov calorimeter comprised of a steel absorber through which quartz fibers are run to collect the Cherenkov light. The light from the quartz fibers is then sent to Photomultiplier Tubes (PMTs) from which an electric signal is produced that is read out and digitized by the front-end electronics. During Run 1, anomalous signals were identified caused by muons or particle showers producing Cherenkov light in the windows of the PMTs. These produce unwanted signals, which are difficult to reject at increasing luminosity. In order to provide a more robust method of rejection, the Phase I upgrade of the HF calorimeter has been done. The upgrade was made in two steps: a replacement of the current phototubes with a multi-anode version which has a thinner window and the replacement of the front-end electronics responsible for the readout. The main problem of the HE and HB is related to the operation of the Hybrid Photodiode which was chosen for their magnetic field tolerance and gain greater than 2×10^3. In this case, the high voltage applied to these devices led to electrical discharges, which are a source of high-amplitude noise and a risk to the longevity of the HPDs themselves. For this reason, the Collaboration decided to substitute them, together with their electronics, with Silicon Photomultiplier (SiPM). For Phase-II the replacement of the electromagnetic and hadronic endcap calorimeters has been also planned due to the possibility of the radiation damage by LS3. The new calorimeter is called the High Granularity Calorimeter. It includes excellent transverse and longitudinal segmentation, allowing detailed three-dimensional images of particle showers. Its electromagnetic sensor consists of 28 tungsten plates interleaved with silicon sensors as the active material. The sensors have pads of size around 1.0 cm^2. This section has 25 X_0 and one hadron interaction length (λ). The hadronic part has a front section comprising 12 stainless steel plates interleaved with silicon sensors for a depth of 3.5 λ. This covers the hadronic shower maximum measurement. It is followed by a backing hadron calorimeter

of similar design to the current endcap hadronic calorimeter detector, brass plates interleaved with plastic scintillating tiles read out with a wavelength shifting fiber, to provide an overall depth of $\sim 10\lambda$ for the full calorimeter [40].

Beam radiation instrumentation and luminosity measurement system. The Beam Radiation Instrumentation and Luminosity control (BRIL) of the CMS experiment are responsible for measuring: luminosity, machine induced background and beam timing. BRIL systems also provide active protection in case of intense beam loss events and give various inputs to the CMS trigger system. In order to ensure reliable luminosity and beam background monitoring for HL-LHC, all the installed beam monitoring devices for Phase-II that are located in high radiation environments close to the beam pipe will be completely replaced due to radiation damage. In this upgrade activity, the beam radiation protection system will be modernized by new polycrystalline diamond sensors and the Machine Induced Background (MIB) and Luminosity measuring systems in the Pixel volume will also be changed [40].

Trigger. Concerning the Level-1 trigger: the electronics for the calorimeter trigger, muon trigger, and the global trigger are planned to be improved. For this aim, during the Phase-I the high bandwidth optical links for most of the data communication between trigger cards was installed, and modern, large FPGAs and large memory resources for the trigger logic were used. Using optical links allows to change the architecture very faster, while large FPGAs allow algorithms to evolve as needed. For Phase-II, the latency of the current L1 trigger will be will be increased from 3.4 μs to 12.5 μs to be provide sufficient time for the hardware track reconstruction and matching of tracks to muons and calorimeter information. Due to this increasing time information readout, the front-end electronics in some present sub-detectors must be upgraded. Taking into account the expected performance of the trigger with track information, the proposed L1-trigger acceptance rate is 500 kHz for beam conditions yielding 140 pileup. This will allow CMS to maintain thresholds comparable to those that will be used in a typical Phase-I trigger menu. To retain comparable performance in beam conditions that result in 200 pileup, the L1 rate must increase to 750 kHz, and so all detectors will have readout capabilities compatible with this possibility. To satisfy these trigger requirements, the Muon system readout electronics in the CSCs and in the DT readout should be upgraded as well [40].

3.8 Overview of the Phase-2 Upgrade of CMS Muon Spectrometer

The muon detectors play a central role in CMS. Muon particles detection is a powerful tool for recognizing signatures of interesting physics processes over the high background rates at the LHC, such as Higgs boson decay $H \to 4\mu$ and B-meson decay $B \to 2\mu$. The Muon Spectrometer has three main functions:

- muon triggering;
- muon identification;
- momentum measurement.

Good muon momentum resolution is provided by the high spatial resolution of the detector and the high magnetic field of the superconducting solenoidal magnet and its flux-return yoke. Thus, the CMS muon system was designed to measure the momentum and charge of muons over a large kinematic range. During the next HL-LHC program, the CMS Muon Spectrometer is to preserve the present muon triggering and reconstruction capabilities which were achieved at the Run-1. In order to reach these aims, it will be necessary to mitigate the efficiency loss due to the aging effect of the existing detectors and to improve the offline reconstruction resolution. In addition, a new Track Trigger, which would match candidate tracks with p_T in the inner tracker to muons at L1 Trigger, will require ultra-high purity muon triggering with low thresholds for a very low fake rate.

3.8.1 The Upgrade of the Existing Muon Stations

As described in Section 3.5, the CMS Muon Spectrometer consists of three types of gaseous detectors: Cathode Strip Chambers, Drift Tubes, and Resistive Plate Chambers. While operating very well at the designed luminosity of LHC, upgrades are foreseen for each of the subsystems, necessary to guarantee its role of muon triggering and tracking also in the HL-LHC phase.

Cathode Strip Chambers. The CSC upgrade plans are focused on electronics, in particular foreseeing the replacement of cathode front-end boards (CFEB) on inner chambers in order to handle the increased L1 trigger latency and rate. The CFEB use analog charge storage within custom Switched Capacitor Array (SCA) chips (ASICs) that sample at 50 ns intervals and contain a depth of 96 cells. These boards are used on all CSCs except ME1/1 chambers which, in 2013-2014, have undergone an upgrade of the front- and back-end electronics to improve rate capability and performance at higher luminosity. With the increased L1 trigger latency (up to 12.5 ms) and rate (up to 750 kHz) that is planned for HL-LHC CMS operation, the 108 inner CSC chambers (ME2/1, ME3/1, and ME4/1) will fill the SCA cells; consequently, no additional data can be stored, causing readout inefficiency. Therefore, the CFEBs will be replaced by boards similar to the "digital" DCFEBs that have already been installed on the ME1/1 chambers. These boards flash-digitize the data continuously and store them in large digital buffers, resulting in zero dead-time and the capability to handle latencies well beyond the current specification. They also send their output data on 3.2 Gb/s optical links, as compared to 1 Gb/s achievable on the copper output cables of the CFEBs; the

higher output data capability of the DCFEBs is important to handle the HL-LHC and CMS L1 trigger conditions. Some additional elements of the CSC data acquisition system, namely the Data Acquisition Motherboards (DMBs) and Detector-Dependant Units (DDUs) that connect to the DCFEBs will be replaced as well in order to handle the high data throughput using the fast optical links. Due to the fact, that new electronics will consume more power, the LV system will be redesigned. Higher background rates and the need for a more accurate monitoring of CSC currents will also imply an incremental upgrade for the present HV system [34] [40].

Drift Tube. DTs modernizations are also focused on electronics. It is known that DT electronics will need replacement due to limited radiation tolerance of some components; this replacement also gives the opportunity to increase the trigger rate capability and performance, and improve maintainability. Each DT chamber houses the L1 Trigger and Readout electronics in an aluminum profile, called a Minicrate, which hosts the time digitization logic and the logic for the L1 trigger primitive generation. During HL-LHC the survival of this system is not guaranteed, and will not be able to cope with increasing the Level 1 trigger acceptance rate beyond 300 kHz. In order to increase their reliability and improving their performance, the DT upgrade will focus in moving them to the Underground Control Room where the environment is more congenial. Moreover, this replacement will allow the implementation of full time (and therefore space) resolution and to provide complete chamber information in the DT trigger system, with improved performance in terms of rate reduction and better matching with the tracker at the Level 1 trigger [34] [40].

Resistive Plate Chambers. During LS1 the fourth RPC endcap station was instrumented in the η region up to $|\eta| = 1.6$. One of the more important requirements of the muon trigger is the achieving of the good enough resolution to identify high-p_T tracks. With the RPC trigger requiring segments in at least three stations, the endcap system did not have the necessary redundancy to control the trigger rate at the increased luminosity while preserving high trigger efficiency. The addition of the fourth layer called RE4 helped to provide the finer timing and redundancy to the corresponding CSC station and preserved a low-p_T threshold [34] [40].

Figure 3.19 shows the simulated trigger efficiency as a function of η is shown in case of the present 3 layers compared to the result for a 4-layer system. The advantage in extending the detector to include the fourth station is clearly evident. RE4 has been installed on the back of the YE3 yoke during LS1, mounted independently of the CSC chambers.

For Phase-II, CMS RPC Collaboration have planned two important upgrades:

- on the existing RPC chamber, which will be continuously operated until the end of 2026, the link system must be replaced.

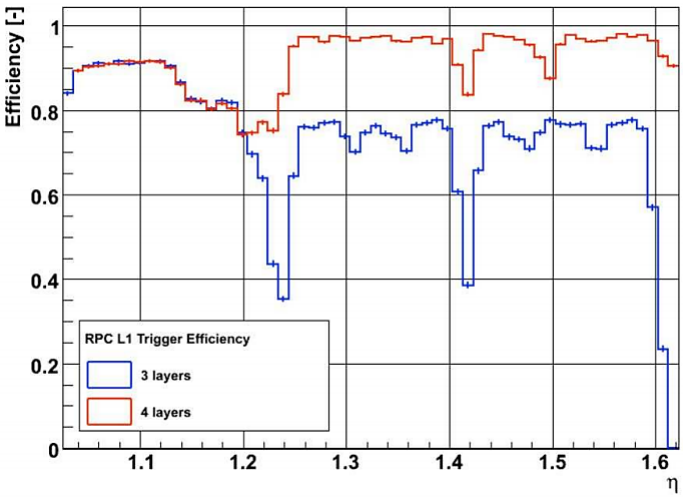

Figure 3.19: Simulated trigger efficiency as a function of the η number of layers numbers of RPCs [34].

- on additional set of new RPC detector will be installed in the high-η regions.

3.8.2 New Stations in the innermost region of the CMS forward Muon Spectrometer

In the region $1.5 < |\eta| < 2.4$ the muon system currently consists of four stations of CSC only. It is the only region of the muon detector that lacks redundant coverage despite being a challenging region for muons in terms of backgrounds and momentum resolution. To maintain good L1 muon trigger acceptance in this region it is therefore proposed to enhance these four stations with additional chambers that make use of new detector technologies with higher rate capability, as originally proposed by the design of CMS.

The CMS Collaboration is planning to install the detectors based on the Gas Electron Multiplier (GEM) [34], [38]. technology and improved generation of the Resistive Plate Chamber (iRPC) that could withstand the hostile environment and high luminosity rates at the LHC and its future upgrades. iRPCs are the same type of RPC technology using for the existing CMS muon system but have improved characteristics. Expected detection efficiency around 96% - 97% even for rate exceeding few kHz/cm^2, good spatial resolution of order 1.5 cm, and good time resolution of order $\sim 1-2$ ns at the efficiency plateau for $C_2H_2F_4/i-C_4H_{10}/SF_6$ (95.2/4.5/0.3) gas mixture.

iRPC detectors are approved to instrument two forward regions at $1.8 < \eta < 2.4$ (see Figure 3.20), called RE3/1 and RE4/1 station during the annual Year-End Technical Stops 2022 & 2023, respectively. The RE3/1 and RE4/1 detectors are "trapezoidal shape chambers", each made of a double layer of the

trapezoidal gas gap. They will cover of 20° in RE3/1 and in RE4/1 stations, overlapping in φ just like the corresponding CSC detectors in ME3/1 and ME4/1 stations, complementing them and providing redundancy and enhanced triggering and tracking capabilities in the region which currently suffering from the highest background rates and a non-uniform magnetic field. Therefore, 36 iRPC chambers will be installed for the RE3/1 station and 36 for the RE4/1 station in each muon endcap in order to ensure the full azimuthal coverage [34], [40].

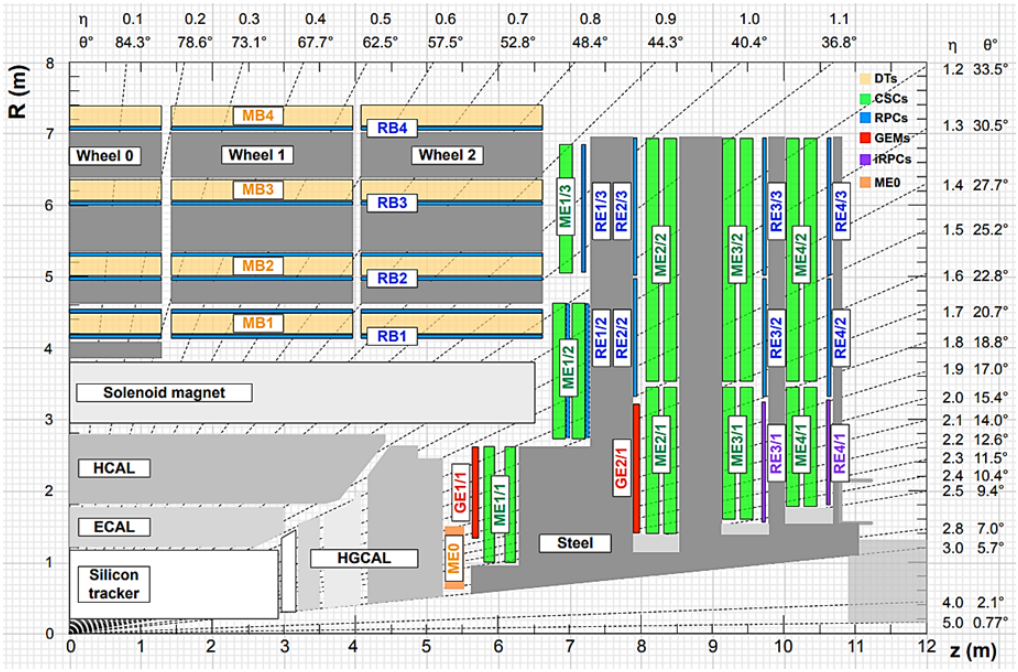

Figure 3.20: A quadrant of the CMS Muon Spectrometer, showing DT chambers (yellow), RPC (light blue), and CSC (green). The locations of new forward muon detectors for HL-LHC phase are contained within the dashed box and indicated in red for GEM stations (ME0, GE1/1, and GE2/1) and violet for improved RPC stations (RE3/1 and RE4/1) [34].

Thus, the new hits provided by the new iRPC detectors will recover the efficiency losses due to acceptance gaps in this region. The effect will be especially pronounced for high-quality muons with hits identified in all four muon stations.

Chapter 4

Resistive Plate Chamber

Resistive plate chambers are a family of gaseous detectors for charged particles, energetic photons, and neutrons, whose active medium is a gas, and which are characterized by having at least one of the electrodes made of resistive materials, whose resistivity typically ranges between 10^8 and $10^{12}\Omega cm$. The main advantage of these devices is that they are capable of tagging the time of an ionizing event in a much shorter time than the 25 ns between two consecutive LHC bunch crossings (BX). The fast dedicated muon trigger device based on RPCs identify unambiguously the relevant BX to which a muon track is associated to even in the high rate and background expected at HL-LHC. Signals from such devices directly provide the time and the position of muon hits at LHC with the required accuracy. This section gives an overview of the Resistive Plate Chambers and their general working principle; design and configuration inside the CMS experiment are also described.

4.1 Resistive Plate Chamber Overview

4.1.1 Historical Note

At the end of 1970, a very important change was introduced in the development of planar gaseous detectors [41]: the high resistive electrodes substituted one or both the metal electrodes. The main advantage is that the high voltage switching-off circuit is no longer necessary and consequently higher detection rate can be achieved. The electrodes get recharged with a time constant that is proportional to the resistivity of the electrodes and usually, it is much longer than the typical time scale of the avalanche development (around 10 ns). In this case, the charge multiplication is self-extinguishing when the resistive electrodes are used. The first chamber with resistive electrodes ($10^9 - 10^{10}$ Ωcm) made of glass was built by Yuri Pestov and was named Planar Spark Chamber [42]. It used a gas mixture based on Argon or Neon plus an organic gas for UV photon absorption at a pressure around 10 atm. This detector had

a time resolution of about 100 ps, which, at the time, was very impressive, especially taking into consideration the status of development of wideband electronics [42], [43]. The Pestov Planar Spark Chambers actually were the first prototype of modern RPCs.

At the beginning of the 1980s, Rinaldo Santonico and Roberto Cardarelli started from the technology introduced by Pestov to develop a new detector. Their new detector was made of High Pressure Laminate (HPL), commonly referred as "bakelite" and was tested for the first time in Rome [44]. The HPL is a standard material used in the furniture industry obtained by pressing and heating a pile of Kraft paper foils previously impregnated into a phenolic resin bath. Afterward, this detector has been named "Bakelite" Resistive Plate Chamber (RPC).

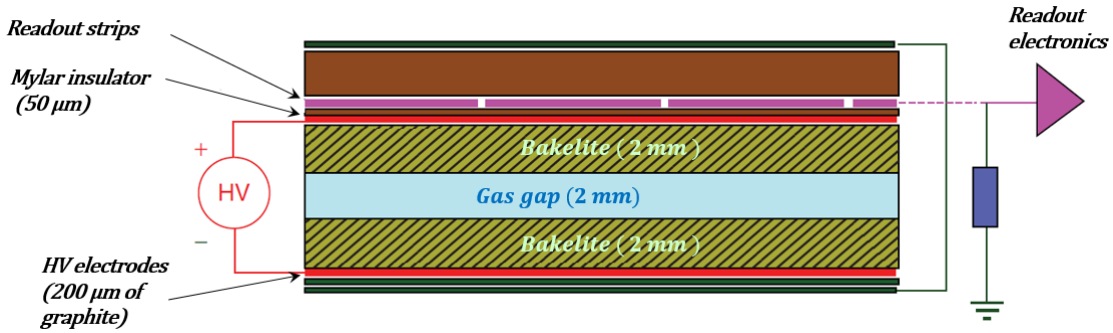

Figure 4.1: Schematic view of R. Santonico and R. Cardarelli's RPC chamber [44].

The main advantages of RPC are the following:

- Planar geometry (with the consequent advantages of time resolution);
- Use of resistive materials for the electrodes (which allowed detector self-quenching and no need for a pulsed operation mode and high-voltage (HV) removal after the passage of an ionizing particle and the subsequent discharge mitigation);
- Application of the HV to the electrodes via a signal-transparent resistive layer;
- They are easy to build, in order to make them suitable to cover large surfaces.

As shown in Fig. 4.1 the RPCs have a very simple design. The detector is made of two bakelite planar electrodes 2 mm thick with a bulk resistivity in the range $10^{10} \div 10^{12}$ Ωcm and the gas gap is 2 mm wide. The external electrodes surfaces are painted with a conductive paint (based on graphite) with a surface resistivity of about 200-300 $k\Omega/\square$. The signal readout is done using copper

strips about 2 cm wide glued on the detector. At the beginning, the RPCs were single gap counters, working in the streamer mode. Soon the double gap design was introduced in order to improve the detection efficiency and the avalanche working mode which extends the detector capacity of sustaining high particles rates, on order of magnitude higher than in the streamer mode. This is important especially for the muon physics at LHC where detectors must sustain particle fluxes up to hundreds of Hz/cm^2.

4.1.2 Working Principle

The working principle of any radiation detector basically depends on the manner in which the radiation to be detected interacts with the material of the detector itself. In the case of a gaseous environment, the interaction ways for fast charged particles are different but the electromagnetic interaction is the most probable. In a gaseous detector when a charged particle passes through the gas, it ionizes the gas molecules in such a way that electron-ion pairs are created (primary ionization). The electrons ejected can have enough energy (larger than the ionizing potential of the environment) to further ionize, producing secondary ion pairs. The total number of electron-ion pairs in a given volume produced by both primary and secondary ionization can be expressed by:

$$n_{tot} = \frac{\Delta E}{W_i} \tag{4.1}$$

where ΔE is the total energy loss transferred to the given volume and W_i is the effective average energy to produce one electron-ion pair.

Due to the electromagnetic interaction with the environment the particle along its track losses energy. The average energy lost is given by the Bethe-Bloch formula [45]:

$$-\left\langle \frac{dE}{dx} \right\rangle = \frac{2\pi e^4 z^2}{m_e c^2 \beta^2} NZ \left[ln\left(\frac{2m_e c^2 \beta^2 \gamma^2 T_m}{I^2} \right) - 2\beta^2 - \delta(\beta\gamma) \right] \tag{4.2}$$

where ze is the charge of the incoming particle, m_e the mass of the electron at rest, N and Z the atomic density and atomic number of the medium, respectively. The parameter I represents the average ionization and excitation potential of the medium. The maximum energy transfer for a single interaction is represented by the parameter T_m given by [45]

$$T_m = \frac{2m_e c^2 \beta^2}{1 - \beta^2} \tag{4.3}$$

The signal development in RPC, as in all gaseous detectors, is based on the gas ionization process and on the electrons avalanche multiplication. The passage of a charged particle in a gas volume causes ionization in the gas. If a high electric field (above few kV/cm) is applied more and more electrons can have enough energy between two collisions to produce inelastic phenomena. Gas multiplication is a consequence of increasing the electric field within the gas to a sufficiently high value. At low values of the field, the electrons and ions created by the incident radiation simply drift to their respective collecting electrodes. During the migration of these charges, many collisions normally occur with neutral gas molecules. Because of their low mobility, positive or negative ions achieve very little average energy between collisions. Free electrons, on the other hand, are easily accelerated by the applied field and may have significant kinetic energy when undergoing such a collision. If this energy is greater than the ionization energy of the neutral gas molecule, it is possible for an additional ion pair to be created in the collision. Because the average energy of the electron between collisions increases with increasing electric field, there is a threshold value of the field above which this secondary ionization will occur. In typical gases, at atmospheric pressure, the threshold field is of the order of 10^6 V/m [46], [47].

The electron liberated by this secondary ionization process will also be accelerated by an electric field. During its subsequent drift, it undergoes collisions with other neutral gas molecules and thus can create additional ionization. The gas multiplication process takes the form of a cascade, known as *Townsend avalanche*, in which each free electron can create more free electrons by the same process. The fractional increase in the number of electrons per unit path length is governed by the Townsend equation:

$$\frac{dn}{n} = \alpha dx \tag{4.4}$$

where α is called the first Townsend coefficient for the gas and corresponds to the inverse of the electron mean free path for the ionization. Its value is zero for electric field values below the threshold and generally increases with increasing field strength above this minimum. In the case of constant field as in the parallel plate geometry, α is a constant. The solution of 4.1.2 then predicts that the density of electrons grows exponentially with distance as the avalanche progresses:

$$n(x) = n(0)e^{\alpha x} \tag{4.5}$$

Moreover, for RPCs operating in avalanche mode, the average charge q_e of a single avalanche can be defined as [47]:

$$\langle q_e \rangle = \frac{k}{(\alpha - \beta)d} \langle Q_e(d) \rangle = e n_0 \left(\frac{k}{(\alpha - \beta)d} \right) \left(\frac{\lambda}{(\alpha - \beta) + \lambda} \right) e^{(\alpha - \beta)d} \qquad (4.6)$$

where k is defined as

$$k = \frac{(\varepsilon_r d/s)}{(\varepsilon_r d/s + 2)} \qquad (4.7)$$

and

- α is the the Townsend coefficient,
- β is the attachment coefficient describing the average number of electrons attached to form a negative ion,
- e is the electron charge,
- n_0 is the average size of the primary ionization cluster,
- λ is the cluster density for the used gas mixture,
- ε_r is the relative dielectric constant of the electrode,
- d is the gap width
- s is the electrode thinckness
- Q_e is electron charge developed within a gap width d.

The maximum useful signal on the readout electrodes for a given $(\alpha - \beta)d$ is obtained when the factors k and λ are as large as possible.

4.2 RPCs as Muon Detector in the CMS Experiment

4.2.1 Current CMS RPC Detector Design

CMS experiment uses a double-gap of RPCs detectors. The reason for this detector design is that in the double-gap configuration, the two anodes of the gaps can be placed against each other, adding the two signals of the gaps together. This configuration provides a higher detection efficiency that is the logic *OR* combination of the separate detection efficiencies and can be operated with a lower operating voltage. Another advantage of the double-gap structure is related to the charge spectrum. In a single gap RPC, the avalanches arising from individual clusters merge together, i.e. the positive space charge

of a previous avalanche can affect another avalanche by recombination and a reduction in growth. This process makes the fluctuations on avalanche size worse and the most probable value of these fluctuations is zero [48], [49].

In a double-gap RPC version there are two independent avalanches meaning that the fluctuations are averaged with a drastic effect on the charge spectrum. The most probable value is no longer peaked at zero meaning that more avalanches will be detected and thus a higher efficiency can be obtained. This also means that one is able to work at higher thresholds.

Exactly, the RPCs used by CMS are double-gap chambers composed of four High-Pressure Laminate (HPL) planes 2 mm thick [51]. The HPL electrodes bulk resistivity is within $1 - 6 \times 10^{10}$ Ωcm. The HPL plates in each gap are separated by a 10×10 cm^2 grid of polycarbonate spacers to maintain planarity and stiffness. The inside surface of the gaps is coated with a 5 - 10 μm thick linseed oil in order to smoothen the surface and quench the Ultraviolet (UV) photons [50]. The external electrodes surfaces are painted with conductive graphite paint, thus forming the High Voltage and ground electrodes. The two gaps are placed one on top of the other with common readout copper strips placed in between and isolated from the graphite by mylar sheets. A layout of a CMS double-gap RPC chamber is showed in Fig.4.2. The readout strips have different geometry depending on which part of the system they are: in the barrel chambers, the readout strips have a rectangular shape, while in the endcap chambers they have a trapezoidal shape. The pitch of the strips depends on the distance to the beam pipe varying from 1.5 cm for the innermost stations to 4 cm for the outermost stations.

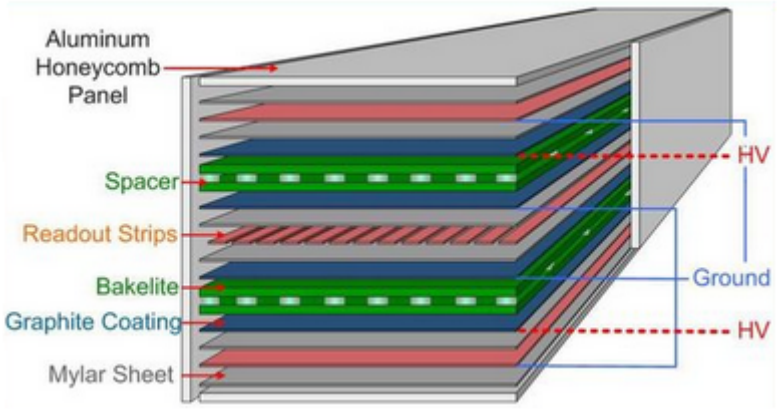

Figure 4.2: A layout of the CMS double-gap RPC chamber.

The choice of the gas mixture for a RPC detector is determined by the following factors: not too high working voltage, a big gain, a good proportionality and the capacity of sustaining high particles rate. An important parameter for understanding the main feature of the RPC is the cluster density (λ). In principle, the cluster density should be as large as possible to maximize the signal and to have high efficiency. Another advantage of having a gas mixture with high λ is related to the fact that a lower streamer probability can be achieved.

In conclusion, the high value of λ in gas mixture has higher efficiency, at the same gas gain value, and lower streamer probability [47].

The drift velocity of electrons in the $C_2H_2F_4$ based mixtures at various electric fields shows that in the region of streamer free operation, the drift velocity increases linearly with the applied electric field [52], [53]. At a high rate, where the effective field applied to the gap is reduced, the decrease of drift velocity may result in longer response time. For this reason the CMS-RPC system uses three components gas mixture based on 95.2% $C_2H_2F_4$(*tetrafluoroethane*) acting as a charge carrier gas, 4.5% $i-C_4H_{10}$ (*isobutane* acting as a quencher gas to absorb UV photons from molecule de-excitation and 0.3% SF_6 (*sulphur hexafluoride*) controlling the excess electrons through its high electron affinity. During the operation of the RPC detector, the gas mixture is kept at $21°C$ and $\sim 40\%$ humidity in order to maintain stable the electode resistivity, which could increase the HPL dries out.

For successful operation in the CMS experiment, all RPC systems must fulfill the following requirements:

- High detector efficiency ($> 95\%$ with more than 300 V long plateau);
- High rate capability ($\sim 300\ Hz/cm^2$);
- Average cluster size ~ 2 strips;
- Time resolution < 1.6 ns (for BX identification);
- Intrinsic Noise $< 5\ Hz/cm^2$;
- Ability to withstand in long-term operation and high background radiation;
- Spatial resolution ~ 10 mm.

The RPC system does not respond to the latter requirement due to the fact that their spatial resolution is at least one order of magnitude lower than DTs and CSCs, and therefore their impact on muon reconstruction performance is very low. However, because of their excellent time resolution, they play an important role in the bunch crossing assignment.

4.2.2 Current CMS-RPC Detector Layout

The need to trigger on the transverse momentum p_T of passing muons is the main driving force behind the detector layout of the CMS RPC system. The p_T is measured with the bending of the muon in the CMS magnetic field and this requires a muon to cross at least 3 out of 4 layers in the Muon system. These layers are interleaved with the steel magnet's return yokes ensuring a maximum muon track bending between them.

The CMS RPC system consists of two regions: Barrel and Endcap, covering up to pseudorapidity value of $|\eta| < 1.2$ in the Barrel and $0.9 < |\eta| < 1.9$ in the Endcap. A total of 1056 RPC detectors with a total active area around 3500 m^2 and with more than 110 000 electronic channels is used in the CMS Muon Spectrometer. Thus, the RPC system is complementary to the DT and CSC systems and adds robustness and redundancy to the muon trigger.

Barrel CMS-RPC system. In the Barrel iron yoke, the RPC chambers form 6 coaxial sensitive cylinders (all around the beam axis) that are approximated with concentric dodecagon arrays arranged into 4 stations. In total the RPC system is distributed in five wheels ($Wheel$ 0, $Wheel$ ± 1, $Wheel$ ± 2). Each wheel is divided into 12 sectors, covering the full azimuthal dimension (Fig.4.3). Each sector consists of four layers of DTs and six layers of RPC.

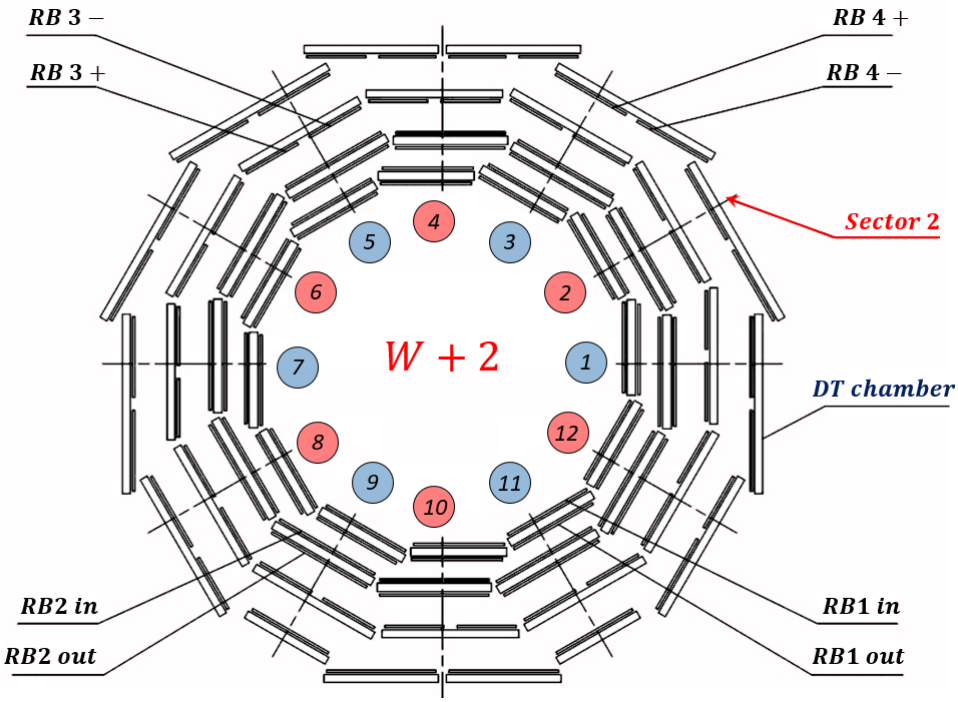

Figure 4.3: Scheme of one of the 5 Barrel wheels which are labeled -2, -1, 0, +1 and +2 respectively. Each wheel is divided into 12 sectors numbered as shown.

In the first and second muon stations, there are 2 arrays of RPC chambers located internally and externally with respect to the drift tube: RB1in and RB2in at the smaller radius and RB1out and RB2out chambers at larger radius. In the third and fourth station there are again two RPC chambers, both located on the inner side of the DT layer (named RB3+ and RB3-; RB4+ and RB4-). A special case is RB4 in sector 4, which consists of 4 chambers: RB4++, RB4+, RB4- and RB4- -. Finally, in sectors 9 and 11 there is only 1 RB4 chamber. A total of 480 rectangular chambers (Table 4.1), each one 2455 mm long defines the barrel RPC system. Exceptions are the chambers in the

sector 3 of Wheel -1 and sector 4 of Wheel +1, which are 2055 mm long to allow the passage of the magnet cooling chimney. Chambers RB1, RB2, and RB3 have widths of 2080, 2500, and 1500 mm, respectively. Widths of RB4 chambers are given in Table 4.2.

Table 4.1: Number of the RPC chambers for different barrel wheels.

RPC	**W+2**	**W+1**	**W0**	**W-1**	**W-2**	**Total**
RB1in	12	12	12	12	12	60
RB1out	12	12	12	12	12	60
RB2/2in	12	-	-	-	12	24
RB2/2out	-	12	12	12	-	36
RB2/3in	-	12	12	12	-	36
RB2/3out	12	-	-	-	12	24
RB3	24	24	24	24	24	120
RB4	24	24	24	24	24	120
Total	**96**	**96**	**96**	**96**	**96**	**480**

Table 4.2: Widths of the RB4 chambers

Sector	**RB4+**	**RB4++**	**RB4-**	**RB4–**	**RB4**
S1-S3	2000 mm	-	2000 mm	-	-
S4	1500 mm	1500 mm	1500 mm	1500 mm	-
S5-S7	2000 mm	-	2000 mm	-	-
S8	1500 mm	-	2000 mm	-	-
S9, S11	-	-	-	-	2000 mm
S10	2500 mm	-	2500 mm	-	-
S12	2000 mm	-	2000 mm	-	-

Physics requirements demand that the strips always run along the beam direction and are divided into 2 parts for chambers RB1, RB3 and RB4. The RB2 chambers, a special case for the trigger algorithm, have the strips divided into 2 (RBin in the wheels +2 and -2, and, RB2out in wheels +1, 0, and -1) and 3 parts (RB2out in wheels +2 and -2, and RBin in wheels +1, 0 and -1). Each chamber, therefore, consists of either 2 or 3 double-gap modules mounted sequentially along the beam direction to cover the active area. For each double-gap module (up to 96 strips/double-gap), the front-end electronics boards are located at one strip end, which minimizes the signal arrival time with respect to the interaction point. The strip width increases accordingly from the inner stations to the outer ones to preserve projectivity (each strip cover $5/16^\circ$ in ϕ). Fig.4.4 presented a schematic view of the chamber modules with 2 and 3 double-gaps.

Endcap CMS-RPC system. The endcap region has 576 trapezoidal shapes chambers, covering 10° of the azimuthal angle. The chambers are

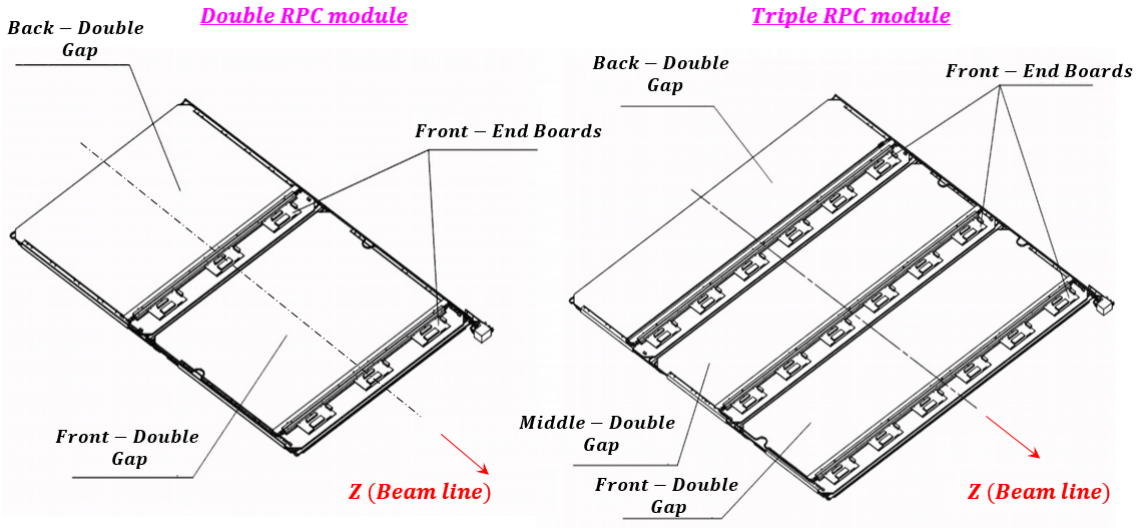

Figure 4.4: A schematic view of the Barrel RPC chamber modules with 2 (left) and 3 (right) double-gaps.

installed in 8 disks (4 for the positive side and 4 for the negative side from the interaction point).

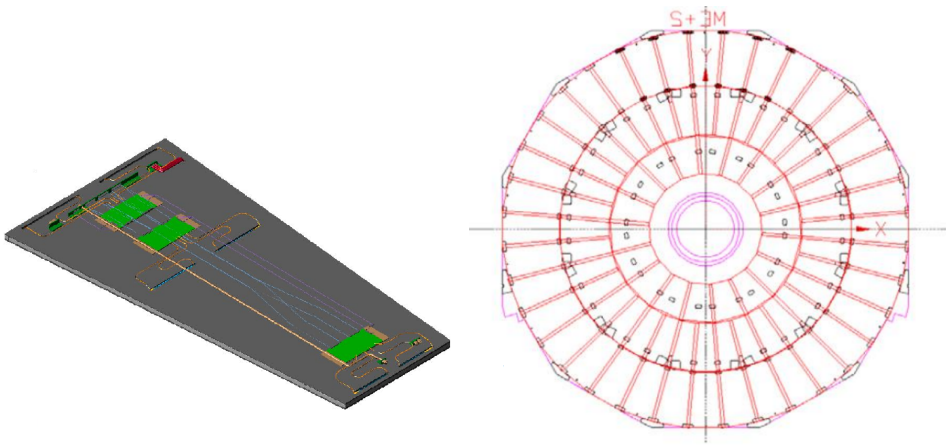

(a) (b)

Figure 4.5: Schematic view of an endcap RPC chamber (a) and schematic $r-\phi$ layout of the RPC station (b).

In the forward and backward regions of the CMS detector, 4 iron disks constitute the endcap yokes. Like in the barrel, 2 complementary muon detector systems are deployed for robust muon identification: CSCs and RPCs respectively. They are mounted on both faces of the disks to yield 4 CSC stations and, for the initial detector, 4 RPC stations. The double-gaps in every station has a trapezoidal shape (see Fig. 4.5a) and are arranged in the 4 concentric rings as shown in the $r-\phi$ view (see Fig. 4.5b). They overlap in ϕ as to avoid

dead space at chamber edges.

Each endcap RPC chamber consists of a double-gap structure enclosed in a flat trapezoidal shaped box made of 2 aluminum honeycomb panels of 6 mm thickness each and a $16 \times 16\ mm^2$ section spacer frame. The strip panel, sandwiched in between the gas gaps, has copper strip sections. Strips run radially and are radially segmented into 3 trigger sections for the REn/2 and REn/3 chambers (n = 1-3). The 32 strips of the RPC chambers (covering 10°) are projective to the beam line and follow a homothetic pattern. Besides the different mechanical shapes and assembly, the front-end electronics, services, trigger, and readout schemes of the endcap RPC system are identical to the barrel system.

4.2.3 Front-End Electronics of the Current RPC System

The electronics have to be very fast in order to read out all the signal induced on the strips. A custom front-end electronics was designed for the RPC. The readout strips are connected to the Front-End Boards (FEB). After having been amplified and discriminated, signals are sent unsynchronized to Link Boards (LB) placed around the detector. The LBs synchronize the signals with the 40 MHz LHC clock and transmit them at 1.6 GHz to the trigger electronics located in the CMS counting room over a 90 m optical link. The FEBs house two (barrel version) or four (endcap version) customs front-end chips [54]. Each chip is made of 8 identical channels, each consisting of an amplifier, zero-crossing discriminator, one-shot, and Low Voltage Differential Signal driver (LVDS). The preamplifier is a trans-resistance stage with 15-Ω input impedance to match the characteristic impedance of the strips. It is followed by a gain stage to provide an overall charge sensitivity of 2 mV/fC. Since accurate RPC timing information is crucial for providing an unambiguous bunch crossing assignment of the event, the zero-crossing discrimination technique was adopted to make the timing response amplitude-independent. In fact, considering that the RPC signals have a wide dynamic range (from few tens of fC to 10 pC), the implemented architecture provides a time walk below 1 ns. The discriminator is followed by a one-shot circuit. This produces a pulse-shaped at 100 ns to mask possible after-pulses that may follow the avalanche pulse. Finally, an LVDS driver is used to send the signals to the LB in differential mode [33], [55].

Chapter 5

The New Generation of the Resistive Plate Chamber for the RPC Muon System Extension

The LHC has approved a schedule of a major upgrade of the accelerators in order to increase the sensitivity for new physics searches and high precision measurements (LHC upgrade schedule reported in Section 3). During this HL-LHC operation, the expected conditions in terms of background and pile-up and the probable aging of the present detectors will make the muon identification and correct p_T assignment a challenge for the muon system. In order to ensure redundancy and guarantee the optimal conditions of the CMS muon system under the HL-LHC conditions, the present RPC system will be extended. The RPC system coverage will be extended from $|\eta| = 1.9$ up to 2.4. The additional new chambers will increase the efficiency for both trigger and offline reconstruction in the difficult region where the background is the highest and the magnetic field is the lowest within the muon system. Moreover the extended RPC system will improve the performance and the robustness of the muon trigger. This Doctoral Thesis is conducted in the framework of the improved Resistive Plate Chamber detector development for the future upgrade of the CMS muon system. In this Chapter, an overview of the improved RPC detector project will be presented.

5.1 Motivation

To extend the sensitivity for new physics searches, a major upgrade of the LHC machine for HL-LHC era has been decided. The instantaneous luminosity of LHC is expected to exceed the nominal value and reach $2 \times 10^{34}\ cm^{-2}s^{-1}$, during Run 3 that will start in 2021. A further increase is planned in Run 4, from 2026 on, up to $5 \times 10^{34}\ cm^{-2}s^{-1}$, i.e. a yield five times greater than the initial design value of LHC. The increase of the energy and luminosity during

the future upgrades of the LHC machine will adversely affect the performance of the CMS Muon System due to the harsh background environment and the high pile-up. As a consequence, a general upgrade of the present detectors is mandatory.

The CMS collaboration is currently improving the Muon System to maintain the high level of performance achieved during the Run 1 period of operation also in the challenging environment of the high-luminosity LHC. The Muon System of CMS experiment was originally designed as a highly hermetic and redundant system that employs three gas-based detectors. Precision measurements and Level-1 triggering are provided by Drift Tubes in the barrel, covering acceptances up to $|\eta| < 1.2$, and Cathode Strip Chambers in the endcaps covering $1.0 < |\eta| < 2.4$. Additionally, RPCs provide redundant trigger and coarse position measurement in both barrel and endcap regions, but were not implemented beyond $|\eta| > 1.6$ due to concerns about their capability to handle the high background particle rates. Operating in the high background particle rate imposes severe restrictions on the gaseous detection technology that can be used: new detector requirements include high rate capability, good spatial resolution for tracking, good time resolution for triggering, and in addition, radiation hardness.

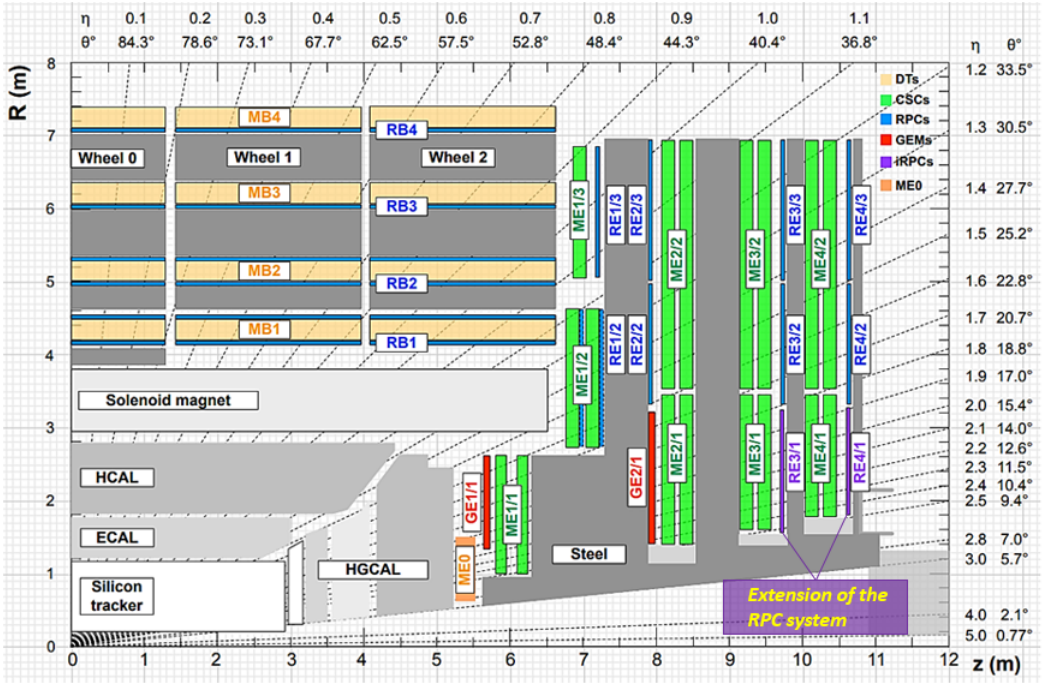

Figure 5.1: A longitudinal quadrant of the CMS detector: the violet box marks the extension of the RPC system (iRPC project) [57].

To fulfil these requirements, new and improved technologies of the gaseous detectors have been chosen in the so-called improved Resistive Plate Chambers (iRPC) [59],[60] and Gas Electron Multiplier (GEM) project [56]. Therefore, additional sets of muon detectors have been planned to be installed. Before this

upgrade, eight RPC layers in total were installed in the four existing endcap disks covering up to the value of pseudorapidity $|\eta| < 1.9$. At the moment the very forward region still remains incomplete after the first Long Shutdown (LS1) and could be instrumented up to $|\eta| = 2.4$ during LS2 (for GEM project) and the annual Year-End Technical Stops in 2022 and 2023 (for iRPC project) (Fig. 5.1). The presence of an inner layer in the endcap region equipped with improved RPC stations, called RE3/1 and RE4/1, will increase the overall robustness of the CMS muon spectrometer. The new iRPC RE3/1 and RE4/1 chambers will complement the CSC stations ME3/1 and ME4/1 and enhance the local muon measurement by adding track hits. The new hits provided by the new detectors will recover the efficiency losses due to the acceptance gaps in this region. The effect will be especially pronounced for high quality muons with hits identified in all four muon stations.

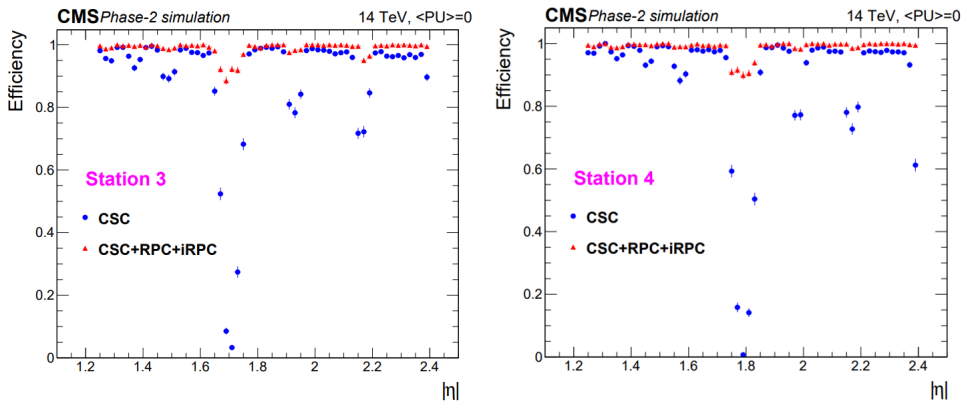

(a) (b)

Figure 5.2: Effect of RPC hit inclusion on the local trigger primitive efficiency in station 3 (a) and station 4 (b) of the $1.8 < |\eta| < 2.4$ region [57].

Even though the CSCs system covers the region, there are steep drops in efficiency in some regions due to the geometry of the system itself: the presence of high-voltage spacers inside the CSC chambers reduces trigger efficiency at some values of $|\eta|$. Including the RPC information into the trigger primitive will mitigate this effect, resulting in an overall increase in efficiency. Fig. 5.2 shows the efficiency of finding trigger primitive stubs at the level of station 3 and station 4, with and without the addition of the current RPC and new iRPC information. As shown in Fig. 5.3, it is expected to be an improvement at the level of 15% in the region from $|\eta| = 2.1$ to 2.2. In case of any CSC trigger problems in ME3/1 and ME4/1, additional improvement would be expected also.

Moreover, the information provided by new iRPC stations will help to remove CSC ambiguities at the L1 trigger, when several tracks are present in a CSC chamber crossed by muon particles. CSC chamber has 1D strip and 1D wire readouts. This structure leads to a combinatorial background in presence

of multiple tracks.

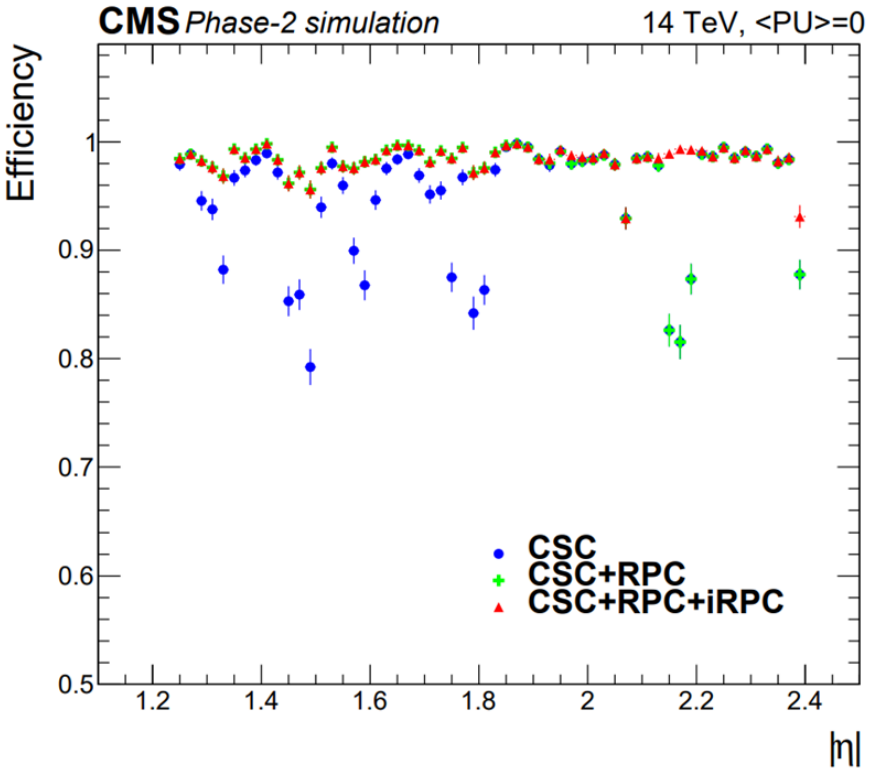

Figure 5.3: Simulated comparison between the L1 single muon trigger efficiencies with and without the improved RPC chambers contribution, as a function of $|\eta|$ [57].

Taking into account the experience from the past LHC operation to the HL-LHC luminosity, the propobility to have a spurious Local Charged Track (LCT) inside a ME3/1 or ME4/1 chambers, is about 13% per bunch crossing. In the presence of a real muon, these extra ghost LCTs can result in a high-p_T muon solution in the Endcap Muon Track Finder, even though the actual muon was low-p_T. The RE3/1 and RE4/1 chambers will have radial strips readout from both ends of each strip. From the time difference of these two signals, a spatial resolution of the order of a few centimeters is expected along the strip direction, which will resolve almost all of the combinatorial ambiguity in the ME3/1 and ME4/1 CSCs directly at a single-station level. Moreover, this can help triggering on and reconstructing slow-moving particles in this region improving the Heavy Stable Charged Particles (HSCPs) search sensitivity [58].

5.2 CMS Requirements and technology choice

The fundamental requirements on the detection performance that a RPC detector has to fulfill in the innermost regions in the CMS Muon System are:

- **High particle rate capability.** The expected background components and their corresponding hit rates in the RE3/1 and RE4/1 regions in the CMS Muon System have been computed using the CMS-FLUKA simulation software. Additionally, the sensitivity of CMS-RPC detectors to the different background components and energies has been simulated with the GEANT4 framework. The results of the simulation, as shown in Fig. 5.4, indicate that the background hit rate is mainly dominated by neutrons and photons: neutrons are produced by the hadronic interactions in the inner part of the detector and by the interactions of protons of the beam with the collimators, with energies between few meV and hundreds of GeV; photons instead come from neutron capture, with typical energies between few keV and tens of MeV. The maximum expected background hit rates in the hottest RE3/1 and RE4/1 stations will be about 700 Hz/cm^2 for HL-LHC running at 14 TeV and 5×10^{34} $cm^{-2}s^{-1}$. Multiplying with a safety factor of 3 then requires a hit-rate capability of 2.1 kHz/cm^2 for the 10 years operation of the HL-LHC program [61].

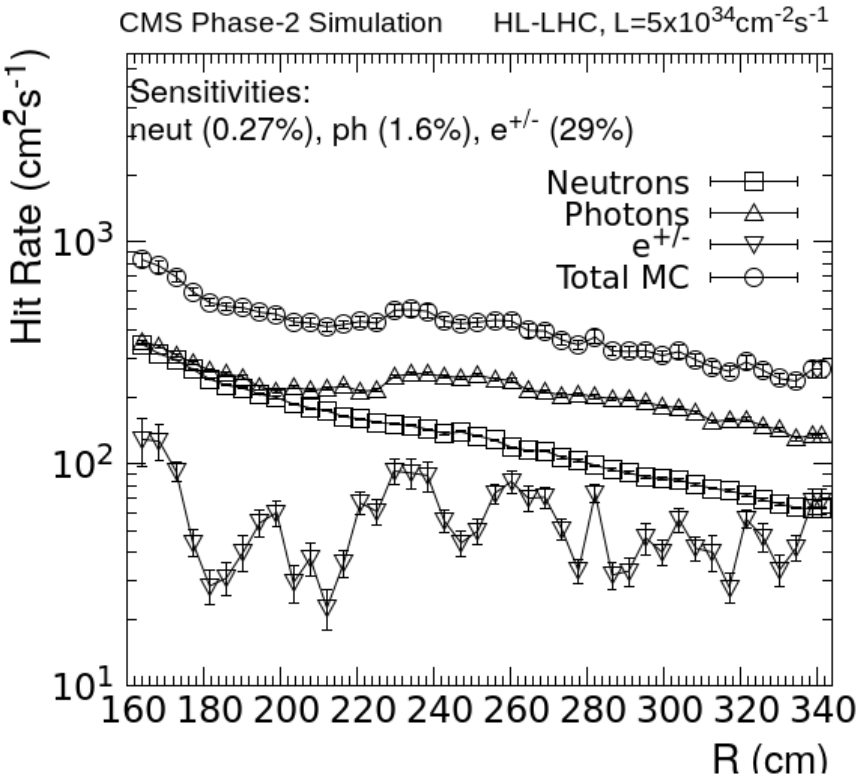

Figure 5.4: The CMS-FLUKA simulation of the expected hit rate due to neutrons, photons, electrons and positrons at the HL-LHC luminosity of 5×10^{34} $cm^{-2}s^{-1}$ in the RE3/1 station. A similar background hit rate is expected in the RE4/1 station [61].

- **Good time and spatial resolutions.** The resolution requirements are similar to those of the present RPC system: a time resolution of the order

of 1.5 ns and a spatial resolution of the order of a few cm along the strip direction. The average strip pitch will be around 1 cm, corresponding to a factor of two smaller than the average strip pitch of the chambers in the present endcap RPCs at $|\eta| \sim 1.6 - 1.8$. This spatial resolution of a few centimeters in the radial direction will improve the ghost (i.e. ambiguous and/or fake) track cancellation logic, will reduce the pretrigger deadtime thus optimizing pattern recognition and improving timing.

- **High detection efficiency.** To maintain the high level of performance achieved during the first period of operation (Run 1) also in the challenging environment of the high-luminosity LHC, each single RE3/1 and RE4/1 detectors must have an efficiency higher then 95% for detecting minimum ionizing particles.

All the above requirements are fulfilled with a double-gap RPC with High-Pressure Laminate (HPL) electrodes readout by pick-up strips in the middle. This technology is similar to the present endcap RPC system and will be described in next Section 4.3. In order to mitigate the possible aging effects on the detector performance, and improve the rate capability, both the electrode and gas gap thickness have been reduced with respect to the design of the present system. It has been demonstrated [47] that the reduction of the gas gap thickness can be used to reduce the total charge generated during the avalanche amplification process, and consequently enhance the rate capability and radiation hardness. Consequently, part of the signal amplification is transferred to an improved front-end electronics system capable of handling the increased background rate in the forward innermost region (see the Section 4.4).

In the periods from 2015 to 2017 an intense R&D activities have been performed in order to define the optimal gas gap thickness for long-term operation during the HL-LHC. The pickup charge has been studied in six double-gap RPC with gap thickness between 1.0 mm and 2.0 mm performed by the KOrean DEtector Laboratory (KODEL) [63]. The induced charges drawn in double-gap RPCs for the different gas gap thickness as a function of the effective electric field strength is shown in Fig.5.5. Electric field values are converted to the effective ones at the reference values of pressure, P = 990hPa, and temperature, T = 293K. The standard CMS RPC gas mixture has been used for these measurements. The thinner gap thicknesses more effectively retard the fast growth of the pickup charges per ionization avalanches, which implies that the use of thinner gaps will effectively preserve the size of the operational plateau when a lower threshold will be used in order to increase the detector sensitivity. The reduction of the gap thickness and threshold will decrease the operational high voltage, which will, in turn, improve the robustness of the system. In the current baseline design for the iRPCs, a thickness of 1.4 mm for both gaps and electrodes is chosen, compared to the 2 mm used for the present CMS double-gap RPCs. Thinner gas gaps would be more sensitive to

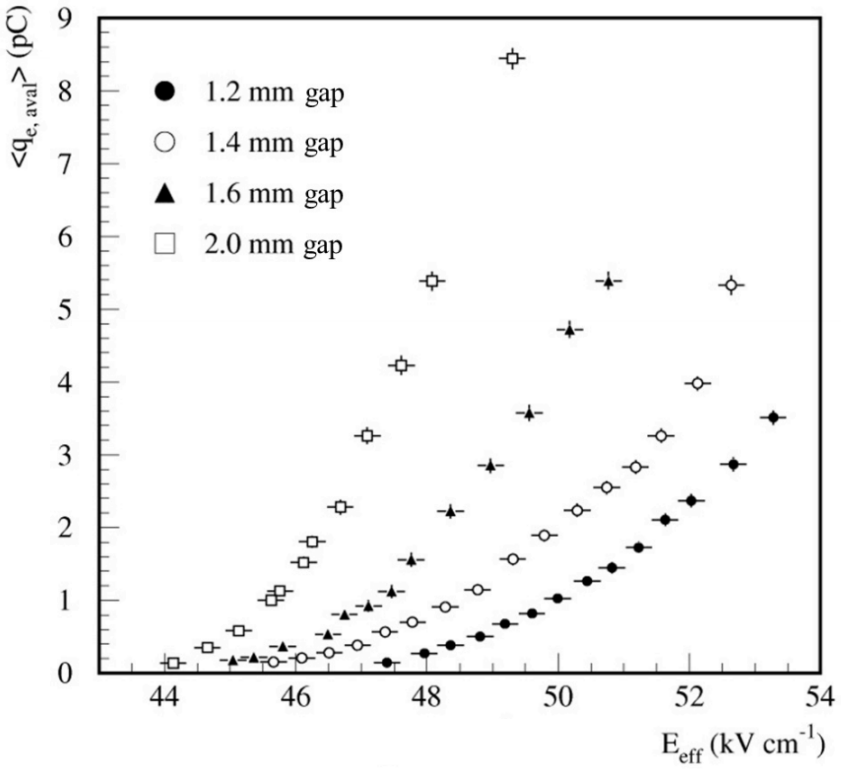

Figure 5.5: Average charge per avalanche measured for double-gap RPCs with different gas gap thickness as a function of the effective electric field strength [63].

non-uniformities in the distance between electrodes, and the value of 1.4 mm is a safe compromise. The electrode resistivity of the High-Pressure Laminate plates has been reduced to be in the range from 0.9 to 3.0 $\times 10^{10}$ Ωcm, which is about a factor two less than in the present system.

5.3 Baseline Design of New iRPC Detector

The 3D drawing of the new improved Resistive Plate Chambers (iRPC) for inner layers of the endcap stations is shown in Fig. 5.6 and the main geometrical parameters of the RE3/1 and RE4/1 detectors are given in Table 5.1. In order to uniformly fill in along the radius and to reduce the number of dead areas in the inner layers the endcap stations, the design of the iRPC chambers was chosen identical to the existing trapezoidal shaped RPC detectors. The new set of the chambers will be covering 20° of the azimuthal angle and will be installed with overlap in order to avoid the dead space at chamber edges also (see Fig. 5.7).

The iRPC RE3/1 and RE4/1 detectors will contain a double 1.4 mm thick High-Pressure Laminates plate 1.4 mm thick gas gap, coated with a conductive graphite paint to form electrodes. The graphite layer is in turn covered by

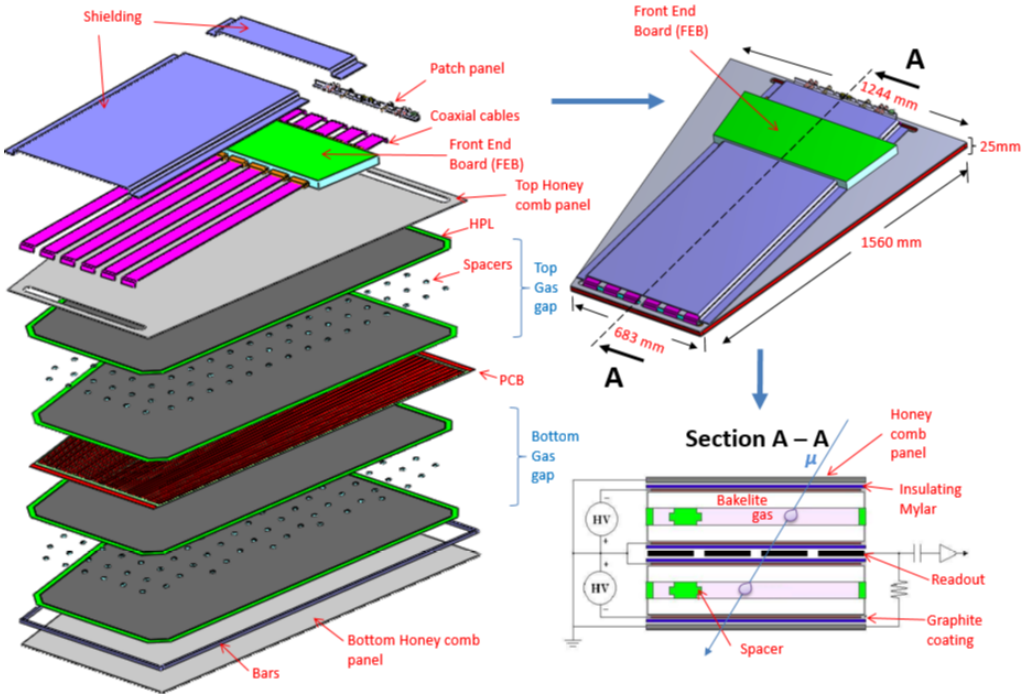

Figure 5.6: Schematic layout of the iRPC RE3/1 and RE4/1 chambers.

Table 5.1: The geometrical parameters of the RE3/1 and RE4/1 chambers.

	RE3/1 chamber	**RE4/1 chamber**
$\mathbf{R_{in}}$, **[mm]**	1527	1770
$\mathbf{R_{out}}$, **[mm]**	3192	3140
Area, $\mathbf{[m^2]}$	1.39	1.19
Number of strips	96	96
Strip pitch, [cm]	0.6-1.1	0.6-1.2

Table 5.2: Comparison between present RPC chamber and new iRPC detector.

	present RPC	**improved RPC**
Gas gap & electrode width, [mm]	2	1.4
Resistivity, $\mathbf{[\Omega cm]}$	$1.0\text{-}6.0\times10^{10}$	$0.9\text{-}3.0\times10^{10}$
Strip pitch, [cm]	2.0-4.0	0.6-1.2
Design electronics threshold, [fC]	150	50
ϕ **– coverage, [degree]**	10	20
Total chamber thickness, [mm]	36	25

plastic material in order to insulate the conductive layer from the external environment. In fact, the design will use two identical large gas gaps at the bottom and on top of the chamber with a radially oriented readout panel placed in between. The entire *"sandwich"* will be gas tight. The chamber

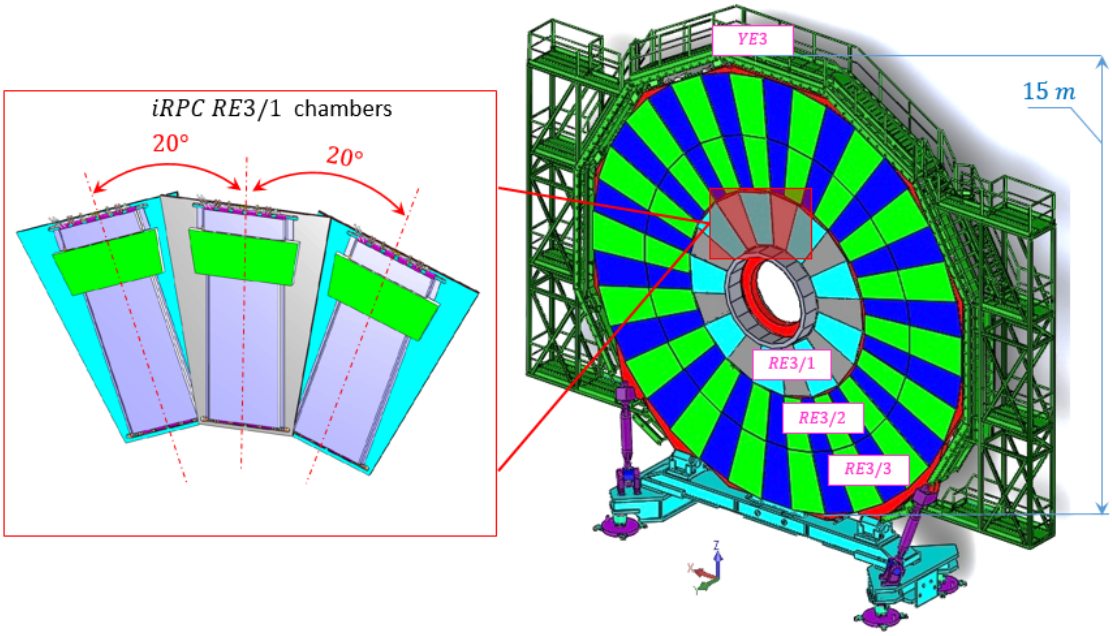

Figure 5.7: Schematic view of the RE3/1 chambers covering 20° and installed with the overlapping on the iron disk Yoke Endcap 3 of the CMS muon system.

will be contained within a honeycomb box with the chamber services (readout electronics, gas distribution and water cooling circuit) mounted on the outside.

The readout panel will consist of the signal pick up strips embedded in a readout board made of two parts, i.e. a two large trapezoidal printed circuit boards. Both ends of each strip will be connected through coaxial cables (with the same impedance of the strips) to the different channels of the front-end chip located on the front-end board (FEB). The iRPC's front-end electronics is a 32-channel PETIROC ASIC developed by OMEGA based on the SiGe technology [65], includes a broadband fast pre-amplifier and a fast discriminator (more details are given in Section 4.4). Each channel provides a charge measurement and a trigger output that can be used to measure the signal arrival time. The FEB will include a field-programmable gate array device running a Time-to-Digital Converter for the time measurement. Each chamber will be divided in 4 η-partitions, with 24 strips each, yielding a total of 96 strips per chambers.

The iRPC project will add 18 new chambers per muon disk, or 72 chambers in total for the RE3/1 and RE4/1 stations in both endcaps [57]. Each station will provide one single hit for muon reconstruction with precise time information within 2 ns, spatial resolution in the transversal direction of about 0.3 cm and along the strip around 2 cm.

Thus, the improved iRPC technology will have a number of advantages: the thinner electrodes and a narrower gas gap will reduce the recovery time of the electrodes and also the total charge produced in an ionization avalanche; the reduction of the integrated charge deposited will slow down the aging

process; the resulting loss in gas gain will be compensated by the higher signal amplification of new front-end electronics; in addition, the operational high voltage will be lower. All differences between the present RPC and the new iRPC chambers are shown in Table 5.2.

5.4 iRPC Front-End Electronics and Data Acquisition System

The fundamental requirements on the performance that a new front-end electronics have to fulfill in the RE3/1 and RE4/1 regions is the possibility to detect signals with a charge lower than about 50 fC and it needs also to be fast and reliable, and it must sustain the high irradiation environment in the innermost region of the CMS muon system expected during the HL-LHC era.

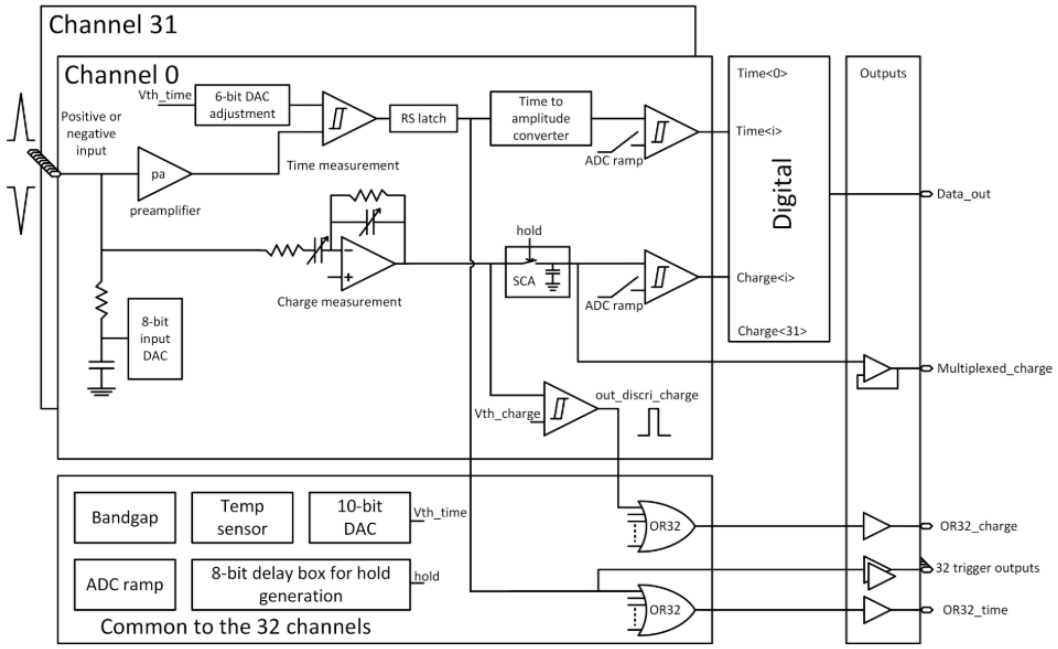

Figure 5.8: Block diagram of PETIROC front-end ASIC [65].

The front-end electronics of the iRPCs is based on two main components: a fast front-end ASIC and a time-to-digital converter. The front-end is based on the PETIROC ASIC and is called CMS RPCROC [65], it is a 32 channels version developed in SiGe technology and consists of a pre-amplifier with a 1 GHz bandwidth and gain of 25 associated with a fast programmable comparator (Fig. 5.8). The overall jitter of PETIROC is kept at 20 ps for an input charge of 300 fC. To equalize the 32 channels response, the threshold and pedestal alignments of each channel are made by individually adjusting the internal 6-bit DAC for both pedestal and comparator level.

The latest available ASIC technology has been designed in order to better fulfill the CMS RPC specifications and is a suitable choice for the iRPC requirements. Taking into account that the PETIROC ASIC allows the time measurements on both rising and falling edges, the charge has been estimated using the Time-Over-Threshold technique. The 350 nm SiGe technology usually employed in the PETIROC electronics has been replaced by the Taiwan Semiconductor Manufacturing Company (TSMC) 130 nm CMOS one, to increase its radiation hardness. The number of readout channels has been increased from 32 to 64.

The ASICs are mounted on the FEB which is connected to the iRPC detector. This FEB also hosts an FPGA device running a TDC devoted to the time measurement. A coaxial cable with the same strip impedance is used to connect the strip's ends to an ASIC channel on the FEB. This card host, for each of the coaxial cables, a dedicated circuit to match the ASIC input entry impedance of about 200 Ω. On the same FEB card, a GigaBit Transceiver (GBT) link allows the communication between the RPCROCs and the TDCs on one hand, and the off-detector RPC DAQ system on the other hand. The TDC time resolution of the order of 50-100 ps allows obtaining the information of signal arrival time from the strip's two ends, which provides the hit coordinate along the strip length with a spacial resolution of the order of a few centimeters. Finally, every front-end board includes three RPCROC ASIC and three TDC FPGAs each with 64 readout channels [57].

5.5 Integration of the new iRPC System in the Innermost Region of the CMS Muon Detector

This section describes the survey measurements performed in order to determine the space actually available for the future installation of the new iRPC in the innermost region of the CMS Muon System. The Doctoral Student has been directly involved in the survey measurements, by taking a leading role in the preparation and validation of the test infrastructure and the responsibility of the tests execution and data analysis.

5.5.1 Estimation of the available space in the CMS Endcap Region for iRPC Detectors

The new iRPC will be installed in the $1.8<|\eta|<2.4$ Endcap region that corresponds to an inner radius of 1593 mm for $\eta = 1.8$ and to an inner radius of 3283.5 mm for $\eta = 2.4$ (Fig. 5.1).

In order to estimate the available space needed for the future installation of the iRPC RE3/1 chambers during the Yearly Technical Stops at the end of 2022 and 2023, the surfaces topology and geometry of the Yoke Endcap

Figure 5.9: Survey campaign for the future iRPC RE+3/1 station installation in the Yoke Endcap ±3 iron disk.

(YE) ±2 and YE±3 iron disks in the region $1.8<|\eta|<2.4$ have been studied in detail with the photogrammetry technique, particularly taking into account the space occupied by the present CSC ME±3/1 chambers. Photography and photogrammetry of the YE±2 and YE±3 iron disks with present CSC-ME3/1 and ME3/2 and RPC-RE3/2 and RE3/3 muon stations are shown in Fig. 5.10.

Additionally, a survey measurements based on the traditional theodolite [66] and laser scanner [67] techniques (Fig. 5.9) provided accurate knowledge of the actual positions and orientations of the muon chambers and their services, allowing a reconstruction of the surfaces topology and geometry for both the mentioned Yoke Endcap iron disks. The strategy of such survey measurements was to combine the photogrammetry information and the results of theodolite and laser scanner techniques in order to determine the precise positions and orientations of the muon chambers and their services with respect to their design position. Then, the precise survey informations have been analyzed by dedicated engineering frameworks, such as Cyclone software [68] and Geomagic Studio Software [69] in order to reconstruct the surfaces topology and geometry of all the elements (muon chambers, HV/LV system components, cooling system, neutron shielding, structural members, etc.) mounted on the YE±2 and YE±3 iron disks of the Endcap region. Finally, the analyzed data, containing the information on the surfaces topology, have been exported in .igs file format in order to be imported and displayed by the CATIA software [70].

Fig.5.11 shows the surface topology and geometry for a sector of the YE-2 (Fig. 5.11a) and YE-3 (Fig. 5.11b) of the Yoke Endcap, which have been obtained on the basis of the survey measurements performed at CERN CMS-

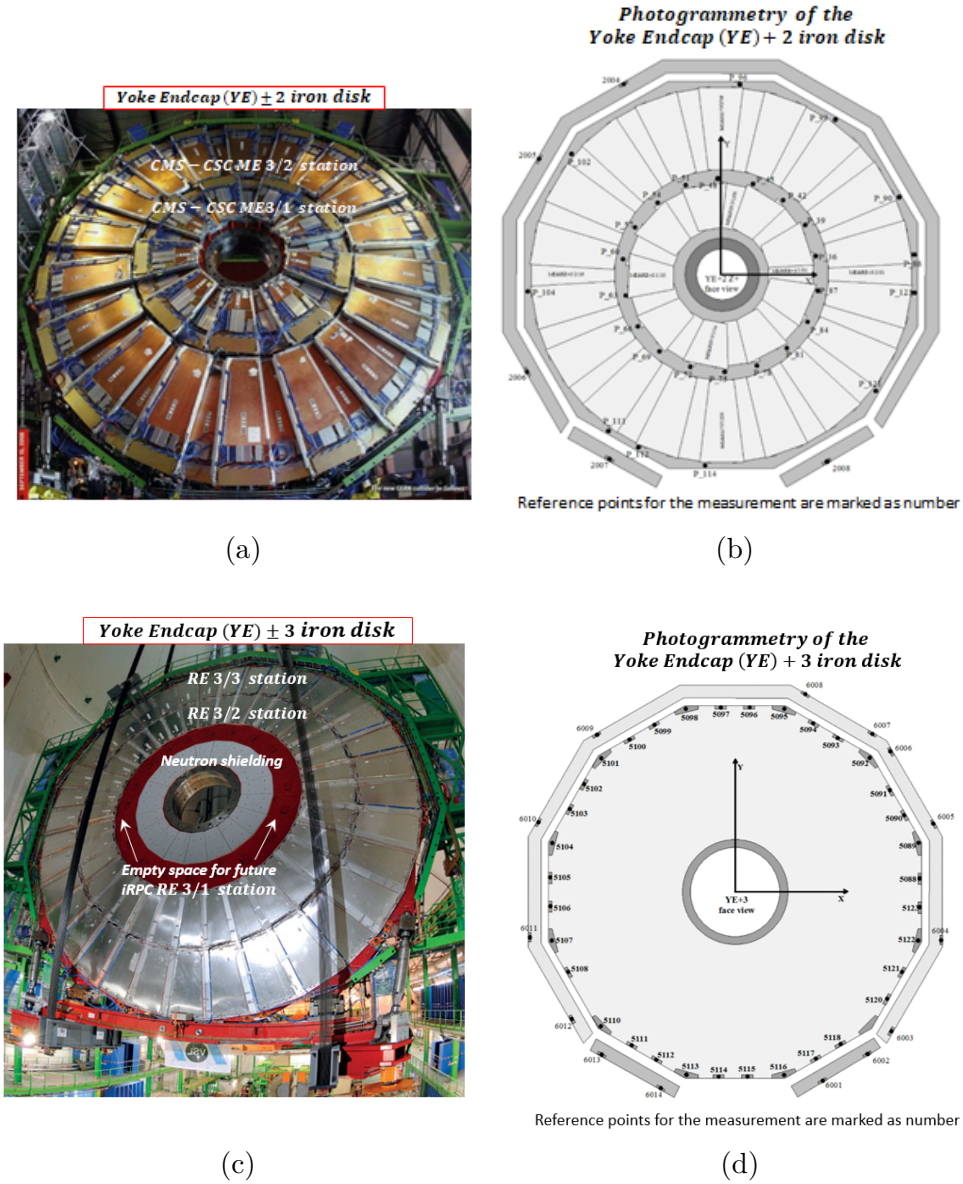

Figure 5.10: Photography and photogrammetry of the YE±2 and YE±3 iron disks with present CSC-ME3/1 and ME3/2 and RPC-RE3/2 and RE3/3 muon stations. Measured points on the iron disks are labeled as the number.

UXC55 on 19th December 2016. In this context, it is interesting to note that the YE-2 (Fig. 5.11a) is characterized by a non-uniform surface topology due to the presence of the CSC ME-3/1 muon station (i.e. CMS muon chamber, HV/LV system components, cooling system, structural members, etc.). On the contrary, the YE-3 (Fig. 5.11b) is characterized by a fairly uniform surface topology, since in this region only the neutron shielding, characterized by a planar surface, is installed.

Fig. 5.12 shows the surface topology and geometry for a sector of the YE+2

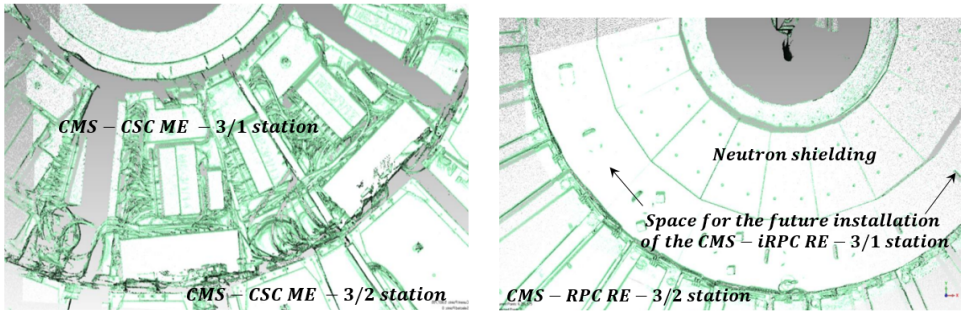

(a) (b)

Figure 5.11: Surface topology and geometry of the one sector of the YE-2 included the present CMS-CSC ME-3/1 muon stations (a). Surface topology of the YE-3 included the neutron shielding where the future new CMS-iRPC chamber will be attached (b). Scanning data are presented as the point cloud, survey reference points and yoke endcap center which have been exported in .igs file format for further import in CATIA software.

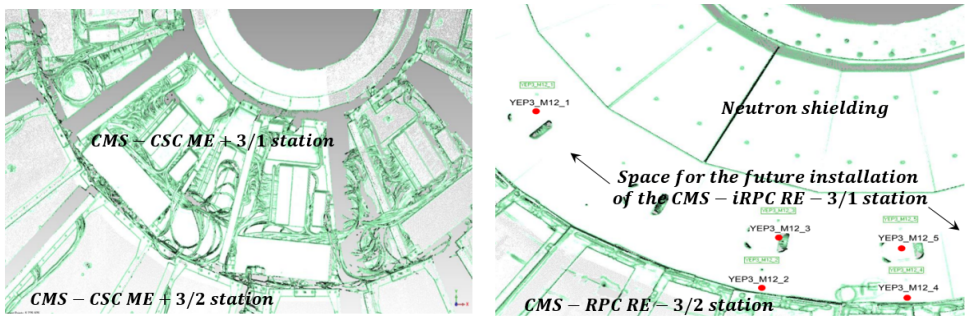

(a) (b)

Figure 5.12: Surface topology and geometry of the YE+2 included the present CMS-CSC ME+3/1 stations (a). Surface topology of the YE+3 with the neutron shielding (b). Scanning data are presented as the point clouds.

(Fig. 5.12a) and YE+3 (Fig. 5.12b) iron disk in the Endcap region, which have been obtained on the basis of the survey measurements performed at CERN CMS-UXC55 on 10th January 2017. Similar results have been obtained for the YE+2 and YE+3 iron disks.

The presence of a non-uniform surface topology around the CSC ME±3/1 muon stations makes it extremely difficult to estimate the space actually available between the YE±2 and YE±3 iron disks of the Endcap region for the future installation of the iRPC RE3/1 chambers.

A first method used to determine the available space between the surfaces of the YE±2 and YE±3 iron disks was the study of the CATIA-V5 3D model of the CMS Muon System. Fig. 5.13-left shows a cross-section of the YE±2 and YE±3 iron disks in the Endcap region.

By using the SolidWorks engineering software [71], the distance between

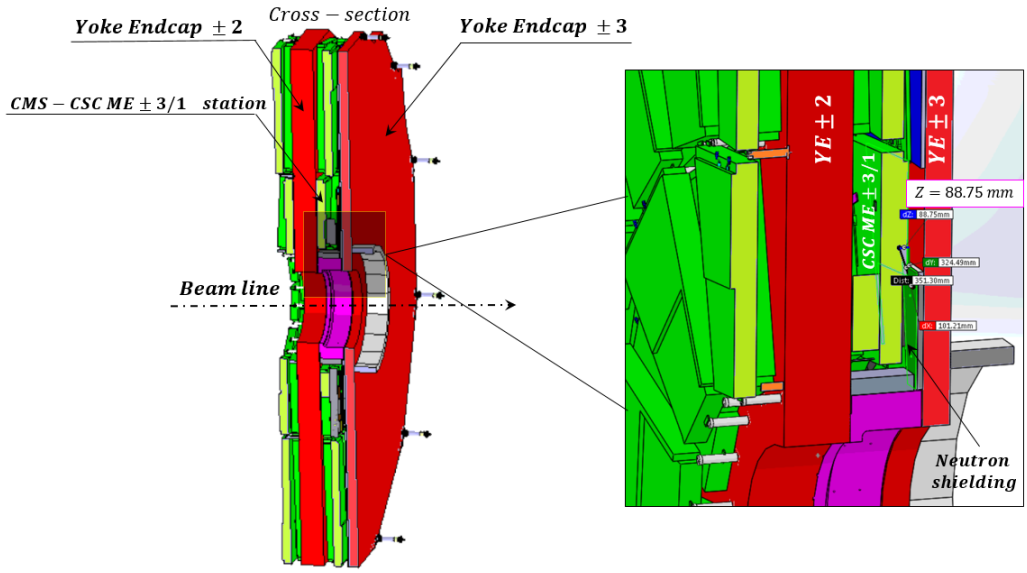

Figure 5.13: Left: Cross-section of the YE2 and YE3 iron disks in the Endcap region. Right: Close view of the Endcap region cross-section showing the available space between the YE2 and YE3 iron disks. By using engineering drawings, the distance between the CMS-CSC ME3/1 station and the neutron shielding has been found to be 88.75 mm.

the CMS-CSC ME3/1 station and the neutron shielding has been determined. As shown on the engineering drawing (see Fig. 5.13-right), the available space has been found to be 88.75 mm.

However, the CMS engineering drawing (3D model) does not reflect appropriately the actual situation since the muon chambers and their services have been modeled/ simulated using simplified elements in order to compile/create the 3D Model of the CMS Muon System.

For this reason, it has been decided to carry out a survey in the CMS underground experimental area during the YETS in December 2016.

A preliminary manual measurements have been performed in order to estimate the distance between the surfaces of the YE±2 and YE±3 iron disks in the innermost regions of the CMS Muon System and to determine the available space for future installation of the iRPC RE3/1 chambers.

Taking into account that the YE±2 iron disks are characterized by a non-uniform surface topology, the thickness of the main elements which constitute the CSC ME±3/1 station have been carefully measured by using a ruler and a high-resolution digital caliper. Fig.5.14 shows the overview of the CMS-CSC ME±3/1 chamber and its main elements whose thickness has been measured during the survey. The results of the survey measurements are summarized in Fig. 5.15. Additionally, the thickness of the neutron shielding installed in the YE±3 iron disks has been measured.

As shown in Fig.5.15, the space actually available for the iRPC RE3/1 chambers is essentially determined by the thickness of the CSC Anode Front-

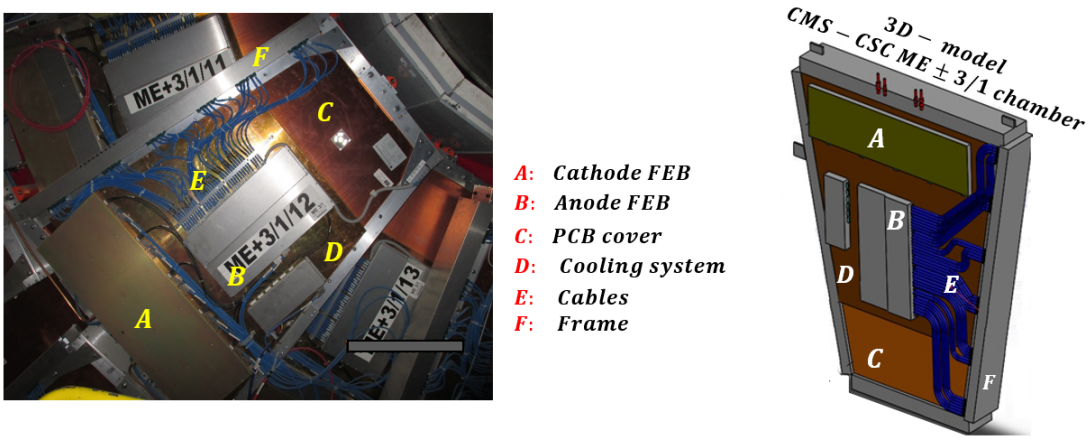

Figure 5.14: Photography of the CMS-CSC ME+3/1/12 chamber on the YE+2 iron disk obtained during the measurement in December 2016. The CSC detector components, which could reduce the available space between YE2 and YE3, are marked with capital letters.

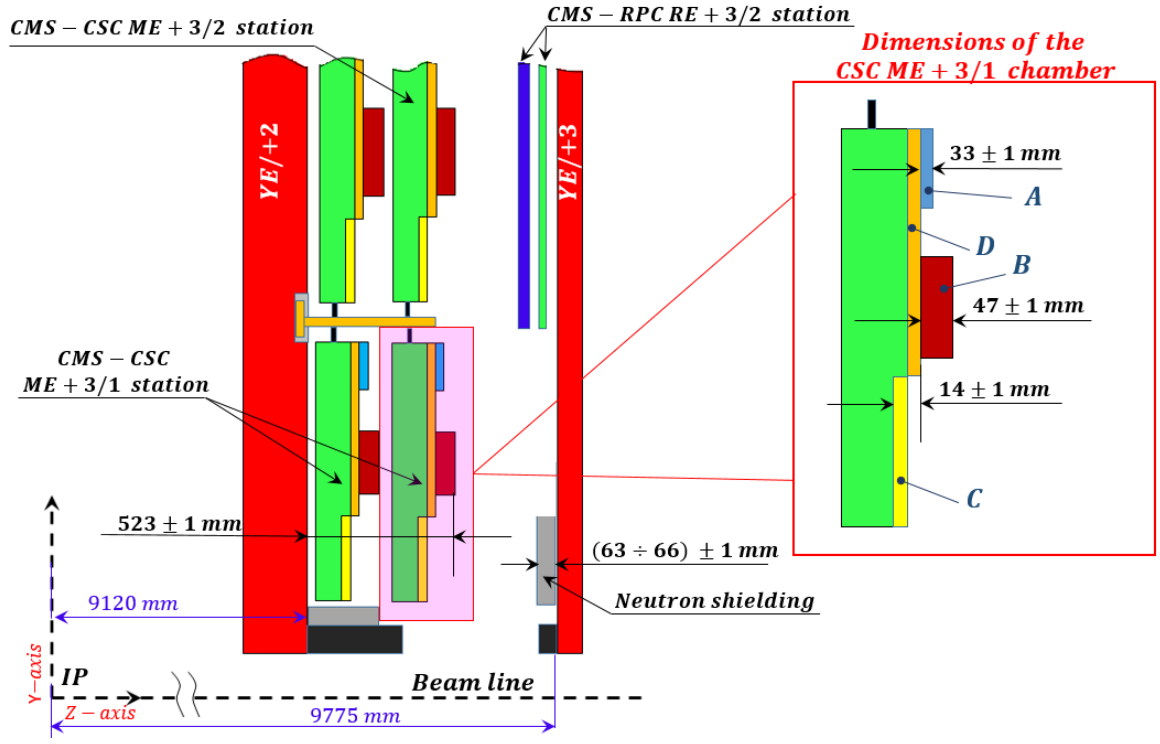

Figure 5.15: Left: Cross-section of the YE2 and YE3 iron disks in the Endcap region. Right: Close view of the CSC ME3/1 chamber cross-section. Results of the survey manual measurements are reported on the scheme.

End Board (element labeled to as *B* in Fig. 5.14 and 5.15) on the YE±2 iron disks and the thickness of the neutron shielding on the YE±3 iron disks. Moreover, the survey measurements demonstrated that even the surface of the

neutron shielding is not perfectly uniform and its thickness value fluctuates in the range between 63 mm and 66 mm due to the mechanical unconformities and manufacturing defects.

By combining the survey manual measurements and precise information provide by CMS Engineering and Integration Office on the position of the YE±2 and YE±3 iron disks relative to the interaction point after closing of the CMS detector, the space actually available for the iRPC RE3/1 chambers has been found to be 80±1 mm.

However, an additional survey measurement has been performed using the Infrared Proximity Sensor - Sharp GP2Y0A21YK able to accurately determine the distance between the surfaces of the YE±2 and YE±3 iron disks after closing of the CMS detector. Fig. 5.16 shows the view, schematic drawing and the operating sketch of the Infrared Proximity Sensor - Sharp GP2Y0A21YK. For this purpose, in January of 2017, the five infrared sensors have been installed in YE±3 iron disk during the End Year Technical Stop LHC. Taking into account that the YE±2 iron disks are characterized by a non-uniform surface topology due to the presence of the CSC ME±3/1 station, the IR-sensors have been installed in specified places on the surface of the YE±3 iron disks in order to have a complete mapping of the available space between the YE±2 and the YE±3 iron disks. Schematic overview of the IR-sensor installation on YE+3 disk is shown in Fig. 5.17-left.

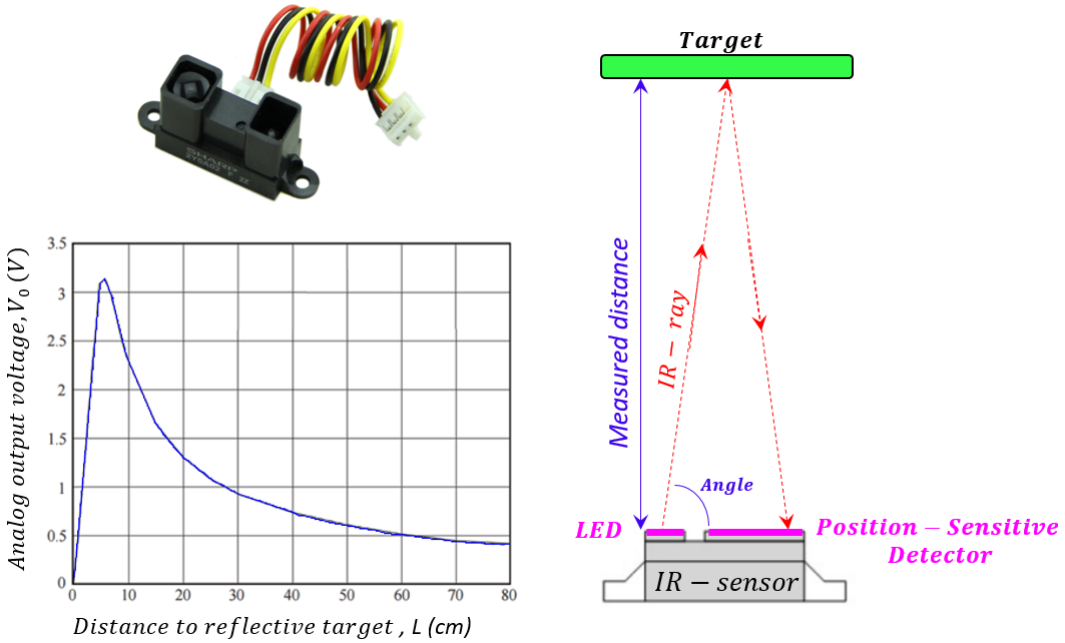

Figure 5.16: The device specs and an operating sketch of the Infrared Proximity Sensor - Sharp GP2Y0A21YK

As shown in Fig. 5.17, three of the five IR-sensors, labeled to as S1, measured the distance between the surface of the YE±3 iron disks and the CSC

Cathode FEB (element labeled to as A). Another infrared sensor labeled to as IRS4 determined the distance between the surface of the YE±3 iron disks and the CSC Anode FEB (element labeled to as B). Finally, the last sensor labeled to as IRS5 measured the distance between the neutron shielding and CSC PCB cover (element labeled to as C).

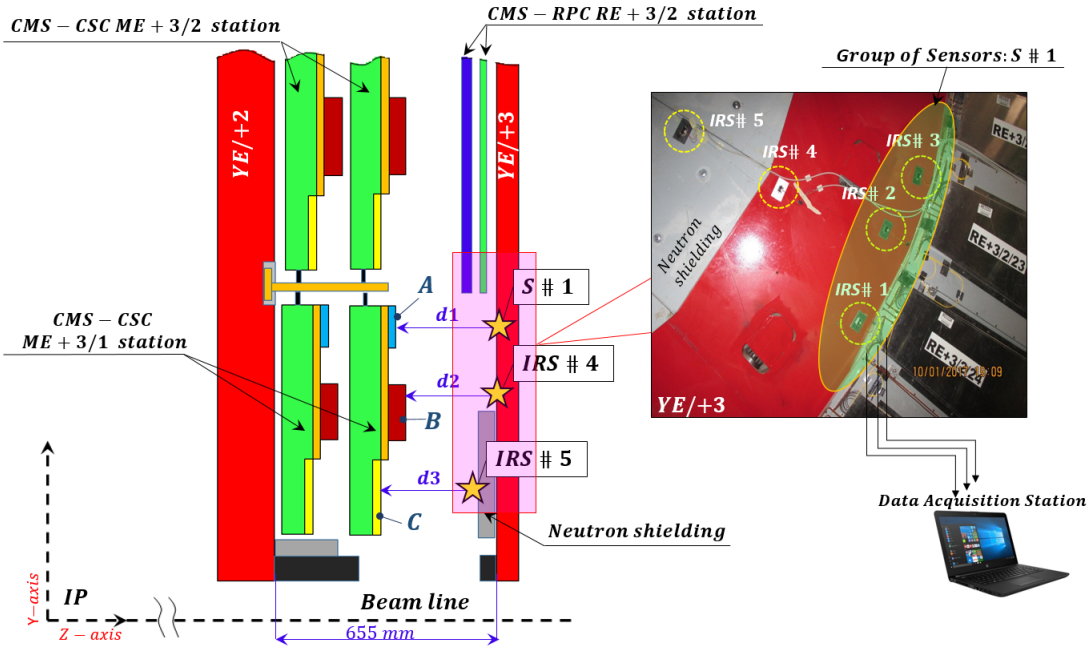

Figure 5.17: Left: Schematic overview of the IR-sensor installation on YE+3 disk. Right: Photography of the Infrared Proximity Sensors - Sharp GP2Y0A21YK positions on the YE+3 iron disk.

The results of the IR-sensor measurements survey are summarized in the Tab. 5.3.

Table 5.3: Results of the IR-sensor measurements survey

ID sensor	Result, mm
IRS1	161.5±0.8
IRS2	159.2±0.5
IRS3	157.1±1.0
IRS4	145.8±0.8
IRS5	142.4±1.0

As shown in Fig. 4.15 and 4.17, the space actually available for the future installation of the iRPC RE3/1 chamber is essentially determined by the distance between the CSC Anode Front-End Board (element labeled to as B in Fig. 4.15 and 4.17) on the YE±2 iron disk and the neutron schielding on the YE±3 iron disk. Therefore, the available space for the chambers installation

depends on the thickness of these two elements. Such available space can be estimated by combining the information on the thicknesses of the CSC chamber components, obtained during the manual measurements survey, together with the results of the IR-sensor measurements survey.

Survey Results ♯1. The available space has been estimated combining the information of the thickness of the CSC chamber components together with the results of the IRS1, IRS2 and IRS3 infrared sensors measurements campaign and taking into account the possible non-uniformity of the neutron schielding.

1. Maximum available space. The maximum available space has been estimated considering the smaller thickness of the neutron shielding:

   Max. available space = d1(IRS1) - Min. neutron shielding thickness + CSC Chatode FEB thickness - CSC Anode FEB thickness = 83.5 ± 3.8 mm.

   Max. available space = d1(IRS2) - Min. neutron shielding thickness + CSC Chatode FEB thickness - CSC Anode FEB thickness = 82.2 ± 3.5 mm.

   Max. available space = d1(IRS3) - Min. neutron shielding thickness + CSC Chatode FEB thickness - CSC Anode FEB thickness = 80.1 ± 4.0 mm.

2. Minimum available space. The minimum available space has been estimated considering the bigger thickness of the neutron shielding:

   Min. available space = d1(IRS1) - Min. neutron shielding thickness + CSC Chatode FEB thickness - CSC Anode FEB thickness = 81.5 ± 3.8 mm.

   Min. available space = d1(IRS2) - Min. neutron shielding thickness + CSC Chatode FEB thickness - CSC Anode FEB thickness = 79.2 ± 3.5 mm.

   Min. available space = d1(IRS3) - Min. neutron shielding thickness + CSC Chatode FEB thickness - CSC Anode FEB thickness = 77.1 ± 4.0 mm.

where d1(IRS1), d1(IRS2) and d1(IRS3) are the distances between the YE3/+ iron disk and the CSC Cathode FEB (element labeled to as A in Fig. 5.15 and 5.17) measured by the IRS1, IRS2 and IRS3 infrared sensors, respectively. Therefore, the average minimum distance available for chamber installation is (79.3 ± 1.3) mm, while the average maximum distance available is (82.3 ± 1.3) mm. Finally, taking into account the non-uniformity of the neutron schielding, the average distance available for chamber installation is (80.1 ± 1.0) mm.

Survey Results ♯2. The available space has been estimated combining the information of the thickness of the CSC chamber components together with the results of the IRS4 infrared sensor measurements campaign and taking into account the possible non-uniformity of the neutron schielding.

1. Maximum available space. The maximum available space has been estimated considering the smaller thickness of the neutron shielding:

   Max. available space = d2(IRS4) - Min. neutron shielding thickness = 82.8 ± 1.8 mm.

2. Minimum available space. The minimum available space has been estimated considering the greater thickness of the neutron shielding:

   Min. available space = d2(IRS4) - Max. neutron shielding thickness = 7.8 ± 1.8 mm.

where d2(IRS4) is the distances between the YE±3iron disk and the CSC Anode FEB (element labeled to as B in Fig. 5.15 and 5.17, the most protruding element) measured by the IRS4 infrared sensor. Therefore, taking into account the non-uniformity of the neutron schielding, the average distance available for chamber installation is (81.3 ± 1.5) mm.

Survey Results ♯3. The available space has been estimated combining the information of the thickness of the CSC chamber components together with the results of the IRS5 infrared sensor measurements campaign.

1. Available space:

   Available space = d3(IRS5) - CSC Cooling System thickness - CSC Anode FEB thickness = 87.4 ± 3.0 mm.

where d3(IRS5) is the distances between the neutron shielding on YE±3 iron disk and the CSC PCB cover (element labeled to as C in Fig. 5.15 and 5.17) measured by the IRS5 infrared sensor. However, the latter measure does not take into account the possible non-uniformity of the neutron shielding since the IRS5 infrared sensor has been installed in a single fixed position on the neutron shielding. Therefore, such measurement only represents an approximation of the space available for chamber installation.

Finally, taking into account all results obtained with different methods, the final value of the available space has been established to be (83.2 ± 0.9) mm. Therefore, the survey measurements demonstrated that the currently available space between neutron shielding and CSC ME3/1 station will allow installing the future iRPC RE3/1 detectors and their services (front-end electronics, cooling system, gas pipes, and mounting elements) in the endcap region of the CMS muon system.

A similar procedure will be repeated in order to estimate the available space between YE±3 and YE±4 for the future installation of the iRPC RE4/1 station. The survey measurements have been scheduled during the upcoming Long Shutdown-2.

5.5.2 Installation and integration in the Endcap region

Taking into account the information obtained during the survey performed to estimate the available space needed for future installation of the iRPC chambers during the Yearly Technical Stops at the end of 2022 and 2023, the RE3/1 chambers will be installed directly on the endcap yoke 3 (YE3) iron disk (Fig. 5.18-right), using the foreseen mounting points threaded into the yoke steel. In this case, they will cover the circular neutron shielding attached to the inner part of YE3 and reach the cylindrical neutron shielding surrounding the flange that separates the yokes YE2 and YE3 (Fig. 5.18-right). Allowance for sagitta in the yoke when the magnetic field is applied will be made using simplified kinematic mounts (Fig. 5.18-left).

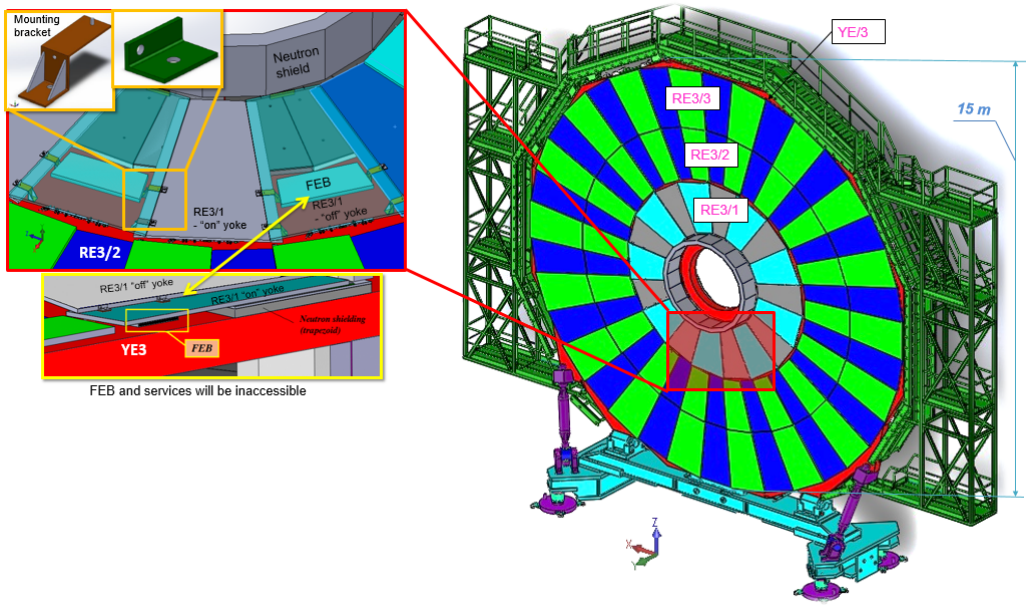

Figure 5.18: 3D-drawing of the RE3/1 chambers fixed on the YE3 (right). Top left: Detailed scheme of installation of the RE3/1 chambers on the YE3. Bottom left: The Front-End Board mounted behind RE3/1 chambers.

The screws and washers securing the neutron shielding will be modified to make them flush with the outer lead part of the shield so increasing the available space in the "Z" direction. The CSC alignment system will be decommissioned to give space for the chambers over the neutron shielding. However, due to the limited space between YE3 iron disk and CSC chambers, the electronics and cooling system will be inaccessible during the operation.

For RE4/1 chamber, the installation will be completely different since they will be mounted to the same side of YE3 iron disk close to the RPCs super modules (Fig. 5.19-right), over the CSC ME4/1 station, taking advantage of the CSC mounting posts. In this case, a thin lightweight mounting frame, made of aluminum alloy 8 mm thick, will be installed back of the CSCs, to which the iRPCs will be attached (Fig. 5.19-left). The chambers will be directly

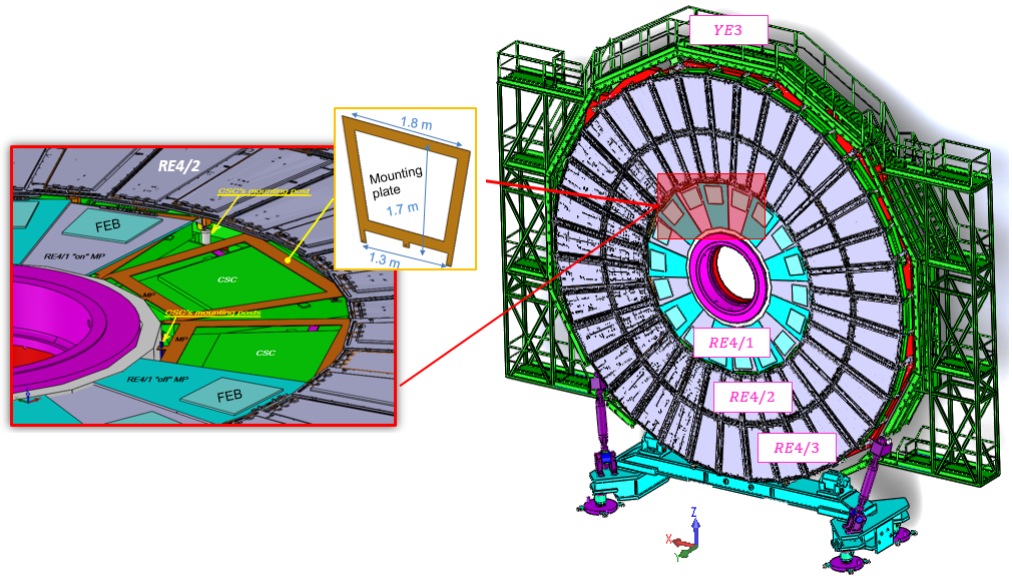

Figure 5.19: 3D-drawing of the RE4/1 chambers fixed on the YE3 (right). Bottom left: Schematic view of the RE4/1 chambers mounted on the mounting plate. Top left: Schematic layout of the mounting plate.

screwed to this frame, following the similar configuration currently used for the mounting system of the RE4/2 and RE4/3 detectors. The installation procedure will be performed in two steps: first the aluminum mounting systems will be installed on the yoke iron disk and then the chambers will be fixed on the latter.

The future iRPC high voltage power system will be hosted in the present RPC HV power system, occupying 10 racks located in the underground service cavern (USC), therefore no additional branches or mainframes will be needed. The new HV system will be shared in four existing racks following the same regional power collection scheme of the present RPC system. The RE3/1 and RE4/1 low voltage (LV) power will be supplied by an extension of the present RPCs LV a power system, located mainly in the underground experiment cavern (UXS). The new iRPC chambers will use the same $C_2H_2F_6/iC_4H_{10}/SF_6$ (96.2/3.5/0.3) gas mixture used at present. The current gas distribution system will be extended by adding the new pipings and bulkheads around the yoke.

Chapter 6

Performance Studies of the Improved RPC Detector: real-size iRPC RE3/1 & RE4/1 Detector Prototypes with New PETIROC ASIC Electronics

This Chapter presents the production of the first large-size improved RPC detector prototypes with the new PETIROC ASIC front-end electronics and their performance study. As a member of the CMS-RPC Collaboration, participating in the production process, the doctorate candidate takes part in all activities on construction and testing the detecting elements, assembling of the new prototypes, testing of the prototypes with new electronics under muon particles beam impact at the CERN Gamma Irradiation Facility (GIF++) in August 2018 and the subsequent data analysis. A detailed description of all production steps and the main results obtained during the Test Beam campaign are discussed below.

6.1 Overview of the New Strip Panels and the PETIROC ASIC Electronics Design

6.1.1 Strip panels design

The strip panel PCB will only cover a half of the detector prototype active area. The size of the two PCBs exceeds slightly that of the KODEL RPC gas gap used for the RE3/1 and RE3/1 detectors assembly. In the Fig. 6.1 and Fig. 6.2 the PCB's design for RE3/1 and RE4/1 detector prototypes are presented. The strips panels are a three-layer structure: the main part consists of the copper strips with a longitudinal shape to cope with the RPC gas gap's

own shape. The minimum of the strip pitch is of 6.5 mm for short base of the PCB panel and the maximum is of 11.5 mm for the large base, respectively.

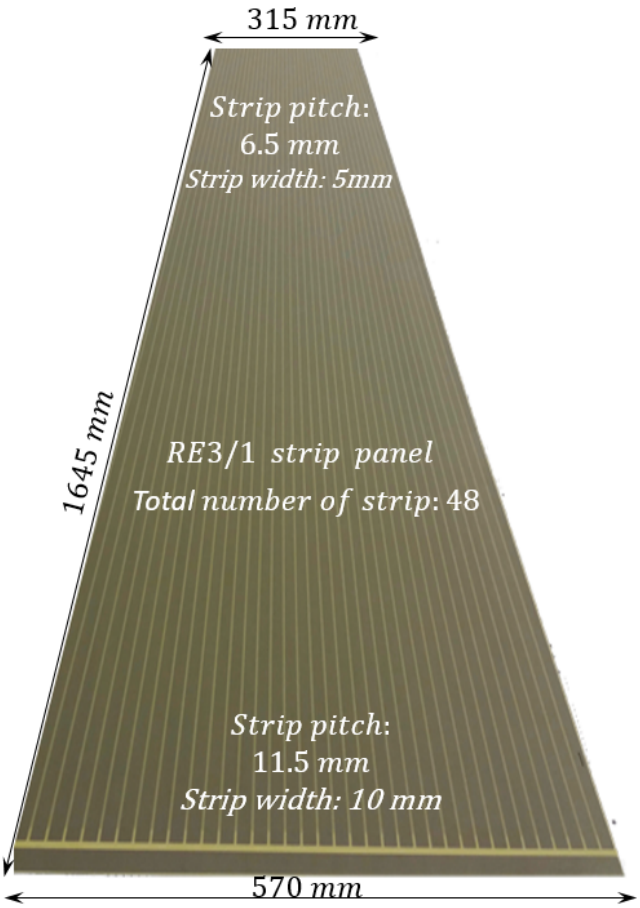

Figure 6.1: Picture of readout strip panel with its main characteristics for the iRPC RE3/1 detector prototype.

All trapezoidal strips are covered on both sides by 300 μm FR4 insulator layer. The FR4 is a composite material composed of woven fiberglass cloth with an epoxy resin binder that is flame resistant. In the PCB for RE3/1 detector, the ends of each strip are not covered by FR4 layer (the length of the uncoated strip is 10 mm) in order to solder 50 Ohm coaxial cables directly on the strips. The impedance value of the coaxial cables has been chosen identical to the strips in order to avoid any possible signal reflexions. The Frond-End Electronics (FEBs) is connected to the PCB through the coaxial cables by using the LEMO-01 connectors. In addition, both ends of the strip panel PCB for RE3/1 detector have a copper layer with 79 mm width for a grounding.

For the RE4/1 chamber, the strips readout board design is slightly different than for RE3/1. The two ends of each strip are prolonged by much thinner strips (200 microns width). These thin strips run along the edge of the PCB

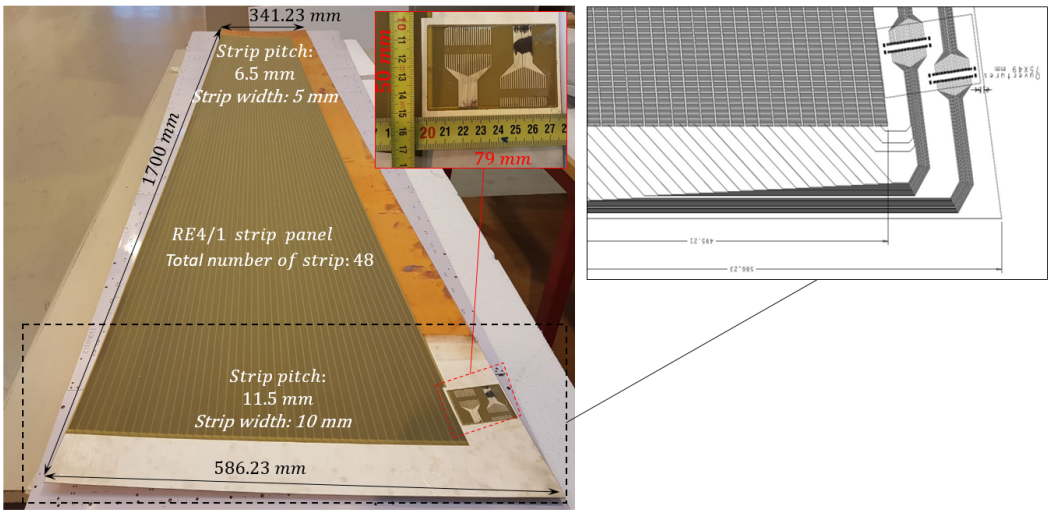

Figure 6.2: View of readout strip panel with its main characteristics for the iRPC RE4/1 detector prototype. Zoomed view - schema of the distribution of the strip lines and layout of connectors.

outside the gap in a zone of less than 10 cm width. These strips, called return strips, cover, in addition to the same dielectric layers covering the main strips (receiving strips), by two extra conductive layers placed outside the dielectric ones. The purpose of the conductive layers is to ensure for these thin strips the same impedance as one of the main strips and also to protect them from external electromagnetic perturbation. The dimensions of the strips and their return strips, as well as the thickness of the dielectric layers, were worked out to ensure the best impedance matching all along the signal path. Moreover, the strip panel PCB for the RE4/1 chamber has two connectors whose pins are connected to the two ends of all the PCB's strips. These connectors are used to connect two FEBs by using the flat ribbon connectors.

As previously discussed, in order to avoid any possible signal reflexions in each long strip panel, it is important that the impedance of the chain from strip to the FEB input for both prototypes will be identical. The resistivity of the high voltage graphite conductive layers of the RPC detector is too high for these layers to behave as the ground reference for the transmission line and does not define the strip impedance. In this case, the FR4 layer of the PCB and the iRPC detector behave as a dielectric and the mechanical layers of the cassette (the two gas gaps with strip panel PCB in the middle are closed by the Faraday cage) play the role of the line ground planes.

The values of the strip impedance for the RE3/1 and RE4/1 chambers have been estimated by the following equation:

$$Z_C = \sqrt{\left(\frac{R_S + j \cdot L_S \cdot w}{G_p + j \cdot C_p \cdot w}\right)} \tag{6.1}$$

where j is the imaginary unit, and w is the angular frequency and other four parameters define the strip impedance.

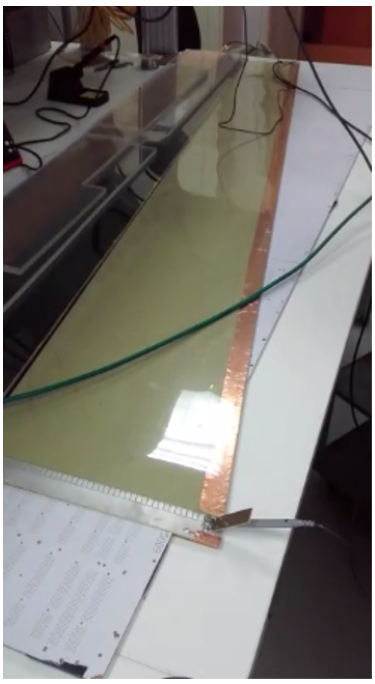

Figure 6.3: The experimental measurement of strip panel impedance for the iRPC RE3/1 detector prototype.

Geometrical dimensions of the strips and strip material define the ohmic resistance R_S value that describes the ohmic losses along the transmission line conductor. Strip dimensions are a function of the number of channels on each detector (48 channels), width and length of the iRPC detector active area. Strips material is defined by the manufacturing process (copper). Then strip impedance L_S is also defined in a similar way by the strips material and strip geometry. The dielectric capacitance C_p is defined by the dielectric thickness (iRPC detector and FR4) and material. The dielectric conductance G_p, describing losses in the dielectric part of the transmission line, is also defined by iRPC detector and FR4 thickness and material.

In order to maximize charge transfer between the iRPC detector and its strips, the thickness of the FR4 layers of the strips panel PCB should be minimized to reduce a distance between strips and conductive layers of the gas gaps. Considering the large size of the PCB, 300 μm of FR4 on each side of the strips seems to be the minimal acceptable value in terms of mechanical rigidity and handling capabilities. Therefore, the only way to adjust strip impedance is by modifying the distance between the strips and the mechanical ground plane of the cassette.

Table 6.1: The results of the strip panel impedance measurements for the RE3/1 prototype.

Measured parameter	**Measurement result**
R_S $(m\Omega)$	461
L_S (nH)	487
G_p (μS)	934
C_p (pF)	244
Z_c (Ω)	44

After the strips panel PCB with coaxial cables has been installed inside the cassette between the two gas gaps, the first attempt of numerical simulation of the impedance of the whole system has been performed by using software TNT Transmission line electromagnetic simulation tool suite version 1.2.2 [73]. However, due to limited knowledge of the RPC detector dielectric permeability, it is not possible to build reliable models or simulation tools that can predict the impedance of the whole system. Therefore, the only reliable way to predict the strip panel PCB impedance consists of a direct measurement of it. Three different methods have been used to estimate the strips impedance value.

The first method consists in measuring separately each line parameter (R_S, L_S, C_p and G_p) with a RLC meter (Quadtech 7600). R_S and L_S have been measured by shorting the end of the line to ground, while C_p and G_p have been measured with an opened line.

The second method (load matching) has been performed by injecting a pulse at one side of the strip and adjusting a variable load at the other side of the strip to suppress reflections. Finally, the third method (reflective) is based on a behavior of a non-adapted line at the very first instants of an injected pulse where the line behaves as if it was an ohmic resistor whose value is its characteristic impedance of the line.

All these methods lead to the results given in Table 6.1. The measurements have been performed for both sides of the strips giving similar results. Knowing the line parameters, the impedance value of the return strips has been found to be 44 Ω. It is interesting to notice that in case of a lossless transmission line, G_p and R_S are negligible and the line impedance is then defined only by L_S and C_p. In our case, although R_S is small and could be neglected due to the wide geometry of the strips, G_p cannot be neglected (because of the intrinsic structure of the RPC detector itself) [74].

For PCB version of the RE4/1 prototypes, the impedance of the strips has been also carefully measured to define the geometry of the return strips in order to match their impedance to the impedance of the receiving strips. The impedance measurement results are not presented here.

6.1.2 Front-End Electronics design

The front-end board prototype consists of two main components: a fast front-end ASIC and a Time-to-Digital Converter (TDC). The ASIC knowns as PETIROC [75], it is a 32 channels version by developed in the SiGe technology [76]. It hosts a preamplifier with a 1 GHz bandwidth and gain of 25 associated with a fast programmable comparator (Fig. 6.4). The overall jitter of PETIROC keeps at 20 ps for an input charge of 300 fC. Threshold and pedestal alignments of the 32 channels made by individually adjusting internal Digital-to-Analog Converter (DAC) for both pedestal and comparator levels.

The output of the comparator for each PETIROC channel is fed into an Altera Cyclone II FPGA [77] hosting the TDC conversion module. This TDC, called wave union, is based on a set of identical delays whose each output is connected to a latch stage. The input signal is propagated across the delay chain and on each rising edge of the system clock, value of output of each delay is frozen and, knowing the individual propagation delay of cells, the state of each delay cell output gives access to the global delay between the incoming signal and the edge of the clock. A coarse clock counter completes time measurement by respect to an acquisition window or a common start signal. In this system, the quantification step is given by the propagation delay of one delay element (around 20 ps for a carrying element inside a Cyclone II FPGA.

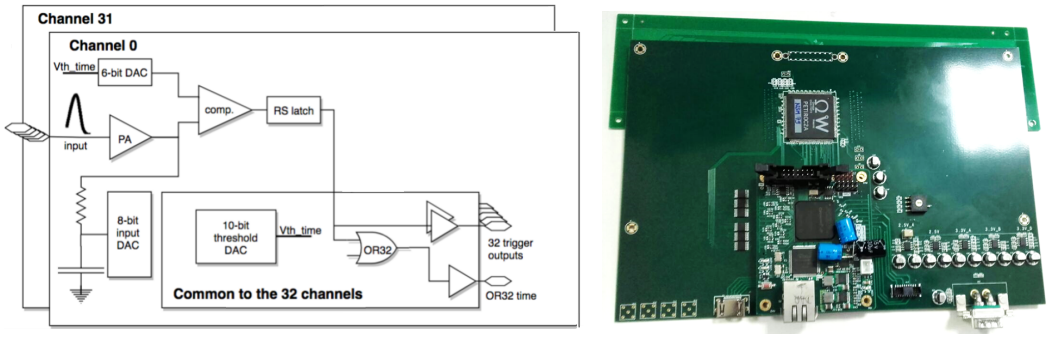

(a) (b)

Figure 6.4: Block diagram and view of the PETIROC ASIC.

Inside a standard FPGA, logic elements are organized in Logic Array Blocks (LAB) and even if delay between two elements inside one LAB is small and well known, due to routing constraints inside the FPGA, the delay between elements of separated LABs can be of the same order of magnitude as one delay element of the chain. This problem is solved in the wave union TDC by generating two consecutive edges for each input signal and wisely separating them to ensure that at any time at least one of those signals is not located between two LAB.

6.2 Prototypes Technical Design

The integration study of the new iRPC station in the innermost region of the CMS endcap, described in Section 5.5, helped to determine the final design of the new generation RPC chambers (called RE3/1 and RE4/1) that will be installed here to increase the redundancy in $1.8 < |\eta| < 2.4$ region.

Before the construction of the first large-size prototype of the new improved RPC (iRPC) detector, the methodology of the assembly procedures and quality control tests have been studied. This activity allowed to select the needed tools, materials and components for a proper detector prototype construction. The main detector components specification with their characteristics required to construct the iRPC chamber are presented in Table 6.2.

Following CMS-RPC traditions, the improved RPC RE3/1 and RE4/1 detector prototypes will have a similar design to the existing 2 mm gas gap RPC detector as described in Chapter 5. The main distinctive characteristic of this chamber is the thinner gas gap of 1.4 mm.

Gas gap consists of two High-Pressure Laminate (HPLs - bakelite sheets) sheets with 1.4 mm thickness and resistivity value of 0.9 - 3.0×10^{10} Ωcm and $\sigma/\mu < 0.5$, which is coated with thin layer of graphite insulated with the Polyethylene Terephthalate (PET®) film. The surface resistivity of the electrodes ranges from 100 to 250 $k\Omega/\square$. The raw material for HPL panels have been produced by Puricelli company (Milan) and have been cut by Riva firm (Milan). Then cut HPL panels have been shipped to the Korean DEtector Laboratory (KODEL, South Korea) to develop the needed gas gaps. In the KODEL workshops, the gaps have been produced by using the HPL's bakelite sheets without linseed oil treatment on the inside surface, with the graphite coating on the outer surface and with the mounting the 1.4 mm thick button spacers, side spacers, and gas nozzles.

Coin-shaped spacers are placed inside the gas gap between the two electrodes in order to achieve of 1.4 mm homogeneous separation and ensure an uniform electric field within the gap. The four edges of the gap gaps are sealed with four edge strips. The spacers are placed ∼7.5 cm apart from each other in the orthogonal direction to provide the mechanical support of the gap, while the edge strip, sealing the edge of the gap, make the gas volume leak-tight.

The overall dimensions of the RE3/1 and RE4/1 chambers will be different due to the mechanical constraints in the regions in which they will be installed. Taking into account of the mechanical constraints of the existing muon endcap, the overall dimensions of the gas gaps for the new chambers will be: larger base is 1176.02 mm (987.01 mm), the small base is 693.98 mm (562.52 mm) and height is 1563.82 mm (1655.85) mm for the RE3/1 (RE4/1). Both chambers will use two identical large gas gaps placed one on the top of other with common radially oriented readout strips in the middle. The engineering drawings of the gas gaps for RE3/1 and RE4/1 detectors produced by KODEL is shown in Fig. 6.5. The chamber will be housed within a custom detector casing, while the services (readout electronics, high and low voltages, and gas distributions) will

Table 6.2: The main detector components specification with their characteristics required to construct the iRPC chamber.

Component	**Material**	**Dimentions**
Gas gaps	HPL	**RE3/1** LB: 987.01 mm, SB: 562.52 mm, H: 1655.85 mm, Thickness: 5.3 mm **RE4/1** LB: 1176.02 mm, SB: 693.98 mm, H: 1563.82 mm, Thickness: 5.3 mm
Strip panel	PCB	**RE3/1** LB: 987.01 mm, SB: 562.52 mm, H: 1655.85 mm, Thickness: $\sim$ 1 mm **RE4/1** LB: 1176.02 mm, SB: 693.98 mm, H: 1563.82 mm, Thickness: $\sim$ 1 mm
Honeycomb panel	Al	**RE3/1** LB: 1244 mm, SB: 645 mm, H: 1665 mm, Thickness: 5 mm **RE4/1** LB: 1196.02 mm, SB: 713.93 mm, H: 1616.82 mm, Thickness: 5 mm
Faraday cage	Cu	**RE3/1** LB: 1286.5 mm, SB: 794 mm, H: 1564 mm, Thickness: 50 μm **RE4/1** LB: 1087 mm, SB: 662.5 mm, H: 1656 mm, Thickness: 50 μm
Insulation	$Mylar$	**RE3/1** LB: 1176.02 mm, SB: 693.98 mm, H: 1563.82 mm, Thickness: 175 μm **RE4/1** LB: 987.01 mm, SB: 562.52 mm, H: 1655.85 mm, Thickness: 175 μm
"L"-brackets	Al	13 $\times$ 13 $\times$ 2 mm^3
Bars	Al	13 $\times$ 13 mm^2
Gas pipes	$Rilsan^{®}$ $Polyamide$	Diameter (inner/outer): 6 mm/5 mm

be installed outside it.

In order to reduce a cost of the needed materials and components to assemble the prototypes, it has been decided to recycle the components of the spare RE 4/3 RPC chamber, which has been stored at the CERN CMS-RPC QA/QC facility. The RE4/3 chamber has the trapezoidal shape with following overall dimensions: larger base is 1336 mm, the lower base is 992 mm and height is 1967 mm (Fig. 6.6). Its dimensions are large enough to allow the re-use of all the mechanical components in order to construct a new detector

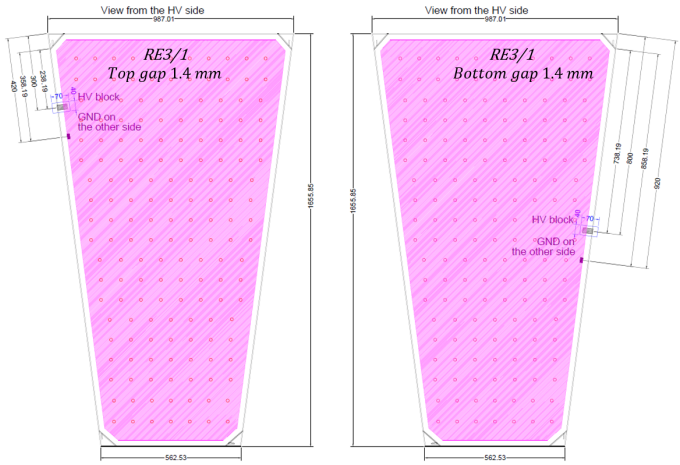

(a)

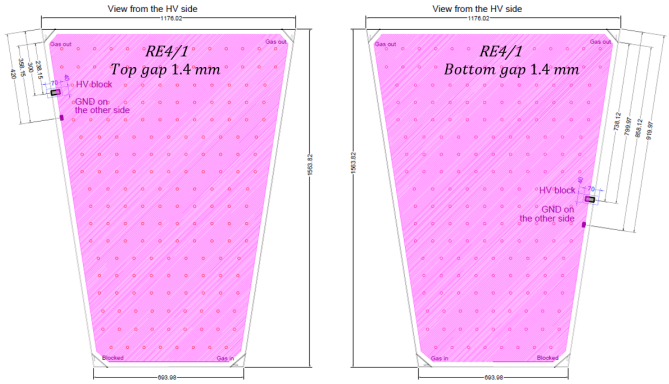

(b)

Figure 6.5: The engineering drawings of the gas gaps for RE3/1 (a) and RE4/1 (b) detector prototypes produced by KODEL.

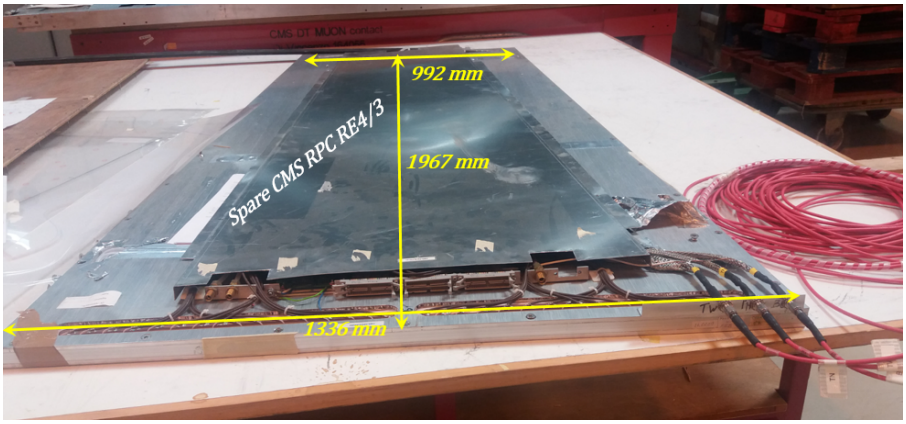

Figure 6.6: The present CMS RPC RE4/3 chamber (spare) with its overall dimensions.

casing for the real-size iRPC RE3/1 and RE4/1 prototypes and to avoid the unnecessary costs, such as the purchase of the expensive copper foils for the Faraday cage.

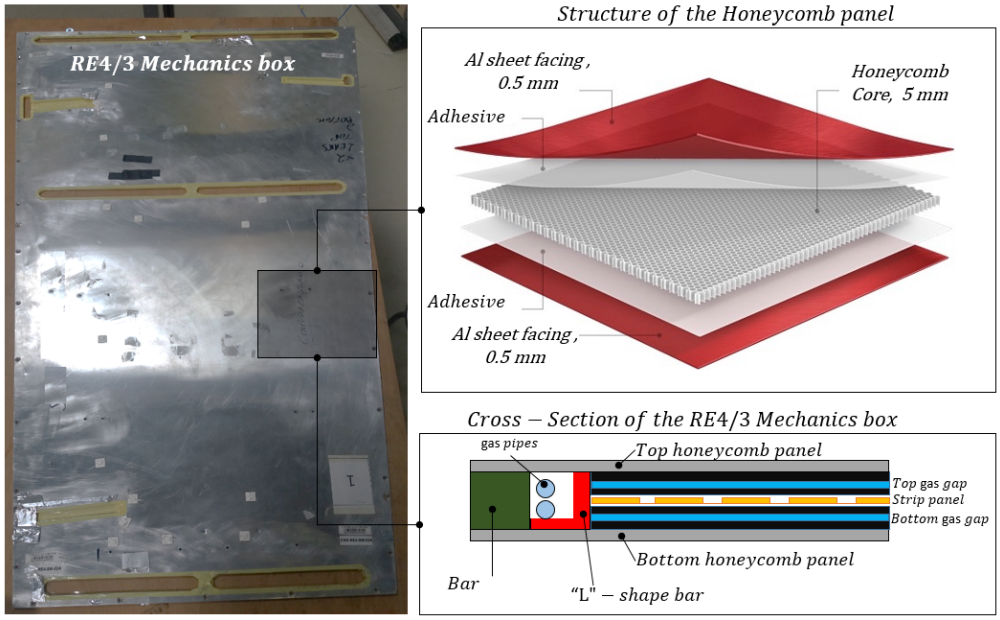

Figure 6.7: The picture and scheme of the typical honeycomb plate for the CMS- RPC RE4/3 chambers

The existing detector casing, which housed the spare RE4/3 chamber, consists of two honeycomb plates screwed onto four aluminum edge-bars. During the prototype construction, the detector casing has been appropriately adapted to allow the installation of the electronics and housing of the services, such as the gas and high voltage lines. The layout of a typical CMS-RPC RE4/3 honeycomb plate is shown in Fig.6.7. A honeycomb plate has in a total thickness of 6 mm and it consists of the top and the bottom aluminum cover sheets with a thickness 0.5 mm and solid honeycomb core with a thickness 5 mm, respectively. At the four edges and few other positions around the perimeter where threaded holes are located, the honeycomb core is strengthened by the insertion of 5 mm thick solid aluminum plates. The cross-section of the edge bars are $15 \times 15\ mm^2$. In order to fix the gas gaps inside the chamber, the "L"-shape bars are used with dimensions of $15 \times 15 \times 2\ mm^3$.

6.2.1 Mechanical Simulation

Before the start of the real assembly of the large size iRPC RE3/1 and RE4/1 detectors, the mechanical simulation has been performed by using a special engineering software, such as AutoCAD and SolidWorks. This type of activity is an important step to successfully develop prototypes. It allowed to reveal any

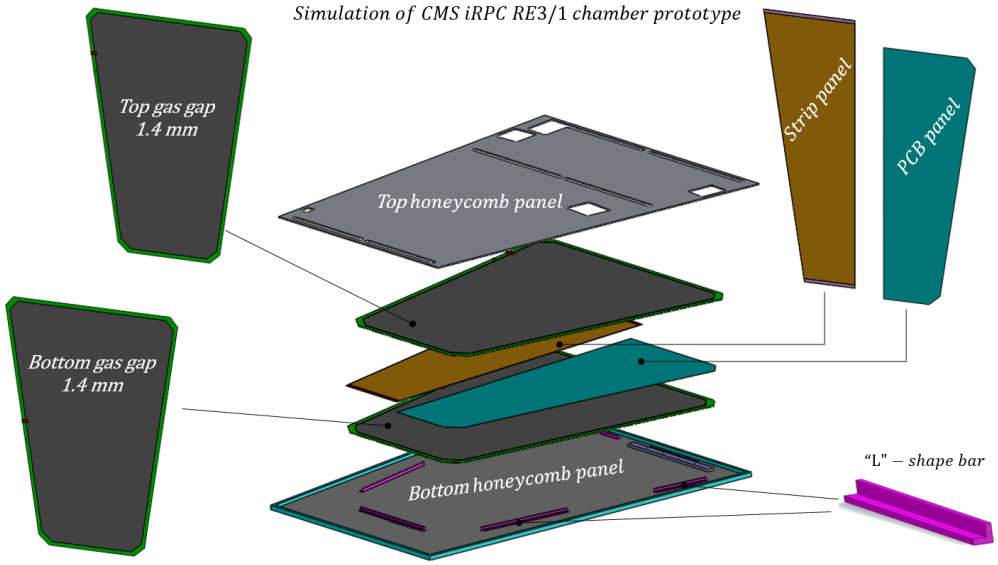

(a)

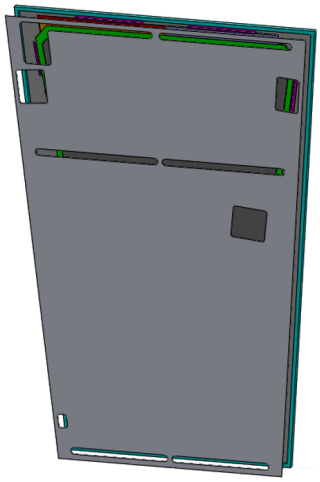

(b)

Figure 6.8: Exploded view (a) and final design (b) of the CMS- iRPC RE4/1 detector prototype. The 3D model simulation allowed to reveal any possible problematic aspects of the detectors assembly. The same procedure has been performed to simulated the 3D model of the CMS RPC RE3/1 detector prototype.

possible problematic aspects of the detector assembly such as the components fixation and their alignment inside a large RE4/3 mechanic box and solve them in the early stages of the prototype assembling.

The 3D models of the new RE3/1 and RE4/1 hambers have been simulated in scale 1:1 (Fig. 6.8b). As shown in Fig.6.8 the simulation of the RE4/3 honeycomb panels, gas gaps, and fixing components have been performed.

The CMS-RPC Collaboration approved the construction of two different

detector prototype layout in order to study the architecture and implementation of the front-end electronics and data acquisition (DAQ) system of the future improved RPC chambers. For the RE3/1, the expected pick-up signal from both ends of the strip panel will readout through 50 Ω coaxial cables while for RE4/1 the collected charges in the cathode will be read by a strips panel via conductive lines printed directly on the PCB panel. These peculiarities in the readout system require different ways of connecting electronics to the strip panel using the LEMO-01 and flat ribbon cable connectors, respectively. More details about the readout strips panel were given in Section 6.2.

Taking into account these different constructive constraints of the two readout strip boards, the RE4/3 top honeycomb panels have been appropriately modified to connect the strips panel to the front-end electronics. In addition, during the construction of the detector prototypes, two different designs of the readout strip panel will use to instrumentate only half of the detector active area. It will allow to reduce the construction costs. In order to avoid possible deformations and/or bending of the gap gaps, the non-instrumented half region will be compensated by inserting a PCB panel with the same size as the actual readout strip panel.

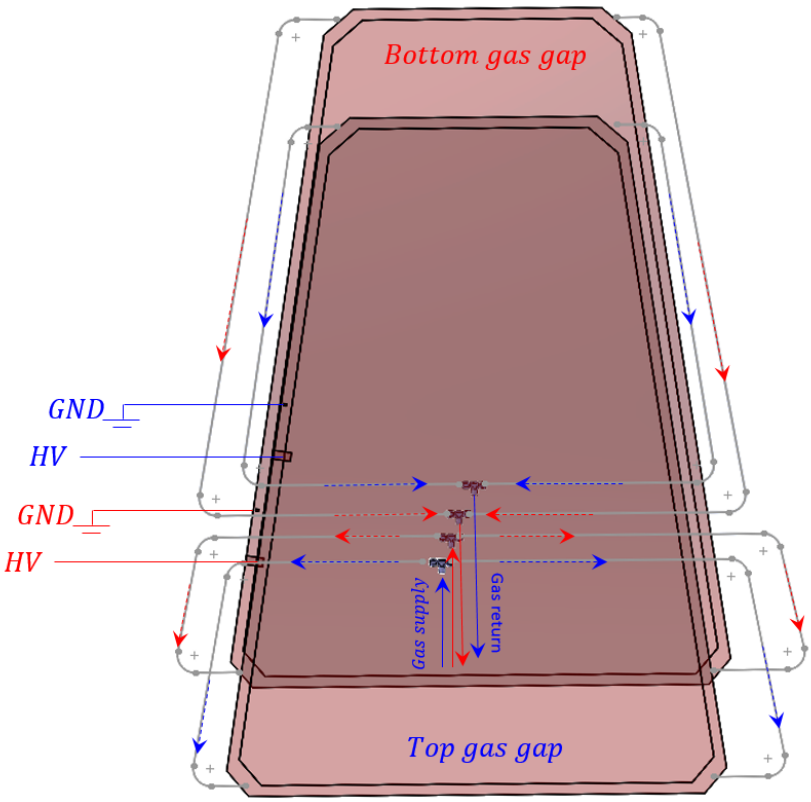

Figure 6.9: The principle scheme of the HV cables and gas pipeline routing for the RE3/1 and RE4/1 detector prototypes.

At the final stage of the prototype development, the high voltage cables and gas pipeline routing have been simulated for each detector prototype in order to optimize the connection and the limited space available inside the detector casing. The principle scheme of the HV cables and gas pipeline routing for the RE3/1 and RE4/1 detector prototypes is shown in Fig.6.9.

6.2.2 Prototype Construction and Quality Control

In this Section are reviewed the main aspects relevant to the detector prototypes assembly and quality control. The final detector quality and performance depend on the quality of the detector elements and on the accuracy of the assembly procedures. The final detector Quality Control (QC) is a key element to ensure the delivery of fully efficient detector prototypes.

6.2.2.1 Assembly and Quality Control Site

The CMS-RPC QA/QC facility at CERN has been chosen in order to assemble and quality the first real-size new generation of the RPC detector prototype. The CMS-RPC facility is located in CERN building 904 at the Prevessin site, where were assembled all RPC chambers for the barrel and endcap regions of the CMS experiment in the past. This facility includes a laboratory where the detectors are assembled and tested through multiple stages and strict quality control and a place for material storage. The laboratory is equipped with high voltage power systems, the gas system with the standard CMS-RPC gas mixture: $C_2H_2F_4$ / $iso-C_4H_{10}$ / SF_6 (95.2/4.5/0.3), large assembly tables and tooling for gas gap quality control, such as gas leak and high voltage test. Picture of the RPC laboratory installed at the CMS-RPC QA/QC facility at CERN are shown on Fig.6.10. There is also a cosmic telescope to test at once up to ten detectors in order to study all physical working chamber parameters.

Table 6.3: The gas gap ID code

ID code
KODEL-CMS-COA-DG14-B01
KODEL-CMS-COA-DG14-B02
KODEL-CMS-COA-DG14-T01
KODEL-CMS-PCB-DG14-B01
KODEL-CMS-PCB-DG14-B02
KODEL-CMS-PCB-DG14-T01
KODEL-CMS-PCB-DG14-T02

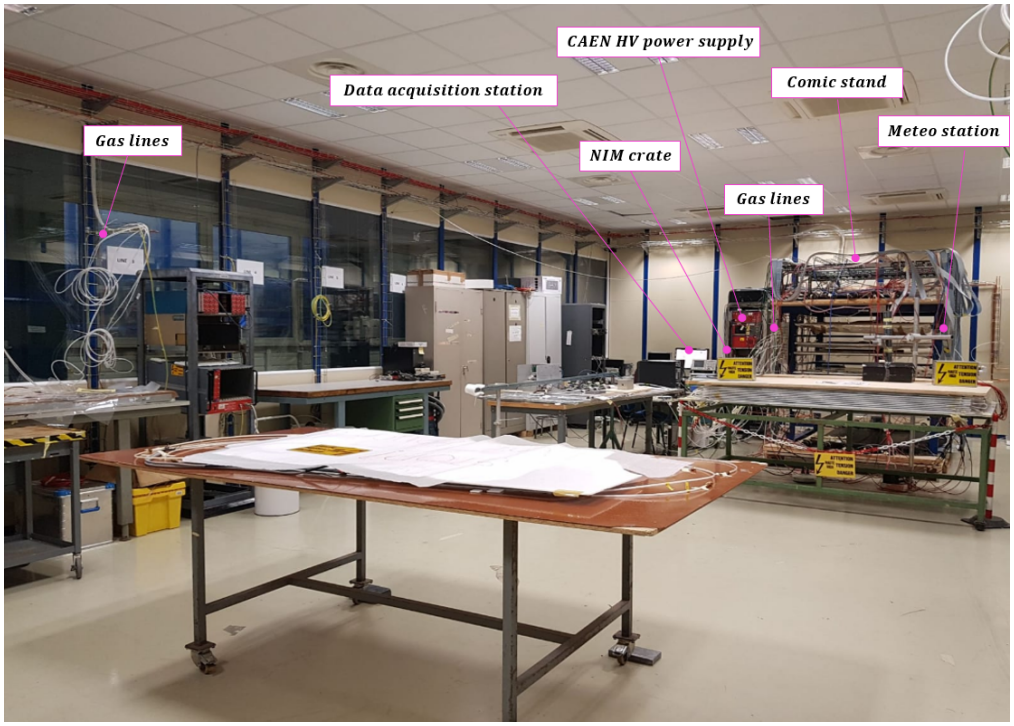

Figure 6.10: Picture of the RPC laboratory installed at the CMS-RPC QA/QC facility at CERN.

6.2.2.2 Pre-assembly Quality Control of the Detector Components

In July 2017 KODEL produced in a total of 7 gas gaps for r prototypes: 2 gaps (+1 spare) for RE3/1 chamber and 2 gaps (+2 spare) for RE4/1. At the KODEL workshops, all gas gaps have been tested in order to ensure the integrity and quality of the detecting elements and then shipped to the CERN. In August the gas gaps have been delivered to the CERN CMS-RPC assembly laboratory. The gas gap ID codes are given in Tab. 6.3 where the KODEL-CMS-COA-DG14-B01 (T01) is the bottom (top) gas gap for RE3/1 with strip panel consisting of the coaxial signal cables (COA), while the KODEL-CMS-PCB-DG14-B01 (T01) is the bottom (top) for the RE4/1 detector with Printed Circuit Board (PCB), respectively. DG14 means the double gap with 1.4 mm thickness.

All the detector components produced by industrial companies are delivered to CERN where they are immediately verified for defects and tested. Visual inspection is a commonly used method for quality assurance of the various detector components during the manufacturing and assembly. Therefore, optical inspection of the main detector components is performed to ensure the integrity and the quality of the gas gaps, readout strips panel, gas inlets and outlets, etc. Some of the preliminary inspections and tests on the main detector components are described below:

Mechanical Test of the Readout Strip Panels. An initial inspection is performed to check the planarity of the readout board. The readout board under test is placed on a flat optical table (in horizontal position) and its possible bending is verified by measuring the height of the readout board in several points along its perimeter with respect to the plane of the optical table using a high-resolution digital caliper. Additionally, optical inspection is performed in order to identify possible macroscopic scratches and defects on the readout strips or adopters for signal readout. The readout strip panels can be used to assemble the detector prototype if during the visual inspection no macroscopic damage is revealed that could compromise the integrity and the quality of the detector prototype.

Mechanical Test of the Gas Gaps. An optical inspection is performed in order to identify possible cracks, mechanical unconformities and manufacturing defects and/or any type of bending/bulges on the gas gaps surface, improper graphite/pet coating, broken nozzles or excess of glue, etc., that might have been incurred during a large distance transportation of the gas gaps, which includes air flights and handling at the airports, etc. The initial inspection and qualification procedures of the gas gaps are presented in the Fig.6.11.

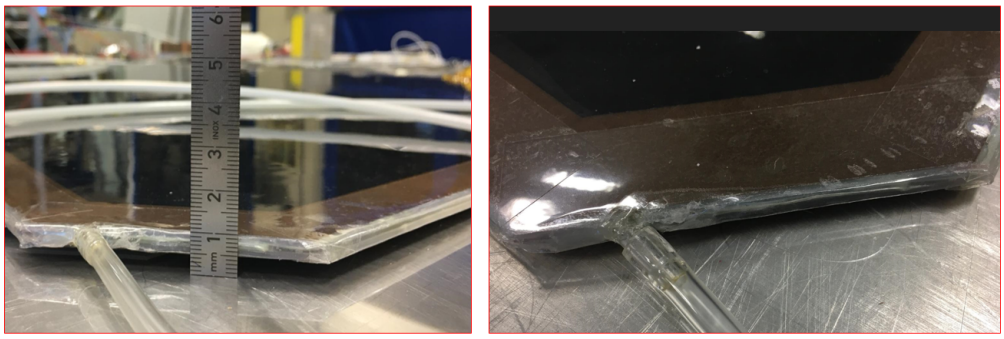

Figure 6.11: Pictures of the initial inspection and qualification procedures of the gas gaps.

A gas leak test is performed on the gas gaps in order to identify a possible gas leak. Gas leaks are not only a pointless waste of gas but also a source of possible pollution, humidity and unknown species from the external environment that could contaminate the active gas volume, react in the avalanche plasma, trigger the polymerization and lead a degradation of the performance of the detector. In order to perform this QC test, we made the "low cost" version of the pressure drop setup involves a simple U-shape tube. As shown in Fig.6.12, the U-tube is filled with water and connected to the detector through a safety container to prevent water overflow. When the output valve is open, both water levels are equal to h_0. When the valve is closed, raising the left tip of the U-tube creates a difference of water levels that correspond to an overpressure in the detector. In case of a gas leak, the water levels will go back

to the equilibrium level h_0. The linear dependency between the difference of levels $\triangle\ h$ and the overpressure P is given by:

$$\triangle\ h = 10\ m \Longleftrightarrow P = 1\ bar \tag{6.2}$$

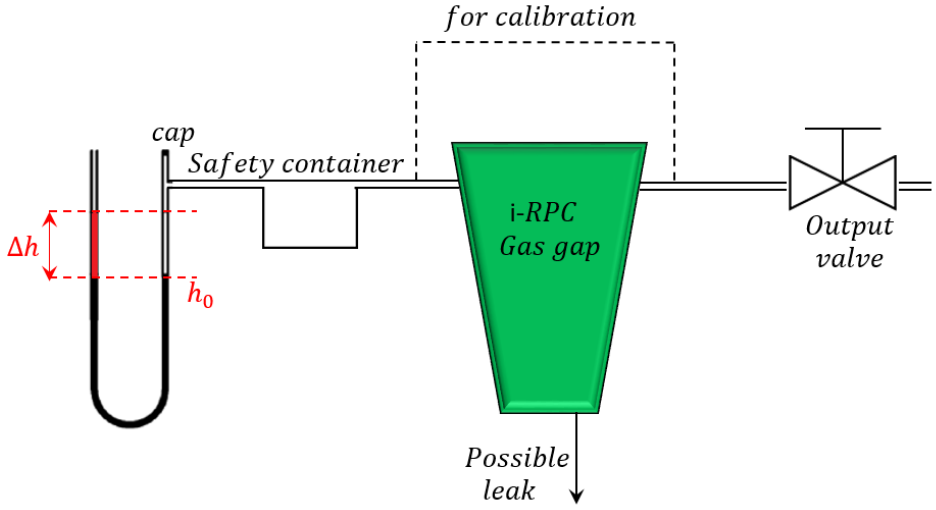

Figure 6.12: Principle scheme of the typical setup for the pressure drop measurement using the U-tube.

The KODEL gas gaps have been successfully assembled and qualified by demonstrating a perfect gas tightness of the entire gas system under test. The gas gaps passing the mechanical test criteria are put further for electrical tests.

Electrical Test of the Gas Gaps. The electrical test aims to determine the Current-Voltage curve of a RPC gas gap, in order to identify possible malfunctions, defects in the high voltage circuit and dark current before using the gas gap for the detector prototype assembling.

Each gas gap is connected to the gas system and flushed with the standard CMS RPC gas mixture, $C_2H_2F_4$ / $iso-C_4H_{10}$ / SF_6 (95.2/4.5/0.3), with 40% relative humidity in the gas mixture at a flow rate of 5 L/hr for 24 hours in order to clean the gas gap and pipeline after a long-term of a non-operation period and before undergoing the dark current test. The dark current of a gas gap is the current which is drawn when the high voltage is powered in the absence of irradiation. The current arises from incoming cosmic rays, electrons coming from the cathode, even the spacers separating the plates and/or possible manufacture imperfections of the gas gap. This dark current is important concerning power consumption and detection efficiency and should be kept as low as possible. The maximum power consumption allowed at CMS is 3 W/m^2. A too high dark current leads to a voltage drop in the gas gap and thus a reduction in the detection efficiency.

The dark current test includes high voltage scan performed by ramping the high voltage ih the range 0 V - 6000 V with steps of 1000 V and 6000 V - 7900 V with steps of 100 V. The last high voltage value is kept at least 1 hr in order to monitor the stable operation of the gas gap. After each step the high voltage is maintained for 15 min. in order to obtain a steady-state current and an average value of this current corresponds to one data point in Fig. 6.13. Before the actual dark current test, the high voltage is increased step by step to burn away any possible dust inside the gap since the gap is not constructed in a clean room. The dark current first slowly rises up to about 6000 V. Up to this HV point there is no gas multiplication and the gas gap acts as a resistor and the current is determined by the resistance of the spacers. Afterward, there is a very rapid increase due to gas breakdown by ohmic conduction.

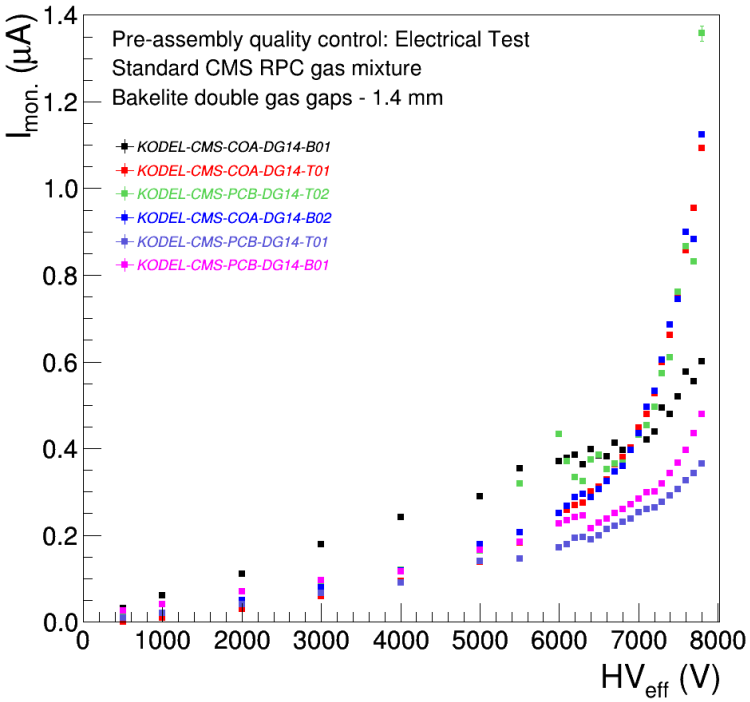

Figure 6.13: Typical current versus voltage behavior for the KODEL RPC gas gaps.

Fig.6.13 shows a typical current versus voltage curve for the KODEL RPC gas gaps. For voltages below approximately 6000 V the current depends linearly on the applied high voltage: the behavior is ohmic. Once gas amplification sets in (above approximately 6000 V), the current increases exponentially. During the electrical test, all applied high voltage values ($HV_{app.}$) have been corrected in order to take into account the pressure and temperature variations and obtain the effective voltage ($HV_{eff.}$). The correction is performed

according to the formula below:

$$HV_{app.} = \beta HV_{eff.} = HV_{eff.}[(1-\alpha) + \alpha \frac{P}{P_0}\frac{T_0}{T}], \tag{6.3}$$

where $\alpha = 0.8$ and T_0= 293 K, $P_0 = 990$ mbar are the reference temperature and pressure. T and P are measured during the test by using the environmental control station installed in the RPC laboratory at the CERN CMS-RPC QA/QC facility. When a set of gas gaps with the required geometry is fully validated, these are used to start the detector prototype construction.

6.2.2.3 Detector Prototype Assembly

Before the start of the actual detector assembly, the low-cost materials have been used to simulate each single stage of the assembly (Fig. 6.14) in order to understand the correct position, alignment and fixing of all the detector components inside the large mechanical box avoiding to use the real parts with possible damage to them.

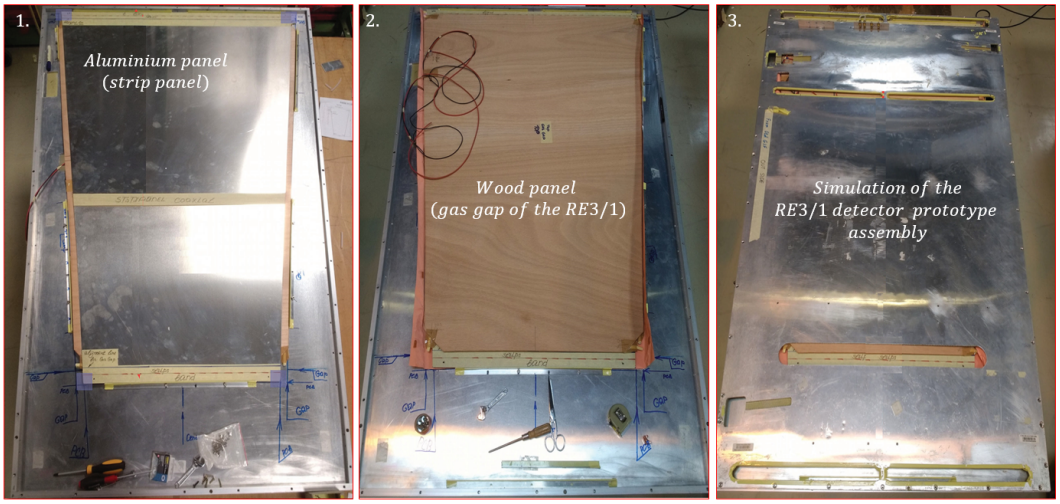

Figure 6.14: Simulation of the CMS-iRPC RE3/1 and RE4/1 detector prototypes assembly by using low-cost materials: 1 - an aluminum panel simulated the readout strip panel; 2 - the wood panel imitating of top gas gap; 3 - view of completed iRPC detector prototype.

The gas gap and the readout strip panel were simulated by using 5 mm thick of the wood panel and 1.5 mm thick of PCB panel with the sizes and shapes similar to the real gas gaps and actual readout strips panel (see Fig. 6.14). These components have been installed and aligned inside the mechanical box. Due to the fact that the PCB will be longer than the gas gap, it has been

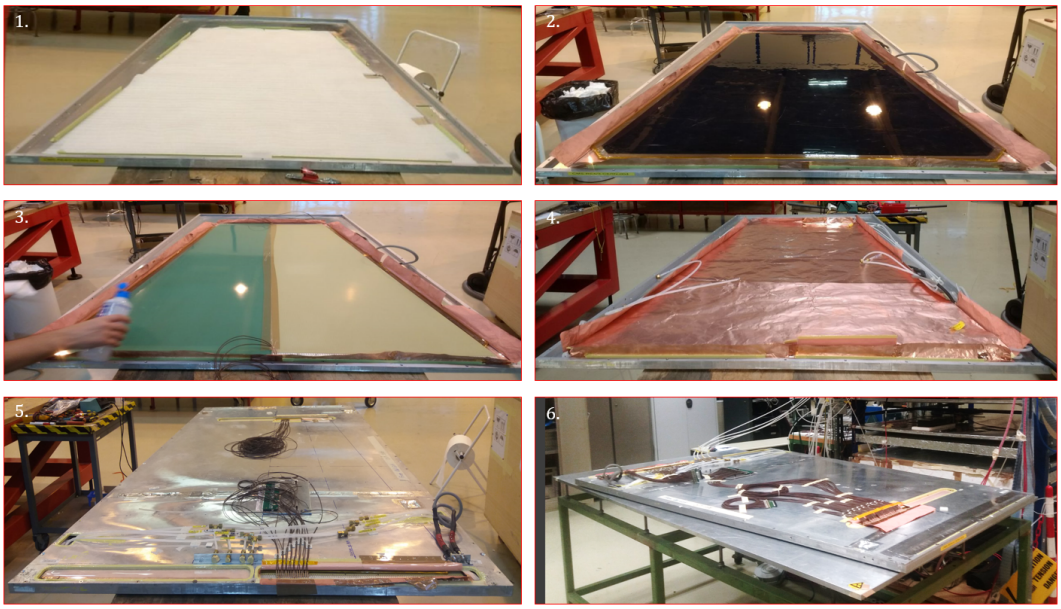

Figure 6.15: iRPC RPC RE3/1 detector prototype assembly procedures: 1 - preparation of detector casing by covering it of Mylar layer and fixing insulated holding bars into place; 2 - installation of bottom gap inside the prepared detector casing; 3 - the installation of readout and fake strip by covering the a bottom gas gap, cleaning procedures of the components of strip panel by using an isopropyl alcohol ($(CH_3)_2CHOH$) 4 - closing of the Faraday Cage; 5 - closing of prototype by using the prepared top honeycomb panel and preparation of pipelines and cables laying; 6 - completed of iRPC RE3/1 detector prototype assembly and flushing of gas gaps.

Figure 6.16: Few steps of the iRPC RPC RE4/1 detector prototype assembly procedures: 1 - installation of readout and fake strip panel; 2 placing of top gas gap and fixing it by using the polycarbonate spacers; 3 - closing the Faraday cage; 4 - the completed of the iRPC RE4/1 detector prototype assembly and flushing gas gaps.

proposed to use plastic spacers to extend the length of the gas gap and fill in the empty space between the PCB, the bottom and top honeycomb panels.

After the installation of all components, a series of threaded holes have been made in order to mount "L"-shaped brackets. "L"-shaped brackets will be fixed around all components in order to provide good alignment and to avoid possible movements of the elements inside the larger mechanical box.

Using the results from the mechanical simulation described in Section 6.2.1., the honeycomb panel and bars have been properly modified: services holes have been produced and bars have been shorted up to 13 mm at the CMS-RPC workshop. Finally, the gas pipes and HV cables routings have been made by using the scheme in the Fig. 6.9.

The actual prototype assembly has been started by following the standard procedure for the CMS RPC detector construction [78] first of all, the aluminum detector casing and bars have been prepared for the gas gap installation by using a Mylar layer to cover all the conductive parts in order to ensure the proper insulation between honeycomb panel and the copper Faraday cage. Then the holding bars, fixing the gaps into place, are insulated by using tape and installed inside the frame. Next, a copper sheet, which acts as a Faraday cage, is laid onto the frame and cleaned carefully with Isopropyl alcohol ($(CH_3)_2CHOH$).

When the frame was ready, the preparation of the bottom gap began. It is carefully cleaned and put inside with the HV cable at the bottom. Once it is sled into place, gas pipes and spacers, filling in the empty space between

the bottom gap and bar, have been installed. After that, the actual readout panel with 48 strips and fake PCB has been laid onto it. Top gap is then cleaned and put onto the readout strips with the HV connection on top. Gas pipes are installed and closing part of the copper sheet is put to cover the top gaps. Once the HV openings are cut, the copper sheet is closed. The Fig. 6.16 (right top) shows the final stack consisting of the two gas gap and plastic spacers, closed into the Faraday cage. Using the slots on the aluminum fixing "L"-shaped brackets, the later has been tightened around the perimeter of the stack, in order to ensure a proper stack fixing inside the large mechanical box and preventing it from moving inside during the installation phase of the Test Beam. All these activities take place on specially designed tables: one granite and a few assemblies tables. Transportation of fragile or heavy materials from one part of the laboratory to the other is done with special rotated tables.

6.2.2.4 Post-assembly Quality Control of the Detector Prototype

Once the chamber is closed, it's time for the leak and the high voltage integrity tests. The gas leak test takes place again in order to check the gap gas inlets were correctly connected to the chamber service panel, while the HV test is repeated to be sure the electrodes preserved the integrity after mechanical manipulations during the assembly. The procedures are the same as the one at the gas leak and the high voltage integrity tests during the pre-assembling quality control stage. In Fig. 6.17 results of the post-assembly high voltage integrity test for the RE3/1(a) and RE4/1(b) detector prototypes are shown. The slight increase in the current value of the bottom gas gaps with respect to the top gas gaps has been observed and it is due to the mechanical stress of the top gas gap.

In order to start the RE3/1 and RE4/1 detectors prototypes performance studies on the cosmic telescope, for each prototypes four FEBs card with a total of 96 readout channels (48 channel per side) have been mounted outside the mechanical box. For RE3/1 chamber, the 96 coaxial cables have been directly soldered to strip panel and electronic cards, while for RE4/1 flat ribbon cable connectors have been used. The detailed description of the new front-end electronics was given in Section 6.1.

6.3 Electronics Calibration

As shown in Fig. 6.18, the 48 strips, forming the strip panel of the RE3/1 detector prototype, have been read out by using four PETIROC ASIC boards. In order to collect signal from each strip, in total 96 LIMO cables with two types of length (4 ns cables towards the detector large base and 8 ns cables towards to small base) have been soldered directly to the strips on one side and to the mezzanine board on the other. FEBs have been connected to the mezzanine board via a flat connector mounted on the mezzanine. Due

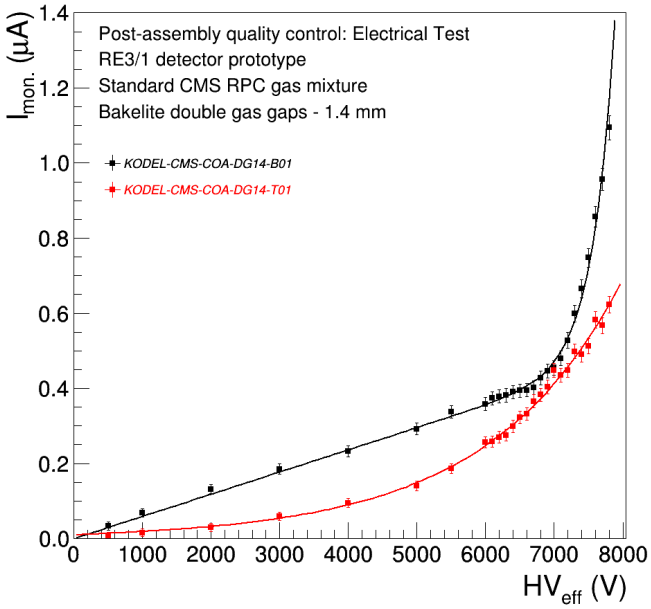

(a)

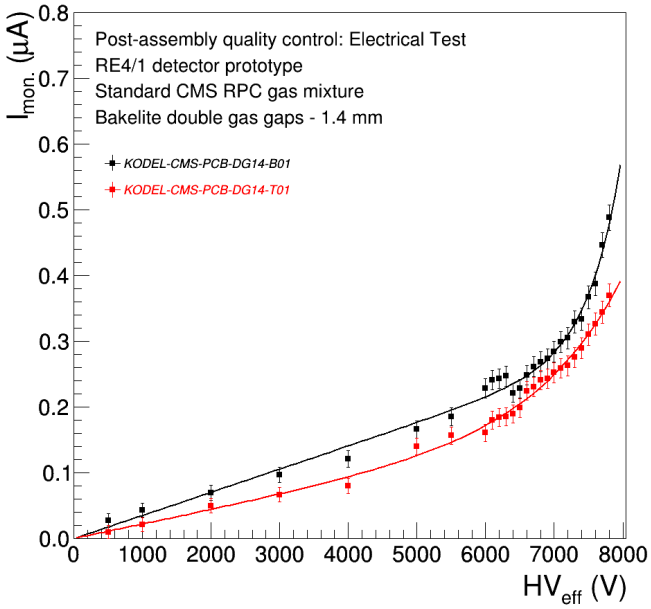

(b)

Figure 6.17: Results of the post-assembly high voltage integrety test for the RE3/1(a) and RE4/1(b) detector prototypes.

to the different strip panel PCB design, only two FEBs have been installed on the RE4/1 detector prototype. FEBs have been connected to the strip panel PCB by using the flat ribbon cable as shown in Fig. **??**. Each FEBs

have been in turn connected with TDC installed outside the chambers. FEBs communication with DAQ station has been carried out via the Ethernet cables. Each FEB has been supplied by 5 V.

When all electronics have been connected to the RE3/1 and RE4/1 prototypes, it is time to the FEBs calibration procedure. It is important to have all channels of the PETIROC ASIC in each front-end bords aligned to the same pedestal value in order to have good behavior and a coherent response of each channel. The pedestal calibration for each FEBs has been performed to define the proper threshold value. This procedure has been performed in two stages. Each time, the threshold of the comparator has been lowered step by step with a short acquisition window and output data are recorded.

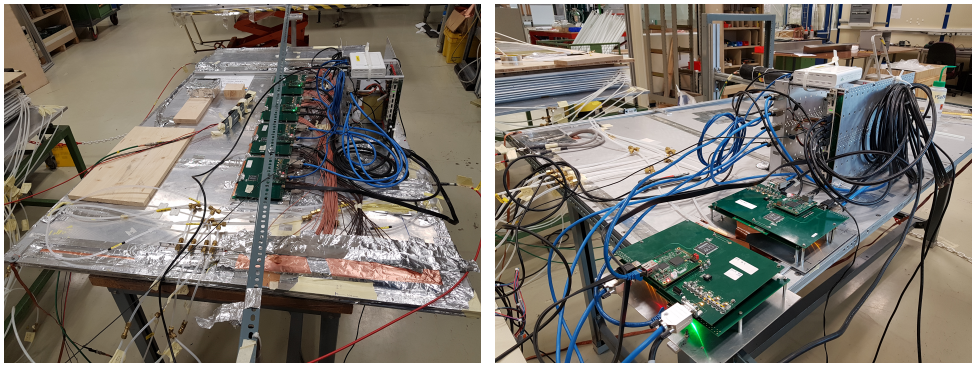

(a) (b)

Figure 6.18: iRPC RE3/1 (a) and RE4/1 (b) chambers with the connected PETIROC ASIC electronics.

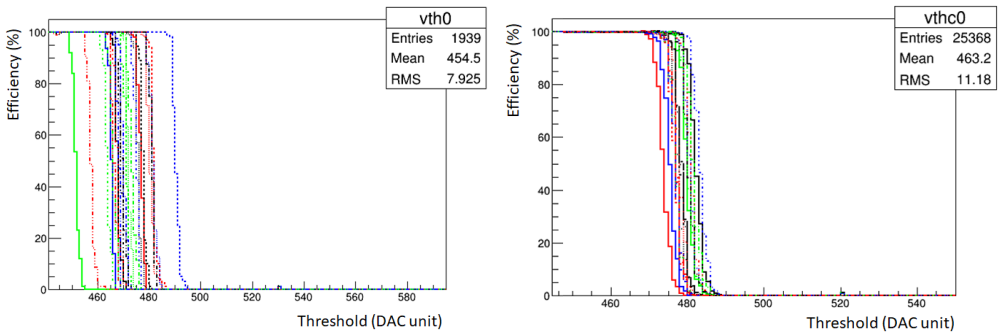

(a) (b)

Figure 6.19: "S"-curve for 24 channels of one FEB before channels alignment for the RE3/1 (a) and RE4/1 (b) prototypes.

At 7.2 kV applied on the RE3/1 and RE4/1 detectors, in the each PETIROC ASIC the channel by channel has been activated. Size of acquisition window for each channel has been chosen around 900 ms. At the different pedestal value during the acquisition time, the number of hits has been

recorded. In the Fig. 6.19 efficiency versus the pedestal DAC value is presented obtained for one FEBs of the RE3/1 and RE4/1 detector prototypes. As can notice, that all channel in the FEBs has different behavior and response and, thus, they will have different threshold values.

In order to find the same minimum pedestal value for all channels, the S-curves has been fitted by a complementary error function, which has the following form:

$$Efficiency\ (\%) = \frac{a_0}{2} \cdot errfc\left(\frac{a_1 - DACunit}{a_2}\right) + a_3 \tag{6.4}$$

where a_0 measures the magnitude of the step, a_1 identifies the location of the step (or pedestal), $(2\sqrt{ln2})a_2$ is the full width at half maximum ($FWHM$) of the Gaussian used to compute the complementary error function ($errfc$) and a_3 represents a constant offset. By plotting the DAC pedestal value distribution, the same minimum of DAC value for each channel can be obtained. After that by using the two Digital-to-Analog Conversions (DAC) settings on the FEBs (see Fig. 6.4a): a global threshold with a 10-bit DAC and a 6-bit DAC on each channel, the minimum DAC value has been adjusted by the FEBs software for each channel. After that, again all channels have been activated in order to check alignment computed in the first step.

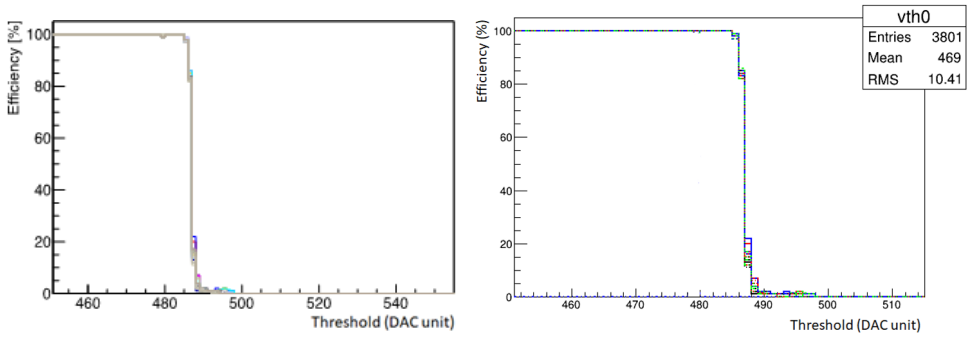

(a) (b)

Figure 6.20: "S"-curve for 24 channels of one FEB after channels alignment for the RE3/1 (a) and RE4/1 (b) detector prototypes.

Fig. 6.20 shows the S-curves after alignment for one FEBs of the RE3/1 and RE4/1 detector prototypes. The minimum pedestal value is 480 DAC unit for FEBs of the RE3/1 detector and 480 DAC unit for FEBs of the RE4/1 chamber. In the region from 497 DACu to 502 DACu for RE3/1 and 486 DACu to 498 DACu for RE4/1 we can see the noise increasing which most probably coming from chambers due to the following effects: crosstalk, retriggering, the grounding issue and so on. In order to avoid these effect, the optimal pedestal value has been chosen after 5σ. Thus, the optimal pedestal value to reduce the

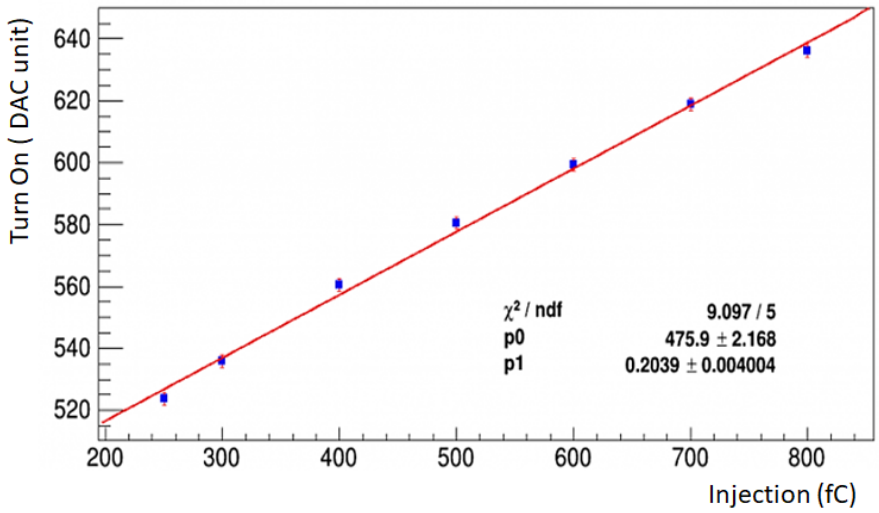

Figure 6.21: DAC unit versus the number of charges, where 1 DACu corresponds to 2.45 fC.

noise are 524 DACu for FEB of the RE3/1 chamber and 513 DACu for FEBs of the RE4/1 chamber. Using the plot of DACu versus the number of charges (see Fig. 6.21), we defined that 44 DACu corresponds to the 107.8 fC for the RE3/1 FEBs and 33 DACu corresponds to the 80.85 fC for the RE4/1 FEBs, respectively.

6.4 Preliminary Performance Evaluation with Cosmic Rays

The main goal of the iRPC detector prototype preliminary performance evaluation is to check that the assembled prototypes can operate effective and stable. The evaluation procedure aims to study the detector response by measuring the main detector performance parameters such as efficiency, working point and noise. These studies are performed at the RPC cosmic stand (telescope) in the CERN CMS-RPC QA/QC facility.

6.4.1 CMS-RPC cosmic ray stand overview

The CMS-RPC cosmic ray stand at CERN consists of several subsystems: gas system, power system (high voltage distribution), Data Acquisition System, Detector Control System and Trigger System each one with a specific task. With it is possible to test the ten large-size RPC detector at the same time using five RPC units to produce the trigger and a tracker system. Custom made DAQ and Detector Control System (WebDCS) allow to set and monitor

all operational parameters of the test stand. In this Section, the overview of the CMS-RPC cosmic ray stand at CERN will be described in detail.

6.4.1.1 Gas System

The main important parts of the CMS-RPC gas system at CERN CMS-RPC QA/QC facility are a set of gas cylinders together with manual and pneumatic valves, gas distribution system with a bypass line, gas mixer, humidifier, safety and isolation bubblers, moisture meters, controls for monitoring and remote operation. A schematic diagram of the CMS-RPC system in CERN RPC laboratory is shown in Fig. 6.22. The flow of the gas mixture $C_2H_2F_4$ / $iso-C_4H_{10}$ / SF_6 with 95.2/4.5/0.3 ratio of gas fraction at the relative humidity of 40% is provided by the system.

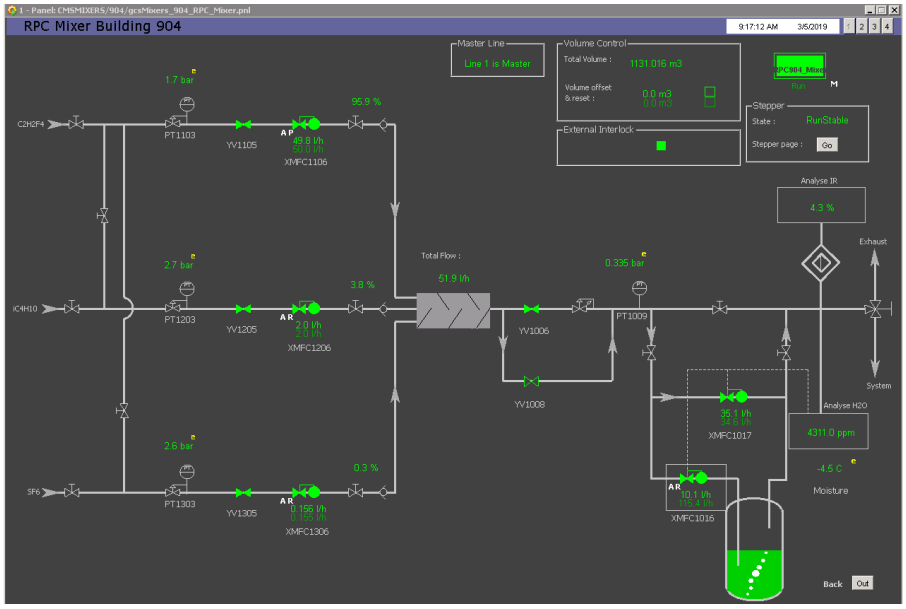

Figure 6.22: A schematic diagram of the CMS-RPC gas system at CMS-RPC QA/QC facility.

The gas components to be mixed are contained in bottles located outside of the building 904 and three different gas lines connect the bottles to the three mass flow controllers (MFCs) F-210CM, provided by Bronkhorst company, adjust the proportion of each component $C_2H_2F_4$ / $iso-C_4H_{10}$ / SF_6 (95.2/4.5/0.3) in order to inject a constant and fresh gas mixture into the main gas line at CMS-RPC QA/QC facility. All mass flow controllers are controlled by a dedicated Data Contol System based on the SIMATIC WinCC Open Architecture (Siemens) software module running on a dedicated computer which allows to set and easily control the gas mixture and the gas flow rate. The three lines are sent to a gas mixer and if the gas composition deviates from the selected amount by more than 5% or other reasons the gas supply is stopped

and an automatic hardware system switches off high voltage on the iRPC detector.

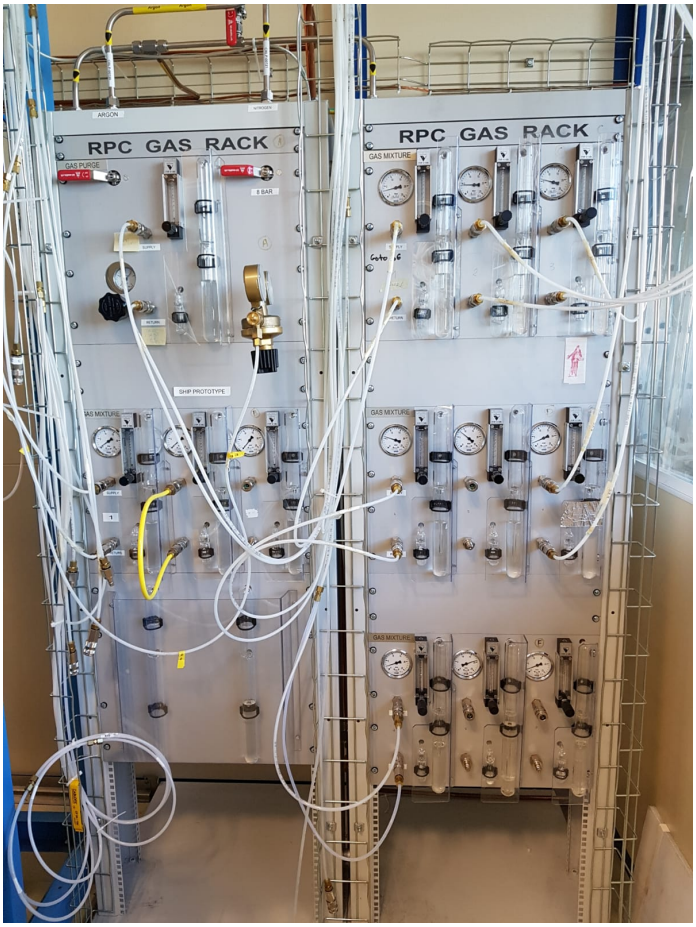

Figure 6.23: Picture of the gas distribution panel at CMS-RPC QA/QC facility.

As noted above, all the hardware necessary to the gas system is located outside the building 904 isolated from the environments, while the gas distribution panel is located inside the CMS-RPC QA/QC facility. A picture of the gas distribution pannel is shown in Fig. 6.23. The gas distribution panel allows to connect of twelve RPC gas gaps in parallel and maintains uniform flow in all of them. Each line in the gas distribution panel is equipped with the safety bubblers and the rota-meters with a differential pressure meters. The rota-meters are used to control the gas flow rate through the line precisely, while the safety bubblers mounted on individual output lines take care of the back pressure and protect the RPCs from possible damage due to overpressure. Each of these bubblers is made of borosilicate glass and is connected to a stainless steel tube by a flexible Tygon tube. Every bubble has a 70 mm column (typically about 5.5 ml) of silicone diffusion pump oil (DC704), which

has a density of 1.08 g/cm^3 and very low vapour pressure at room temperature. This bubbler prevents over pressurization of RPC that might occur due to blockages in the flow path, by relieving the excess gas to bubble through the oil. Thus, under proper flow conditions, gas should not bubble through safety bubblers.

6.4.1.2 Power System

High Voltage System. A multichannel system for the High Voltage (HV) supply has been setup in order to provide power to the RE3/1 and RE4/1 detector prototypes. HV system has been built based on CAEN SY1527 power supply mainframe equipped with one CAEN A1526 boards with six independent high voltage channels. Each gas gap of the iRPC chambers under test is connected to a single high voltage supply. The high granularity allows to control and read out for each gas gap under test the current that flows inside the gas gap. The high voltage system is remotely controlled, by using the CAEN HV Wrapper Library, that allows the Detector Control System (DCS) to generate complete configuration and control of the HV system. A hardware kill signal is sent to the mainframe by the gas system in case of abnormal flow or abnormal mixture composition.

Figure 6.24: Picture of the high voltage system components based on CAEN SY1527 power supply mainframe and CAEN A1526 module.

Low Voltage System. The special metallic mechanical structure has been developed in order to place together service support (e.g. TDC, the low voltage power supplies and Ethernet Port 8-channels Switch TP LINK LAN) for the PETIROC ASICS front-end electronics of the iRPC RE3/1 and RE4/1 detector prototypes. Picture of the Low Voltage Power Supply system for the PETIROC ASICS electronics is given in Fig. 6.25. The Low Voltage Power Supply system is located at the middle of the structures in the outer side of the iRPC chamber and supplies a +4V power to the on-detector electronics, serving the analog and digital components. Each on-detector board (or FEBs)

then uses Low Drop Out (LDO) voltage regulator to supply the locally needed voltages.

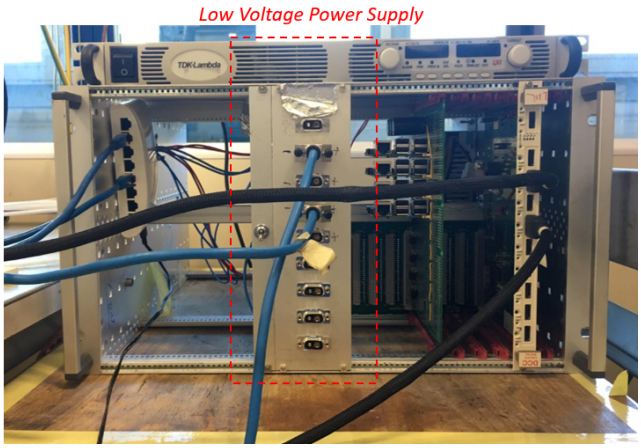

Figure 6.25: Picture of the Low Voltage Power Supply system for the PETIROC ASICS electronics.

6.4.1.3 Detector Control System

The visualization of the webDCS software principle work at the CMS-RPC QA/QC facility is presented in Fig. 6.26.

The aim of the Detector Control System (called webDCS) is to allow the user to set and monitor parameters that determine the response of the detector (high voltage, currents, gas flow, etc.). Moreover, the webDCS has to monitor all the environmental parameters that can modify the detector response (Atmospheric pressure, Temperature, and Humidity). An important task of the webDCS-software is the management of the automatic procedures for data acquisition: a generic sequence of runs can be set, and the webDCS can setup the DAQ configuration to provide the correct execution of the loaded sequence. This high level of automation of the run control software makes possible to collect the whole data sets and sequences required for detector performance studies without human intervention.

High Voltage System. The webDCS runs on a computer connected to the CAEN HV 1527 mainframe through TPC/IP. The webDCS uses the CAEN library written in C++ in order to remotely communicate with HV power supply board and to monitoring and recording the high voltage and the current through the gas gaps during the entire test. The webDCS-software, based on CAEN HV Wrapper Library, has been developed to:

- increase (ramp-up) and/or decrease (ramp-down) gradually the high voltage applied to the gas gaps with programmable with consecutive high voltage steps. The high voltage output ramp-up and ramp-down

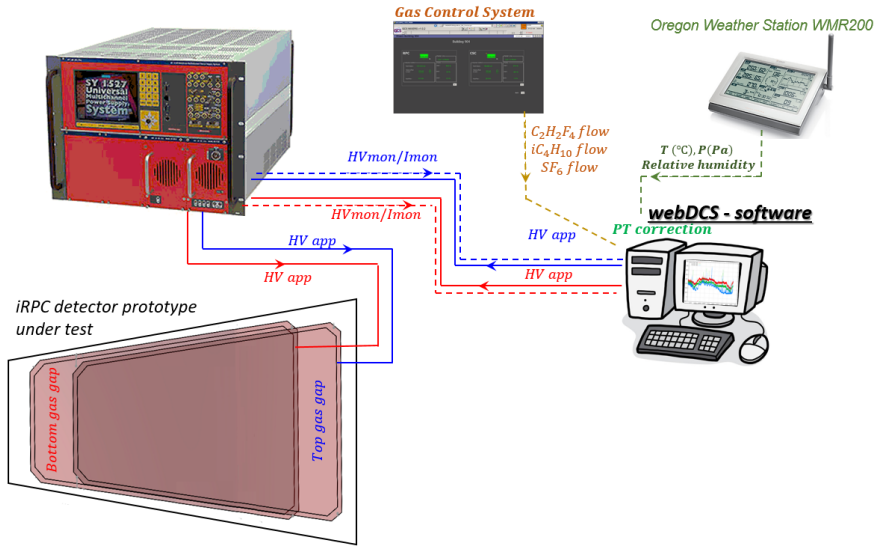

Figure 6.26: Visualization of the webDCS software principle work at the CMS-RPC QA/QC facility. The red and blue dashed/solid lines are for the CAEN data flow through which the WebDCS communicates the voltages to be applied on the gas gaps. The green dashed line marked the data flow transferred from meteo station to the webDCS and orange dashed line is gas status information sent from GCS to webDCS.

rates can be selected independently in the range 1 - 500 V/s in 1 V/s steps.

- set the operating current limit I_{set} value and the maximum time T_{wnd} which an "overcurrent" is allowed to last. The high voltage channel in "overcurrent" works as a current generator; the output high voltage varies in order to keep the output lower than the programmed value I_{set}. The "overcurrent" lasting more than set value T_{wnd} causes the high voltage channel to "TRIP" and the output high voltage is drop to the zero at the programmed ramp-down rate.
- monitor and record the operating current and high voltage at a programmable rate expressed in second.

Environmental Monitoring Parameters. The performance of RPCs strongly depends on the temperature and pressure of the environment. Therefore, it is important to measure the environmental parameters (temperature, atmospheric pressure and relative humidity) at different locations. The applied voltage is corrected for the environmental temperature and pressure in order to include its effects.

One of the main reasons of possible performance variations is due to the fact that, since RPCs are gaseous detectors, the avalanche processes taking place therein depend on the environmental conditions, in particular on temperature and pressure, which directly affect the density of the gas and its first effective

Townsend coefficient. While the temperature in the CMS-RPC QA/QC facility is fairly constant, pressure in the gas system depends on the atmospheric pressure, which can undergo significant changes with time, following different weather patterns. Therefore, the idea is essentially to adjust the applied operating voltage V_{app}, in such a way that the effective operating voltage HV_{eff} of the chamber stays constant even when environmental conditions changed. The relation between HV_{eff} and HV_{app} is given by a well-known formula described in Section 6.4.2.

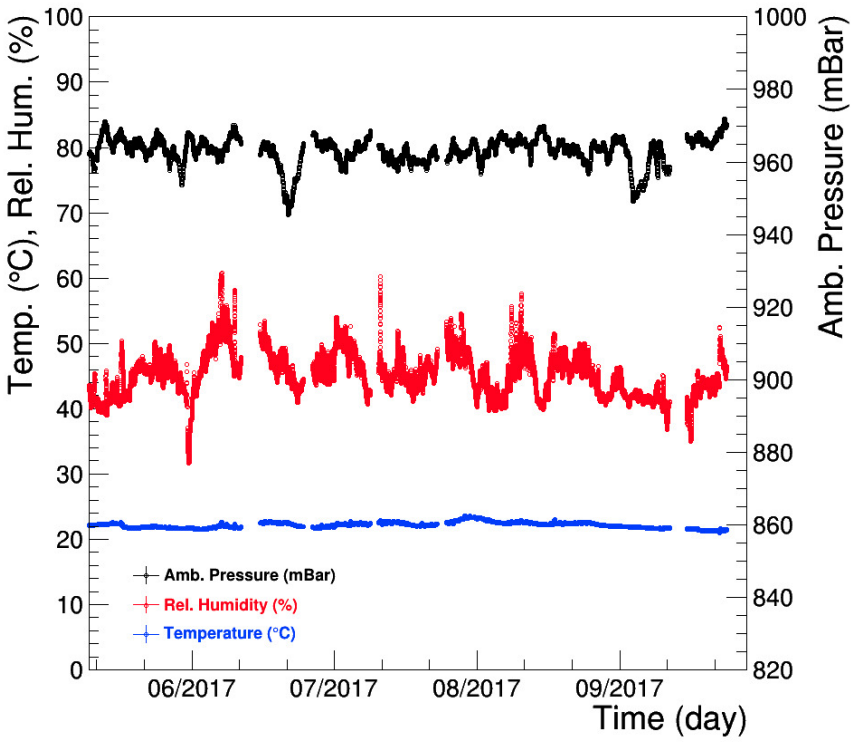

Figure 6.27: Environmental temperature ($°C$), pressure (mbar) and humidity (%). Time is on x-axis. Pressure and temperature values used for voltage correction.

Fig. 6.27 gives a plots for environmental temperature, pressure and humidity. The environmental sensors are readable through Oregon Weather Station WMR200, directly connected to the webDCS computer. The values are stored and transferred to the WebDCS-software, which reads online the environmental parameters in order to apply the pressure and temperature correction on the high voltage value.

Gas Monitoring Parameters. As previously described in Section 6.4.1.1, the gas system for the CMS-RPC QA/QC facility at CERN essentially consists of mass flow controllers (MFCs) and gas mixer unit, which supplies the entire facility. Three mass flow controllers F-210CM, provided by Bronkhorst

company, adjust the proportion of each component $C_2H_2F_4$ / $iso-C_4H_{10}$ / SF_6 (95.2/4.5/0.3) in order to inject a constant and fresh gas mixture into the main gas line at CMS-RPC QA/QC facility. The WebDCS-software reads online the gas parameters, which are continuously published by the CERN Gas Group in order to avoid damages to iRPC detectors during unexpected situations due to any possible variation in gas mixture composition and also provided with a basic interface for easy monitoring. In Fig. 6.28 shows the gas flow for each component of the CMS standard gas mixture and the total gas flow versus time.

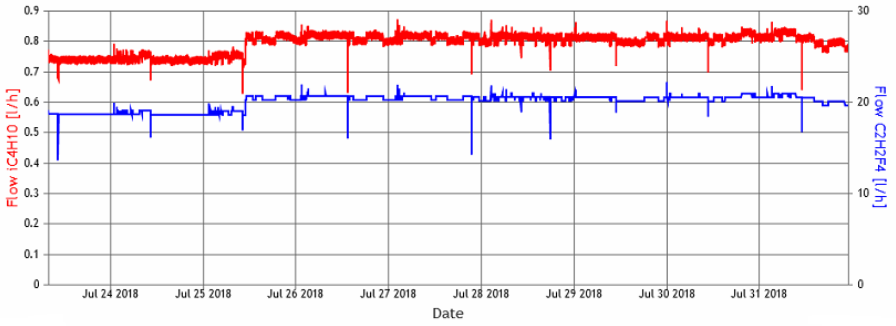

(a)

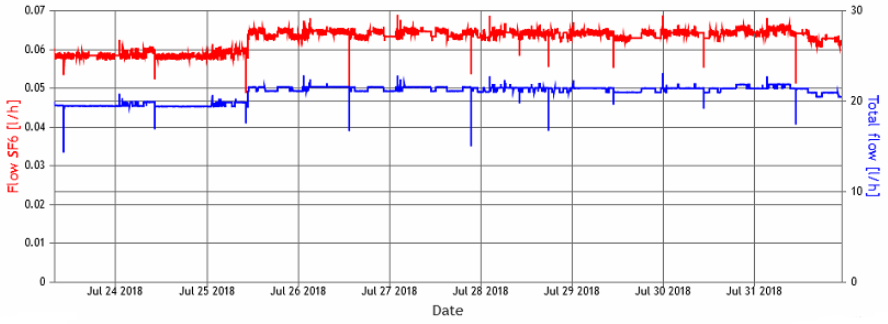

(b)

Figure 6.28: The gas flow for each component of the CMS standard gas mixture and the total gas flow versus time.

6.4.1.4 Cosmic ray muon telescope

The iRPC RE3/1 and RE4/1 detector prototypes have been tested for their preliminary performance evaluation by using a cosmic ray muon telescope which consist of several combinations of plastic scintillators and photomultiplier tubes. A schematic view of cosmic telescope arrangement as well the logic and timing sequence of generation of the cosmic ray muon trigger are shown in Fig. 6.29.

The telescope consists of two (S1 and S2) cosmic ray muon trigger. The scintillators have a form of the paddle with the active areas of 16 cm×20 cm and 15 cm×20 cm, respectively. A paddle is made up of a scintillator tile of 1

cm in thickness, which is optically coupled to a Photo Multiplier Tube (PMT) for converting the scintillation light into an electrical signal. When the PMT is operated with a calibrated high voltage, the paddle gives a signal indicating the passage of a cosmic ray muon or any other charged particle through its scintillator tile volume.

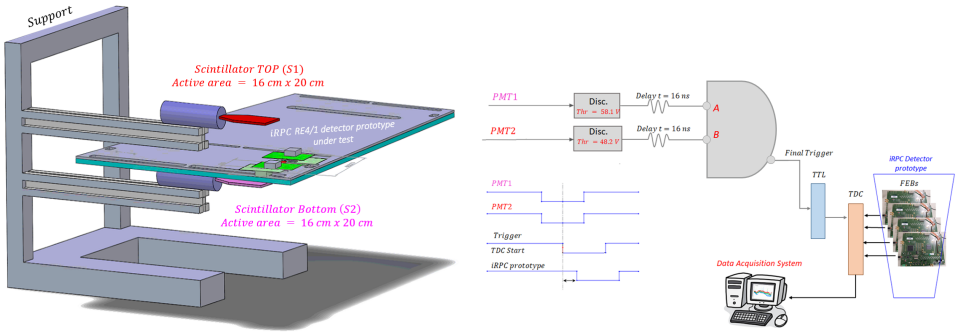

(a) (b)

Figure 6.29: Scheme of scintillator paddles based cosmic muon telescope (a) with its trigger logic and the signal timing chart (b).

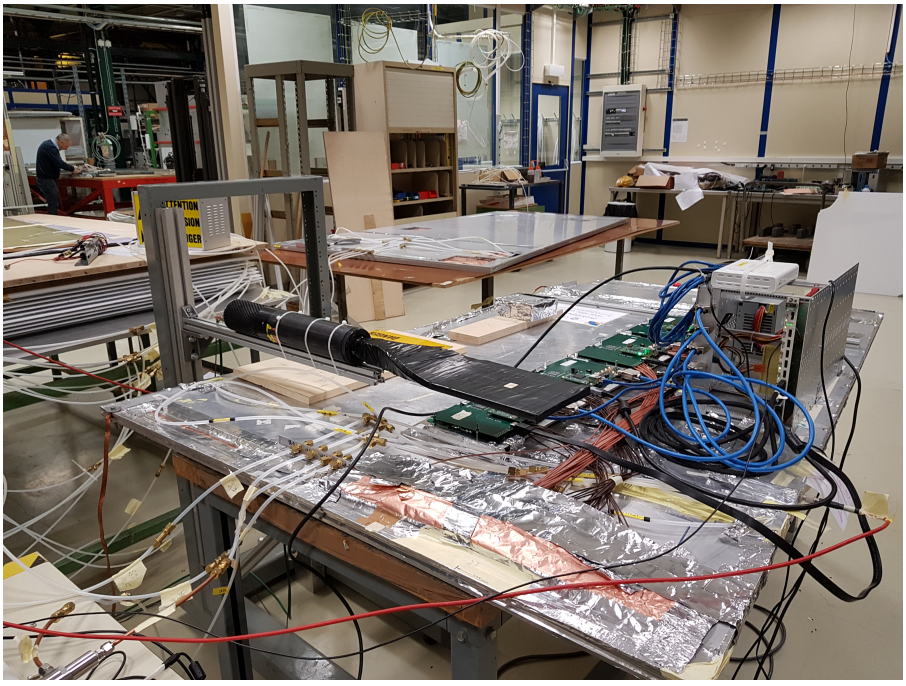

Figure 6.30: Picture of the cosmic ray muon telescope experimental setup and a close-up view of iRPC RE3/1 detector prototype under test.

The telescope geometry by using scintillator paddles has been set up such way the active window has been defined of about 15 cm×20 cm for the cosmic ray muons passed through the telescope as well as through of 20 of the pickup

strips of the iRPC detector prototype under test. Data has been recorded from iRPC pickup strips whenever a cosmic ray muon particle has passed through the telescoping window. This is indicated by a trigger signal, which is generated according to the following logic equation: $Trigger = S1 \cap S2$. Experimental trigger rate was 4.67 Hz.

During the test, iRPC detector prototypes have been located in a horizontal position on the special movable table allows to easily move the prototypes. A suitable telescope support structure has been designed and built employing light-weight aluminum profiles (see the Fig. 6.29a). This has allowed us to quickly and accurately rearrange the telescope to meet day-to-day requirements based on the type of study that we want to perform. Provision has also been made to align the paddles and the iRPC prototype under test by using a ruler for a better geometrical alignment. This test set up is shown in Fig. 6.30

The stability of the cosmic ray muon telescope is vital for the reliability and accuracy of the measurements that we make on the iRPC detector prototype performance. One of the easiest ways to ascertain this is by monitoring the individual counting rates of the paddles as well as various coincidence logic signal rates of the telescope. This is achieved by a dedicated data acquisition system operated on a continuous basis. The scintillator paddle based cosmic ray muon telescope was found to exhibit excellent stability.

6.4.1.5 Data Acquisition and Analysis Procedure

The final trigger signal from the coincidence of two scintillation signals has been sent to the TTL by using the CAEN NIM-TTL-NIM Adapter module. Then the TTL signal has been transferred to the MDCC (Modified Differential Current Conveyor) in order to fan-in the TTL signal on the four independent signals while maintaining their original amplitude. Each signal has been transferred to the Altera Cyclone II FPGA hosting the TDC conversion module. In turn, all TDCs have been connected to the dedicated PC via Ethernet cables in order to read/write the experimental data in the buffer memory of the Data Acquisition System installed and launched in this computer during the measurements.

By using the reference signals of the scintillators based on the coincidence unit, the arrival time of the detector associated signals of each of the two strip ends have been recorded (see Fig. 6.31). The time distribution for each of the two ends can be described by a Gaussian function plus a constant function.

In order to calculate the muon detection efficiency of the iRPC detector prototypes the raw data at the different high voltage value is analyzed using C++ based code. The data flows obtained from each FEBs consist of the following information: events, time and number of channel. By using the analysis steps, the efficiency of the detector can be easily computed:

1. Fix the high voltage value.

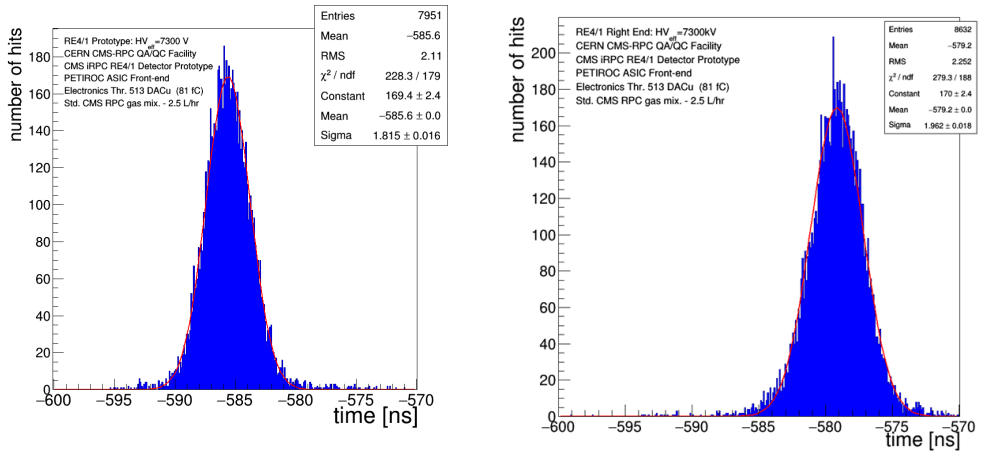

(a) (b)

Figure 6.31: Example of the strips signal time distribution associated to the cosmic muon particles beam: the time signal from left end (a) and time signal from the right end (b) of the strip readout panel.

2. Find the muon time window, where can clearly distinguish the cosmic muon particle beam.

3. Fit the muon particles beam by using the Gaussian function:

$$G(T) = \frac{1}{\sigma\sqrt{2\pi}} exp^{\frac{(T-\mu)^2}{2\sigma^2}} \tag{6.5}$$

4. Compute the mean value (μ) and the standard deviation (σ).

5. Determine the time window for the cosmic muon beam by using results obtained in the previous step.

6. All events inside the $[\mu - 3\sigma;\ \mu + 3\sigma]$ time window determine as the muon events, where at least a strip is fired.

7. All event inside the $(-\infty;\ \mu - 3\sigma]$ and $[\mu + 3\sigma;\ +\infty)$ time windows (outside the muon time window) determine as the noise hits or gamma background hits where at least a strip is fired in a time interval of the same length but uncorrelated with the trigger.

8. Calculate the true muon efficiency by using the next formula:

$$\varepsilon = \frac{\frac{N}{N_{trig}}\frac{N_{bkg}}{N_{trig}}}{1 - \frac{N_{bkg}}{N_{trig}}} \tag{6.6}$$

where ε is measured muon detection efficiency of the detector, N is the number of the measured events, N_{trig} is number of muon triggers and N_{bkg} is the number of the noise hits or gamma background hits expected in the time interval, respectively.

6.4.2 First results and discussions

The first test runs have been performed at the working voltage (7300 V) in order to check the detector prototypes performances. The runs were analyzed and the FEB connectivity to the mezzanine board which in turn connected to the readout strip panel was checked. If some dead electronics channel were found, the mezzanine board was replaced by a new one. At the end of the electronics connectivity and characterization test, a new test run was made. In Fig. 6.32 a example of the "good" strip profile at the high voltage value of 7300 V is presented for the RE4/1.

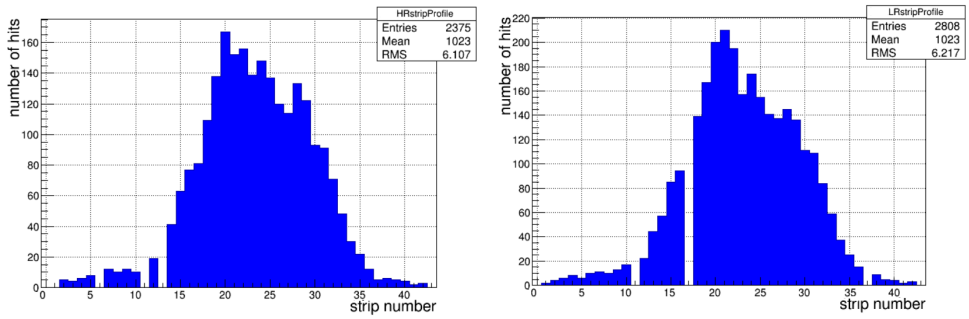

(a) (b)

Figure 6.32: Example of the strip profiles for the two strip ends of the iRPC RE4/1 detector.

Due to the new design of the readout strip board, the cosmic ray runs have been taken at different high voltage values in three different configurations of the readout signal for the double-gas gaps iRPC RE3/1 and RE4/1 prototypes: readout signal from the left end (readout logical "OR" called "High Radius"-HR), readout signal from right end (readout logical "OR" named "Low Radius"-LR) and readout signal from both ends (readout logical "AND"). For each configuration and for each high voltage step the detection efficiency, noise hit rate and dark current for top and bottom gas gaps have been measured. Results of the first measurements obtained during the cosmic ray test are shown in Fig. 6.33 - Fig. 6.35.

The first results of the detection efficiency have been evaluated by using the coincidence method, i.e. the detector prototypes have been considered efficient when, in correspondence of the trigger signal, a strip inside the iRPC provided a signal above the electronics threshold equal to the 524 DACu and 513 DACu, corresponding to about a charge of 107.8 fC for the signal induced inside the RE3/1 detector and about a charge of 81 fC for the signal induced inside the

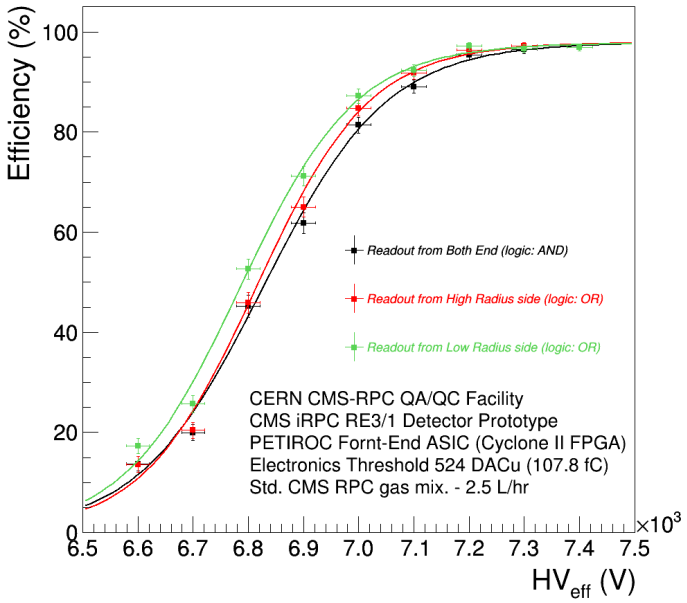

(a)

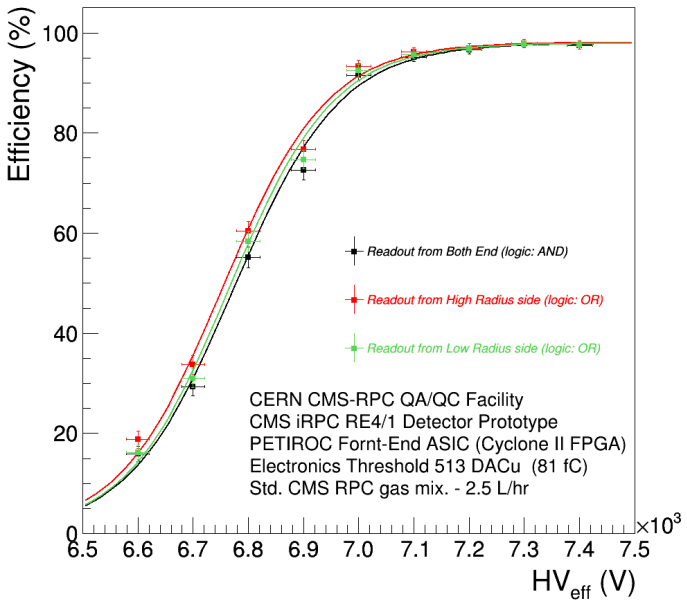

(b)

Figure 6.33: Detection efficiency as a function of the high voltage applied to the double-gap iRPC RE3/1 and RE4/1 detectors at the three different configurations of the readout signal from the strip (the type of the readout logic is indicated). The applied high voltage values have been normalized by using the PT correction formula.

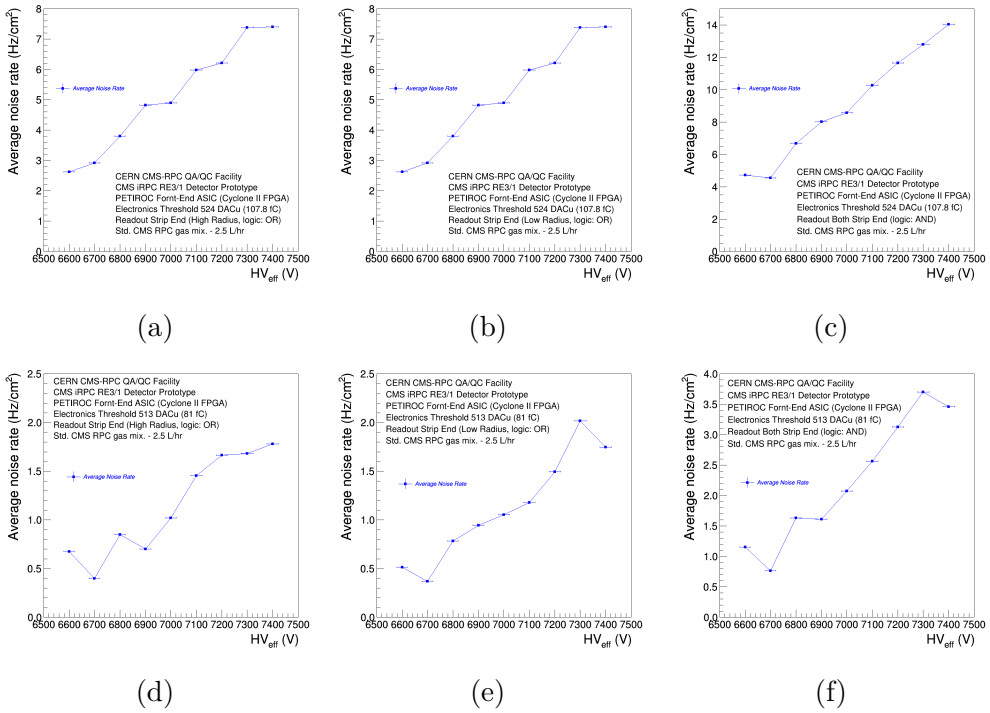

Figure 6.34: Noise hit rate as a function of the high voltage applied to the double-gap iRPC RE3/1(a-c) and RE4/1 (d-f) prototypes at the three different configurations of the readout signal from the strip (the type of the readout logic is indicated). The applied high voltage values have been normalized by using the PT correction formula.

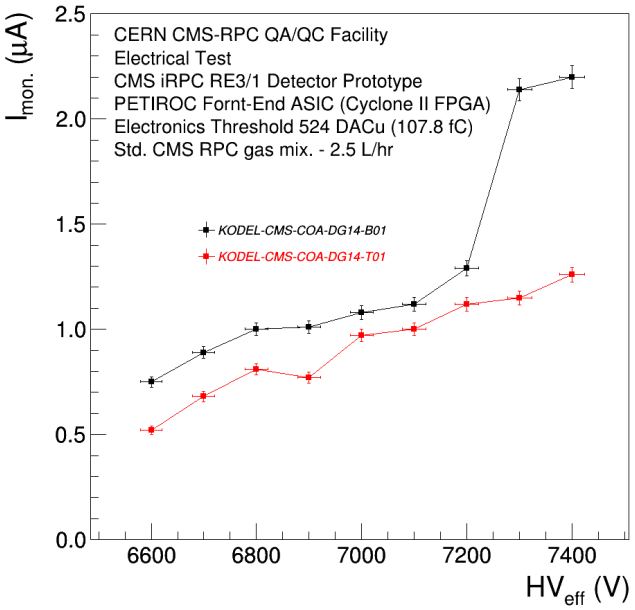

(a)

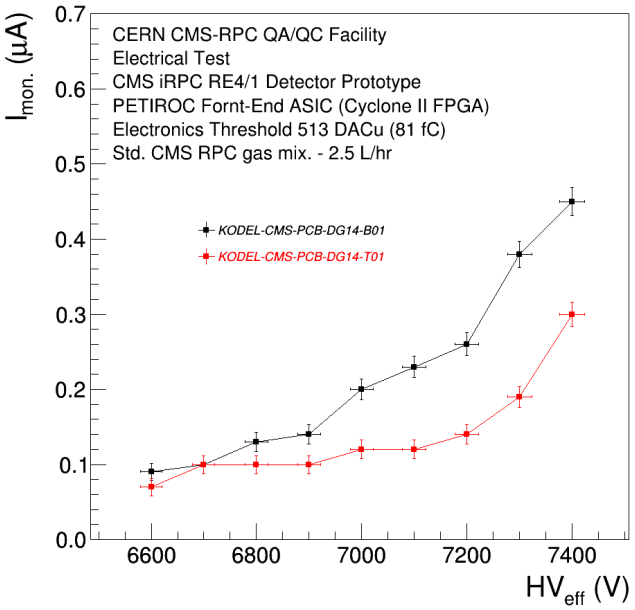

(b)

Figure 6.35: Example of a conditioning plots: the current behaviour for the top and bottom gaps for the RE3/1 (a) and RE4/1 (b) chambers.

RE4/1 prototype, respectively. The efficiency plots versus high voltage have been fitted by means of a sigmoid function in order to extropolate the working point and efficiency at the working point:

$$\varepsilon = \frac{\varepsilon_{max}}{1 + exp[-\lambda(HV_{eff.} - HV_{50\%})]} \tag{6.7}$$

where ε_{max} is the maximum efficiency reached by chambers at $HV \longrightarrow \infty$ and λ is proportional to the slope of sigmoid at inflection. The $HV_{50\%}$ used in the fitting sigmoid function is defined as the high voltage at which every roll reaches 50% of the efficiency plateau. $HV_{eff.}$ is the high voltage corrected for temperature and pressure value according to the following:

$$HV_{app.} = \beta HV_{eff.} = HV_{eff.}[(1-\alpha) + \alpha\frac{P}{P_0}\frac{T_0}{T}], \tag{6.8}$$

where $\lambda = 0.8$ and $T_0 = 293\ K$, $P_0 = 990\ mbar$ are the reference pressure and temperature values, T and P are the corresponding environmental values during the test. The working point is defined as WP = "Knee" + 150V. The "Knee" is the high voltage point on the sigmoid where the efficiency is 95% of the efficiency plateau.

Table 6.4: The summary results of the measurements obtained during the first iRPC RE3/1 and RE4/1 detector prototypes tests in the cosmic stand at the CERN CMS-RPC QA/QC Facility.

	RE4/1 prototype				**RE3/1 prototype**			
	$\varepsilon_{\mathbf{max}}$ [%]	**WP [V]**	ε(**WP**) [%]	$\mathbf{R_{Noise}}$ **Hz/cm²**	$\varepsilon_{\mathbf{max}}$ [%]	**WP [V]**	ε(**WP**) [%]	$\mathbf{R_{Noise}}$ **Hz/cm²**
AND	97.9	7206.1	98.6	2.23	97.9	7308.1	96.6	9.03
HR	98.1	7181.7	97.2	1.14	97.9	7267.6	96.7	5.12
LR	97.9	7191.6	96.9	1.11	97.7	7244.7	96.5	5.11

The summary of the first results for RE3/1 and RE4/1 chambers are presented in Table 6.4: at the electronics threshold value of 524 DACu (107.8 fC) applied to the RE3/1 detector, the maximum detection efficiency is 97.8%, the working point value is around 7273.5 V and $\varepsilon(WP)$ is 96.7%, while for RE4/1 chamber at the electronics threshold value of 513 DACu (81 fC), the maximum detection efficiency is around 98%, the working point value is around 7193 V and $\varepsilon(WP)$ is 97.6%. Due to the peculiarities in the readout system used for the two detector prototypes (in the first prototype the pick-up signal pass throught 50 Ω coaxial cable, while in other chamber the signal pass throught flat ribbon cable), in the RE3/1 chamber the average noise rate is 5

times high observed into the RE4/1 prototype. Thus, the coaxial signal cable in the RE3/1 chamber require to be better shield in order to reduse the pick-up noise.

6.5 Performance Studies with Muon Particles Beam at CERN

The real-size iRPC RE3/1 and RE4/1 detectors for the innermost region of the CMS Muon Spectrometer have been tested during August 2018 Test Beam. The prototypes were exposed to high irradiation flux using the CERN Gamma Irradiation Facility (GIF++) and the 100 GeV/c muon beam from H4 beam-line. The main purpose of the iRPC RE3/1 and RE4/1 detector prototypes testing with a high-energy muon beam and a high-intensity ^{137}Cs source (662 keV gamma photons) is to a detailed study of all detector parameters such as: detection efficiency, cluster size, rate capability and time resolution, at the similar conditions which will expected in the CMS detector after the High -Luminosity LHC (HL-LHC) upgrade. These performances studies are crucial for optimized design and efficient operation of the detector.

6.5.1 Overview of the Gamma Irradiation Facility at CERN

The Gamma Irradiation Facility (GIF++) [79] at CERN is an unique test area in which an high-energy muon beam (100 GeV/c), from the secondary SPS beam line H4 in EHN1, is combined with a gamma photons from a radioactive ^{137}Cs source. Located in the CERN SPS North Area [80], the facility has been designed in order to provide a high intensity gamma field for high rate and longevety studies. The ^{137}Cs isotope, with an activity $\sim$ 14.1 TBq (December 2015), has been chosen instead of ^{60}Co isotope due to its long half-life of 30.08 years, leading to a smaller decrease of the photon rate over the expected life-time of facility.

Further, the spectrum of the ^{137}Cs source, composed of the primary 662 keV photons and lower energetic scattered photons. The main source of the inter-action background in the CMS muon system are neutron-induced photons, with an energy in the range 0.1-10 MeV. The GIF++ photons have an energy fairly representative of the energy of LHC/HL-LHC photons seen by the muon detectors [57]. The intense gamma field background, which is a factor 30 more intense than that at original GIF facility, allows to simulate the conditions that detectors will suffer in their future operating environment at the HL-LHC.
The GIF++ irradiation area has a total surface of 100 m^2 divided in two different radiation zones: the Upstream zone (30 m^2) and the Downstream zone (70 m^2). It has been realized in order to host and test simultaneously full-size detectors and to allow their positioning at different distances from

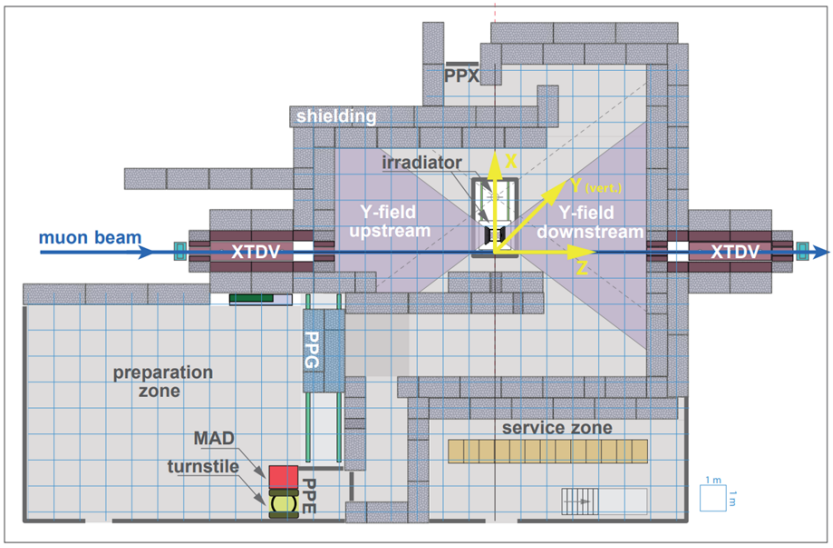

Figure 6.36: Floor plan of the GIF++ facility [79].

the source point. The irradiation area is shielded by 1.6 m thick concrete walls; it is equipped with a raised floor allowing effective distribution of gas lines and high voltage and/or signal cables. The free height between the floor of the facility and the raised floor is $\sim$ 0.42 m. The schematic overview of the GIF++ facility is shown in Fig. 6.36. Close to the the irradiation area, is present a two-floor service zone for hosting the gas (*gas zone*) and the electronic services (*rack zone*). In addition, a preparation zone (80 m^2) is available for preliminary tests on the detectors and their electronics before installing them inside the irradiation area.

The radioactive source in the irradiation position is at 2.06 ± 0.01 m from the floor of the facility, and it is located at the same height of the muon beam, or at 1.64 ± 0.01 m from the raised floor where the detectors under irradiation test are placed. The wide opening angle of both areas is 37° on the horizontal and vertical planes in order to cover a large part of the irradiation area, both in the Downstream and Upstream zones. Both irradiation windows are equipped with lens shaped angular correction aluminium filter to provide an uniform photons flux in order to fully irradiate the flat large area detectors, allowing to study the effects of different background radiations on the detector rate capability. In Fig. 6.37a, one of the two irradiation windows equipped with the aluminum angular correction lens is shown. For each irradiation zone, the photons flux can be independently fine tuned using two complete and independent attenuation systems (Fig. 6.37b), each consisting of an array of 3×3 convex lead attenuation filters. In total, 24 different nominal attenuation factors between 1 and 46415 can be selected according to the 27 possible combinations of the filters (Fig. 6.37c).

The irradiation field inside the GIF++ irradiation area has been simulated: Fig. 6.38 shows the simulation of the 662 keV photons flux inside the irradi-

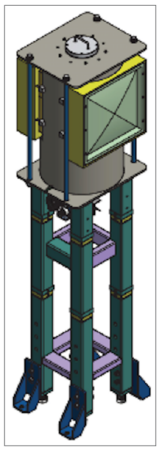

(a) Irradiator with angular correction filters

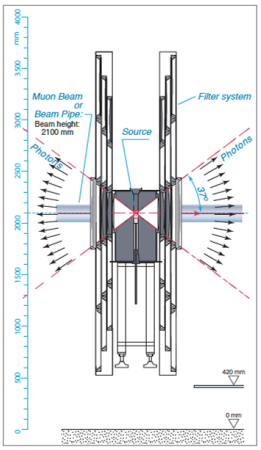

(b) Irradiator with filter system

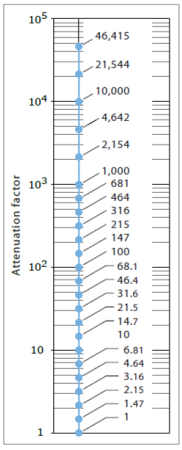

(c) Nominal attenuation factors

Figure 6.37: (a) Schematic structure of the irradiator at GIF++ facility with the angular correction aluminium filters and independent filter systems at both sides. (b) On both sides a set of independently movable and remotely controlled attenuation lead filters and collimator frames permits to fine tune the intensity of emitted photons. (c) Each set of 3×3 movable attenuation filters, with 27 combinations of filters, leads to 24 different attenuation factors between 1 and 46415 [79].

ation area in the xz plane without any attenuation applied; this is thus the highest photons flux obtainable at GIF++ facility. The simulation has been validated with experimental measurement, both in Upstream and in Downstream zones. The position of the experimental measurement D1-to-D5 (in Downstream zone) and U1-to-U6 (in Upstream zone) are also marked in Fig. 6.38 and 6.39.

Fig. 6.39 shows the simulated absorbed dose rate in air in the xz plane of the GIF++ irradiation zone. In Fig. 6.39a the irradiator is fully opened downstream (i.e. attenuation factor 1) and fully closed upstream (i.e. attenuation factor of 46415), whereas in Fig. 6.39b the irradiator is fully closed downstream and fully opened upstream. For instance, in Fig. 6.39b it is clearly possible to see the presence of scattered photon from the shielding walls, floor and roof of the irradiation area on the downstream zone. In any case the radiation is almost a factor 10^4 lower than the radiation on the upstream, where the irradiator is completely open. Nevertheless, the two figures confirm that the downstream and upstream zones of the GIF++ facility are basically independent.

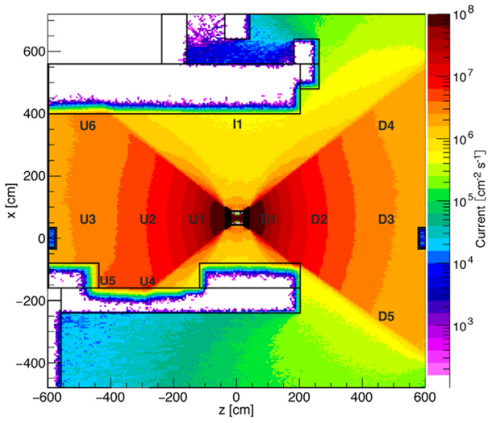

Figure 6.38: Simulated photons current in air $[cm^{-2}s^{-1}]$ in xz plane at $y = 0.0\ m$; attenuation filters system at factor 1 [79].

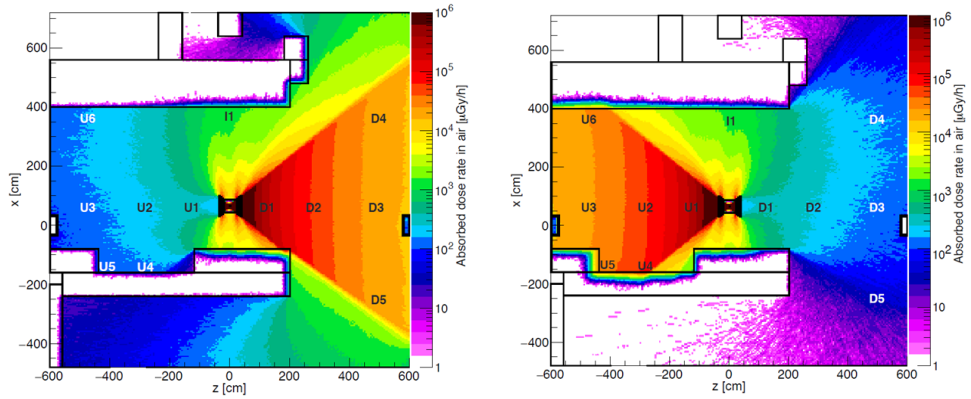

(a) D open / U closed

(b) D closed / U opned

Figure 6.39: Absorbed dose rate in air $[\mu Gy/h]$ in xz plane at $y = 0.0\ m$ of the facility [79].

6.5.2 Muon Particles from H4 beamline

The H4 beamline of the Super Proton Synchrotron (SPS), located in CERN's North Experimental Area (EHN1) facility, is a multi-purpose beam line capable of transporting secondary or tertiary particle beams, produced on the T2 primary target, over a very wide momentum range, from 10 GeV/c up to 400 GeV/c [81]. These secondary particles are transported to three experimental areas ("zones"), PPE-134, GIF++ (PPE-154), and the CMS reserved zone (PPE-164). An additional zone, PPE-144, is located between PPE-134 and GIF++. The schematic overview of the H4 beamline with the detail of the Hall EHN1 SPS North Experimental Area is shown in Fig. 6.40.

The GIF++ facility is located directly downstream of PPE-144 and offers to its users the possibility to test detector components or experimental equipment exposed simultaneously to gamma photons (produced by a strong ^{137}Cs source) and muon particle beams.

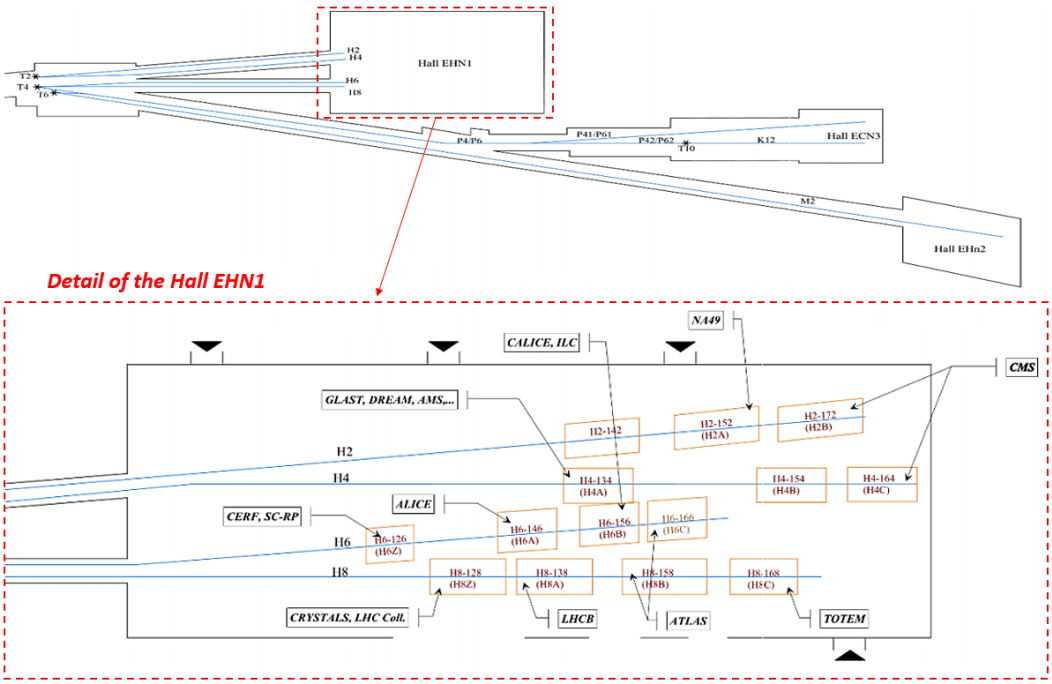

Figure 6.40: The schematic overview of the H4 beamline with the detail of the Hall EHN1 SPS North Experimental Area [82].

Before reaching the GIF++, the muon beam, consisting of a lot of different particles (protons, electrons, neutrons, pions, muons) is filtered to obtain a beam mainly composed of the muon particles. At GIF++ the muon beam has an energy equal to 100 GeV and each bunch is formed by 10^6 muons. The beam size is 12 $cm \times 12$ cm and it is at 2060 mm from the ground level. The beam structure is in "spill" (or bunches) of length 4.8s - 9.6s, separated by 14s - 48s and ordered in a "super-cycle" usually of around 1-2 spills. The muon beam is usually available for 6-8 weeks per year.

6.5.3 iRPC Experimental Setup for the Test Beam Period

1^{st} of August 2018, the characterization studies of the real-size iRPC detector prototypes have been continued with the high-radiation background environment at GIF++ facility with muon particles beam.

For this aim, in the CERN CMS-RPC QA/QC facility both prototypes have been mounted on the existing trolley, referred to as T3, in a vertical position in such a way that the beam line and the chambers irradiation zone are located in the middle of the strip panel (1.64 m from floor level). The preparation of the real-size iRPC detector prototypes for August 2018 Test Beam is shown in Fig. 6.41 and 6.42. By using the aluminum bosch-profiles and the nylon ties allowed to secure the two large prototypes on the opposite sides (distance

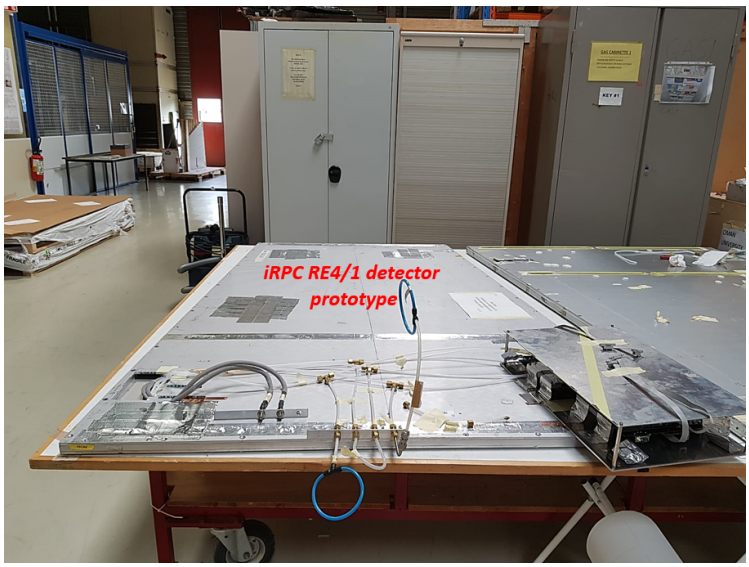

Figure 6.41: Picture of the iRPC RE4/1 detector prototype during the Test Beam preparation session in the CERN CMS-RPC QA/QC facility.

between two chambers was $\sim 80\ cm$) of the trolley in such a way that the weight of the prototypes is distributed uniformly. In order to avoid the FEBs damage during the manipulation with prototypes, the electronics have been covered with the 1 mm thick aluminum plates. In addition, the position of the two large-size iRPC detector prototypes on the trolley T3 allowed to install two additional 100 $cm \times 70\ cm$ standard RPC chambers from General Tecnica in the middle. These two chambers are representative of the RPCs detectors actually installed in the CMS Muon system which were used to compare the detection performance between the RPC and the iRPC detector prototypes.

After having completed the experimental setup, transportation of the trolley T3 and needed materials have been organized from the CERN CMS-RPC QA/QC facility to the preparation zone at GIF++ facility by using the CERN transport logistic service. The two prototypes have been successfully installed in the upstream area $\gamma - field\ upstream$ at about $\sim 2.63\ m$ from the GIF++ cesium source. The distance between the source and experimental setup corresponds to the irradiation conditions corresponding to the expected CMS condition after HL-LHC upgrade. In front of the real-size iRPC RE3/1 and RE4/1 detector prototypes, other experimental setups were installed in order to participate in the August 2018 Test Beam period. The picture of the iRPC experimental setup installed in the GIF++ irradiation area is shown in Fig.6.43.

The DAQ electronics and the low voltage modules, necessary for supplying the front end electronics, have been placed below the detector structure outside the irradiation cone of the ^{137}Cs source. It is noteworthy that the during Test Beam period the whole setup was a versatile stand which allowed a easy

Figure 6.42: Picture of the iRPC RE3/1 detector prototype installed on the Trolley T3 and prepared for August 2018 Test Beam period.

movement of the experimental system in the required positions with respect to the irradiator and beamline.

6.5.3.1 High Voltage and Low Voltage Power Systems

The high voltage is provided by a CAEN module A1526N (negative polarity) installed outside the irradiation area in the opposite rack zone (Fig.6.44). The cables, 30 meters long, have been routed under the concrete walls and the false floor inside the irradiation area to power the iRPC RE3/1 and RE4/1 detector prototypes. The CAEN HV power supplier can be remotely controlled and an dedicated data acquisition program has been developed in order to monitor and record the high voltage and current through the gas gap during the entire radiation exposure test. The low voltage for the Front-end electronics is substantially identical to the LV power system described in Section 6.4.1.2.

6.5.3.2 Gas System

The gas system at CERN GIF++ facility is the same as at the CMS-RPC QA/QC facility. The gas system is located on the first floor of the gas service area at the GIF++ facility (Fig.6.44). The gas system was designed and built in 2014 by the CERN Gas Group, following strict guidelines concerning the materials to be used, and cleanliness conditions in general. The gas system, schematically shown in Fig.6.45, in the last 2015 version is constructed in stainless-steel tube. Each gas line has the pressure regulator, mass flow controllers (MFCs) and gas mixer unit, which supplies the entire CMS-RPC experimental setups at GIF++ facility. Three mass flow controllers FIV-1005 adjust the proportion of each component ($C_2H_2F_4$, $iso-C_4H_{10}$ and SF_6) in order to receive the final gas mixture having a composition of 95.2 % $C_2H_2F_4$, 4.5% $iso-C_4H_{10}$ and 0.3% SF_6. The gas flow rate of each gas components could vary according to the number of detectors installed inside the GIF++ bunker. Therefore, the total gas flow rate is properly adjusted in order to take into account the installation/dismounting of one or more detectors.

The RPC bakelite is very sensitive to environmental parameters [83], especially the relative humidity (RH) and temperature. For operating the RPCs in avalanche mode of operation, a standard mixture of $C_2H_2F_4$, $iso-C_4H_{10}$, SF_6 is used in a particular percentage combination of 95.2:4.5:0.3 in order to achieve an optimal signal output. If the gas mixture inside the gas gaps has a different humidity, which in case of dry gases is typical of the order of 0.4 - 0.5 ppm (parts per million - commonly used as a unit of concentration), then a drastic change in the humidity inside and outside of the bakelite sheet starts affecting the resistivity of bakelite which in turn has an adverse effect in its performance characteristics. Due to the variation of the bakelite resistivity, the electric field inside the gas gaps of RPC changes in an uncontrolled fashion which is very unsatisfactory in the proportional mode of operation [84]. Simple estimation for RPC operating at the high rate (1 kHz/cm^2) was shown [78]

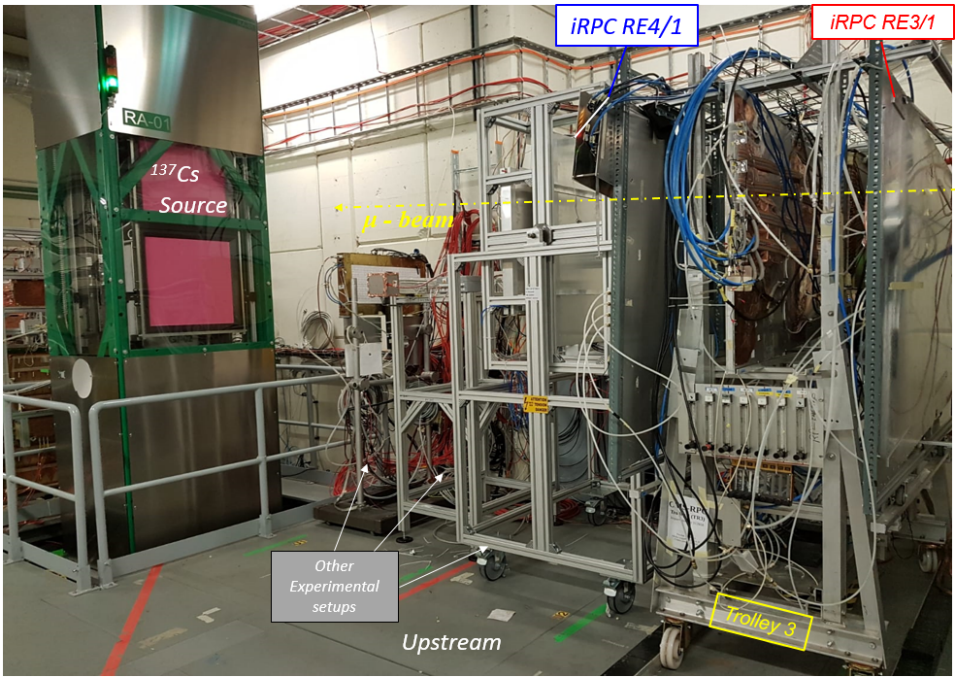

(a)

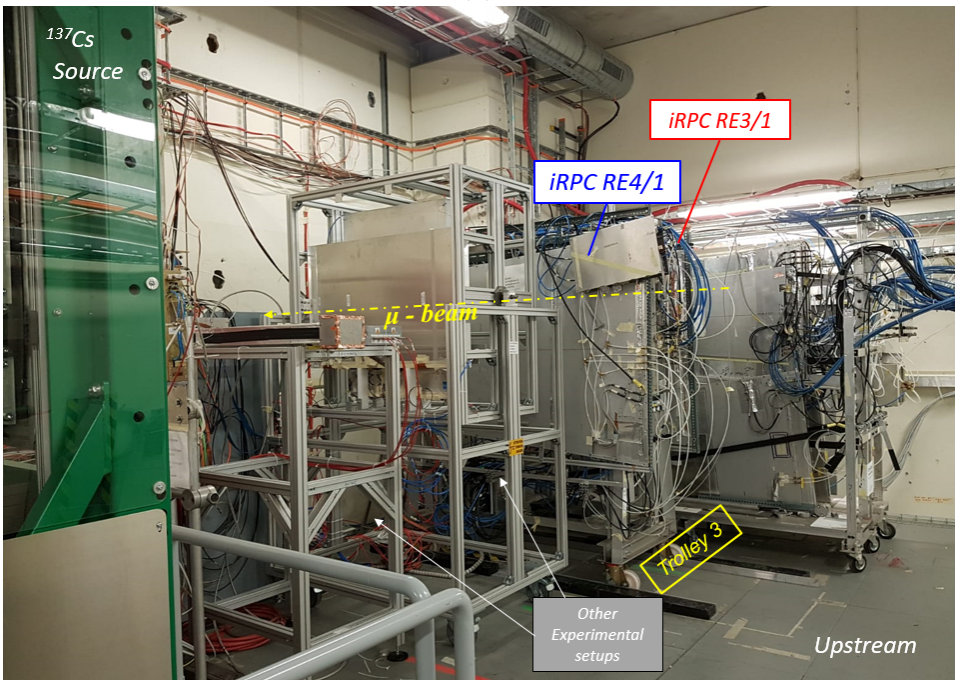

(b)

Figure 6.43: Pictures of the iRPC RE3/1 and RE4/1 detectors experimental setup installed in the Gamma Irradiation Facility in order to participate in August 2018 Test Beam period. Pictures of the experimental setup were taken from different positions: back view (a) and front view (b).

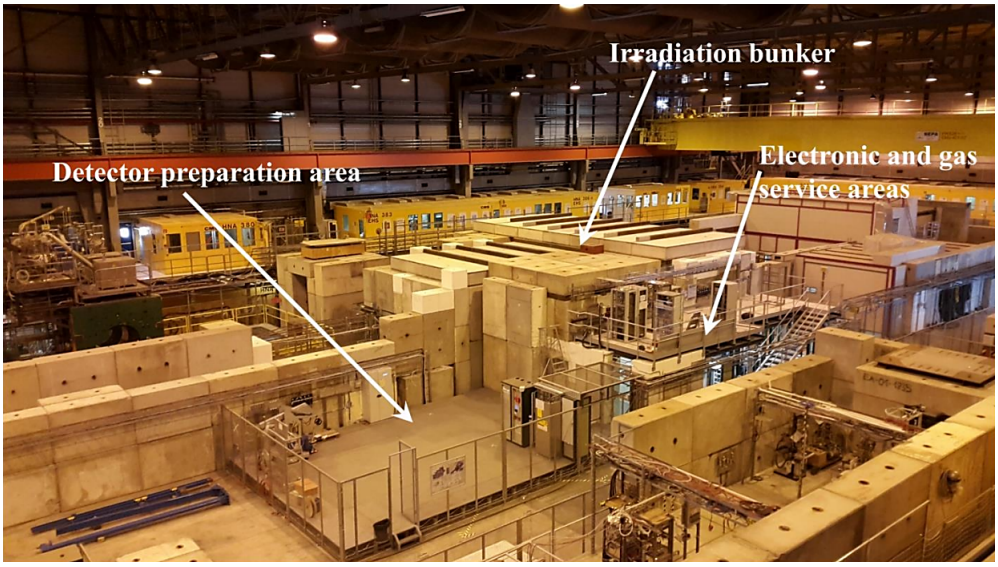

Figure 6.44: Picture of the gas systems and the electronics infrastructures at GIF++ facility.

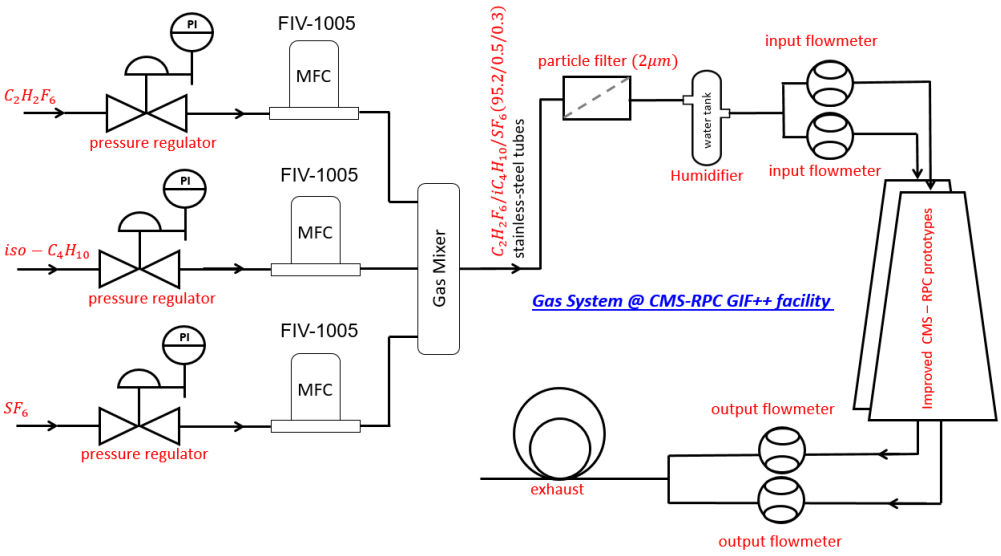

Figure 6.45: Principle scheme of the RPC gas system at CERN GIF++ facility.

that variation in resistivity can cause the noticeable voltage drop in electrodes which is resulted by the flow of current across the plates. A humidifier module has been installed on the gas input line in order to maintain the gas mixture requirements: it consists in a tank having the form of a bottle filled with distilled water. The inlet RPC gas mixture coming into humidifier is dry (dew point -79 corresponding to a water content of 0.5 ppm). The RPC gas mixture bubbles through the humidifier module water column and saturates with the required amount of water to achieve a relative humidity of 40%.

6.5.3.3 GIF ++ Detector Control System

From the GIF++ bunker area, the iRPC detector prototypes have been connected to the GIF++ Electronics area through the wooden floor by using the long enough cable. The service area hosts the high voltage power supplies and computers used for data acquisition and preliminary offline analysis used to fill the Detector Control System (DCS) webpage, called webDCS GIF++ software, with Data Quality Monitoring (DQM) histograms. During the data taking, a constant monitoring of all the environmental parameters, in different points of the bunker area, of the gas parameters, to control its composition, temperature and pressure, and of the voltages and currents delivered by the high voltage power supplies is remotely executed by webDCS GIF++ software. All the data are collected in an appropiate server installed in the electronics service area accesible from the CERN network, minimizing the need to stopping the irradiation to access inside the irradiation area.

Environmental and Gas Parameters. The Data Interchange Protocol (DIP) communication system allows to exchange all information in the real-time between all systems. The DIP read and distribute the data coming from the gas composition, temperature and humidity, the environmental temperature and pressure, the source status, attenuation values, and the radiation monitoring sensors. From GIF++ experimental area, these type of data is interesting to all GIF++ users. Retrieving this data is done by accessing to the database of the experimental hall in which GIF++ is located via DIP communication system. More specific data such as gas flow, temperature and humidity at the level of the detectors (upstream and downstream of the detectors) as well as environmental parameters are even made available for the users. For this reason, several pressure, temperature and humidity sensors were installed on the gas distribution system of the iRPC detector prototypes and RPC trolleys. The corresponding data flow, although not related to DIP itself, is saved together with the DIP data into the local CMS RPC database and displayed on the front page of the WebDCS GIF++ together with alerts in the case the values measured are out of optimal working range. The data is particularly important to perform the PT correction described in Section 6.2.2.2. and keep stable the effective voltage of the detectors.

High Voltage System. Thanks to the communication between the running webDCS GIF++ software and the CAEN HV 1527 mainframe via TPC/IP, the data of the high voltage and current values are read and stored. These values can be accessed any time through the bus of the CAEN mainframe hosting the CAEN 1526N module power supplies.

6.5.3.4 Trigger setup

In order to perform detection performance measurements as a function of the high voltage supplied to the iRPC gas gaps, it has been needed to install a

trigger setup on the beamline. This has been provided by two pairs of scintillators as shown in Fig.6.46. The two scintillator counters (S_{Up} and S_{Down}), which are a part of the GIF++ bunker are located at the front and rear bunker walls, at the beam's entry and exit points. This location gives an opportunity to reduce gamma radiation effect, coming from the source, on the scintillator counters. The upstream scintillator S_{Up} is placed at the distance of $\sim$ 11 meters from the source and the downstream scintillator S_{Down} – at $\sim$ 7 meters. In the upstream zone, the scintillator has a surface of 40 cm $\times$ 40 cm and the LEMO cable for the signal has a length of 39.1 m, which gives a delay of 195.5 ns; in the downstream zone, the scintillator surface is equal to 35 cm $\times$ 80 cm and the LEMO cable is 22 m long, creating a delay of 110 ns. The thickness of both the scintillators is equal to 2.2 cm.

The big distance between trigger counters in the GIF ++ bunker complicates the detection efficiency measurement in the iRPC RE3/1 and RE4/1 detector prototypes. In order to avoid this problem two additional scintillators (S_1 - bottom and S_2 - top) have been mounted close to the prototypes ($\sim 10cm$). S_1 and S_2 have a surface of 5 cm $\times$ 23 cm and the LEMO cables for the readout signal have a length around 30 m, which gives a delay of 38 ns for S_2 only. Both scintillators have been fixed on a movable support in the vertical position. This system is flexible enough and allows to easily modify the trigger area. During the test beam, trigger active area has been chosen of 5 cm $\times$ 20 cm.

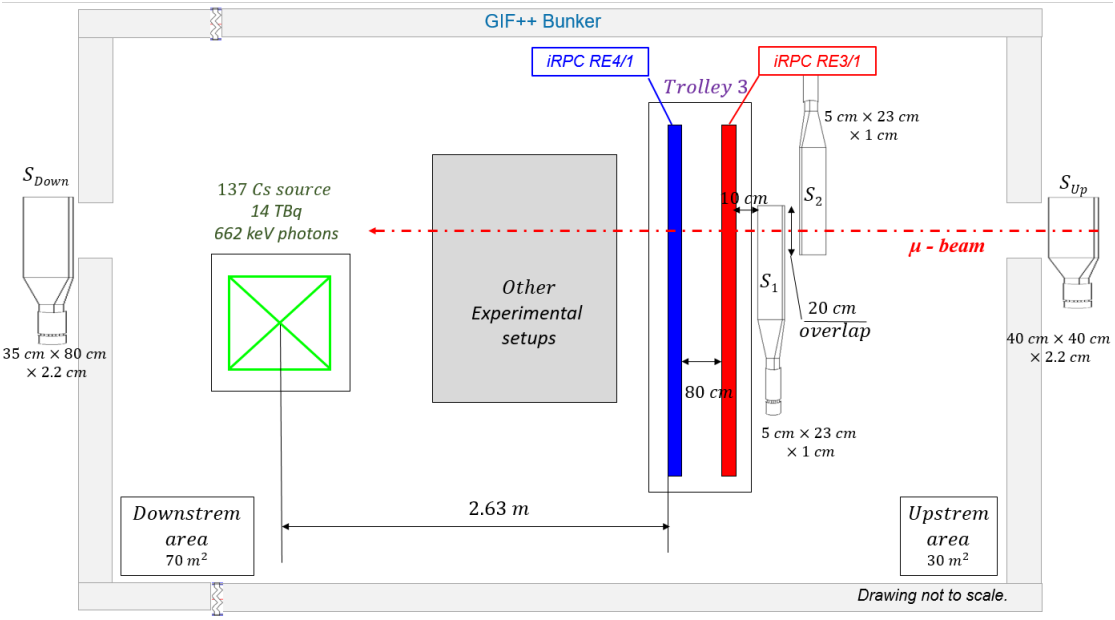

Figure 6.46: Scheme of the Trigger setup used during the Test Beam in August 2018.

The ends of each scintillator were coupled to photomultipliers supplied by a CAEN HV N470 module. Each signal via LEMO cables coming from the

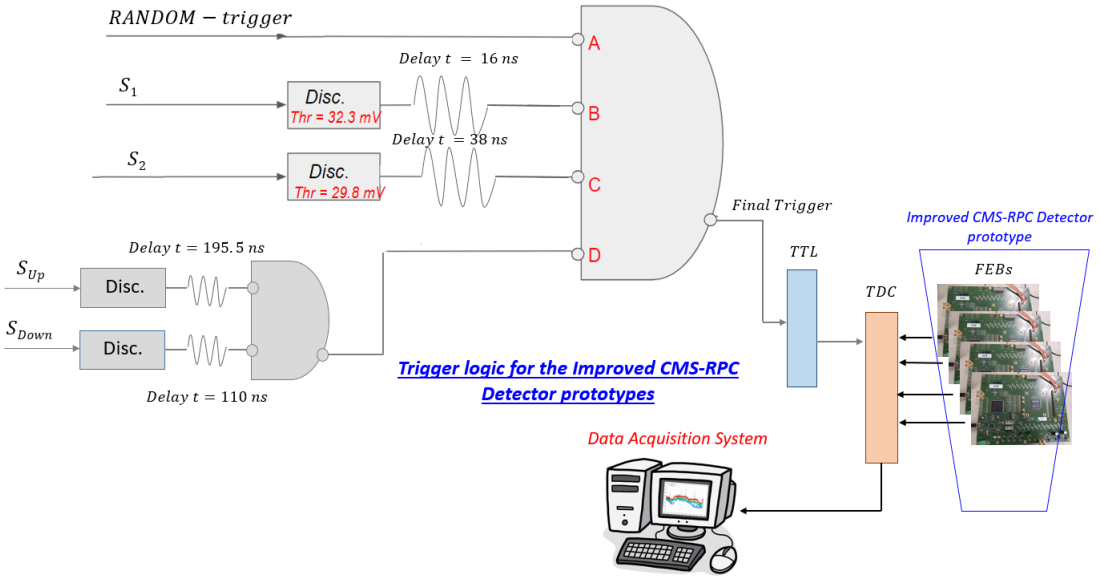

Figure 6.47: Principle scheme of the Trigger logic used during Test Beam in August 2018.

scintillators was sent to NIM modules at the GIF++ electronics service area, where they were discriminated and handled in such a way to have different types of trigger. The working configuration consisted of four scintillators signals in two pairs of the coincidence (S_{Up} with S_{Down} and S_1 with S_2), in an "AND" logic port in order to generate towers of coincidence. The trigger logic diagram block is given in Fig.6.47. The signal produced by the coincidence of two or more scintillators have been sent to a Transistor-Transistor Logic (TTL) module. Finally the TTL signal has been transferred to the MDCC (Modified Differential Current Conveyor) in order to fan-in the TTL signal on the four independent signals while maintaining their original amplitude. Each signal has been transferred to the Altera Cyclone II FPGA hosting the TDC conversion module. In turn, all TDCs have been connected to the dedicated PC via Ethernet cables in order to read/write experimental data. All experimental data have been stored in the memory buffer.

In order to analyze the experimental data obtained during the Test Beam period, the algorithm follows the same procedures presented in Section 6.4.1.5.

6.5.4 Characterisation of the iRPC RE3/1 and RE4/1 Prototypes

During summer 2018, in particular from 1^{st} August to 30^{rd} August, an extensive test beam have been conducted in the GIF++ irradiation area on improved RPC detector prototype of type RE3/1 and RE4/1 produced for the future extension of the CMS Muon End-cap in 2022-2023. The purpose of the

study was to have a comprehensive understanding of the detection efficiency and rate capability of the improved RPC technology with the new PETIROC ASIC front-end electronics.

6.5.4.1 Rate studies at different gamma fluxes

During the irradiation test, the detector prototypes behaviour has been monitored for different background conditions. Detector prototypes rates were measured as a function of the applied voltage with several values for the absorption factor ABS factors of 3.3, 4.6, 6.9, 10, 15, 22, and 46. These seven different absorber settings have been used and compared to the case where the detector prototypes were not irradiated in order to study the evolution of the detection performance of the detector with increasing exposition to gamma photon flux. For each absorption factor ABS the simulated gamma photon flux value (ϕ_{ABS}) impinging on the detector prototypes is given in Table 6.4. In the same table, the rate of expected hits (R_{ABS}) due to converted γ photons is shown. R_{ABS} is calculated by scaling the gamma photons flux values with the iRPC sensitivity [95]. In the evaluation of the sensitivity, due to its energy dependence, contributions both of the direct 662 keV gamma photons and of lower energetic scattered photons should be considered. However, these values are an approximation, as in the relation the geometric acceptance of the source and the attenuation produced by other setups must also be considered.

Table 6.5: Theoretical gamma flux from the Cesium-137 source at GIF++.

	RE4/1 prototype		**RE3/1 prototype**	
ABS [**a.u.**]	$\phi_{\mathbf{ABS}}$ [$\gamma/\mathbf{cm^2 \cdot s}$]	$\mathbf{R_{ABS}}$ [$\mathbf{Hz/cm^2}$]	$\phi_{\mathbf{ABS}}$ [$\gamma/\mathbf{cm^2 \cdot s}$]	$\mathbf{R_{ABS}}$ [$\mathbf{Hz/cm^2}$]
3.3	2.43×10^6	4.99×10^3	2.61×10^6	2.94×10^3
4.6	3.18×10^6	3.91×10^3	1.87×10^6	2.09×10^3
6.9	2.12×10^6	3.39×10^3	1.25×10^6	1.71×10^3
10	1.46×10^6	2.52×10^3	8.60×10^5	1.21×10^3
15	9.76×10^5	2.16×10^3	5.74×10^5	1.08×10^3
22	6.65×10^5	1.52×10^3	3.91×10^5	7.26×10^2
46	3.18×10^5	8.39×10^2	1.87×10^5	4.08×10^2

The Fig. 6.48 and Fig. 6.49 show the data collected with both source OFF and ON using seven different absorber settings (ABS factor: 3.3, 4.6, 6.9, 10, 15, 22, 46) in order to vary the irradiation on the iRPC detectors. The gamma radiation flux values reported in the legends of the graphs are the ones reported in Table 6.5. First of all, the average background hit rate or gamma rate seen by the iRPC detector prototypes has been estimated in double gap mode modifying the high voltage applied to the prototypes. The applied high voltage values have been normalize by using the PT correction formula explained in Section 6.2.2.2. The same measurements have been repeated with

different incident gamma flux values, obtained by varying the gamma source absorption factor.

The experimental data show that the number of counts actually increases with the increase of the applied high voltage. Moreover, as the incident flux, the measured counting rate also increases. The maximum recorded counting rate values was about 8 kHz/cm^2 for RE3/1 prototype and about 14 kHz/cm^2 for RE4/1 chamber, larger than the ones expected in the muon endcaps for the Phase-II upgrade ($\sim$ 900 kHz/cm^2). The counting rate measurements with the source OFF have been performed in order to evaluate the intrinsic noise of the detectors (noise rate), mainly due to the electronics. As shown in the graphs, the noise rate is 10 Hz/cm^2, thus so much low compared to the measured background hit rates. Finally, because of the double gap layout, the observed background hit rate for ionization taking place in both the gas gaps. Under the assumption that no ionization from a given gamma goes from one gap to the other, a single gap rate half of the measured one should be considered as an estimate of the background.

6.5.4.2 Current studies at different gamma fluxes

In addition to the background hit rates data, the irradiations tests performed on the iRPC prototypes during the test beam at GIF++ facility provide information about the current produced in the detector. The following graphs show the average current density trend as a function of the voltage applied to the bottom and top gas gaps installed in the iRPC detector prototypes. In particular, the experimental measurements do not provide any information on the average current density trend at low voltage (range of values in which the RPC detector is approximately ohmic); the average current density values reported below are thus essentially generated from the avalanche occurs in the gas gap. Furthermore, Fig. 6.50 - 6.53 show the current density values, obtained by dividing the detected current by the total iRPC detector active area for both bottom and top gas gaps, respectively. The data have been collected with both source OFF and ON using seven different absorber settings (ABS factors: 3.3, 4.6, 6.9, 10, 15, 22, 46) in order to vary the irradiation on the prototypes. The gamma radiation flux values reported in the legends of the graphs are the ones reported in Table 6.5.

The experimental data show that the current density increases with the increase of the high voltage applied to the iRPC detector prototypes. Moreover the measured current density also increases with the decreasing of the filter absorption factors.

Current density J_{mon} and counting rate R_γ are two physical quantities closely related to each other. Indeed, monitoring the current in the individual gas gaps composing a iRPC detector prototype, while knowing the rate, the charge deposition per avalanche q_γ can be computed. The current driven by the gas gap is assumed to be due to the irradiation, i.e. to the avalanches developing in the gas gap due to the gamma photons of the ^{137}Cs source.

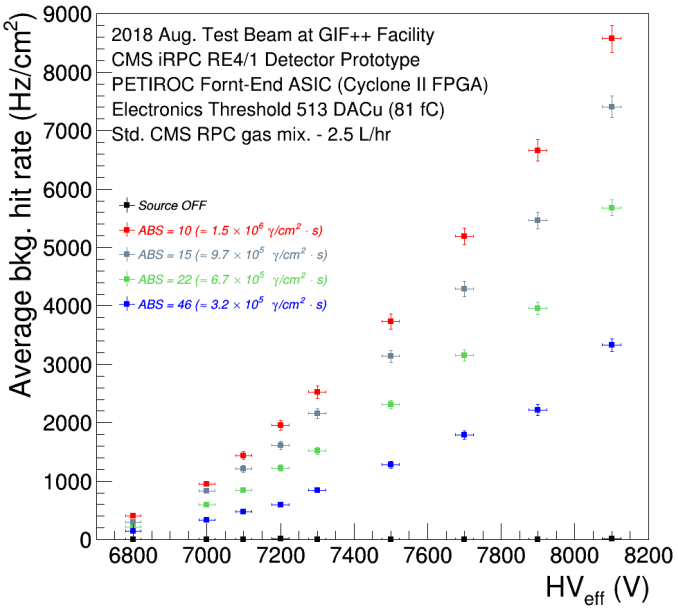

(a) Low gamma background flux.

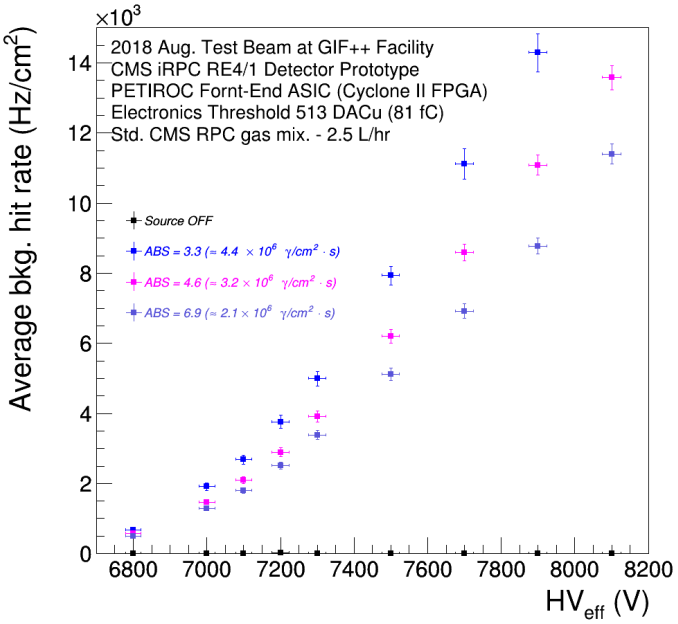

(b) High gamma background flux.

Figure 6.48: Average background hit rate as a function of the high voltage applied to the double-gap RE4/1 detector at the different levels of the gamma photon flux from the source (the nominal filter absorption factors are indicated). The applied high voltage values have been normalized by using the PT correction formula explained in Section 6.2.2.2.

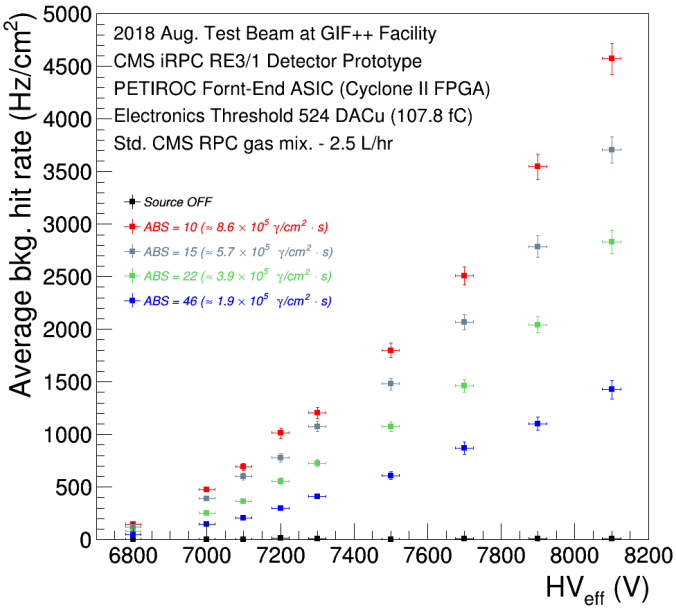

(a) Low gamma background flux.

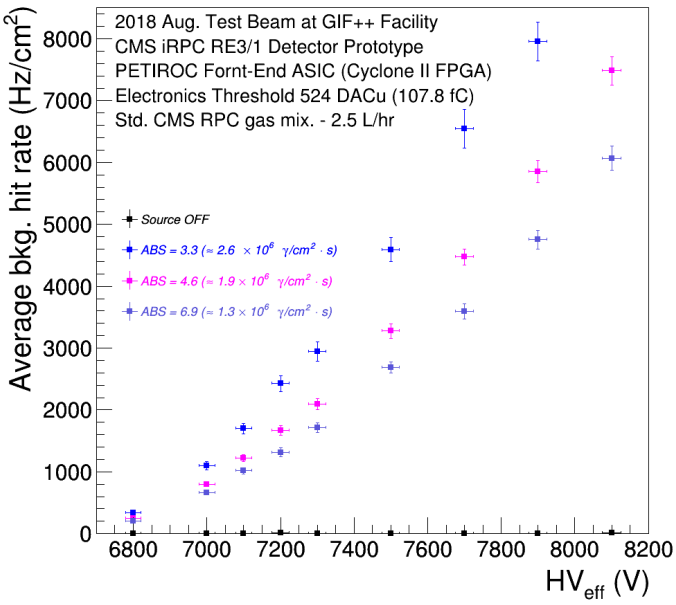

(b) High gamma background flux.

Figure 6.49: Average background hit rate as a function of the high voltage applied to the double-gap RE3/1 prototype at the different levels of the gamma photon flux from the source (the nominal filter absorption factors are indicated). The applied high voltage values have been normalized by using the PT correction formula explained in Section 6.2.2.2.

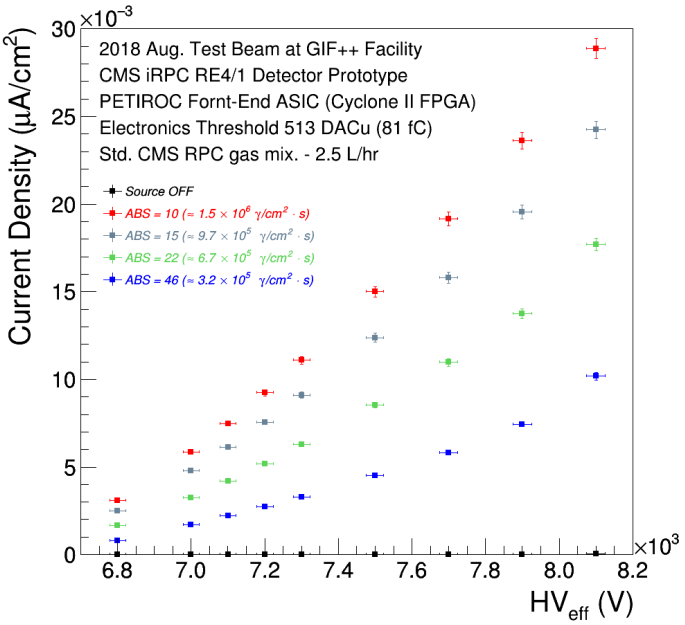

(a) Current density studies at low background irradiation.

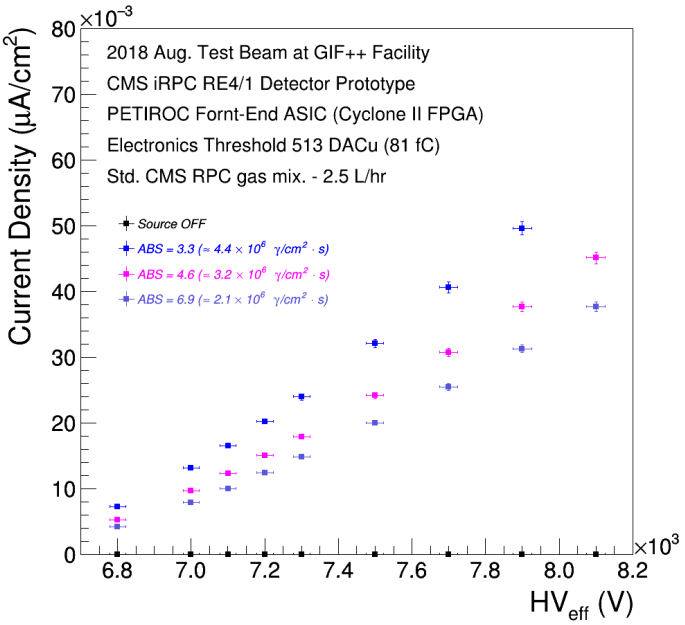

(b) Current density studies at high background irradiation.

Figure 6.50: Average current density as a function of the effective high voltage to the bottom gas gap installed in the RE4/1 detector at the different levels of the gamma photon flux from the source (the nominal filter absorption factors are indicated). The applied high voltage values have been normalized by using the PT correction formula explained in Section 6.2.2.2.

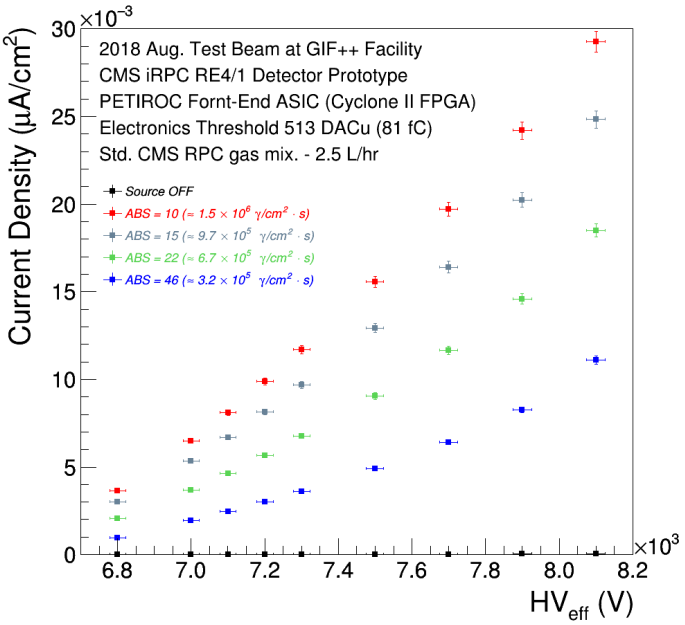

(a) Current density studies at low background irradiation.

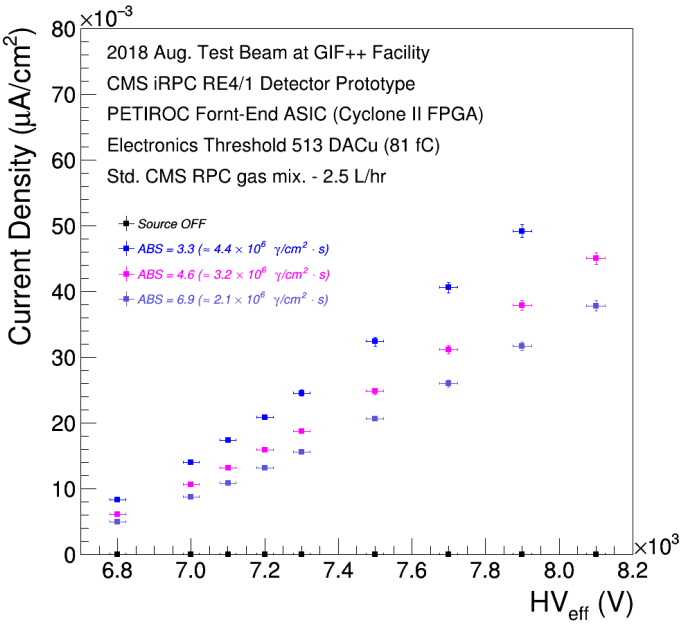

(b) Current density studies at high background irradiation.

Figure 6.51: Average current density as a function of the effective high voltage to the top gas gap installed in the RE4/1 prototype at the different levels of the gamma photon flux from the source (the nominal filter absorption factors are indicated). The applied high voltage values have been normalized by using the PT correction formula explained in Section 6.2.2.2.

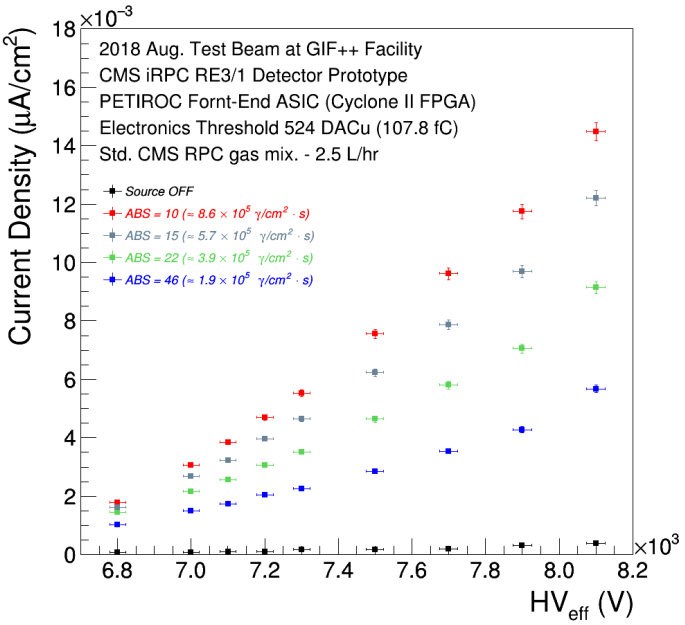

(a) Current density studies at low background irradiation.

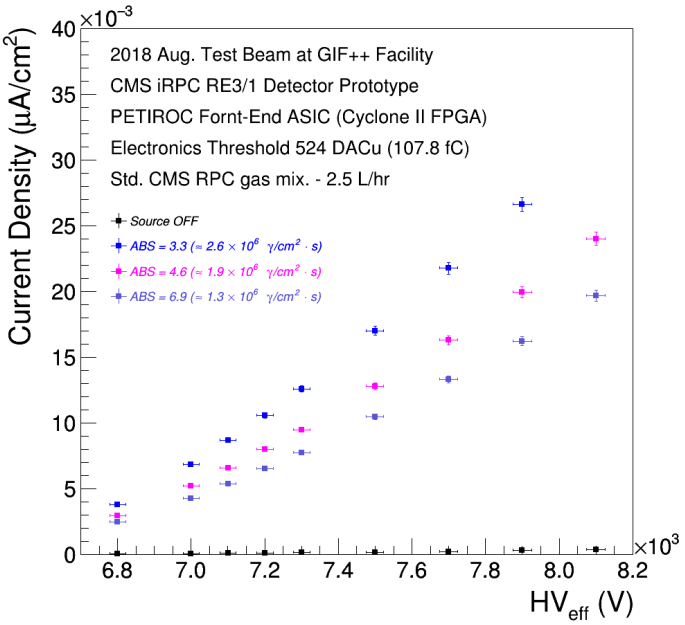

(b) Current density studies at high background irradiation.

Figure 6.52: Average current density as a function of the effective high voltage to the bottom gas gap installed in the RE3/1 detector at the different levels of the gamma photon flux from the source (the nominal filter absorption factors are indicated). The applied high voltage values have been normalized by using the PT correction formula explained in Section 6.2.2.2.

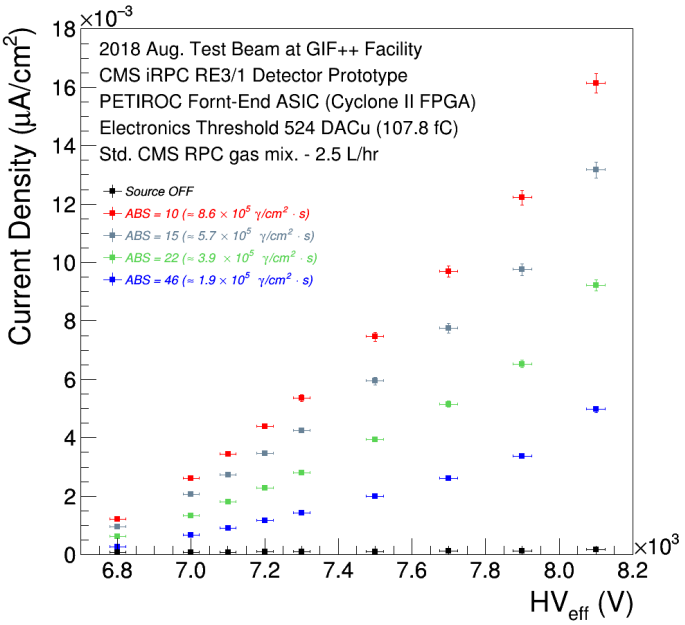

(a) Current density studies at low background irradiation.

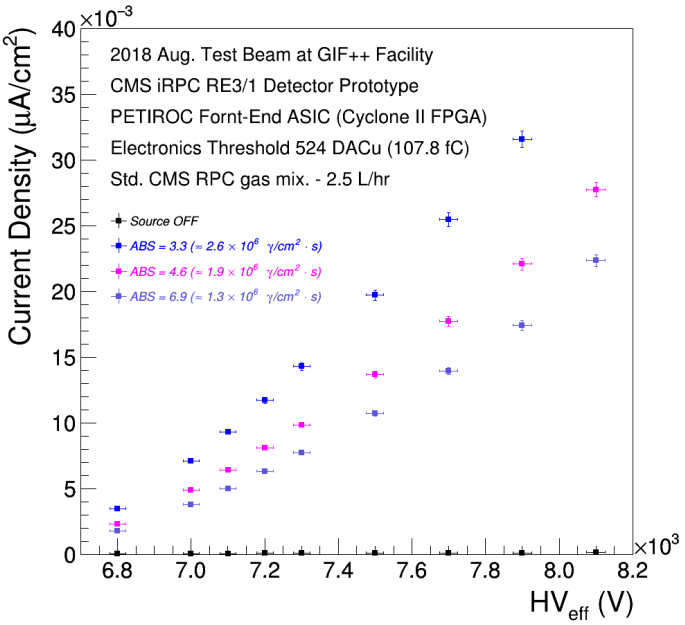

(b) Current density studies at high background irradiation.

Figure 6.53: Average current density as a function of the effective high voltage to the top gas gap installed in the RE3/1 chamber at the different levels of the gamma photon flux from the source (the nominal filter absorption factors are indicated). The applied high voltage values have been normalized by using the PT correction formula explained in Section 6.2.2.2.

Moreover, counting rate is supposed to be a measure of the number of gamma photons interacting with the gas gap of the detector prototype. Therefore, the charge deposition per avalanche is expressed like: $q_\gamma = J_{mon} / R_\gamma$, where J_{mon} is the monitored current density and R_γ the measured average background hit rate. In particular, the relation between current density and counting rate is linear as shown in the Fig. 6.54 - 6.57, where the average current density values are plotted as a function of the average background hit rate at different levels of gamma photon flux from the source both for bottom and top gas gaps.

The solid line represents a linear fit to the experimental data in order to extrapolate the parameters of the relation between current density and counting rate in single-gap mode. Therefore, the slope of the straight line represents the average charge produces by avalanches inside the gas gap of the detector. The average current density values as a function of the average background hit rate at different levels of gamma photon flux from the source both for bottom and top gas gaps of the iRPC RE3/1 detector prototype can be seen in Appendix A.

Furthermore, Fig. 6.58 and Fig. 6.59 show the average avalanche charge as a function of different levels of gamma photon flux from the source for both bottom and top gas gaps of the RE4/1 and RE3/1 prototypes, respectively.

6.5.4.3 Detection efficiency studies at different gamma fluxes

The detection efficiency is a crucial parameter for any detector: by using this detector parameter we can quantify the fraction of detected particles with respect to the total ones. Due to the stringent requirements imposed by the CMS muon trigger [57], the RPCs are required to have efficiency above 95% up to the maximum expected background rate. In order to test the ability of the improved RPC detectors to work within the CMS operational parameters, the detection efficiency and rate capability of the prototypes with the new PETIROC ASIC Front-end electronics have been carefully studied at the different gamma background rate during the Test Beam period.

With both Source OFF and ON by using the seven different absorber settings (ABS 3.3, 4.6, 6.9, 10, 15, 22 and 46), several high voltage scans have been performed to collect the experimental data in order to measure the muon detection efficiency of the prototypes. During the measurements, 9 high voltage points in the ranges 6800 V - 7300 V by steps of 100 V and 7300 V - 8100 V by steps of 200 V have been applied on the iRPC detector prototypes in order to obtain the full detection efficiency curve and estimate the working point. For each chosen high voltage point, a minimum of 5000 muon beam triggers, provided by the coincidence of the 4 scintillators, is required in order to accumulate enough statistics for reliable calculation of the detection efficiency for both iRPC detector prototypes.

Fig. 6.60 and Fig. 6.61 show the detection efficiency as a function of the high voltage applied to the both prototypes at different levels of gamma photon

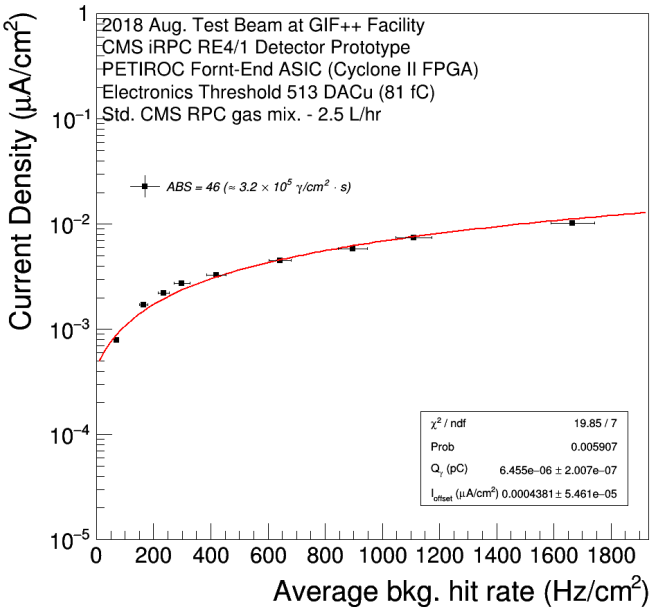

(a) $\phi_\gamma = 3.2 \times 10^5\ \gamma/cm^2 \cdot s$ (ABS 46).

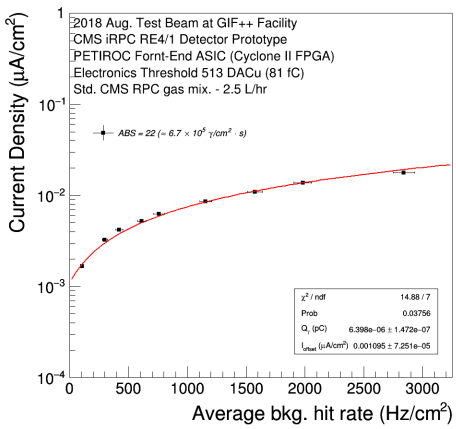

(b) $6.7 \times 10^5\ \gamma/cm^2 \cdot s$ (ABS 22).

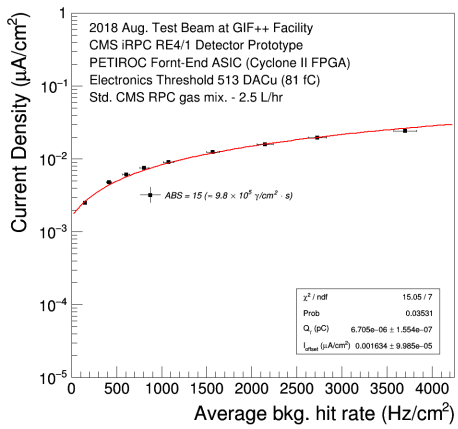

(c) $\phi_\gamma = 9.7 \times 10^5\ \gamma/cm^2 \cdot s$ (ABS 15).

Figure 6.54: Average current density as a function of the average background hit rate for the bottom gas gap of the iRPC RE4/1 detector prototype at the different levels of the gamma photon flux from the source (*ABS factors*: 46, 22, 15).

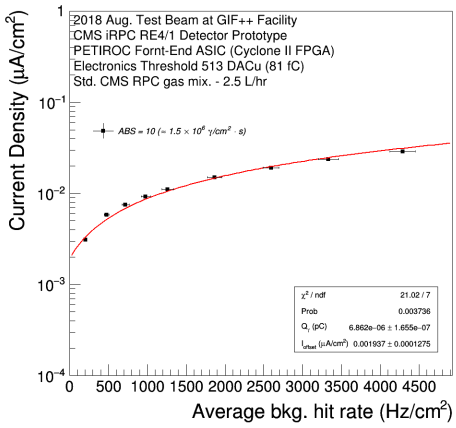

(a) $\phi_\gamma = 1.5 \times 10^6\ \gamma/cm^2 \cdot s$ (ABS 10).

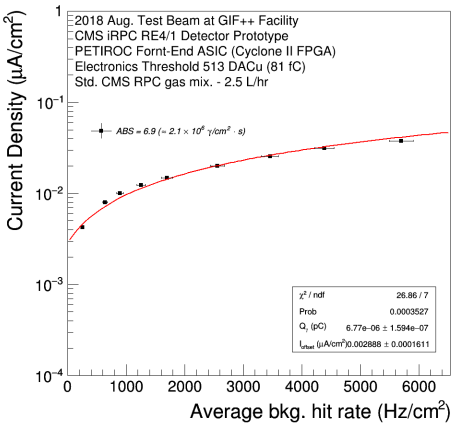

(b) $\phi_\gamma = 2.1 \times 10^6\ \gamma/cm^2 \cdot s$ (ABS 6.9).

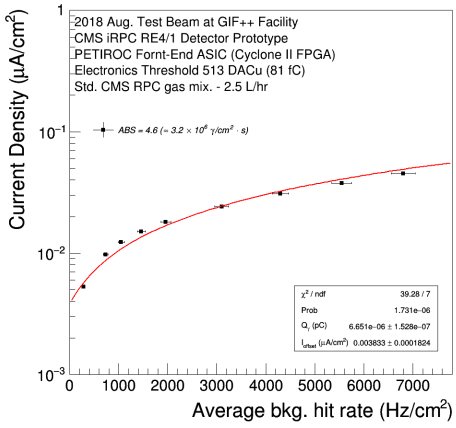

(c) $\phi_\gamma = 3.2 \times 10^6\ \gamma/cm^2 \cdot s$ (ABS 4.6).

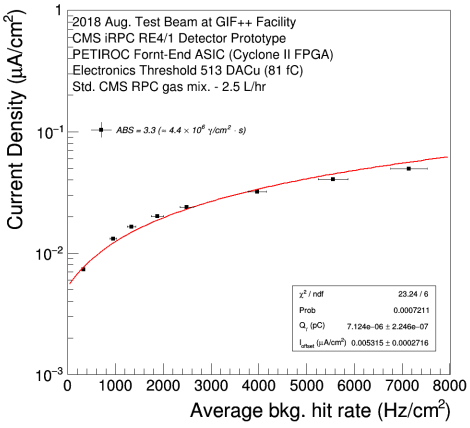

(d) $\phi_\gamma = 4.4 \times 10^6\ \gamma/cm^2 \cdot s$ (ABS 3.3).

Figure 6.55: Average current density as a function of the average background hit rate for the bottom gas gap of the iRPC RE4/1 detector prototype at the different levels of the gamma photon flux from the source (*ABS factors*: 10, 6.9, 4.6, 3.3).

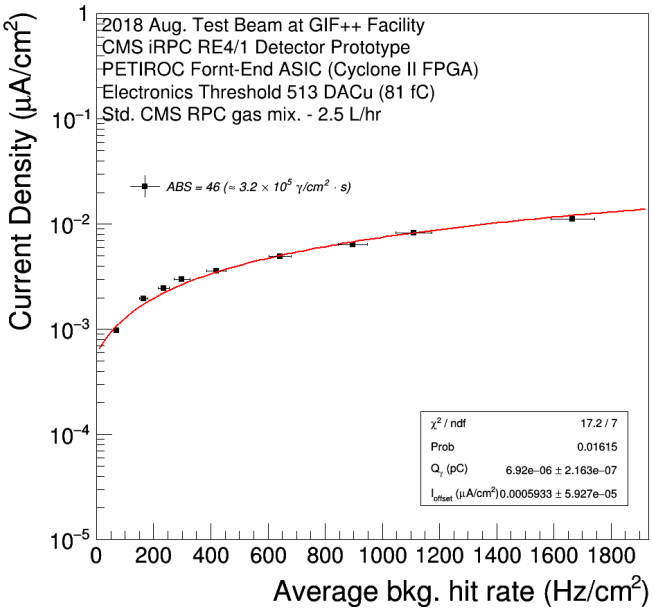

(a) $\phi_\gamma = 3.2 \times 10^5\ \gamma/cm^2 \cdot s$ (ABS 46).

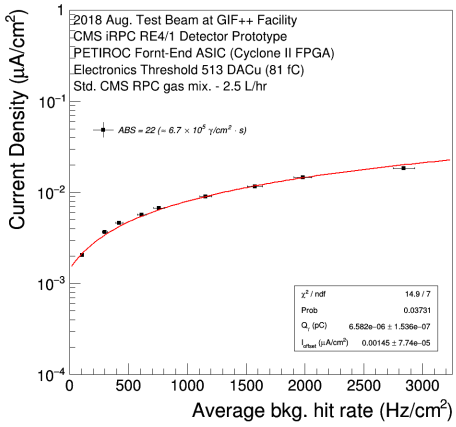

(b) $\phi_\gamma = 6.7 \times 10^5\ \gamma/cm^2 \cdot s$ (ABS 22).

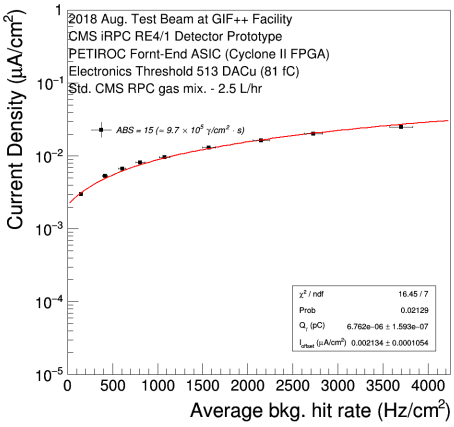

(c) $\phi_\gamma = 9.8 \times 10^5\ \gamma/cm^2 \cdot s$ (ABS 15).

Figure 6.56: Average current density as a function of the average background hit rate for the top gas gap of the iRPC RE4/1 detector prototype at the different levels of the gamma photon flux from the source (*ABS factors*: 46, 22, 15).

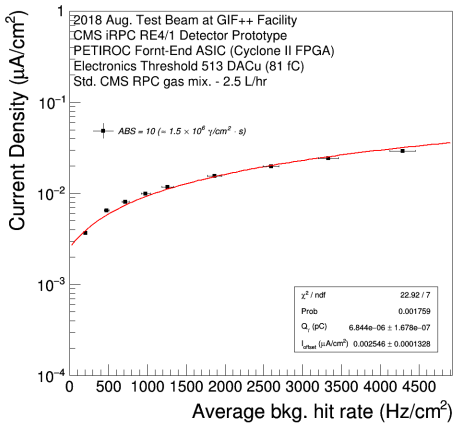

(a) $\phi_\gamma = 1.5 \times 10^6\ \gamma/cm^2 \cdot s$ (ABS 10).

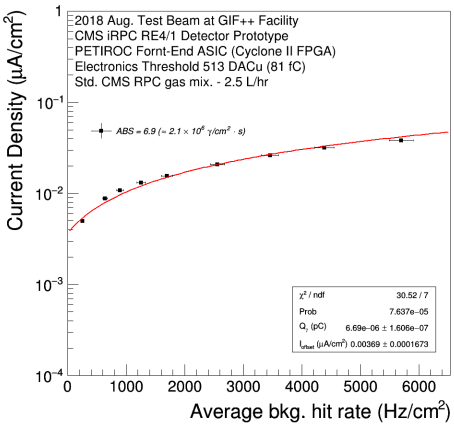

(b) $\phi_\gamma = 2.2 \times 10^6\ \gamma/cm^2 \cdot s$ (ABS 6.9).

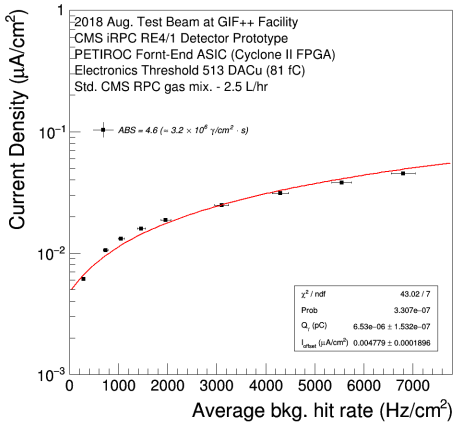

(c) $\phi_\gamma = 3.2 \times 10^6\ \gamma/cm^2 \cdot s$ (ABS 4.6).

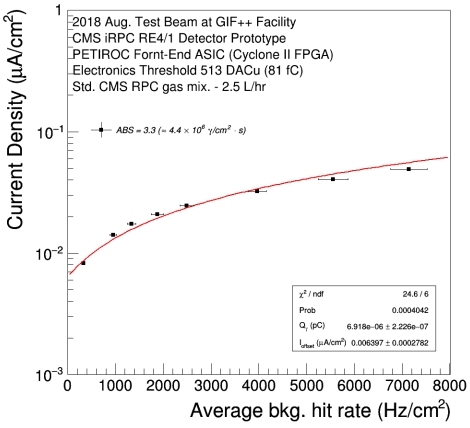

(d) $\phi_\gamma = 4.4 \times 10^6\ \gamma/cm^2 \cdot s$ (ABS 3.3).

Figure 6.57: Average current density as a function of the average background hit rate for the top gas gap of the iRPC RE4/1 detector prototype at the different levels of the gamma photon flux from the source (*ABS factors*: 10, 6.9, 4.6 and 3.3).

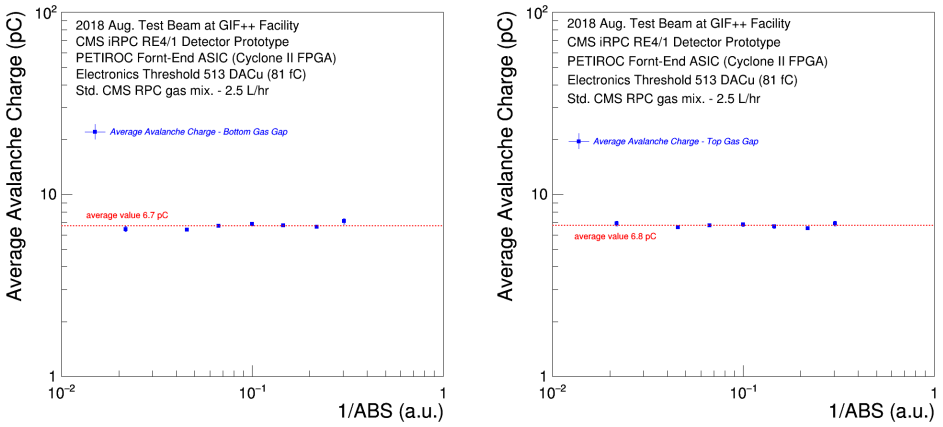

(a) (b)

Figure 6.58: Average avalanche charge as a function of the different levels of the gamma photon flux from the source for the bottom (a) and top (b) gas gaps of the iRPC RE4/1 detector prototype (the inverse of the nominal source absorption factor is indicated).

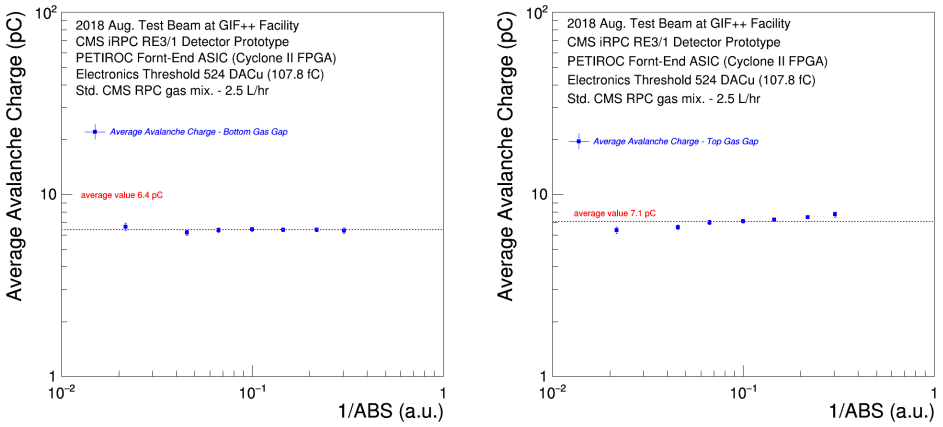

(a) (b)

Figure 6.59: Average avalanche charge as a function of the different levels of gamma photon flux from the source for the bottom (a) and top (b) gas gaps of the iRPC RE3/1 detector prototype (the inverse of the nominal source absorption factor is indicated).

flux from the source (the nominal filter absorption factors are indicated). The applied high voltage values have been normalized by using the PT correction formula explained in Section 6.2.2.2.

In the plots we can see that the detection efficiency increases with the high voltage applied to the double-gap iRPC detector prototypes and at the same time depend on the absorption factor applied to the gamma source: the more the source is opened, the higher is the incident gamma photon flux and thus the detector will be less efficient: the detection efficiency drop has been observed on both detector prototypes. However, these graphs show that at high voltage applied to the double-gap iRPC prototypes, corresponding to rates of the order of 2 kHz/cm^2 (expected rates during the Phase-II at HL-LHC), the maximum detection efficiencies of the RE3/1 and RE4/1 prototypes are approximately 97.3 % and 97.1 %, respectively, at plateau. It is direct evidence, that the new generation of the RPC detector can effectively operate within more than the minimum efficiency required by CMS (95%) at the expected difficult irradiation condition in the CMS muon system.

Fig. 6.61 and Fig. 6.63 present the summary plots of the working point and detection efficiency at the working point as a function of different levels of gamma photon flux from the source (the inverse of the nominal source absorption factor is indicated). These results of the experimental data show that at the increasing values of the incident gamma photon flux, the detection efficiency decreases and the working point moves toward higher voltage values. This effect can be explained by assuming that when an avalanche subsequent to the passage of an ionizing particle reaches one or both resistive electrodes, it neutralizes part of the surface polarization charge, consequently reducing the local electric field in the gas gap. In this case, if another ionizing particle happens to cross the detector and enters the gas where the previous one has just passed, an electric field lower than the usual will be found, and this could be not strong enough to give rise to multiplication processes; in this case, the particle could be undetected. As a consequence, the detection efficiency of the iRPC detector will progressively deteriorate as the particle flux exceeds a certain value. In order to recover the electric field, the working point value for the RE4/1 prototype has been increased from 7280.9 V without gamma photon flux to 7609 V at the highest gamma photon flux: the shift of the working point has been found to be 328.1 V, while for the working point value for the RE3/1 chamber has been increased from 7321.9 V without gamma photon flux to 7434.4 V at the highest gamma photon flux: the shift of the working point has been found to be 112.5 V. The difference in the working point for the RE3/1 and RE4/1 detector prototypes can be explained by the difference of the electronics threshold value applied on the PETIROC ASIC Front-end boards and the difference of the distance from the irradiator. More detailed results are presented below in the summary Table 6.6.

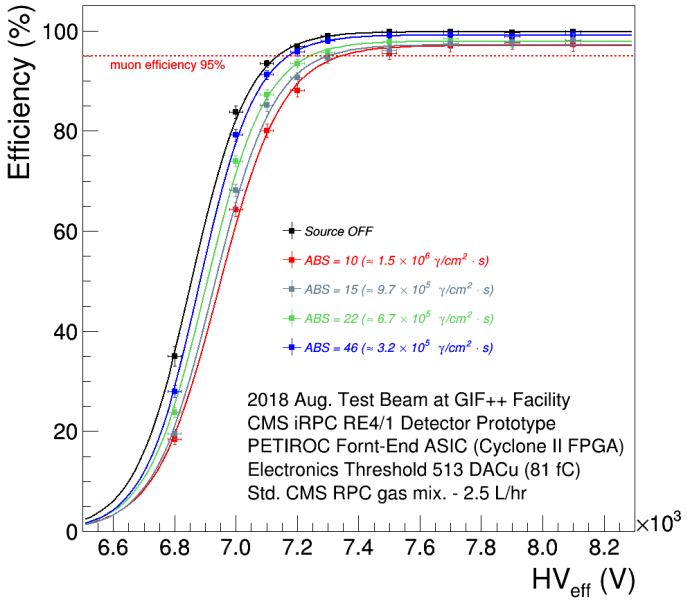

(a) Detection efficiency studies at low background irradiation.

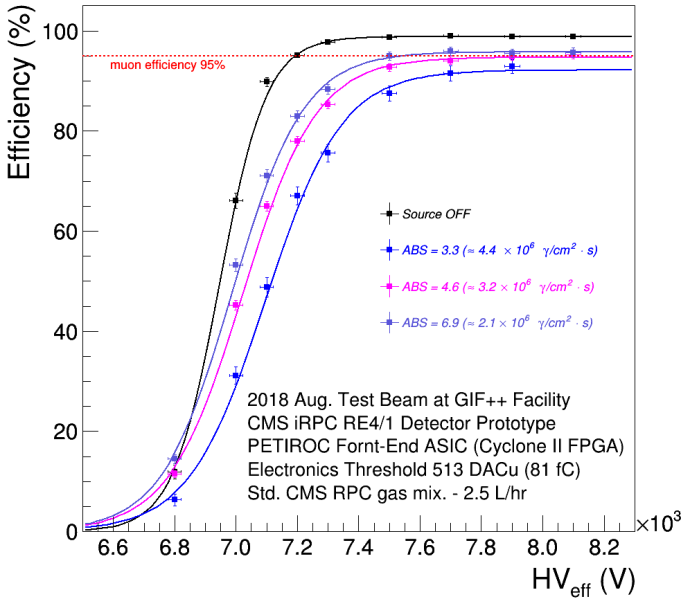

(b) Detection efficiency studies at high background irradiation.

Figure 6.60: Detection efficiency as a function of the high voltage applied to the double-gap iRPC RE4/1 prototype at the different levels of the gamma photon flux from the source (the nominal filter absorption factors are indicated). The applied high voltage values have been normalized by using the PT correction formula explained in Section 6.2.2.2.

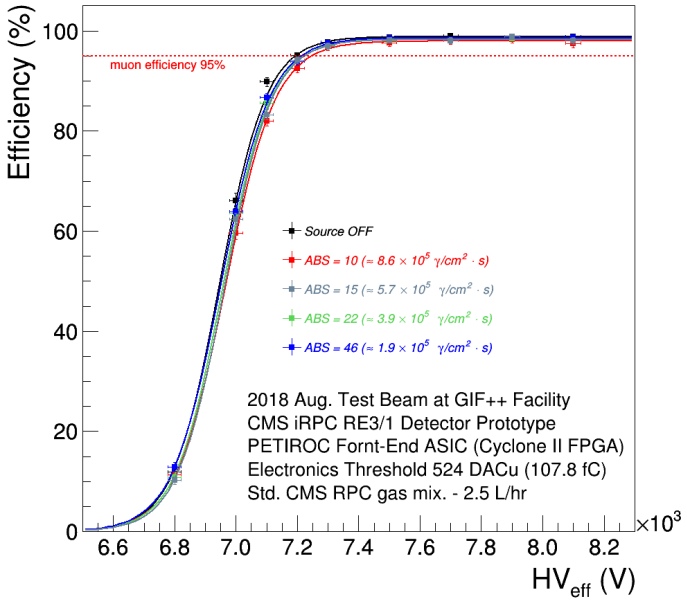

(a) Detection efficiency studies at low background irradiation.

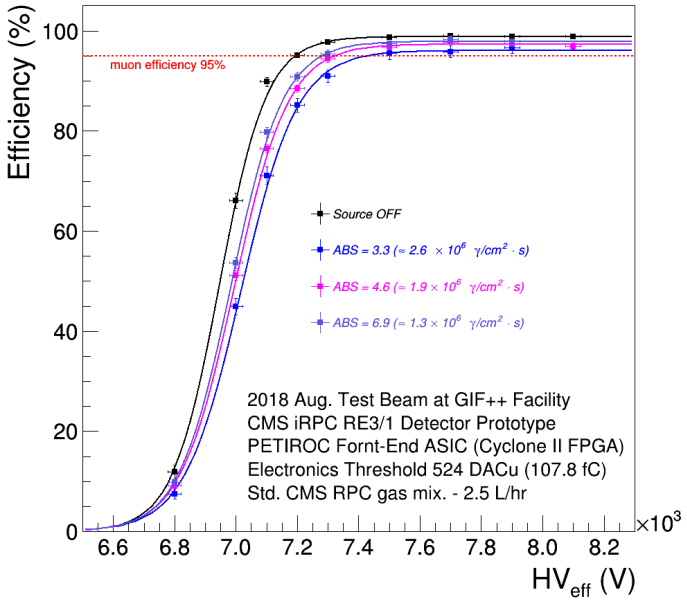

(b) Detection efficiency studies at high background irradiation.

Figure 6.61: Detection efficiency as a function of the high voltage applied to the double-gap iRPC RE3/1 prototype at the different levels of the gamma photon flux from the source (the nominal filter absorption factors are indicated). The applied high voltage values have been normalized by using the PT correction formula explained in Section 6.2.2.2.

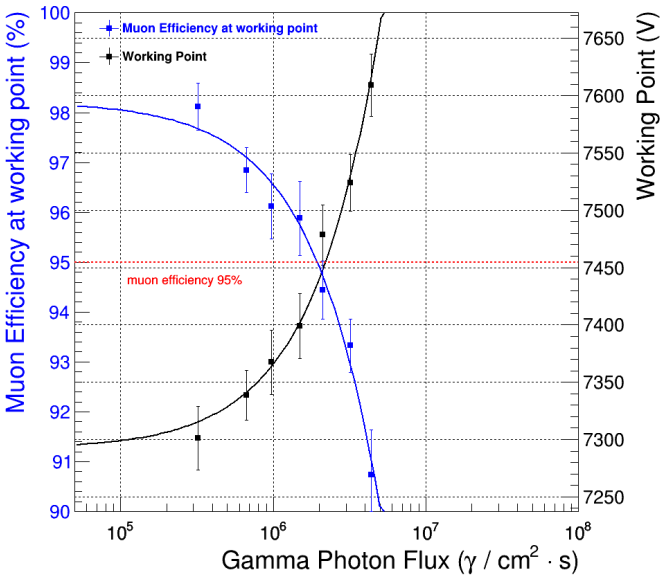

(a)

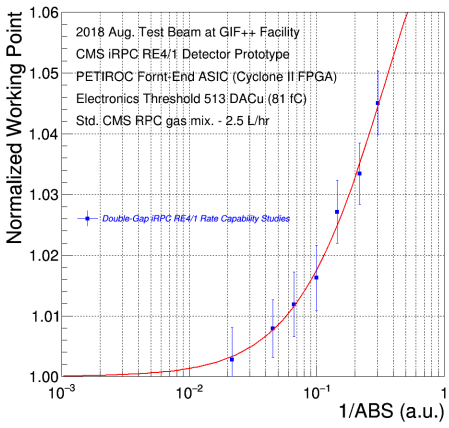

(b)

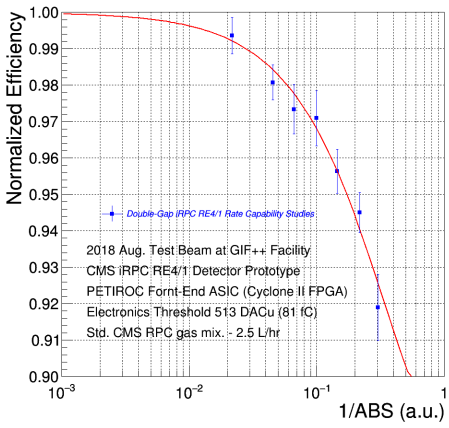

(c)

Figure 6.62: Summary plots: the working point and the detection efficiency at the working point for the RE4/1 chamber as a function of the different levels of the gamma flux from the source (inverse of the nominal source absorption factor is indicated). The detection efficiency values are normalised to those obtained with the source OFF.

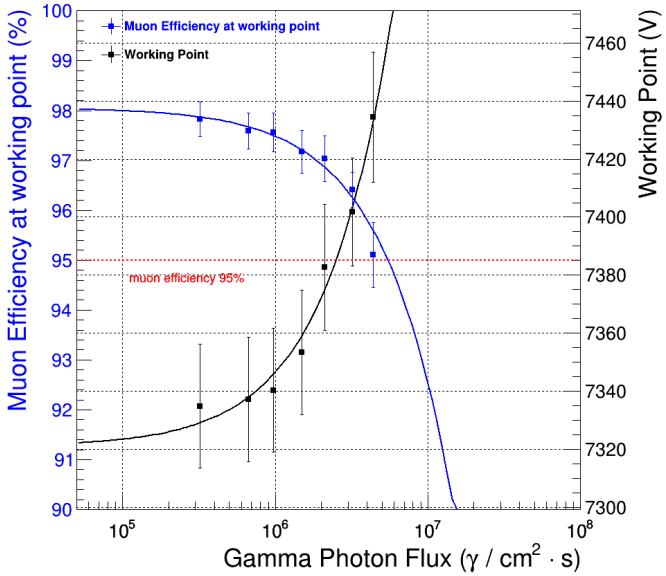

(a)

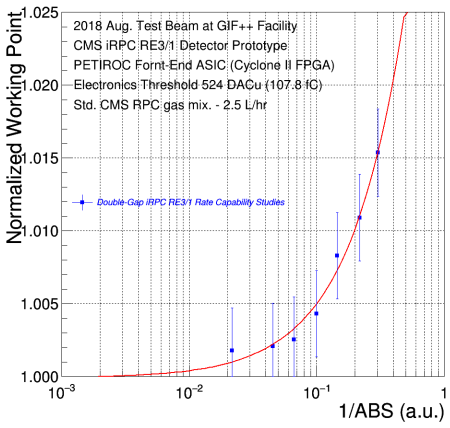

(b)

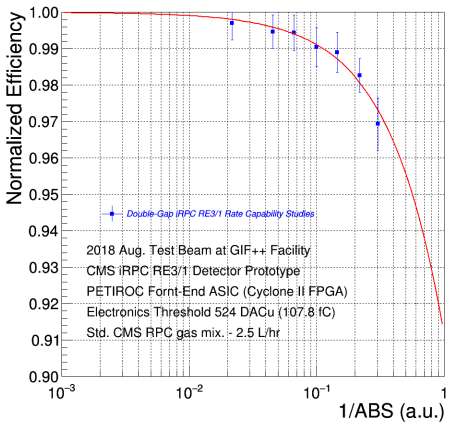

(c)

Figure 6.63: Summary plots: the working point and the detection efficiency at the working point for the RE3/1 chamber as a function of the different levels of the gamma flux from the source (inverse of the nominal source absorption factor is indicated). The detection efficiency values are normalised to those obtained with the source OFF.

Table 6.6: Summary results of the working point and the muon detection efficiency at different attenuation factors of the ^{137}Cs source at GIF++ facility obtained durint the RE4/1 and RE3/1 prototypes Test Beam campaign in August 2018.

Att.	**RE4/1 prototype**			**RE3/1 prototype**		
ABS [**a.u.**]	$\varepsilon_{\mathbf{max}}$ [%]	**WP** [**V**]	ε(**WP**) [%]	$\varepsilon_{\mathbf{max}}$ [%]	**WP** [**V**]	ε(**WP**) [%]
3.3	92.2	7609.0	90.7	96.1	7434.4	95.1
4.6	94.7	7524.0	93.3	97.3	7401.8	96.4
6.9	95.8	7478.5	94.4	97.9	7382.7	97.1
10	97.1	7399.2	95.9	98.0	7353.4	97.2
15	97.2	7367.4	96.1	98.3	7340.3	96.7
22	97.9	7338.5	96.8	98.3	7337.1	97.6
46	99.1	7301.3	98.1	98.6	7334.9	97.8
OFF	99.8	7280.9	98.8	98.8	7321.9	98.1

6.5.4.4 Cluster size studies at different gamma fluxes

After the upgrade program, in the CMS trigger system, which at the moment consists of the present RPC station, will be added to the improved RPC system. The upgraded muon trigger will have to fulfill two basic requirements, namely, efficient detection of high transverse momentum (P_T) muons and high rejection of uninteresting events. The achievement of the former goal mainly depends on the efficiency and timing properties of iRPCs. On the other hand, the RPC cluster size and the random hits, due to both the spurious hits in the chambers and to the severe background expected at the LHC, represents a major source of fake triggers. In order to avoid the big uncertainty in the determining of the muonic pattern and the associated transverse momentum, the CMS muon trigger system requires the cluster size value of the iRPC detector should be less than 2 strips. During the Test Beam campaign in August 2018, the muon and gamma cluster distributions for the RE4/1 and RE3/1 detector prototypes have been studied at different running conditions such as the high voltage and background rate environment.

In our studies, the muon cluster is defined by grouping adjacent strips with signals inside a muon time window with width around 10 ns while the same time window width has been chosen in order to compute the gamma cluster size but outside the total muon window. Inside these chosen time window, the fired strips have been assumed to be part of the same physical avalanche signal generated by a muon passing through the chamber or by the interaction of a gamma stopping into the electrodes of the iRPCs. In Fig. 6.64 and Fig. 6.65 the efficiency curves and average muon and gamma cluster size distribution as a function of the high voltage applied to the double-gap iRPC RE4/1 prototype at different source conditions are presented in order to understand how the

cluster size is affected by different levels of gamma photons flux. The same cluster distribution can be found for RE3/1 chamber in Appendix A of this Doctoral Thesis. In summary plots (see Fig. 6.66 and Fig. 6.67), it is clear that for both chambers the muon cluster size remains below 4 and then decreases as the particle rate of the source increase (as shown in Fig. 6.66d and Fig. 6.67d at the maximum photon flux the cluster size is below 3.3). In the ideal case, we must to observe only one strip crossed by a particle should be fired, but due to the cross-talk or other phenomena can increase this number of fired strips.

By using the ^{137}Cs source at GIF++ facility during the Test Beam campaign, the avalanching charge produced by gamma via Compton scattering is accumulated and distorts the electric field inside gas gaps. The lowered and distorted electric field inside the iRPC gas volume leads to the reduction of the avalanching charge size produced by muon particles. The latest fact can explain the muon cluster size reduction at increasing the gamma photon flux.

In addition, the gamma cluster size has been measured also. The gamma particles induce its pulse in an individual single gap via Compton scattering, thus the expected pick-up charge is about a half of the muon one. In this reason, the observed gamma cluster size is about 2 times less respect to the muon cluster size (see Fig. 6.64 and Fig. 6.65).

In order to summarize this study, the muon detection efficiency and the muon and gamma cluster size as a function of the cluster rate seen at working point by the two double-gap iRPC RE3/1 and RE4/1 detector prototypes have been computed (see Fig. 6.68). The studies show that, at the detector working point, the average muon cluster size is around 2.5 and the average gamma cluster size is basically 1.7 for each chamber.

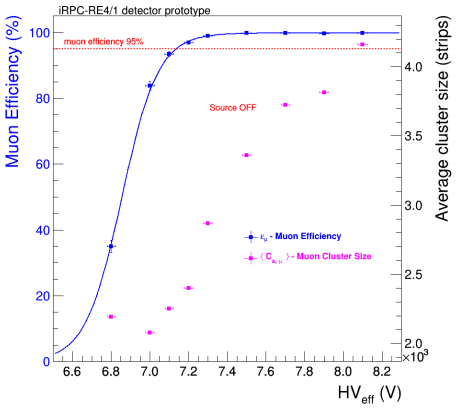

(a) Without gamma photon flux.

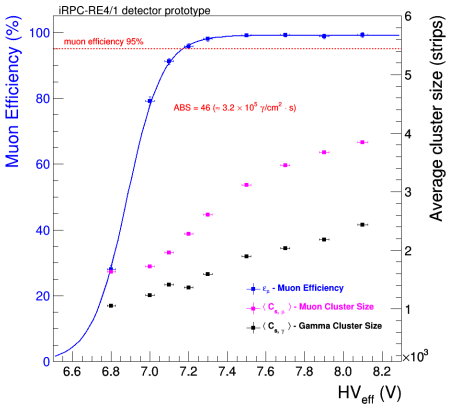

(b) $\phi_\gamma = 3.2 \times 10^5\ \gamma/cm^2 \cdot s$ (ABS 46).

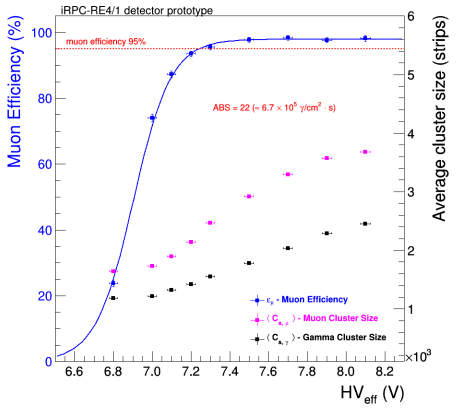

(c) $\phi_\gamma = 6.7 \times 10^5\ \gamma/cm^2 \cdot s$ (ABS 22).

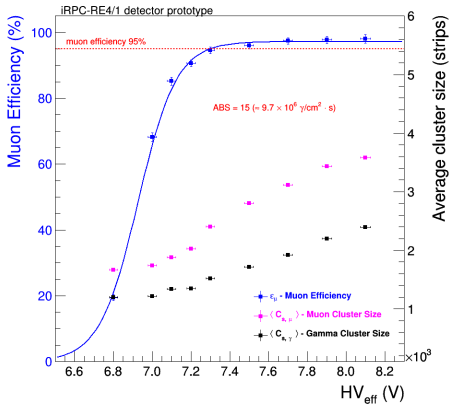

(d) $\phi_\gamma = 9.8 \times 10^5\ \gamma/cm^2 \cdot s$ (ABS 15).

Figure 6.64: Muon detection efficiency, muon and gamma cluster size as a function of the high voltage applied to the RE4/1 prototype at the different levels of the gamma photon flux from the source (the nominal filter absorption factors are indicated). The applied high voltage values have been normalized by using the PT correction formula explained in Section 6.2.2.2.

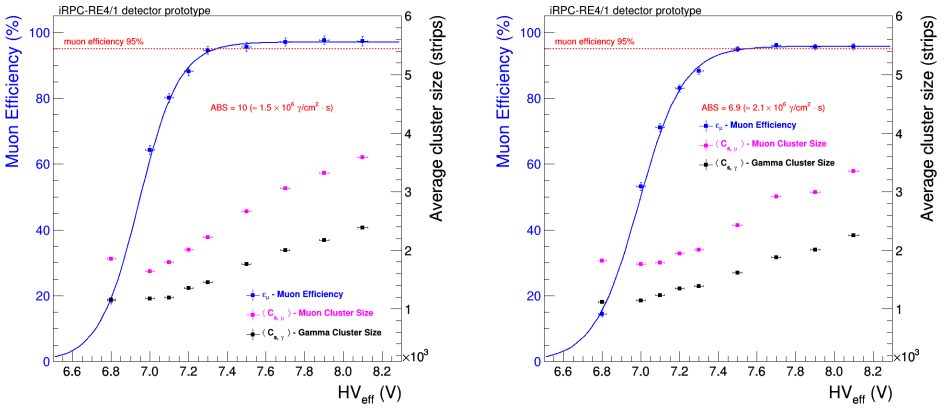

(a) $\phi_\gamma = 1.5 \times 10^6\ \gamma/cm^2 \cdot s$ (ABS 10). (b) $\phi_\gamma = 2.1 \times 10^6\ \gamma/cm^2 \cdot s$ (ABS 6.9).

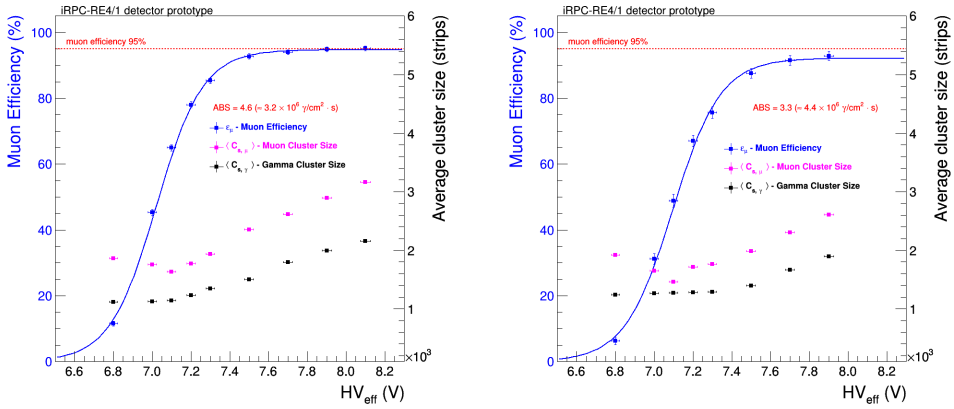

(c) $\phi_\gamma = 3.2 \times 10^6\ \gamma/cm^2 \cdot s$ (ABS 4.6). (d) $\phi_\gamma = 4.4 \times 10^6\ \gamma/cm^2 \cdot s$ (ABS 3.3).

Figure 6.65: Muon detection efficiency, muon and gamma cluster size as a function of the high voltage applied to the RE4/1 prototype at the different levels of the gamma photon flux from the source (the nominal filter absorption factors are indicated). The applied high voltage values have been normalized by using the PT correction formula explained in Section 6.2.2.2.

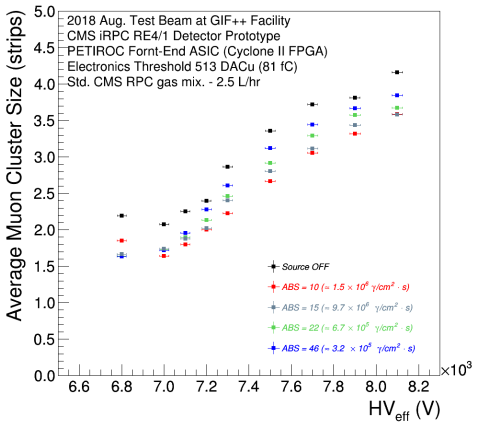

(a) Muon cluster studies at the low background irradiation.

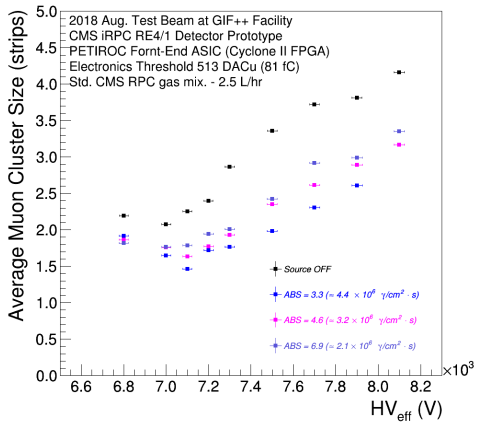

(b) Muon cluster studies at the high background irradiation.

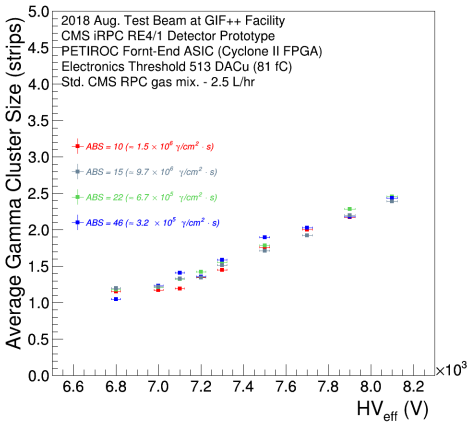

(c) Gamma cluster studies at the low background irradiation.

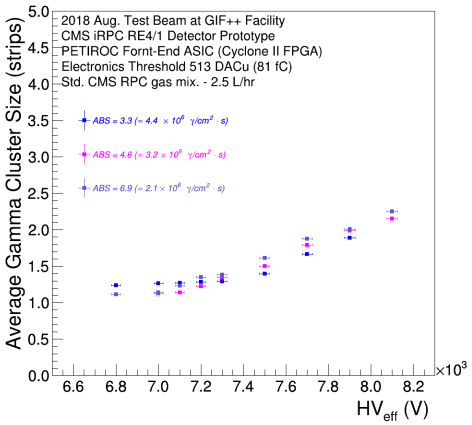

(d) Gamma cluster studies at the high background irradiation.

Figure 6.66: Summary plots of the muon and gamma cluster size as a function of the high voltage applied to the RE4/1 detector at the different levels of the gamma photon flux from the source (the nominal filter absorption factors are indicated). The applied high voltage values have been normalized by using the PT correction formula explained in Section 6.2.2.2.

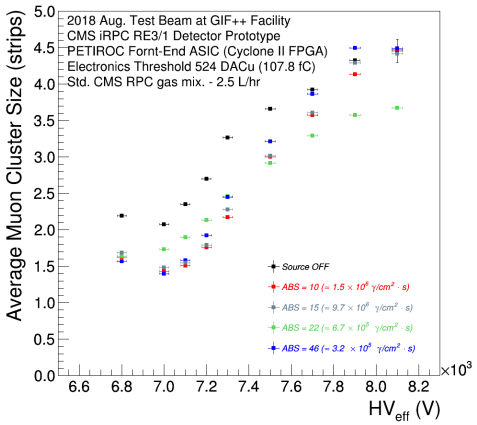

(a) Muon cluster studies at the low background irradiation.

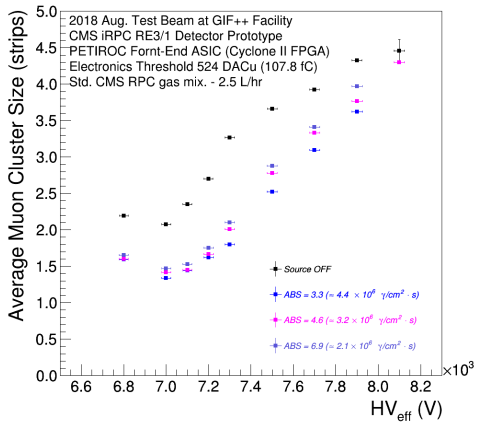

(b) Muon cluster studies at the high background irradiation.

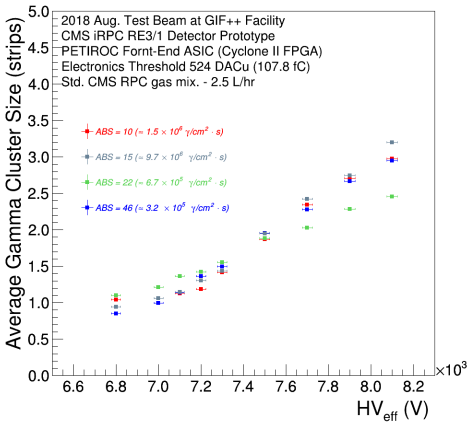

(c) Gamma cluster studies at the low background irradiation.

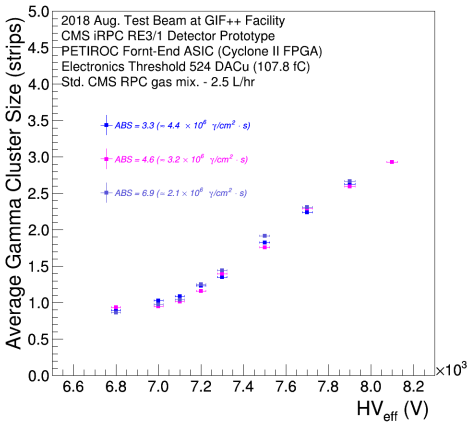

(d) Gamma cluster studies at the high background irradiation.

Figure 6.67: Summary plots of the muon and gamma cluster size as a function of the high voltage applied to the RE3/1 chamber at the different levels of the gamma photon flux from the source (the nominal filter absorption factors are indicated). The applied high voltage values have been normalized by using the PT correction formula explained in Section 6.2.2.2.

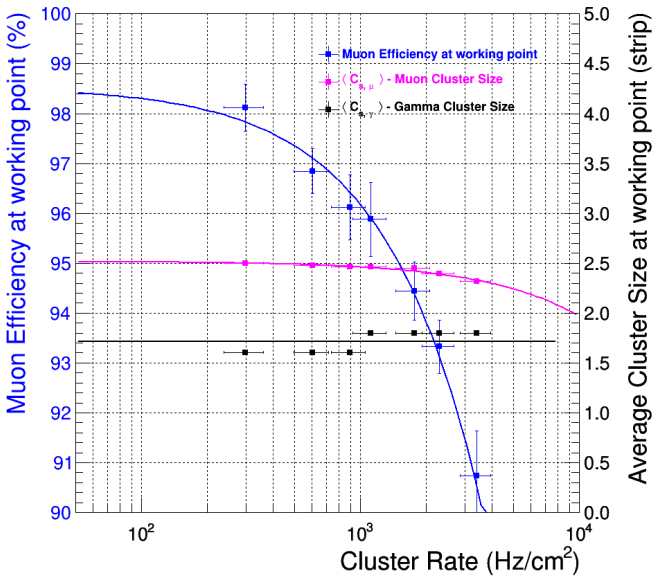

(a)

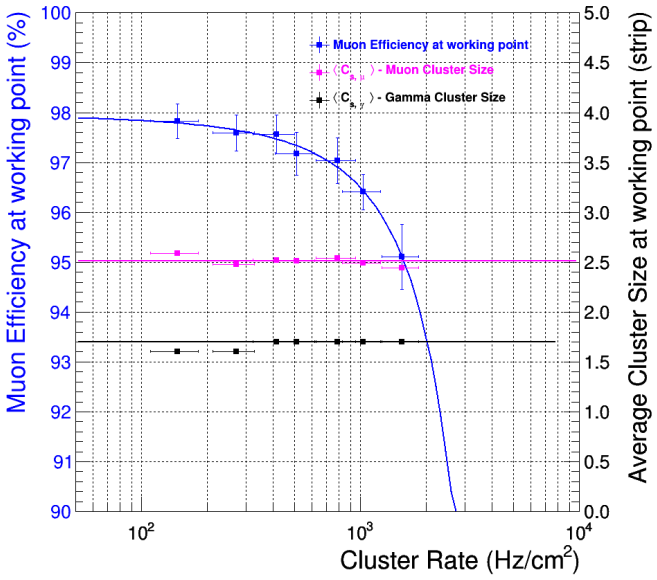

(b)

Figure 6.68: Summary results of the RE4/1 and RE3/1 chambers with new PETIROC ASIC Front-end electronics obtained during the Test Beam period in August 2018. Muon detection efficiency, muon and gamma cluster size at the working point as a function of the cluster rate.

Chapter 7

The Performance Studies of the Improved RPC Detector with new INFN Rome Front-End Electronics

The upgrade of the Resistive Plate Chamber (RPC) detector, in order to increase the detector rate capability and to be able to work efficiently in a high rate environment, consists in the reduction of the operating voltage along with the detection of signals which are few hundreds μV height. The approach chosen by this project to achieve this objective is to develop a new kind of Front-End electronics. The INFN Rome electronics has been proposed as a possible alternative to PETIROC ASIC electronics in order to avoid having a single technology for the CMS-RPC system upgrade project, which would have significantly increased the risk due to a single point of failure such as inability to meet the Front-end electronics requirements for the future upgrade or delay in delivery of the Front-end electronics and DAQ. This has been the strategy adopted by the CMS-RPC community and, consequently, it was necessary to find another available technology in order to develop the Front-end electronics to readout the iRPC detectors. The INFN Rome electronics has been selected as an alternative electronics compatible with the fundamental requirements on the detection performance that an iRPC detector has to fulfill in the CMS RE3/1 and RE4/1 regions. In order to study the performance of the CMS iRPC detector with the INFN front-end electronics, the iRPC RE4/1 detector prototype has been assembled in the INFN Rome Tor Vergata laboratories and tested in the cosmic telescope at the CMS-RPC QA/QC facility and during the last available muon particle beam in the GIF++ facility at CERN.

7.1 The INFN Rome Front-End Electronics and Strip panel

For a reliable improved RPC system operation at the high background particle rates in the innermost region of CMS Muon Spectrometer, an enhancement of the Front-End readout electronics performance is mandatory in order to increase the RPC rate capability. The features of the newly developed Front-End Electronics are:

- Decrease the noise for short shaping, to obtain a low occupancy;
- Decrease the rise time, for improved time-of-flight capability;
- Improve the performance of the discriminator and the time-to-digital converter;
- Minimize complexity in order to achieve high reliability and low cost;
- Minimize the power consumption to avoid the need for active cooling;
- Employ radiation-hard technology, since the Front-End electronics cannot be replaced.

The new Front-End electronics developed by INFN laboratory of Rome Tor Vergata consists of a fast charge preamplifier and a full-custom ASIC discriminator. The new preamplifier is made in Silicon Bipolar Junction Transistor (BJT) technology [88]. The technical characteristics of the new Silicon BJT preamplifier are presented in Table 7.1.

Table 7.1: Technical characteristics of the Silicon BJT preamplifier [87].

Parameter	**Value**
Voltage supply	3-5 V
Sensitivity	2-4 mV/fC
Noise (independent from detector)	4000 e^-RMS
Input impedance	50-100 Ω
Bandwidth	10-100 MHz
Power consumption	10 mW/ch
Rise time $\delta(t)$ output	300-600 ps
Radiation hardness	1 Mrad, 10^{13} n/cm^2

The new Front-End electronics defeloped by INFN laboratory of Rome Tor Vergata consists of a fast charge preamplifier and a full-custom ASIC discriminator. The new preamplifier is made in Silicon Bipolar Junction Transistor (BJT) technology [88]. It is based on the concept of a fast charge integration with the possibility to match the input impedance to a transmission line.

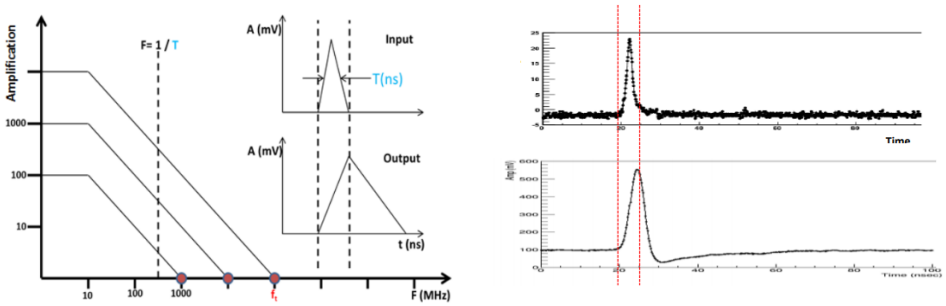

Figure 7.1: Working principle of the new preamplifier based on the Silicon Bipolar Junction Transistor technology [87].

Fig. 7.1 gives the principle idea of how the injected signal is integrated. The output signal from the preamplifier has the rise time and the maximum amplitude which is directly proportional to the duration of the injected signal and its charge, while the fall time parameter is not related to the physical injected signal but depends only on the constants of the preamplifier.

This new low-noise preamplifiers can substantially increase the rate capability of the improved RPCs by providing signal detection for a factor ten less charges produced in the gas compared to the present RPCs. Due to the lower charge produced by the avalanches in the thinner gas gaps, iRPC detectors, for the same hit rate, can be operated at lower currents, which slows down the aging.

The new discriminator ASIC designed for iRPCs is implemented in SiGe BiCMOS technology [89]. The main idea behind this new discriminator is the limit amplifier. If the signal passes the threshold, it will be amplified until saturation, providing as output a square wave. The main features of the discriminator are [87]:

- Optimal characteristic function with the possibility of an easy regulation of the threshold starting from a minimum value of a few mV;
- Very small transition region around 300 μV, practically negligible when the discriminator is used withthe RPC fast pulses;
- Time-Over-Threshold measurement directly within the discriminator;
- Minimum pulse width of 3 ns.

The technical characteristics of the new SiGe discriminator are presented in Table 7.2.

The new eight-channel FEB for the RPC consists of eight of the new discrete-components preamplifiers based on Silicon BJT, and eight discriminators in two ASIC chips based on SiGe BiCMOS technology. This technology provides better performance in terms of noise, bandwidth, and power consumption [87], [90]. The principle scheme and pictures of the new INFN Rome

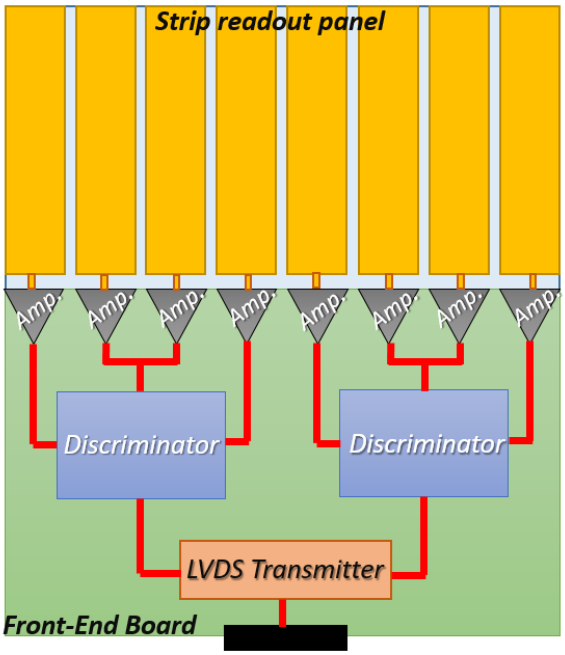

(a)

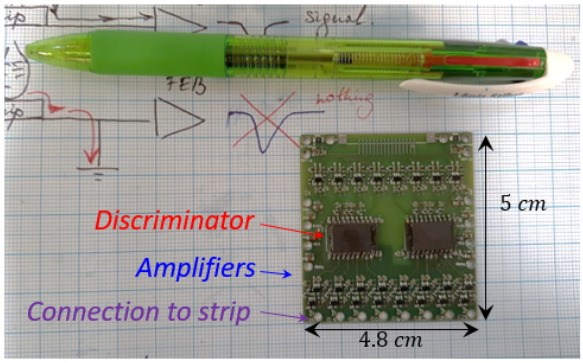

(b)

Figure 7.2: Principle scheme (a) [90] and picture (b) of the new INFN Rome Front-End electronics.

Front-End electronics is shown in Fig. 7.2. It is a very compact electronics board with overall dimension of 4.8 cm x 5 cm. Other construction design features are the low power consumption (less 0.5 W/channel) and the absence of the active cooling of FEBs components.

The strip panel for the second iRPC detector prototype will only cover half of the detector active area. It is exactly the same logic of the prototype construction which was successfully applied to assembly the first RE3/1 and RE4/1 chambers with PETIROC ASIC electronics (see Chapter 5).

The new design of strip readout panel with its dimensions is presented in Fig. 7.3. The strip readout panel has been produced by Eltos S.p.A. company (Italy) [91]. It has been designed for the second real-size iRPC RE4/1 detector

Table 7.2: Technical characteristics of SiGe discriminator [87].

Parameter	**Value**
Voltage supply	2-3 V
Threshold	3-200 mV
Input impedance	100 Ω
Bandwidth	500 MHz
Power consuption	10 mW/ch
Rise time $\delta(t)$ output	300 ps
Radiation hardness	10 kGy, 10^{13} n/cm^2
Minimum duration input pulse	0.5 ns
Double-pulse separation	1 ns
Channels per chip	4

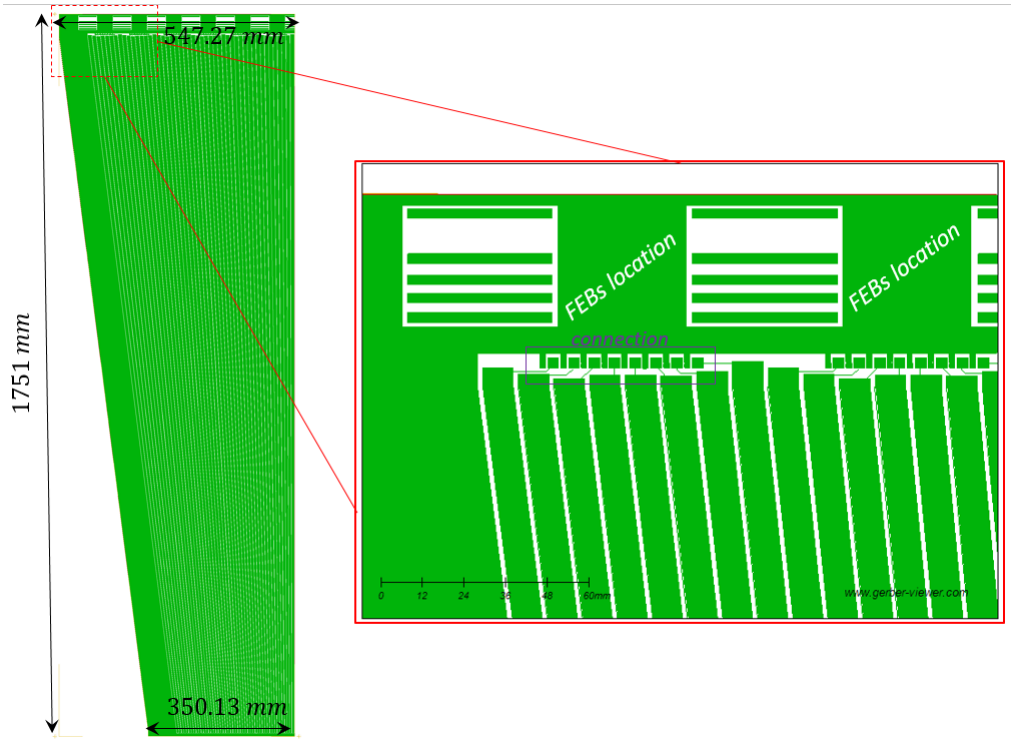

Figure 7.3: PCB layout of the new strip panels and new connection with the Front-End.

prototype with taking into account the active area dimensions and HV pad location. The strip panel is a two-layer structure: a copper layer 35-50 μm thick applied on a fiberglass base layer 1 mm thick, which is generally employed in the printed circuit board construction. The copper strips have a trapezoidal shape in order to cope with the RPC gas gap's own shape. The minimum of the strip pitch is of 5.77 mm for short base of the PCB panel and the maximum is of 10.21 mm for the large base, respectively. Every signal strip

has a Back-End (80 Ω) and a Front-End (50 Ω) resistor of different value. The Front-End electronics and the panel strip are designed to perfectly match, and their integration is done in an innovative way, by soldering the FEB directly on the strip readout panel and not just near it. Fig. 7.4 shows the new strip panel (a) and the integration of the FEB with strip panel (b).

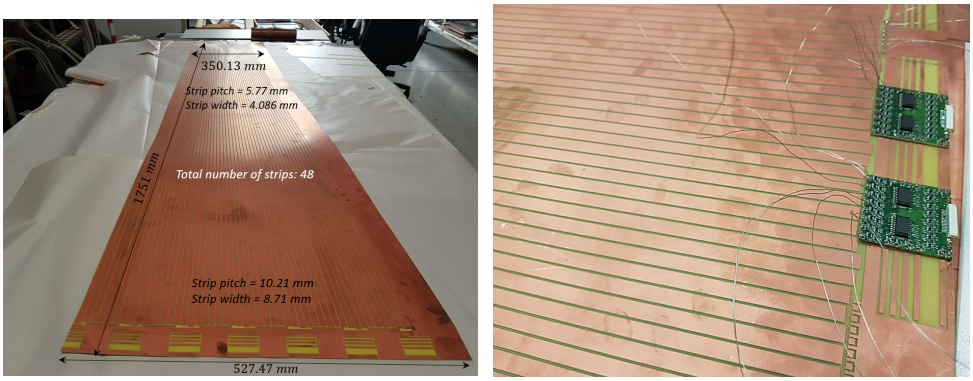

(a) (b)

Figure 7.4: Picture of the new strip panel (a) and the integration of the FEB with strip panel (a).

7.2 Prototype Technical Design with INFN Rome Front-End Electronics

In order to realize the project of a second iRPC RE4/1 detector prototype with INFN Rome electronics, a detailed analysis of the future chamber design has been carried out taking into account the experience obtained during the first iRPC prototypes assembly. The prototype design will use two identical spare KODEL gas gaps placed one on top of the other with common radially oriented readout strips in the middle. Only half of the strips have been instrumented in the second iRPC RE4/1 detector prototype as in the first version of RE4/1 chamber. In order to reduce the cost of the materials and components needed to assemble the second iRPC RE4/1 detector prototype, it has been decided to re-use the components of the spare RE 4/3 RPC chamber, stored at the CERN CMS-RPC QA/QC facility. As was already reported in Chapter 5, the RE4/3 chamber has a trapezoidal shape with the following overall dimensions: larger base 1336 mm, the lower base 992 mm and height 1967 mm. Its dimensions are large enough to allow re-use of all the mechanical components in order to construct a new detector casing for the real-size iRPC RE3/1 and RE4/1 detector prototypes and to avoid the unnecessary costs.

Before to start the real assembly of the second real-size RE4/1 detector prototypes with INFN Rome electronics, a mechanical simulation has been performed by using the AutoCAD and SolidWorks engineering software. This

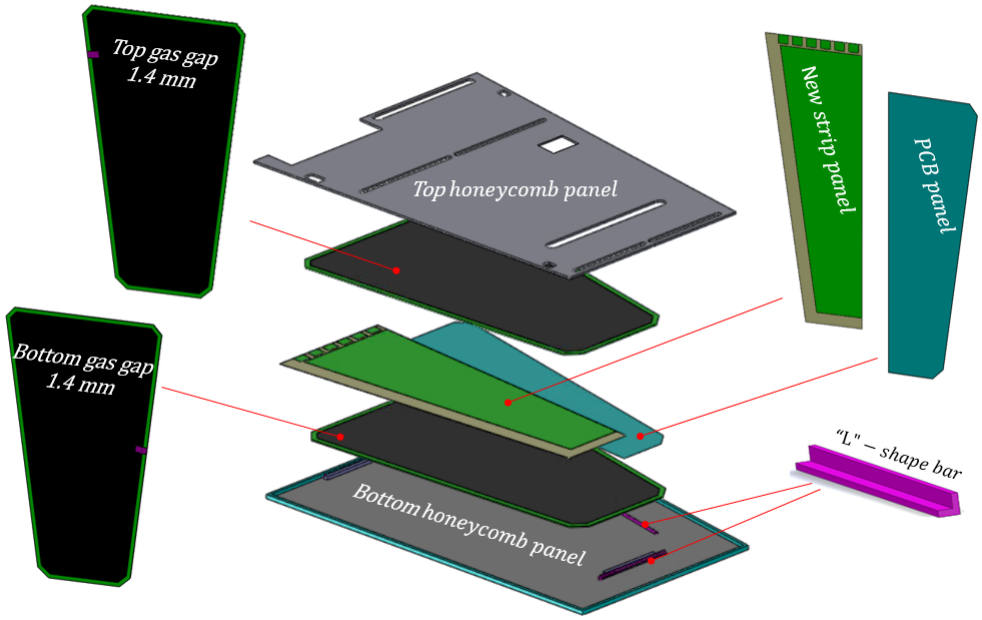

Figure 7.5: Exploded view and final design of the second type of the RE4/1 detector prototype.

type of activity helped to design the readout strip panel for the new detector prototype and determine its dimensions. Additional, It allowed to reveal any possible problematic aspects of the detector assembly such as the components fixation and their alignment inside a large RE4/3 mechanic box and prepare needed materials and components in order to solve them in the early stages of the prototypes assembling. The 3D model of the second type of the RE4/1 detector prototypes has been simulated in scale 1:1 (see the Fig. 7.5).

Proposed for the second RE4/1 detector prototype, the pick-up signal from the strip panel will be read out directly from one side of strips. In order to reduce the noise-induced by external sources, the FEBs will be soldered directly on the strip panel. Taking into account this constructive feature of the new readout strip panels, the existing RE4/3 top honeycomb panels have been appropriately modified to connect the strip panel to the INFN Rome electronics. In addition, during the construction of the detector prototype, the readout strip panel will be used to instrumentate only half of the detector active area. This will allow reducing construction costs. In order to avoid possible deformations and/or bending of the gap gaps, the non-instrumented half region will be compensated by inserting a PCB panel of the same size as the readout strip panel.

7.3 Prototype Construction and Quality Control at the INFN Rome Tor Vergata Facility

At the end of August 2018, CMS Collaboration decided to assemble the second version of the iRPC RE4/1 detector prototype with the new INFN Rome front-end electronics. In order to validate this chamber and the electronics on the last Test Beam session at CERN in October 2018 before the second Long Shutdown (LS2), the prototype assembly has been started at the INFN Tor Vergata Laboratories in September 2018. As a member of the CMS Muon group, the doctorate candidate takes part in all activities on testing the detecting elements, assembling of the new iRPC RE4/1 chambers at the INFN Tor Vergata Laboratories and the subsequent evaluation on their working parameters before the prototype installation on the CERN GIF++ facility. A detailed description on all production steps is given below.

7.3.1 Overview of the INFN Rome Tor Vergata Laboratories

The INFN Rome Tor Vergata facility includes a laboratory where the ATLAS RPC chambers on the cosmic stand have been qualified in the period from 2004 to 2006 before the final installation in the Muon Spectrometer of the ATLAS experiments [85], [86]. The INFN laboratory is equipped with high voltage power system, gas systems with standard ATLAS RPC gas mixture: $C_2H_2F_4$ / $iso-C_4H_{10}$ / SF_6 (95.2/4.5/0.3), large assembly tables and tooling for gas gap quality control, such as gas leak and high voltage test. There is also enough quantity of scintillators and photomultiplier in order to perform a preliminary detection efficiency studies of the chambers.

7.3.2 Pre-assembly and Quality Control of the Detector Components

At the beginning of September 2018, by using the external transport logistic service, the CMS Collaboration shipped from CERN CMS-RPC QA/QC facility to INFN Rome Tor Vergata Laboratories the needed materials, such as the spare KODEL gas gaps with ID numbers of KODEL-CMS-PCB-DG14-B02 and KODEL-CMS-COA-DG14-T02, gas pipes, "Jupiter" high voltage connectors and the detector casing.In order to avoid any possible damages during the long transportation, a wooden box has been specially designed to host safely all the detector components. The detector components have been vertically stored inside the shipping box and clamped by using partially pre-stressed bars and protected by using foam panels, as shown in Fig. 7.6. All gas input and output pipes of the gas gaps were opened in case of sudden change of the atmo-

spheric pressure during the transportation and protected by installing special anti-dust membrane on the inlet and outlet gas plugs.

Figure 7.6: Pictures of the specially designed wooden box for the detector components transportation.

When all detector components for new iRPC RE4/1 detector prototype successfully arrived to INFN Rome Tor Vergata Laboratory, they have been immediately verified for defects and tested. Visual inspection of the main detector components has been performed to ensure the integrity and the quality of the gas gaps, readout strips panel, gas inlets and outlets, etc. The results of the optical inspections and tests on the main detector components are presented below:

Mechanical Test of the Readout Strip Panel. The readout strip panels have been produced by Eltos S.p.A company and they have been directly shipped to INFN Rome Tor Vergata Laboratory. An initial inspection has been performed in order to check the planarity of the panel and to identify possible macroscopic scratches and defects on the readout strips and adapters for signal readout. During the visual inspection, no macroscopic damage was found that could compromise the integrity and the quality of the detector prototype.

Mechanical Test of the Gas Gaps. As in the case of readout strip panel, an accurate optical inspection has been performed in order to identify possible cracks, mechanical unconformities, damages and defects and/or any type of bending/bulges on the gas gaps surface, improper graphite/pet coating, broken nozzles or excess of glue, etc., that might have been incurred during a large distance transportation of the gas gaps. During the visual inspection a broken

nozzle of the gas inlet/outlet has been found in the bottom gas gap. Due to the limited quantity of the gas gaps available, the RPC Collaboration has decided to repair the broken nozzle by using the epoxy resin. In Fig. 7.7 the pictures of the problematic gas inlet/outlet of bottom gas gaps (a) and view of the gas inlet/outlet after repair procedure (b) are given.

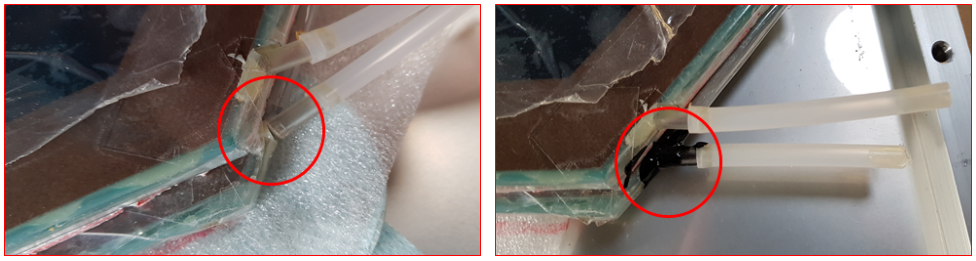

Figure 7.7: Pictures of the problematic gas nozzle of the bottom gap (a) and view of this gas nozzle after repair procedure (b).

After the repair procedure, a gas leak test has been performed in order to identify possible gas leak by using a different version of the pressure drop setup that involves a simple U-shape tube which was earlier reported in Chapter 6. Both KODEL gas gaps have been passed the gas leak test by demonstrating a perfect gas tightness.

Electrical Test of the Gas Gaps. After large distance transportation of the gas gaps, a detailed electrical test has been performed in order to determine the Current-Voltage curve of an iRPC and to identify possible damages and defects in the high voltage circuit.

Each gas gap has been connected to the gas system and flushed with the standard dry CMS/ATLAS RPC gas mixture, $C_2H_2F_4$ / $iso-C_4H_{10}$ / SF_6 (95.2/4.5/0.3) at a flow rate of 1.5 L/hr for 6 hours in order to clean the gas gap and pipeline after a long-term of a non-operation period and before undergoing the dark current test. During 6 hours a single gas gap with 1.77 L volume has been flushed 4 times. Due to the limited amount of the gas mixture available in the INFN Rome Tor Vergata Laboratories and for safety reasons, it was not possible to use continuously the gas system 24 hr/day. Current-Voltage characterization of the iRPC gas gaps was carried out by applying a high and opposite polarity voltage gradually to either of the electrodes by a D.C. power supply system through HV pad on to the graphite coating. The current measure includes the leakage or dark current that exists even without the application of a bias. After application of the highest voltage of 6kV (on either electrode), the RPC was kept at that particular voltage for at least 30 minutes to enable the electrode parameters to be stabilized.

During the electrical test, a gas gap showed a very low abnormal current value (at 6 kV and 7 kV $I_{mon} = 0.1$ μA). The high voltage scan on the top gas gap has been immediately stopped in order to investigate and understand the problem. During the visual inspection of the top gas gap, it has been noticed

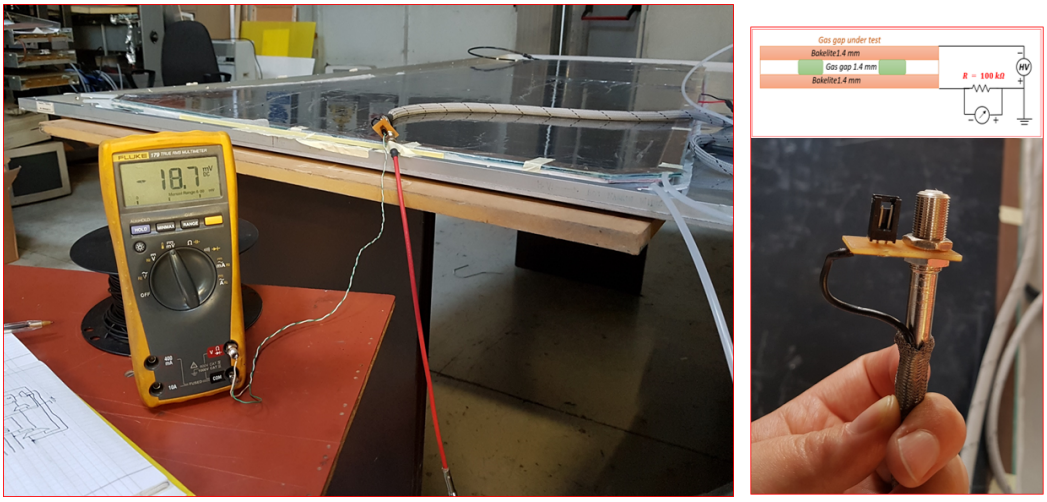

(a) (b)

Figure 7.8: Picture of the experimental setup during the electrical test of gas gaps by using the multimeter (a) and electrical scheme of the electrical test (b).

that the "Jupiter" HV male connector was not properly connected with the HV female connector of the power supply cable. The central pin of the "Jupiter" HV male connector was incorrectly mounted inside the connector itself and, therefore, the electrical contact between the HV male connector of the top gas gap and the HV female connector of the power supply cable was completely absent. After identifying the problem, the "Jupiter" HV male connector was changed. In order to measure the leakage current through the gas gap as a function of the applied high voltage, a 100 kΩ resistor (R) has been connected in series with the return line of the high voltage power supply. The voltage drop (ΔV) across the resistor (R) has been measured with a four and half digit multimeter as a function of the applied voltage. The leakage current through the gas gap has been obtained from Ohm's low ($\Delta V/R$). The electrical scheme connection and picture of the experimental setup are presented in Fig. 7.8. Simultaneously, the actual voltage V_{mon} and current I_{mon} provided by the power supply has been recorded. The Current-Voltage characteristics of the gas gap, which represent the relationship between the leakage current through gas gap and the corresponding high voltage across it, has been estimated both by monitoring the leakage current through digital multimeter and through the high voltage power supply.

During the electrical test, all temperature and humidity values in the INFN Rome Tor Vergata Laboratory have been recorded in order correct the applied high voltage values ($HV_{app.}$) and obtain the effective voltage ($HV_{eff.}$). The correction was performed according to the formula (6.2).

Fig. 7.9 shows a common feature of the Current-Voltage characteristics hthat is two distinctly different slopes as it has been discribed in Section 6.2.2.2.

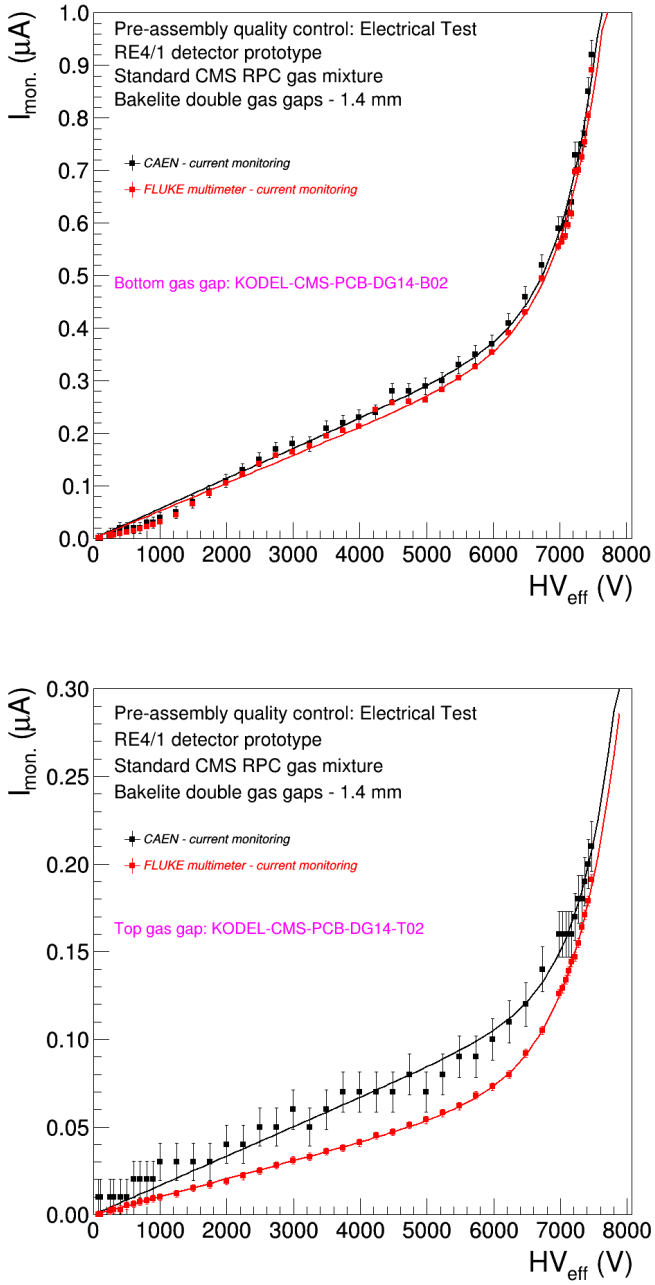

Figure 7.9: I-V curves of two KODEL gas gaps. The applied high voltage values have been normalized by using the PT correction formula explained in Section 6.1.2.2.

The reason is explained by the equivalent circuit of RPC (Fig. 7.10) [92]: the RPC gas gap is represented by a parallel combination of spacer (Ohmic) resistance and gas ionisation volume of the gap (presented by a Zener diode). At lower applied voltages, the primary ionisations in the gas gap do not lead to

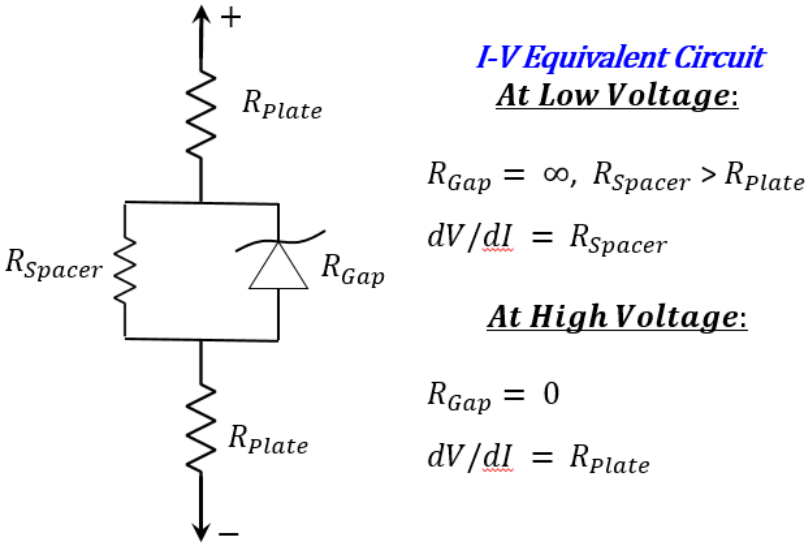

Figure 7.10: Equivalent circuit of an RPC [92].

the development of avalanches. Therefore, the gas gap offers infinite resistance and the gas gap behaves as an insulator in the lower range of applied voltage: the slope over this HV range scales as the conductance of the polycarbonate spacers. Starting from the chamber's turn-on point, the slope of the curve changes drastically as the ionization volume almost dominates. The current flowing through the chamber, in this case, is determined by the bakelite plate resistance i.e. at the higher range of voltage, the gas behaves as a conducting medium due to the formation of streamers. The current versus voltage curves have been interpolated by the following formula:

$$I = \frac{V}{R_{Bulk}} + I_0 e^{\frac{V}{V_0}},$$

where R_{Bulk} is the ohmic contribution, I_0 is the average primary cluster charge per unit time and V_0 depends on the effective Townsend's coefficient of the gas mixture. Gas gaps with high dark currents (greater than about 10 $\mu A/m^2$ at the RPC working point) are rejected and substituted. When the two KODEL gas gaps have been fully validated, these are used to start the detector prototype construction.

7.3.3 Detector Prototype Assembly Procedures

In Fig. 7.11 the several assembly steps of iRPC RE4/1 detector prototype at the INFN Rome Tor Vergata Laboratory are shown. The prototype assembly was started with the preparation of aluminum casing which was covered by using a Mylar layer in order to isolate all the conductive parts. Next, a bottom copper sheet, which acts as a part of Faraday cage, is laid onto the frame and cleaned carefully with Isopropyl alcohol ($(CH_3)_2CHOH$).

Figure 7.11: Pictures of the several assembly steps of the iRPC RE4/1 detector prototype at the INFN Rome Tor Vergata Laboratory: 1 - preparation of detector casing by covering it with a Maylar layer and the bottom copper sheet for Faraday cage; 2 - installation of bottom gas gap and readout strip panel with connected INFN Rome electronics; 3 - placing of top gas gap; 4 - closing of Faraday cage by using the copper tapes.

When the detector casing and bottom copper sheet were ready, the preparation of the bottom gap begins. The bottom gas gap is carefully cleaned and put inside with the HV cable and gas pipes at the bottom. Then the actual readout panel with 48 strips and fake PCB have been laid onto it. When the readout panel is in place, the procedures of the FEBs integration with the readout strip panel and Faraday cage begin. It is a very important step of the prototype assembly, because in order to have the possibility of operating the detector at the lower threshold value, the chamber structure, as a Faraday cage, requires a very careful optimization in order to minimize the noise induced by external sources. Three INFN Front-end electronics read a total of 24 strips from one side. Then the FEB positions on the readout strip panel were marked to make the holes for the ground wires. Wires will be soldered on the bottom copper sheet and passed through made holes and connected to the FEBs and at the same time the electronics connected to the strip. In order to avoid the reflection of the signal, one end of the strips has been terminated with 80 Ohm and he other end matched with 50 Ohm while the unused strips have been terminated by using 80 Ohm at both sides. In Fig. 7.12 the main steps of INFN Rome FEBs integration with components of the iRPC RE4/1 detector prototype are presented. Then the foam spacers, filling in the empty space between the bottom gap and actual and fake strip panel, have been installed.

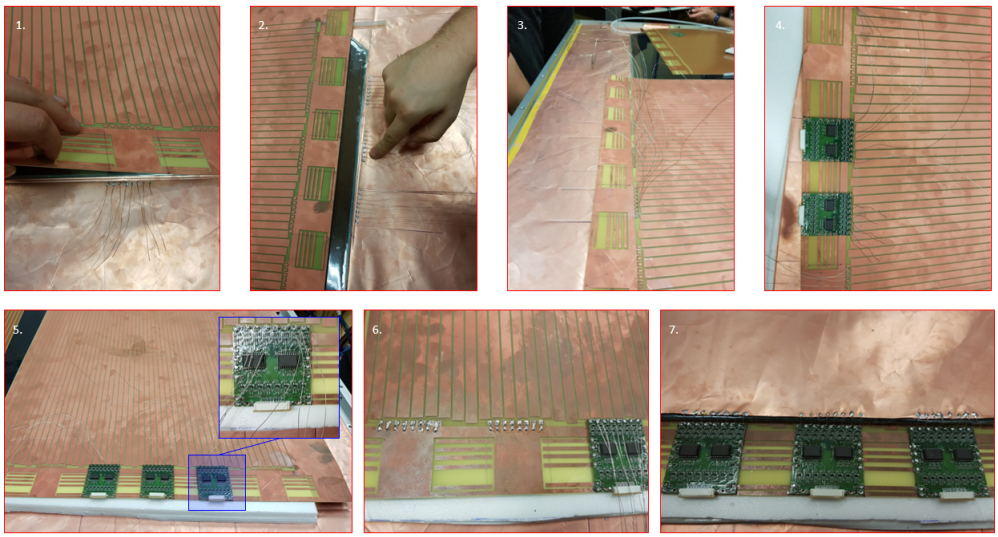

Figure 7.12: Pictures of the main steps of INFN Rome FEBs integration with components of the iRPC RE4/1 detector prototype: 1 - placing of strip panel with the marking of FEBs position, making of holes for the ground wires soldered directly to the bottom copper sheet; 2 - soldering of 24 ground wires for three FEBs; 3 - 24 of ground wires passed through holes made into strip panel; 4 and 5 - installation and grounding FEBs on the readout strip panel; 6 - closing of unused strips in both side of panel by using the 80 Ohm resistors in order to prevent noise interferences; 7 - final step of FEBs integration with prototype structures by soldering of ground wires with the top copper sheet of Faraday cage.

Top gap has been cleaned and put onto the readout strips with the HV connection on top. Gas pipes are installed and closing part of the copper sheet, which had had an identical shape as the top gas gap, is put to cover the top gaps. The copper tape is glued around the perimeter cassette in order to connect the readout strip panel with top and bottom copper sheets in such a way that sheets and strip panel form the Faraday cage. Before closing the chamber by using the top honeycomb, all FEBs have been checked for the existence of a short circuit. The last step consisted in directly soldering the five wires for low voltage power supply to the FEB. Each wire distributes the voltage to the single channel corresponding to the PullUp system, LVDS transmitters, amplifiers, discriminators and threshold channels, which can be regulated.

7.3.4 Post-assembly and Quality Control of the Detector Prototype

Once the chamber is closed, leak and high voltage integrity tests have been done. The gas leak test takes place again in order to check the gap gas inlets

were correctly connected to the chamber service panel, while the HV test is repeated to be sure the electrodes preserved the integrity after mechanical manipulations during the assembly. The procedures are the same used during the pre-assembling quality control stage. In Fig. 7.13 results of the post-assembly high voltage integrity test for the bottom and top gas gaps installed inside the new iRPC RE4/1 detector prototype are shown.

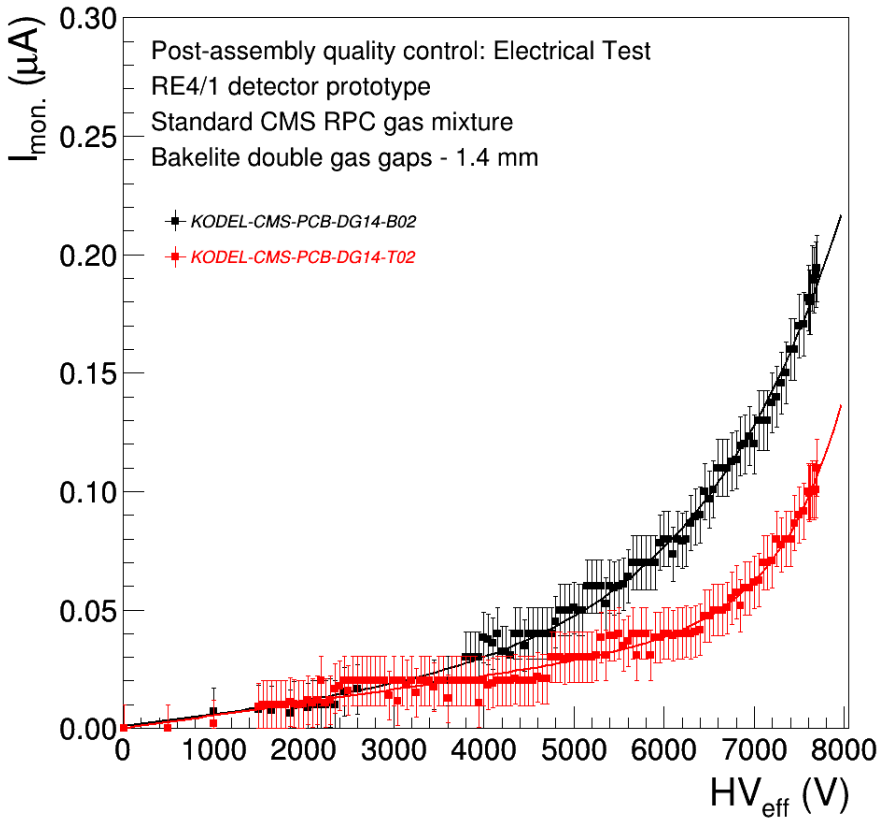

Figure 7.13: Results of the post-assembly high voltage integrity test for the bottom and top gas gaps installed in the new iRPC RE4/1 detector prototype.

7.4 Preliminary Detection Efficiency Study in the Cosmic Ray Telescope

In order to ensure proper operation of the new iRPC RE4/1 detector prototype with new INFN Front-end electronics, a preliminary detection efficiency study has been performed at the INFN Rome Tor Vergata Laboratory by using the standard cosmic ray telescope.

Experimental setup. The chambers were positioned within a scintillator

telescope consisting of a stack of two scintillators (S1 and S2) with same dimensions. The overlapping area of the telescope was approximately 10 x 100 cm^2, which covered less than half of the active area (in a total around 10 pickup readout strips) of the detector, and was used to establish when a cosmic ray had passed through it.

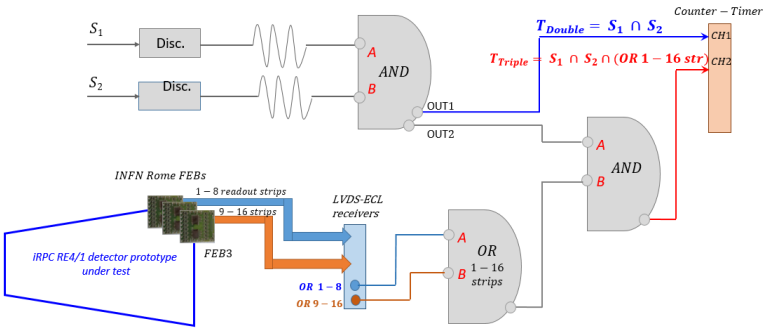

Figure 7.14: Schematic representation of the cosmic ray trigger logic

The scintillator signals were converted to NIM level logic signals by feeding them into discriminator modules operating with a threshold values of -35.1 mV for S1 and -42.6 mV for S2, respectively, and producing a logic pulse of 50 ns in width. After that, the discriminated signals were sent to the coincidence module in order to obtained $T_{Double} = S1 \cap S2$ logic. The RPC signals were picked up by 16 strips and read out by two 8-channel INFN Rome front-end boards. These boards were connected to LVDS-ECL receivers which provided the ORs of two sets of 8 channels. Two ORs signals have been sent to the coincidence submodule in order to create the one common ORs signal. The final trigger consists of $T_{Double} = S1 \cap S2 \cap (ORs\ of\ 16\ channels)$. The T_{Double} and T_{Triple} signals have been sent to a counter. The cosmic ray muon trigger logic and final experimental setup are shown in Fig. 7.14 and Fig. 7.15, respectively.

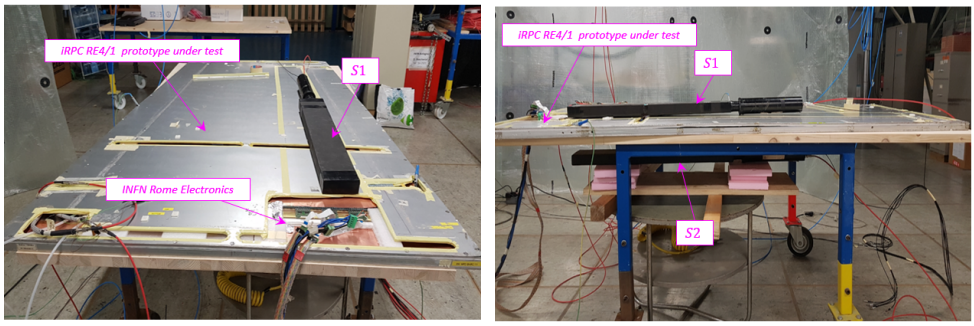

Figure 7.15: Pictures of the cosmic ray trigger experimental set-up: front side view (a) and right side view (b).

Preliminary results. The overall detection efficiency was taken to be the ratio of the number of the cosmic rays detected by the chamber in coincidence

with the scintillator telescope to those detected by the telescope alone, i.e. the final efficiency has been obtained by using the following formula:

$$E = \frac{N_{Triple}}{N_{Double}},$$

where N_{Triple} corresponds to the number of muons which were detected by the iRPC detector prototype and two scintillators and N_{Double} is the number of events which were detected by scintillators only. The detection efficiency of the RPC detectors strongly depends not only on the applied high voltage but on the environment. By using the environmental control station at the INFN Rome Tor Vergata Laboratory the temperature and pressure were determined. Due to temperature and pressure variations, the applied high voltage (HV_{app}) values have been corrected to obtain the effective voltage (HV_{eff}) by using the PT-correction formula which is described in Section 6.4.2.

The efficiency was measured at a fixed electronic threshold (V_{thr} = 1.816 V) and electronics amplification factor (V_{amp} = 1.39 V) values from 6.6 kV to 7.3 kV with a step of 100 V. For each high voltage point, the data have been collected during 30 minutes of measurement in order to reduce the statistical error. It is worth noting that the electronics threshold and amplification factor have been chosen in order to have the final electronics threshold in the range of 10-15 fC. Fig. 7.16 shows the variation of efficiency with applied high voltages at the fixed electronics threshold and amplification factor values.

The study of efficiency dependence on high voltage is fundamental to determine the working point of the detector. Indeed to operate in stable detector conditions the operating high voltage is chosen at the plateau value extracted from this kind of plot. By using the sigmoidal curve, which is described in Section 6.4.2 the working point value can be easily determinated.

Preliminary results show that the new iRPC RE4/1 detector prototype with new INFN Rome electronics responds well: at the electronics threshold value of around 10 -15 fC, the maximum detection efficiency is 99.98%, the working point value is 7050±16.62 V and $\varepsilon(WP)$ is 99.1 ±0.24 %. This result is the reference result which should be checked on the Test Beam at CERN GIF++ facility.

7.5 Performence Studies with Muon Particles Beam at CERN GIF++ Facility

The second full-size iRPC RE4/1 detector prototype has been tested during the last Test Beam period in October 2018. The prototype was exposed to high irradiation flux using the CERN Gamma Irradiation Facility (GIF++) and the 100 GeV muon beam from H4 beamline. I have studied the same number of chamber parameters of second iRPC RE4/1 detector prototype, such as: detection efficiency, cluster size, and rate capability. Results comparison of two iRPC detector prototypes will be presented in this Chapter.

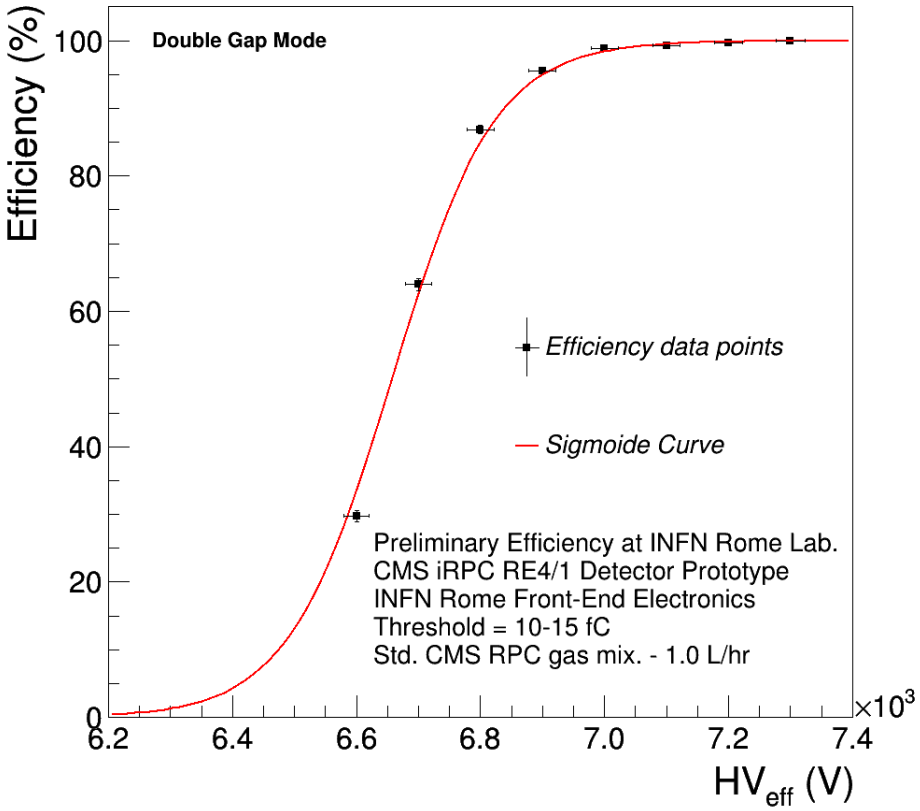

Figure 7.16: Preliminary result of Cosmic Rays detection efficiency for the double gap operation of the iRPC RE4/1 detector prototype with INFN Rome electronics of as a function of the effective high voltage. The measurements were performed at a fixed electronics threshold (V_{thr} = 1.816 V) and electronics amplification factor (V_{amp} = 1.39 V) values, which correspond the overall electronics threshold value around 10-15 fC.

7.5.1 Experimental Setup for the Test Beam Period

One week before the beginning of the last Test Beam period, the new iRPC RE4/1 detector prototype has been shipped from the INFN Rome Tor Vergata Laboratory to the preparation zone of the CERN GIF++ facility by using the external transport logistic service. Upon arrival at CERN, the following activities started:

- visual inspection in order to identify any possible cracks or damage of the iRPC RE4/1 detector prototype after long-distance transportation;
- leak test in order to identify any problem with the gas gaps integrity inside the detector prototype;
- electrical test of gas gaps in order to identify possible damages and

defects in the high voltage circuit and dark current;

- preparation of the trolley-T3 for the detector prototype installation;
- scintillators preparation and NIM logic for trigger set-up inside the GIF++ bunker.

The new iRPC RE4/1 detector prototype with new INFN Rome FEBs has been mounted on the existing trolley-T3 in a vertical position so that the beam line and the chambers irradiation zone were located in the middle of the strip panel. In order to secure the large-size prototype on the trolley - T3, the aluminum bosch-profiles and the nylon ties have been used. In order to avoid any possible FEBs damage during the manipulation with the prototype, the electronics have been covered with 5 mm thick foam plate. Then second iRPC RE4/1 detector prototype has been successfully installed in the GIF++ upstream area at about $\sim 2.63\ m$ from the $^{1}37$Cs source. Such a distance allows a gamma irradiation of the detectors corresponding to the expected CMS gamma background conditions after HL-LHC upgrade. In front of the new iRPC RE4/1 detector, other experimental setups were installed. The picture of the iRPC experimental setup installed in the GIF++ irradiation area is shown in Fig. 7.24. During the Test Beam, the whole setup was a versatile stand which allowed an easy movement of the experimental system in the required positions with respect to the irradiator and beamline.

High and Low Voltage Systems. The gaps inside the RE4/1 detector prototype with new INFN Rome electronics have been powered thanks to a CAEN SY1527 mainframe and a A1526N module (negative polarity) installed outside the irradiation area in the opposite rack zone, while the low voltage power supply modules have been placed in the GIF++ security pocket within the GIF++ bunker.

The GIF++ security pocket is a recess in the wall of the hopper, fenced from gamma irradiation cone by using a lead wall with 10 cm thickness. In this place, the effect of gamma radiation is minimized in order to install any kind of the electronics, power supplies and portable computer for the data acquisition system needed to support the tested chambers. The GIF++ security pocket is shown in Fig. 7.18.

The low voltage power system for the INFN Rome electronics has been based on the KONSTANTER LSP (Laboratory and System Power Supply) developed by the GROSSEN METRAWATT - CAMILLE BAUER company [93] (see Fig. 7.19). This LV supply module is compact, linear controlled with three independent output device. Control mode indicators display a current operating status. The analog interface provides for a monitor, auxiliary power and signal outputs, as well as status display and setpoint inputs. In order to supply five independent electronics channels two low voltage module power supply have been used.

Gas system. During the Test Beam period, the new detector prototype used the standard CMS-RPC gas mixture supplied from the first floor of the gas

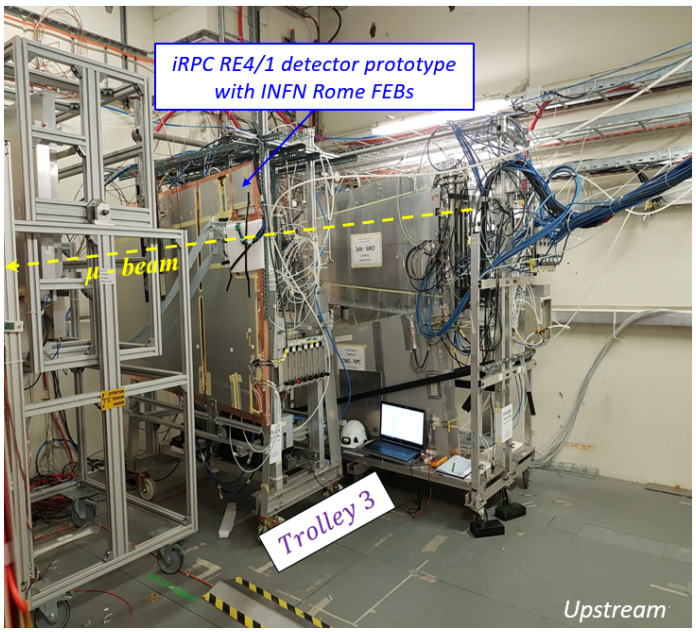

(a)

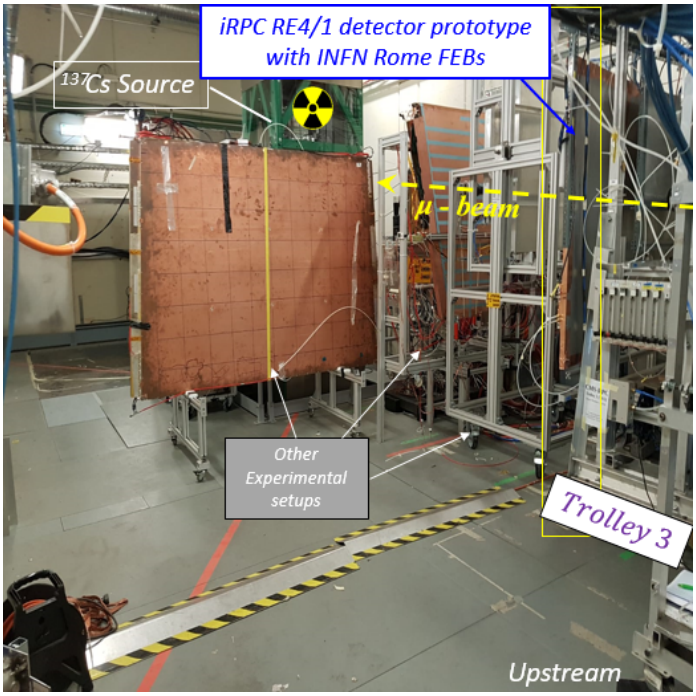

(b)

Figure 7.17: Pictures of the iRPC RE4/1 experimental setup with INFN Rome Front-end electronics installed in the GIF++ irradiation area: front side view (a) and back side view (b).

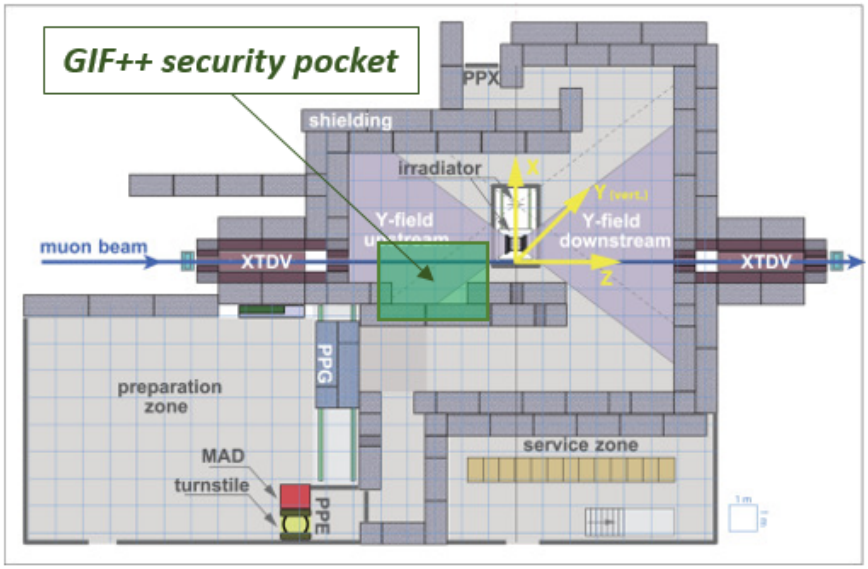

Figure 7.18: Scheme of the GIF++ bunker: the GIF++ security pocket where was installed the low voltage power supply marked green box.

Figure 7.19: Picture of the low voltage power supply for INFN Rome electronics.

service area at the GIF++ facility. More details about the gas system at the GIF++ facility you can find in Section 6.5.3.2.

Trigger setup. Trigger setup has been provided by two sets of scintillators as shown in Fig. 7.20. The two scintillator counters (S_{Up} and S_{Down}), which are a part of the GIF++ bunker are located at the front and rear bunker walls, at the beam's entry and exit points. The upstream scintillator S_{Up} is placed at the distance of $\sim$ 11 meters from the source and the downstream scintillator

S_{Down} – at $\sim$ 7 meters. In the upstream zone, the scintillator has a surface of 40 cm $\times$ 40 cm, while in the upstream zone the scintillator active area is equal to 35 cm $\times$ 80 cm.

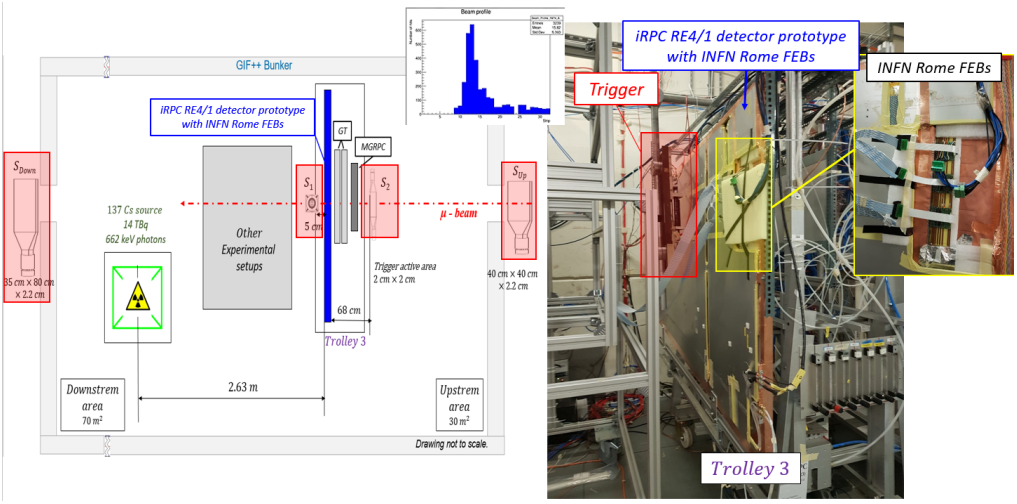

Figure 7.20: Scheme of the Trigger setup used during the last Test Beam in October 2018: the two sets of scintillators are marked by the red box; the INFN Rome electronics is marked by the yellow box; the beam muon particle profile is presented in the top middle side of the picture.

In order to more accurately highlight the particles beam profile in the iRPC detector prototype, a set of additional scintillators (S_1 - bottom and S_2 - top) have been mounted close to the chamber ($\sim 8cm$) in perpendicular orientations to each other. S_1 and S_2 scintillators were identical and had a cylindrical shape. Both ends of each scintillator were coupled to photomultipliers supplied by a CAEN HV N470 module which were installed in the GIF++ electronics service area. Both scintillators have been fixed on the movable support in the vertical position. During the test beam, trigger active area was of 25 cm^2. By using the GIF++ security pocket, the NIM and CAMAC electronics have been directly installed at the irradiation zone in order to develop the trigger logic.

7.5.2 Data Acquisition System

TDCs and computers were used for data acquisition and preliminary offline analysis to fill the Detector Control Software (DCS) webpage, referred to as WebDCSportable software, with Data Quality Monitoring (DQM) histograms. The iRPC RE4/1 detector prototype read-out was realized by using a V1190A 128-Channel Multihit TDC communicating with the DAQ computer thanks to a V1718 VME-USB 2.0 Bridge installed into VME main crate, manufactured by CAEN. Moreover, a constant monitoring of all the environmental parameters, in different points of the bunker area, the gas parameters, temperature and pressure, and the voltages and currents delivered by the power supplies is

performed and displayed on the homepage of the WebDCSportable software. All data acquired through the use of the TDCs, i.e. all the muon or gamma data are recorded and saved by the WEBDCSportable software. Principle scheme of the Data Acquisition System is presented in Fig. 7.21.

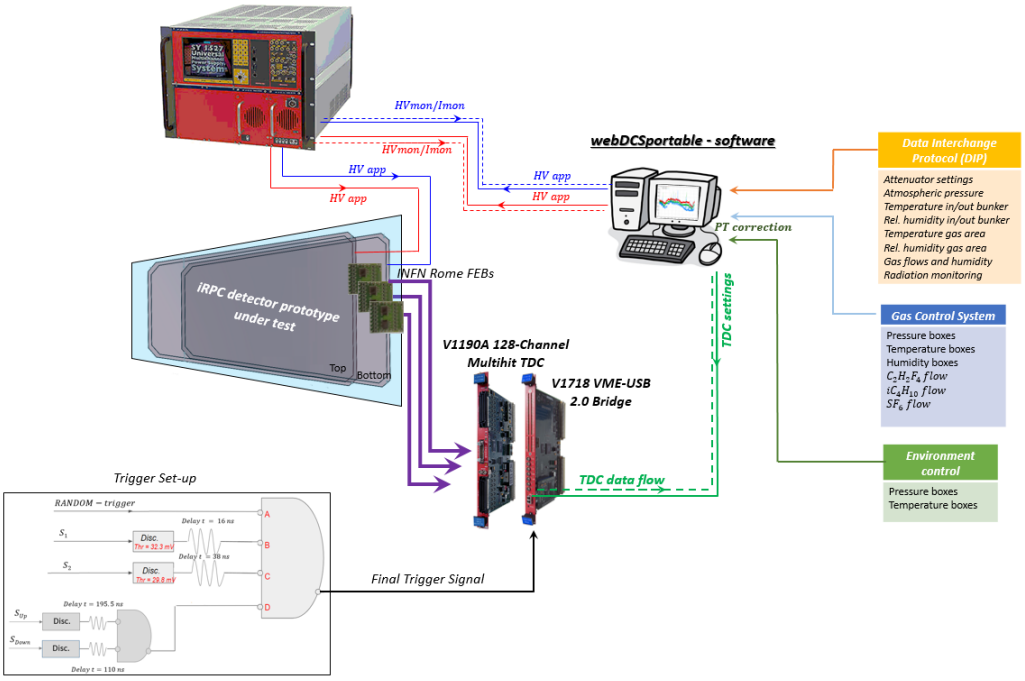

Figure 7.21: Principle scheme of the Data Acquisition System.

As mentioned above, each readout strip is connected to a fast V1190A 128-Channel Multihit TDC module writing continuously in a buffer memory. The coincidence of the six Photo-Multipliers placed before and after the chamber, allows to detect the passage of charged particles and trigger the recording of a buffer V1190A TDC time window. The time window of the TDC depends on the type of run: efficiency scan or rate scan. The knowledge of the run type is important to set the width of the acquisition window to be used for the rate calculation and for muon detection. Indeed, the peak that appears in the time distribution for the detector is then fitted to extract the most probable time window in which the analysis software tool should look for muon hits. The data outside of this time window is then used to evaluate the noise or gamma background the detector was subjected to during the data taking. Computing the position of the peak is done calling the function *SetMuonWindow()* defined in file *src/RPCHit.cc* that loops a first time on the data. The location of the highest bin is determined by using *TH1::GetMaximumBin()* and is used to define a window in which a Gaussian fit will be applied to compute the peak width (σ). This window is defined by formulas around the central bin:

$$T_{peak}(ns) = bin \times widthbin(ns) \tag{7.1}$$

$$[T_{low}; T_{high}] = [T_{peak} - 3\sigma; T_{peak} + 3\sigma] \tag{7.2}$$

where $[T_{peak} - 3\sigma; T_{peak} + 3\sigma]$ is final muon window in order to estimate the detection efficiency for iRPC detector prototype. The example of time distribution of the hits for 3000 events is presented in Fig. 7.22.

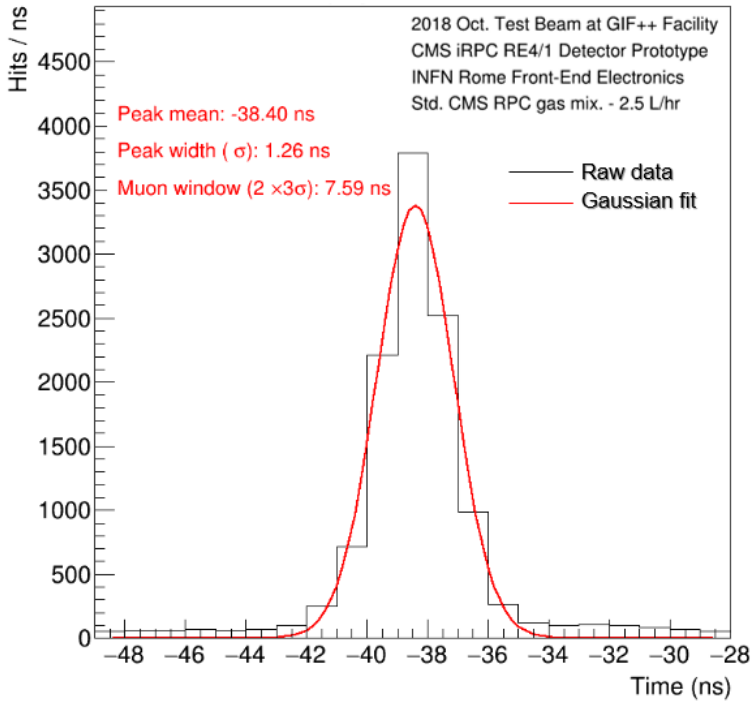

Figure 7.22: Example of time distribution of the hits for 3000 events. Here, the highest bin is observed around $t_{peak} = 215.26$ ns and peak width (σ) is calculated.

Thus, the detection efficiency in the signal zone is calculated as the number of triggers having at least one hit in the muon time window with taking into account the probability that a spurious/fake hit appears in the chamber and in the spatial area affected by the beam:

$$\varepsilon_{\mu} = \frac{(N_{hit,[T_{low};T_{high}]} - N_{fake,[T_{low}-(2\times3\sigma);T_{high}+(2\times3\sigma)]})}{N_{trigger} - N_{fake,[T_{low}-(2\times3\sigma);T_{high}+(2\times3\sigma)]}} \tag{7.3}$$

where $N_{hit,[T_{low};T_{high}]}$ is the total number of observed hits in the $[T_{peak}-3\sigma; T_{peak}+3\sigma]$ muon time window, $N_{fake,[T_{low}-(2\times3\sigma);T_{high}+(2\times3\sigma)]}$ is the number of spurious

hits in outside of the muon time window, in our case is $[T_{peak} - 3\sigma - (2 \times 3\sigma); T_{peak} + 3\sigma + (2 \times 3\sigma)]$ and $N_{trigger}$ is total number of trigger.

Before the Gaussian fit is performed, the gamma or noise rate is evaluated by using the data outside of the muon time window. Excluding the first 100 ns, the gamma or noise rate is defined by following Formula:

$$\triangle T_{noise}(ns) = 600 - T_{high} + T_{low} - 100 \tag{7.4}$$

$$Rate = \frac{\sum_{i=1}^{N_{trigger}} N_i^{hit}}{N_{trigger} \times S \times \triangle T_{noise}} \tag{7.5}$$

where $\sum_{i=1}^{N_{trigger}} N_i^{hit}$ is the total number of gamma hits in the $\triangle T_{noise}$ time window, S is the active area of the detector prototype, in our case, determined by the total active area of the readout strip panel.

7.5.3 Characterization of the iRPC RE4/1 Prototype with the INFN Rome Front-End Electronics

In this Section, we will finally present the results of the analysis of the data taken during the Test Beam at CERN GIF++ facility in October 2018, in particular from 25^{th} October to 1^{st} November. Experimental studies are grouped into several areas of interest: rates, current, charge, efficiency, rate capability, cluster size, cluster multiplicity and those ones related to the working point of the improved RPC detector prototype with INFN Rome electronics.

7.5.3.1 Noise evoluation

The threshold of electronics and the level of noise in the detector arefundamental characteristics. Before the start of the Test Beam campaign, it is important to performse measurement without source and muon beam in order to est a noiimate the intrinsic noise of the new iRPC RE4/1 detector, which is arising mainly due to the electronics itself. Moreover, this measurement helps to check the proper electronics threshold value and grounding of the prototype. In addition, a noise scan allows to identify faulty electronics readout channels and give the possibility to repair them in the early stage of the Test Beam campaign.

The noise measurements are performed only for 6 high voltage points in the range 6900 V - 7400 V, which correspond to the high voltage values around the expected knee and efficiency plateau. In order to precisely estimate the noise,

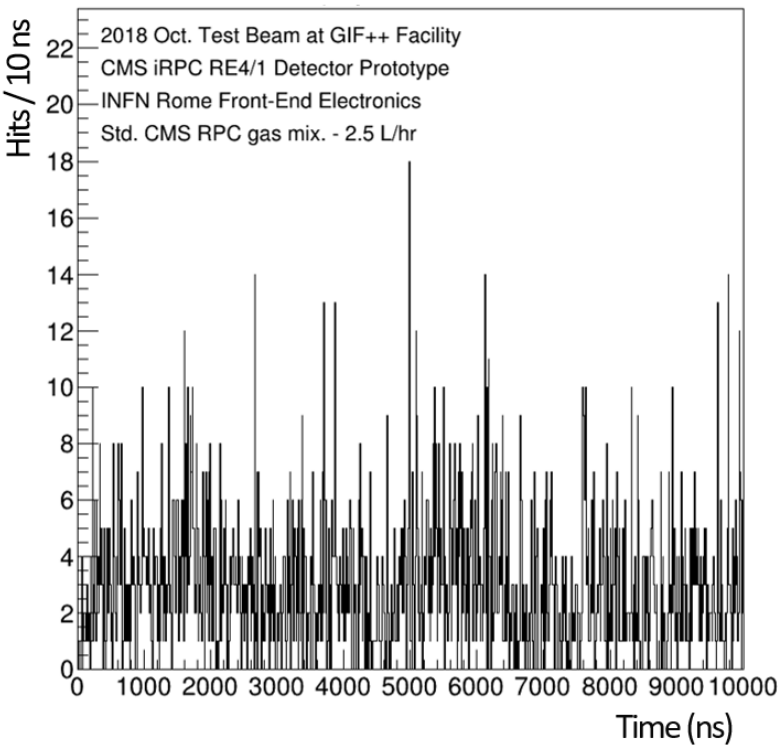

Figure 7.23: Example of time distribution of the hits for 25,000 events obtained during the noise scan at the fixed HV point 7200V.

this type of scan requires a long enough integrating time of data. This was achieved by taking 25,000 random trigger pulses delivered by a CAEN N93B Dual Timer pulse generator at a frequency of 300 Hz during the 10,000 ns of total acquisition time for each HV point while extracting 10 μs of data from the TDC buffers for each trigger. In Fig. 7.23 the example of time distribution of the hits for 25,000 events obtained during the noise scan at the fixed HV point 7200V.

For each high voltage point has been estimated the mean value of the noise has been estimated taking into account the number of hits in the time window from 100 ns to 9900 ns. The mean noise rate as a function of the effective high voltage value is presented in Fig. 7.24: the mean noise rate value at the with source OFF and without muon particle beam is less than 2.5 Hz/cm^2. This result confirms the choice of the threshold value (5-10 fC) on the Front-end electronics and the fact that the muon signals will not be lost into the detector own noise level, which in turn increases the reliability of the detector prototype for the detection of the muon particle. The example of the number of hits distributions per strip is shown in Fig. 7.24. During the preparation of the iRPC detector, a single channel of the Front-end electronics was lost due to the mechanical damage of a SMD resistor which was not repaired due to the complexity of the soldering process in the vertical position. However, the mean value of the noise for each high voltage point does not exceed 2 Hz/cm^2

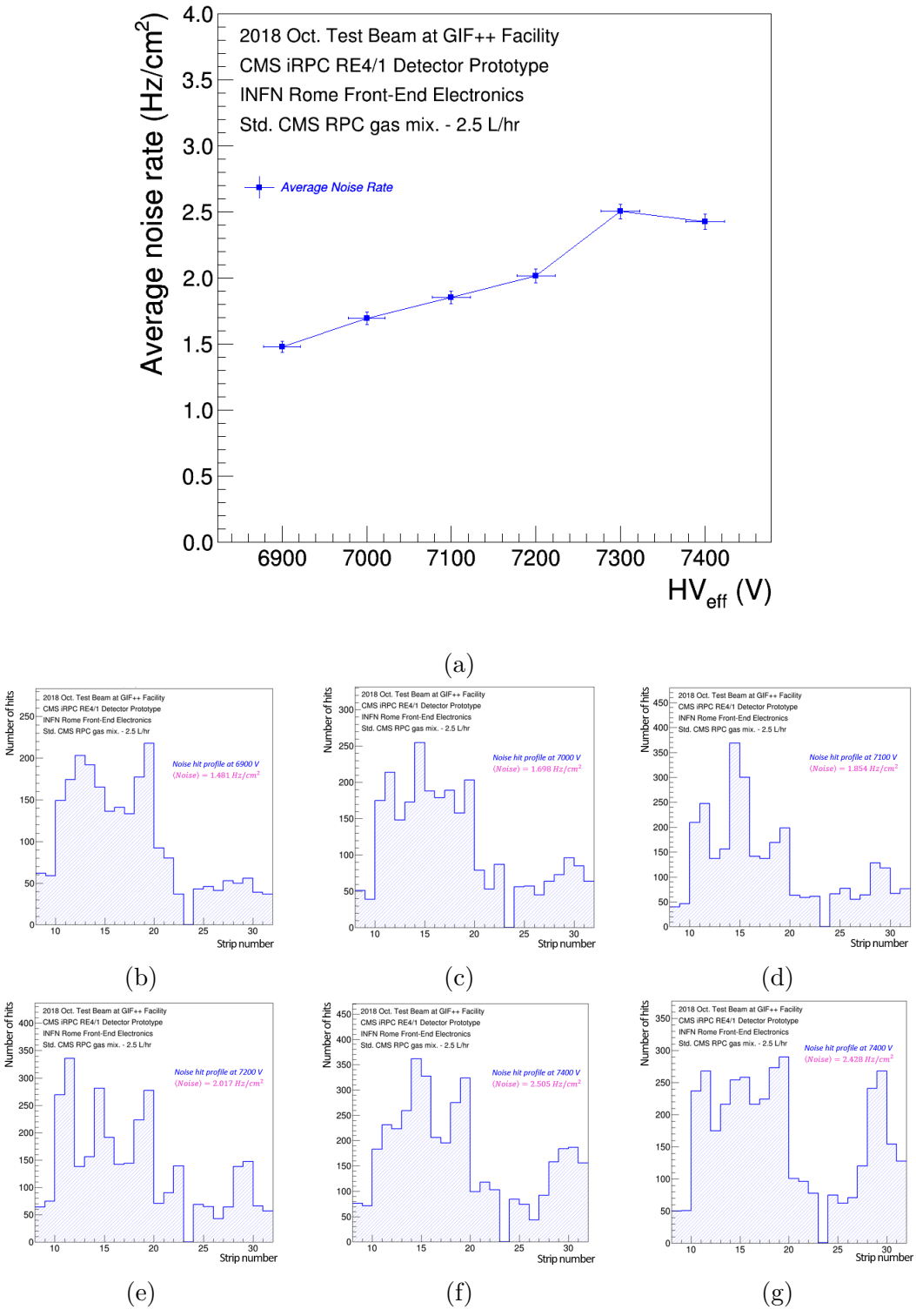

Figure 7.24: Average noise rate as a function of the effective high voltage value obtained at the source OFF and without muon particle beam at CERN GIF++ facility (a). Noise strip profile at the six different high voltage points (b) to (g): 6900 V, 7000 V, 7100 V, 7200 V, 7300 V and 7400 V. One channel in the INFN Front-end electronics was lost due to the mechanical damage of the SMD resistor.

and it confirms that the new iRPC 4/1 detector prototype with new INFN FEBs is a low-noise system.

7.5.3.2 Rate studies at different gamma fluxes

One of the main purpose of the Test Beam at CERN GIF++ facility, as already mentioned, is to verify the detection performance of iRPC detectors prototype with new INFN Front-end electronics in environmental conditions similar to those present in CMS experiment, i.e. hostile conditions due to the high particle background. The background radiation is mainly dominated by neutrons and photons: neutrons are produced by the hadronic interactions in the inner part of the detector and by the interactions of protons of the beam with the collimators, with energies between few MeV and hundreds of GeV; photons instead come from neutron capture, with typical energies between few KeV and tens of MeV. This background radiation could "hide" the muons and their interactions if the detector has exceeded the maximum number of counts at a particular time interval. So it is necessary to estimate the maximum rate a detector can support. At CMS experiment, the muon endcaps and the forward regions are characterized by high particles flux, while in the barrel region flux will be more than one order of magnitude lower. Let's recall that the CMS detectors have a sensitivity of 100% for charged particles, about 1% for gamma rays and about 0.1% for neutrons. Neutrons slightly contribute to the background rate, even if their flux is greater than other particles one. Therefore, the particle background rate is mainly due to the interaction of gamma rays.

The LHC Run-1 and Run-2 data have shown a linear dependence of the background rates as a function of the instantaneous luminosity over five orders of magnitude for all barrel and endcap muon stations. Assuming the same linear dependence up to a luminosity of about one order of magnitude higher, the maximum expected rates in muon endcaps at HL-LHC will be about 200 Hz/cm^2, while in the muon barrel will be significantly lower. The particle background simulations reproduce the measured rates within a factor of two. However, these values must be corrected, even considering the LHC energy increase from 13 TeV to 14 TeV: thus, the rate reference value in the endcap regions closer to the LHC beam (where the iRPC detectors will be installed) will be about 700 - 900 Hz/cm^2 [57]. The aim of the Test Beam at CERN GIF++ facility is to evaluate the detection performance of the iRPC at background rates similar to those expected in CMS experiment with a safety factor 3 before the final installation.

Once the expected background rates in CMS experiment is estimated, it is necessary to measure the rate capability of the detectors, i.e. the maximum number of events per second that a detector is able to count, corresponding to the maximum number of detectable particles per second. The rate capability must therefore be greater than the expected rate and depends on the intrinsic characteristics of the detector. The detector rate capability can be roughly calculated by means of the formula shown in [94]. However, it is necessary

to verify whether the calculated value is compatible with measured one. For this reason, counting rate measurements have been carried out during the irradiation test at GIF++ facility, aimed at verifying that the detectors are able to withstand the new background rate values expected during Phase-II, by maintaining the value of the detection efficiency above the present limit.

We will discuss the counting rate measurements obtained during the irradiation test at the GIF++ facility. Firstly, it is important to calculate the flux of the gamma photons emitted by the GIF++ ^{137}Cs source. Theoretically, this incident gamma photons flux is directly proportional to the activity A of ^{137}Cs source and inversely proportional to the absorption factor ABS applied to the source and to the square of the distance d between the detector and the source:

$$\phi_{ABS} \propto \frac{A}{4\pi \times ABS \times d^2} \tag{7.6}$$

where $A = 12.7$ TBq (October 2018), while the distance from the source in this configuration was equal to 263 cm. Varying the absorption coefficient applied the following approximate flux values have been obtained:

Table 7.3: Theoretical gamma flux from the Cesium-137 source at GIF++.

ABS [**a.u.**]	$\phi_{\mathbf{ABS}}$ [$\gamma/\mathbf{cm^2 \cdot s}$]	$\mathbf{R_{ABS}}$ [$\mathbf{Hz/cm^2}$]
1.5	9.76×10^6	5.63×10^3
2.2	6.65×10^6	3.54×10^3
3.3	4.43×10^6	3.92×10^3
4.6	3.18×10^6	2.81×10^3
6.9	2.12×10^6	2.59×10^3
10	1.46×10^6	1.79×10^3
22	6.65×10^5	1.20×10^3
46	3.18×10^5	5.72×10^2
100	1.46×10^5	4.08×10^2
220	6.65×10^4	1.86×10^2

The theoretical values shown in Table 7.3 are much greater than the current ones at CMS experiment (approximately a factor 10^3 greater). In the same table, the rate of expected hits (R_{ABS}) due to converted gamma photons is shown. R_{ABS} is calculated by scaling the gamma photon flux values with the iRPC sensitivity [95]. In the evaluation of the sensitivity, due to its energy dependence, contributions both of the direct gamma photons (0.662 MeV energy) and of lower energetic scattered photons should be considered. However, these values are an approximation, as in the relation the geometric acceptance of the source and the attenuation produced by other setups must also be considered. The irradiation field inside the GIF++ irradiation area for each ABS has been simulated by GEANT4 [96].

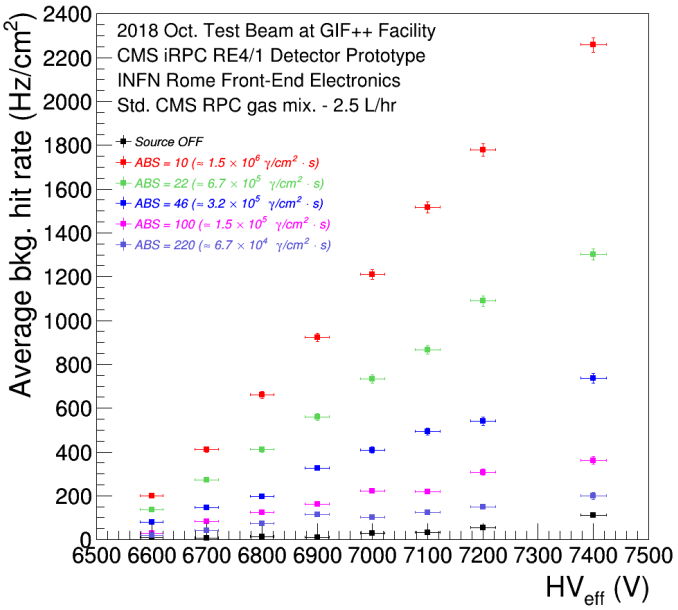

(a) Low gamma background flux.

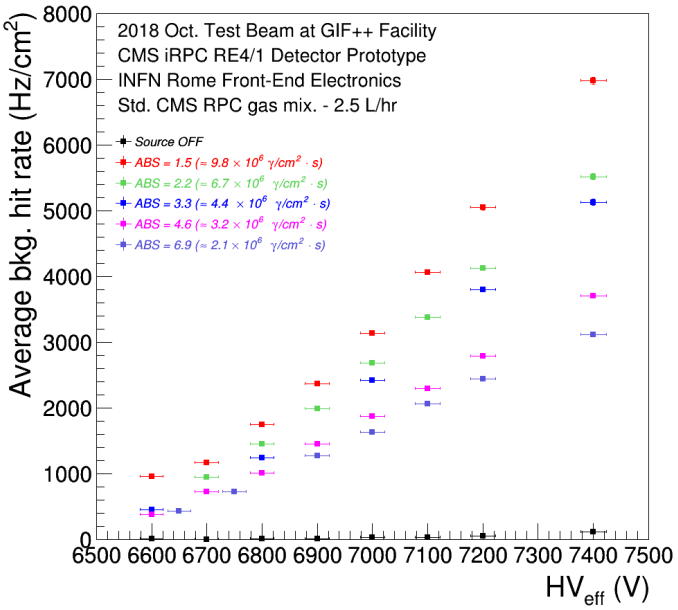

(b) High gamma background flux.

Figure 7.25: Average background hit rate as a function of the high voltage applied to the double-gap iRPC detector prototype at the different levels of the gamma photon flux from the source (the nominal filter absorption factors are indicated). The applied high voltage values have been normalized by using the PT correction formula explained in Section 6.1.2.2.

The average background hit rate or gamma rate seen by the double-gap iRPC detector prototype has been estimated according to the algorithm described in Section 7.5.2. Moreover, the counting rate measurements have been performed in double gap mode modifying the high voltage applied to the iRPC detector prototype. The applied high voltage values have been normalized by using the PT correction formula explained in Section 6.1.2.2. The same measurements have been repeated with different incident gamma flux values, obtained by varying the gamma source absorption factor.

Fig. 7.25a and Fig. 7.25b show the data collected with both source OFF and ON using ten different absorber settings (*ABS factor*: 1.5, 2.2, 3.3, 4.6, 6.9, 10, 22, 46, 100, 220) in order to vary the irradiation on the iRPC. The gamma radiation flux values reported in the legends of the graphs are the ones estimated according to the Equation 6.1 and reported in Table 7.3.

The experimental data show that the number of counts actually increases with the increase of the applied high voltage. Moreover, as the incident flux, the measured counting rate also increases. The maximum recorded counting rate values was about 4-5 kHz/cm^2, larger than the ones expected in the muon endcaps for the Phase-II upgrade ($\sim$900 Hz/cm^2). The counting rate measurements with the source OFF have been performed in order to evaluate the intrinsic noise of the detectors (noise rate), mainly due to the electronics. As shown in the graphs, the noise rate is 2.5 Hz/cm^2, thus so much low compared to the measured background hit rates. Finally, because of the double gap layout, the observed background hit rate for ionization taking place in both the gas gaps. Under the assumption that no ionization from a given γ goes from one gap to the other, a single gap rate half of the measured one should be considered as an estimate of the background.

7.5.3.3 Current studies at different gamma fluxes

In addition to the background hit rates data, the irradiations tests performed on the iRPC during the test beam at GIF++ facility provide information about the current produced in the detector. The following graphs show the average current density trend as a function of the voltage applied to the bottom and top gas gaps. In particular, the experimental measurements do not provide any information on the average current density trend at low voltage (range of values in which the RPC detector has approximately an Ohmic behavior); the average current density values reported below are thus essentially generated from the avalanche occuring in the gas gaps. Furthermore, Fig. 7.26 and Fig. 7.27 show the current density values, obtained by dividing the detected current by the total iRPC detector active area for both gaps, respectively. The data have been collected with both source OFF and ON using ten different absorber settings (*ABS factors*: 1.5, 2.2, 3.3, 4.6, 6.9, 10, 22, 46, 100, 220). The gamma radiation flux values reported in the legends of the graphs are the ones estimated according to the Equation 6.1 and reported in Table 7.3. The experimental data show that the current density increases with the increase of

the effective high voltage to the iRPC detector prototype. Moreover the measured current density also increases with the decreasing of the filter absorption factors.

Current density and counting rate are two physical quantities closely related to each other. In particular, the relation between current density and counting rate is linear as shown in the Fig. 7.28, Fig. 7.29, Fig. 7.30 and Fig. 7.31, where the average current density values are plotted as a function of the average background hit rate at different levels of gamma photon flux from the source both for bottom and top gas gaps.

The solid line represents a linear fit to the experimental data in order to extrapolate the parameters of the relation between current density and counting rate in single-gap mode. Therefore, the slope of the straight line represents the average charge produced by avalanches inside the gas gap of the detector. Furthermore, Fig. 7.32a and Fig. 7.32b show the average avalanche charge as a function of different levels of gamma photon flux from the source for both bottom and top gas gaps, respectively.

7.5.3.4 Efficiency studies at different gamma fluxes

Because of the stringent requirements imposed by the CMS muon trigger [57], the RPCs are required to have an efficiency above 95% up to the maximum expected background rate. In order to test the ability of the improved RPC to work within the CMS operational parameters, the detection efficiency and rate capability of the iRPC RE4/1 detector prototype with the new INFN Rome Front-end electronics have been carefully studied.

The high voltage scans have been performed to specifically measure the muon detection efficiency under different irradiation conditions follow the procedure established in Section 7.5.2. Several high voltage points in the range 6600 V - 7400 V by steps of 100 V have been applied on the iRPC in order to obtain the detection efficiency curve and estimate the working point. For each point, a minimum of 3000 muon beam triggers, provided by the coincidence of the 4 scintillators, is required in order to accumulate enough statistics for reliable computation of the detection efficiency.

The high voltage scans have been carried out with different incident gamma flux values, obtained by varying the gamma source absorption factor. The detailed study of the detection performance of the detector has been performed with both source OFF and ON using ten different absorber settings (ABS factors: 1.5, 2.2, 3.3, 4.6, 6.9, 10, 22, 46, 100, 220) in order attenuate the nominal gamma flux by factors from more than 200 to only 1.5; settings with fully opened source have been avoided with the iRPC in test beam position. As mentioned, adjusting the gamma flux is possible thanks to the 3 layers of absorbers featured on the 137-Cesium source.

Fig. 7.33a and Fig. 7.33b show the detection efficiency as function of high voltage applied to the double-gap iRPC at different levels of gamma photon flux from the source (the nominal filter absorption factors are indicated). The

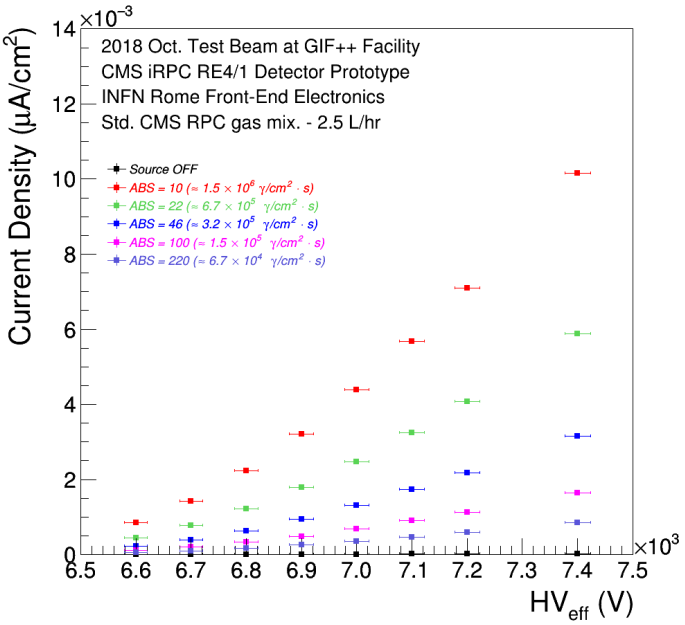

(a) Current density studies at the low background irradiation for bottom gas gap.

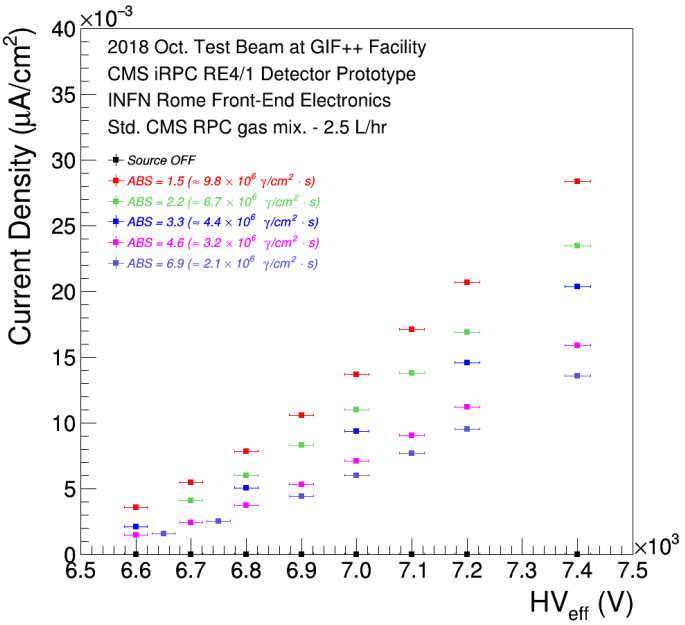

(b) Current density studies at the high background irradiation for bottom gas gap.

Figure 7.26: Average current density as a function of the high voltage applied to the bottom gas gap installed in the iRPC detector prototype at the different levels of the gamma photon flux from the source (the nominal filter absorption factors are indicated). The applied high voltage values have been normalized by using the PT correction formula explained in Section 6.1.2.2.

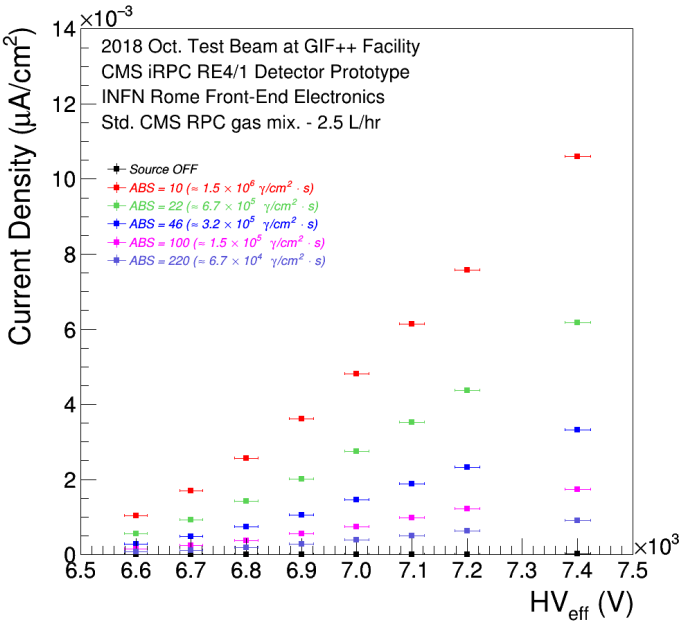

(a) Current density studies at low background irradiation for top gas gap.

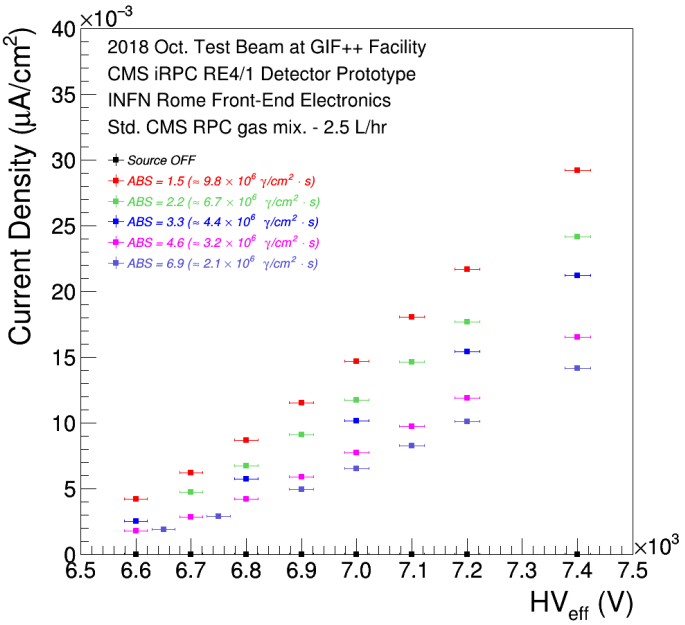

(b) Current density studies at high background irradiation for top gas gap.

Figure 7.27: Average current density as a function of the high voltage applied to the top gas gap installed in the iRPC detector prototype at the different levels of the gamma photon flux from the source (the nominal filter absorption factors are indicated). The applied high voltage values have been normalized by using the PT correction formula explained in Section 6.2.2.2.

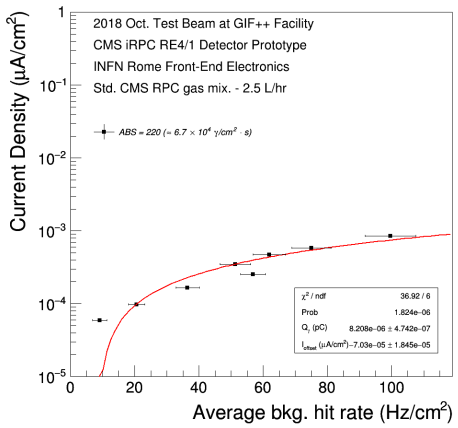

(a) $\phi_\gamma = 6.7 \times 10^4\ \gamma/cm^2 \cdot s$ (ABS 220).

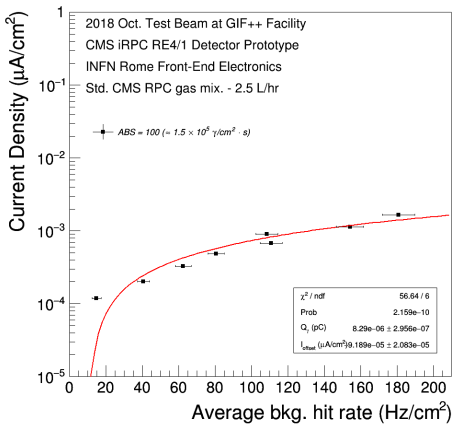

(b) $1.5 \times 10^5\ \gamma/cm^2 \cdot s$ (ABS 100).

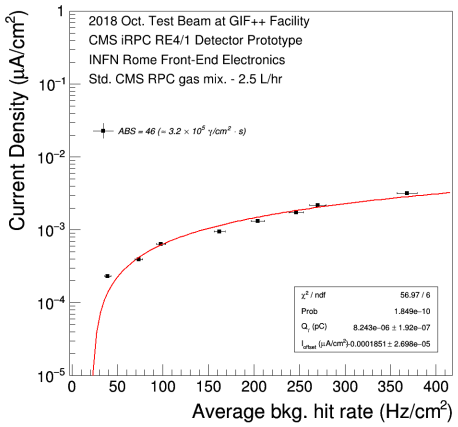

(c) $\phi_\gamma = 3.2 \times 10^5\ \gamma/cm^2 \cdot s$ (ABS 46).

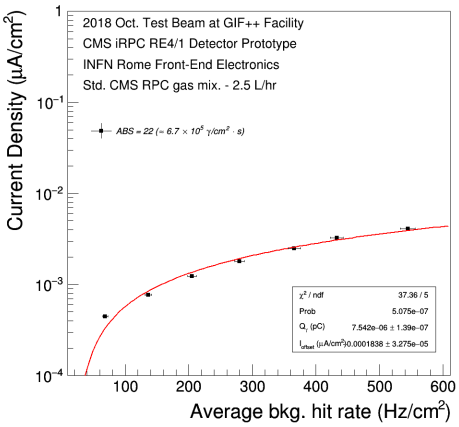

(d) $\phi_\gamma = 6.7 \times 10^5\ \gamma/cm^2 \cdot s$ (ABS 22).

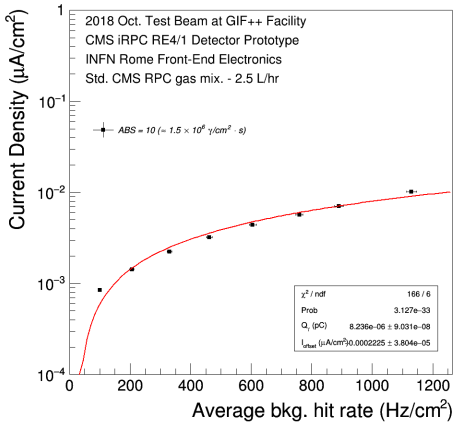

(e) $\phi_\gamma = 1.5 \times 10^6\ \gamma/cm^2 \cdot s$ (ABS 10).

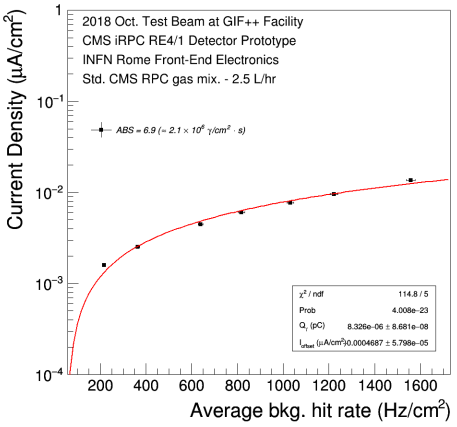

(f) $\phi_\gamma = 2.1 \times 10^6\ \gamma/cm^2 \cdot s$ (ABS 6.9).

Figure 7.28: Average current density as a function of the average background hit rate for the bottom gas gap of the iRPC detector prototype at the different levels of the gamma photon flux from the source (*ABS factors*: 220, 100, 46, 22, 10, 6.9).

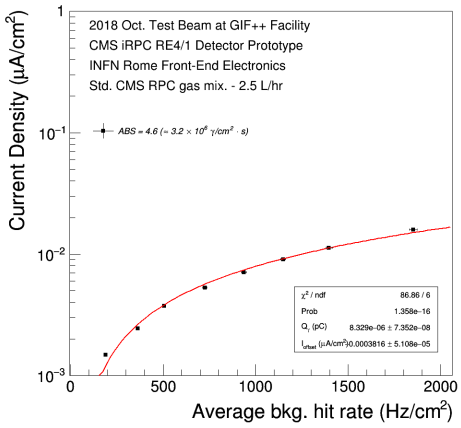

(a) $\phi_\gamma = 3.2 \times 10^6\ \gamma/cm^2 \cdot s$ (ABS 4.6).

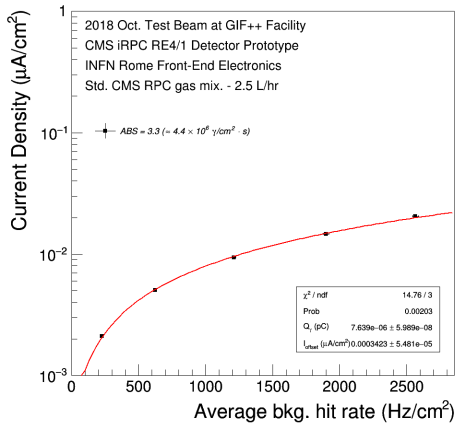

(b) $\phi_\gamma = 4.4 \times 10^6\ \gamma/cm^2 \cdot s$ (ABS 3.3).

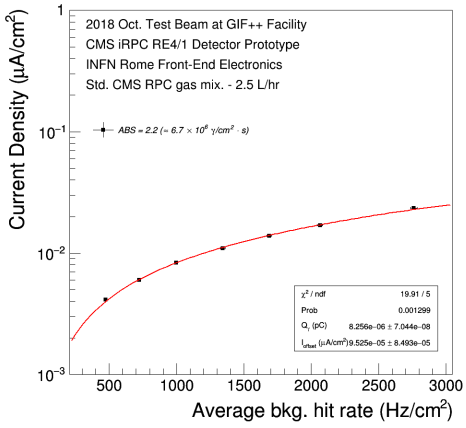

(c) $\phi_\gamma = 6.7 \times 10^6\ \gamma/cm^2 \cdot s$ (ABS 2.2).

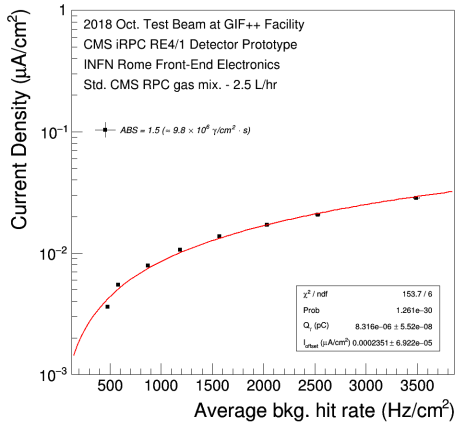

(d) $\phi_\gamma = 9.6 \times 10^6\ \gamma/cm^2 \cdot s$ (ABS 1.5).

Figure 7.29: Average current density as a function of the average background hit rate for the bottom gas gap of the iRPC detector prototype at the different levels of the gamma photon flux from the source (*ABS factors*: 4.6, 3.3, 2.2, 1.5).

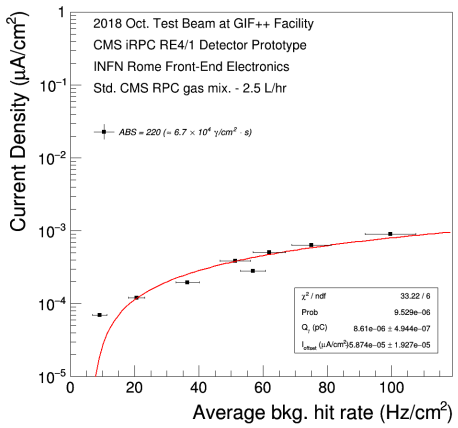

(a) $\phi_\gamma = 6.7 \times 10^4\ \gamma/cm^2 \cdot s$ (ABS 220).

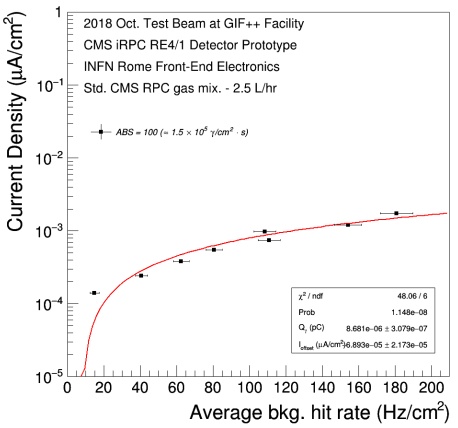

(b) $1.5 \times 10^5\ \gamma/cm^2 \cdot s$ (ABS 100).

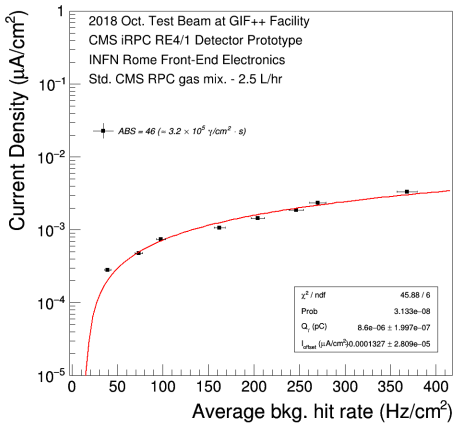

(c) $\phi_\gamma = 3.2 \times 10^5\ \gamma/cm^2 \cdot s$ (ABS 46).

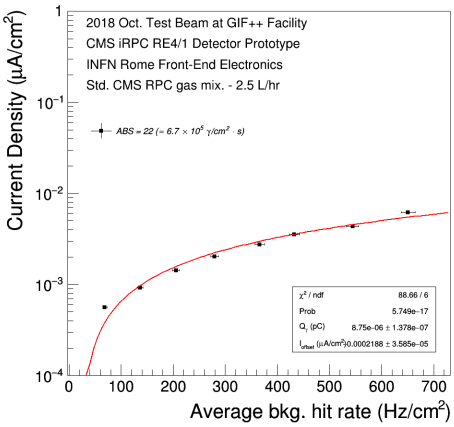

(d) $\phi_\gamma = 6.7 \times 10^5\ \gamma/cm^2 \cdot s$ (ABS 22).

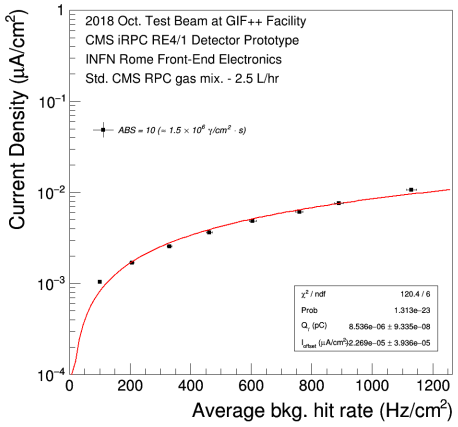

(e) $\phi_\gamma = 1.5 \times 10^6\ \gamma/cm^2 \cdot s$ (ABS 10).

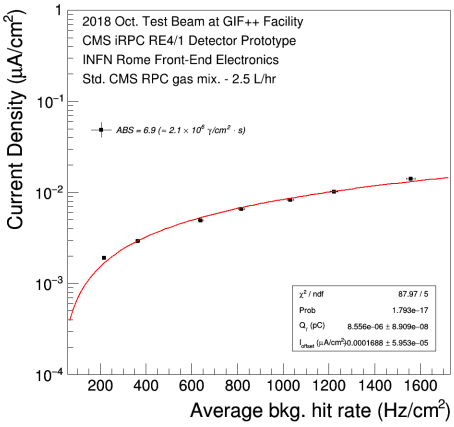

(f) $\phi_\gamma = 2.1 \times 10^6\ \gamma/cm^2 \cdot s$ (ABS 6.9).

Figure 7.30: Average current density as a function of the average background hit rate for the top gas gap of the iRPC detector prototype at the different levels of the gamma photon flux from the source (*ABS factors*: 220, 100, 46, 22, 10, 6.9).

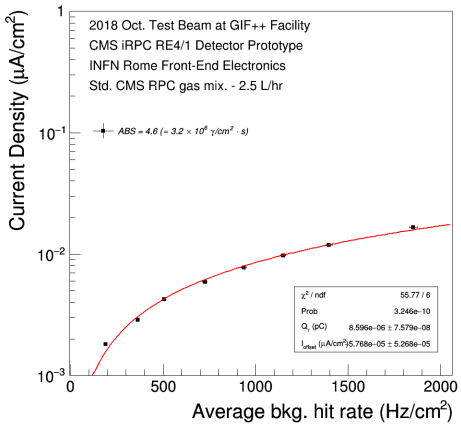

(a) $\phi_\gamma = 3.2 \times 10^6\ \gamma/cm^2 \cdot s$ (ABS 4.6).

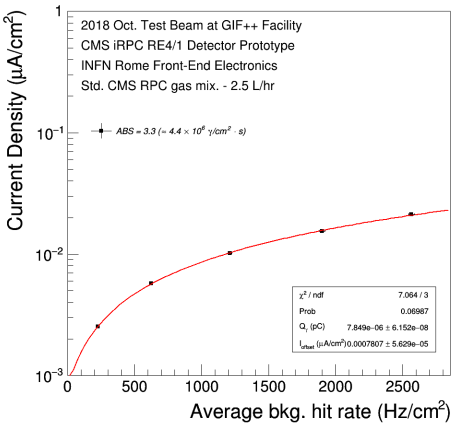

(b) $\phi_\gamma = 4.4 \times 10^6\ \gamma/cm^2 \cdot s$ (ABS 3.3).

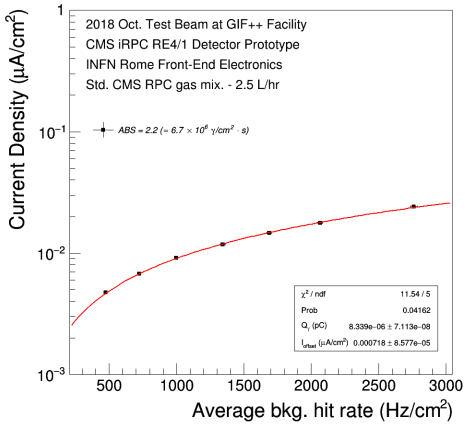

(c) $\phi_\gamma = 6.7 \times 10^6\ \gamma/cm^2 \cdot s$ (ABS 2.2).

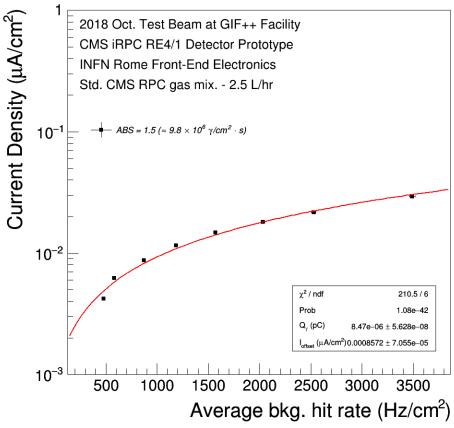

(d) $\phi_\gamma = 9.6 \times 10^6\ \gamma/cm^2 \cdot s$ (ABS 1.5).

Figure 7.31: Average current density as a function of the average background hit rate for the top gas gap of the iRPC detector prototype at the different levels of the gamma photon flux from the source (*ABS factors*: 4.6, 3.3, 2.2, 1.5).

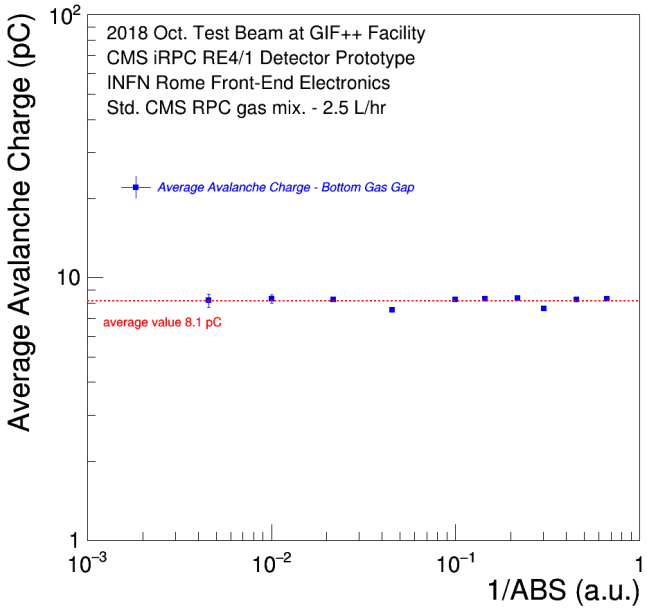

(a) Average avalanche charge studies for bottom gas gap.

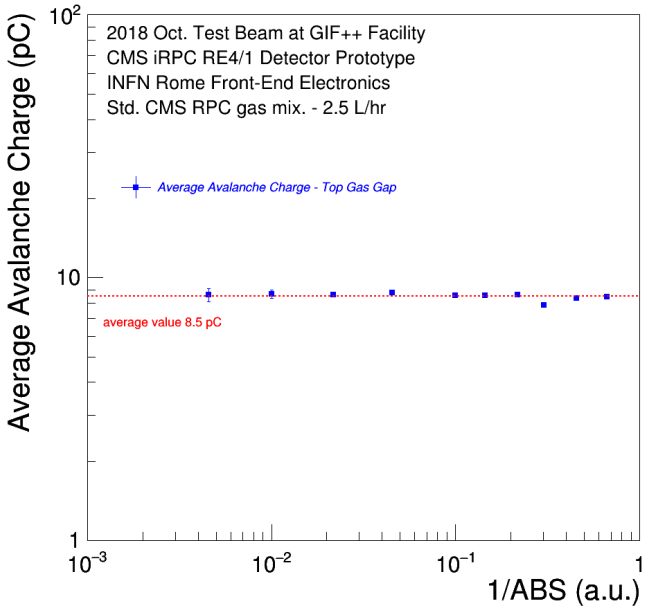

(b) Average avalanche charge studies for top gas gap.

Figure 7.32: Average avalanche charge as a function of the different levels of the gamma photon flux from the source for the bottom (a) and top (a) gas gap of the iRPC detector prototype (the inverse of the nominal source absorption factor is indicated).

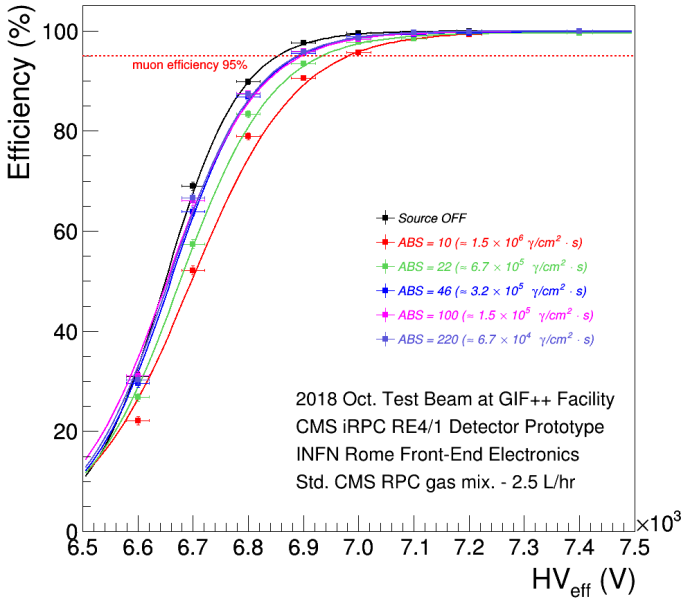

(a) Detection efficiency studies at low background irradiation.

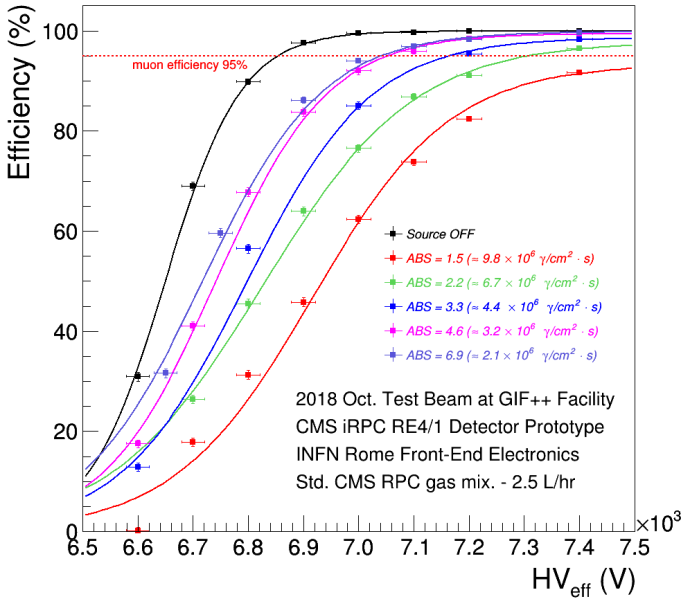

(b) Detection efficiency studies at high background irradiation.

Figure 7.33: Detection efficiency as a function of the high voltage applied to the double-gap iRPC RE4/1 detector prototype at the different levels of the gamma photon flux from the source (the nominal filter absorption factors are indicated). The applied high voltage values have been normalized by using the PT correction formula explained in Section 6.2.2.2.

applied high voltage values have been normalized by using the PT correction formula explained in Section 6.1.2.2.

The detection efficiency actually increases with the high voltage applied to the double-gap iRPC and also depends on the absorption factor applied to the gamma source: the more the source is shielded, the smaller is the incident gamma photon flux and thus the detector will be more efficient. In particular, these graphs show that at high voltage applied and rates of the order of 2 kHz/cm^2 (expected rates during the Phase-II at HL-LHC), the detection efficiency is approximately 98% (see Fig. 7.33b where the efficiency curve is marked in violet color) at plateau, therefore, more than the minimum efficiency required by CMS (95%). The detection efficiency of the detector has been also evaluated with the gamma source turned OFF: in this configuration, there is not a real incident gamma photon flux on the iRPC detector prototype. For this reason, the detection efficiency values corresponding to this configuration are the highest estimated, if compared with those obtained with the shielded source.

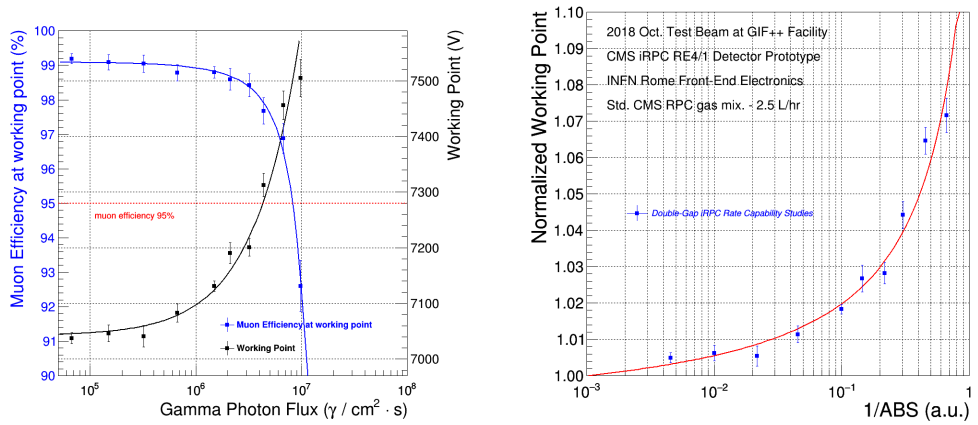

(a) (b)

Figure 7.34: Working point for the iRPC RE4/1 detector prototype as a function of the different levels of the gamma photon flux from the source (the inverse of the nominal source absorption factor is indicated). The detection efficiency values are normalized to those obtained with the source OFF.

However, the detection efficiency and the working point values depend on the incident particles flux: for increasing values of the incident gamma photon flux, the detection efficiency decreases and the working point moves toward higher voltage values. In fact, when an avalanche subsequent to the passage of an ionizing particle reaches one or both resistive electrodes, it neutralizes part of the surface polarization charge, consequently reducing the local electric field in the gas gap. However, only a limited part of the electrodes is discharged, while the rest remains basically untouched. The time needed for the electrodes to be charged up again by an external supply depends on the time constant

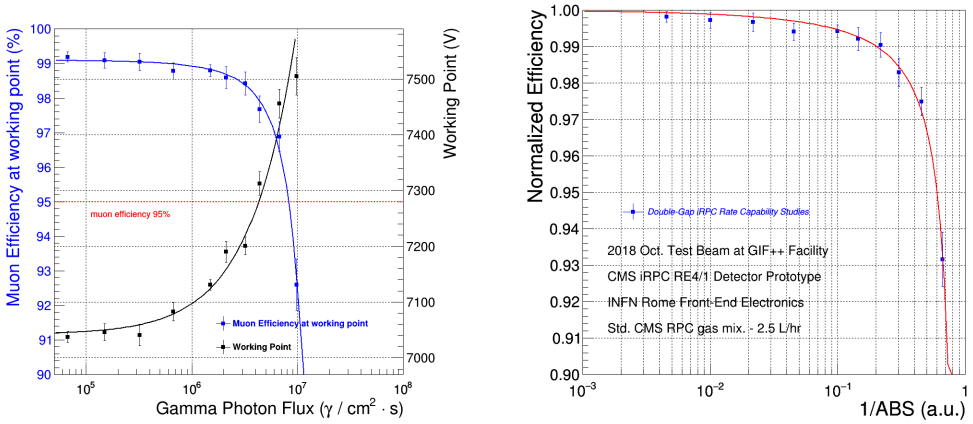

(a) (b)

Figure 7.35: Detection efficiency at working point for the iRPC RE4/1 detector prototype as a function of the different levels of the gamma photon flux from the source (the inverse of the nominal source absorption factor is indicated). The detection efficiency values are normalised to those obtained with the source OFF.

of the detector, that is the product of its equivalent resistance and capacitance. While the detector capacitance depends on its geometry, its equivalent resistance derives from the resistivity of the specific materials used. If another ionizing particle happens to cross the detector and enters the gas where the previous one has just passed, an electric field lower than the usual will be found, and this could be not strong enough to give rise to multiplication processes; in this case, the particle could be undetected. As a consequence, from a macroscopic point of view the efficiency of a RPC detector will progressively deteriorate as the particle flux exceeds a certain value.

Fig. 7.34 and Fig. 7.35 show the summary plots of the working point and detection efficiency as a function of different levels of gamma photon flux from the source (the inverse of the nominal source absorption factor is indicated). The efficiency values have been normalised to those obtained with the source OFF.

At the nominal working point value of about 6996 V, the detection of muon efficiency is of 99.4% without gamma irradiation, while at the working point of about 7361.8 V the efficiency is of 95.7% at the attenuation factor of 2.2 (6.65×10^6 $\gamma/cm^2 \cdot s$) and then the efficiency at the working point of about 7496.2 V decreases down to 93% at the attenuation factor of 1.5 (9.76×10^6 $\gamma/cm^2 \cdot s$). In order to recover the electric field the working point value has been increased from 6996 V without gamma photon flux to 7361.8 V at the highest gamma photon flux: the shift of the working point has been found to be 365.8 V. However, the detection efficiency remains higher than 97.5% even for a background hit rate estimated to be about 2 - 3 kHz/cm^2, well above the

expected background hit rate at the RE3/1 and RE4/1 region in the Moun Spectrometer of the CMS experiment [57]. Therefore, the detailed detection efficiency studies have shown that the iRPC detector prototype with new INFN Front-end electronics can operate in the harsh CMS Endcap environmental at HL-LHC without suffering any degradation of the detection performance in the worst expected background conditions.

7.5.3.5 Cluster size and Cluster multiplicity studies at different gamma fluxes

In addition to the detection efficiency, the cluster size is another important parameter for the reconstruction of the interesting muon events due to the fact that the muon P_T assignment is strongly correlated to the detector cluster size, defined as the number of contiguous strips fired per event. The future CMS iRPC system, as the current RPC system, will be one layer detectors and the reconstructed iRPC hits information will be combined with the other trigger primitives based on the segments built in CSC or DT chambers. The RPC hits coordinates are calculated in the gravity center of the formed clusters of fired strips. Larger cluster size can affect the proper estimation of the bending angle of the muon trajectory. In order to follow the muon trigger requirements, the cluster size of the new iRPC should be not more than 2 strips.

Both minimum ionizing particle and Compton electrons coming from the gamma photons emitted by the source could produce detectable signals in several adjacent strips, forming a cluster. A cluster is defined by grouping adjacent strips with signals inside a time window of fixed width $\triangle t = 10$ ns. These strips were assumed to be part of the same physical avalanche signal generated by a muon passing through the chamber or by the interaction of a gamma stopping into the electrodes of the iRPCs. The cluster size has been studied as a function of the high voltage applied to the double-gap iRPC at different source conditions.

Efficiency curves and average muon and gamma cluster size as a function of a high voltage applied for different levels of gamma photon flux are shown in Fig. 7.36, Fig. 7.37 and Fig. 7.38, while the same plot at source OFF is shown in Fig 7.36. Summary plots (see Fig. 7.39a and Fig. 7.39b) show that the the muon cluster size remains below 4.5 and then decreases as the particle rate of the source increase (as shown in Fig. 7.39b at the maximum photon flux the cluster size is below 2.5). The high value of the muon cluster size can be explained by the sensitivity of the components of the electronics and the low electronics threshold value (5-10 fC) applied. In the ideal case, just the strip crossed by the particle should fire, but due to the cross-talk or other phenomena (for instance the occurrence of streamers in the presence of a sensible front-end electronics) can increase this number. This high cluster size value increases occupancy and spoils the detector spatial resolution. Fig. 7.40 shows the example of a cross-talk events (marked red circle), obtained during the Test Beam. Moreover, due to the high gamma photon flux from

source, the avalanching charge produced by gamma via Compton scattering is accumulated and disturbed the electric field inside gas gaps. The distortion of the electric field leads to the reduction of the avalanching charge size produced by muon particles explaining the muon cluster size reduction at the increasing the gamma photon flux.

The gamma cluster size has been measured also. Since a gamma-ray induces its pulse in an individual single gap via Compton scattering, the expected pick-up charge is about a half of the muon one. For this reason, the gamma cluster size is about 2 times less with respect to the muon cluster size (see Fig. 7.39c and Fig. 7.39d).

The distribution of the number of clusters per event (or cluster multiplicity) has been also measured during the efficiency scan at different levels of gamma photon flux (see Fig. 7.41, Fig. 7.42 and Fig. 7.43). In fact, the cluster size and cluster multiplicity are crucial figures of merit to understand the detector performances. In Fig. 7.44a - Fig. 7.44d the summary plots of the muon and gamma cluster multiplicity are shown as a function of the high voltage. The muon cluster multiplicity increases with increasing high voltage and reaches a plateau level because the muon detection efficiency reaches closely 100% and the muon particles per trigger are nearly constant (average value about 1.4 - 1.5). The gamma cluster multiplicity also reaches a plateau level at a higher voltage value because the efficiency for 662 keV gamma photons is fixed. Fig. 7.45a shows the muon detection efficiency and the muon and gamma cluster size as a function of the cluster rate seen at working point by the double-gap iRPC detector prototype. The studies show that, at the detector working point, the average muon cluster size is typically 3 and the muon cluster multiplicity is basically 1.3, proving that the read-out strip cross-talk and correlated noise are not negligible. The muon cluster size and the muon cluster multiplicity at working point should be nearly constant up to a certain level of the gamma background. However, if the strength of the gamma background keeps increasing the avalanche signals become significantly smaller because of the decrease of the electric field inside the gas gaps due to a space-charge effect and are unable to create pulses over the digitization threshold. This can explain the muon cluster size reduction at increasing gamma flux. Finally, Fig. 7.45b shows the muon detection efficiency and the muon and gamma cluster multiplicity as a function of the cluster rate seen at working point by prototype. As discussed previously, since the gamma-ray induces its pulse in an individual single gap via Compton scattering, the expected pick-up charge is about a half of the muon one. For this reason, the gamma cluster size is about 2 times less the muon cluster size. Moreover, in an ideal case, the gamma cluster multiplicity should be proportional to the gamma photon flux. In fact, the gamma cluster multiplicity by definition is the gamma detection efficiency multiplied by the gamma photons flux and normalized to the trigger windows time. However, if the strength of the gamma photons background is particularly intense, the efficiency of measuring the gamma photons will decrease

and the linearity is broken. At the low gamma background irradiation, the gamma cluster multiplicity becomes flat as the high voltage increases. If the high voltage increases further by 500 V, it is possible to observe the actual efficiency plateau for the 662 keV gamma photons. However, at the high gamma background irradiation, the gamma cluster multiplicity keeps increasing as the high voltage increases and it is no longer possible to observe efficiency plateau because of the reduction of the avalanche gain due to the high space-charge effect in the gas gaps.

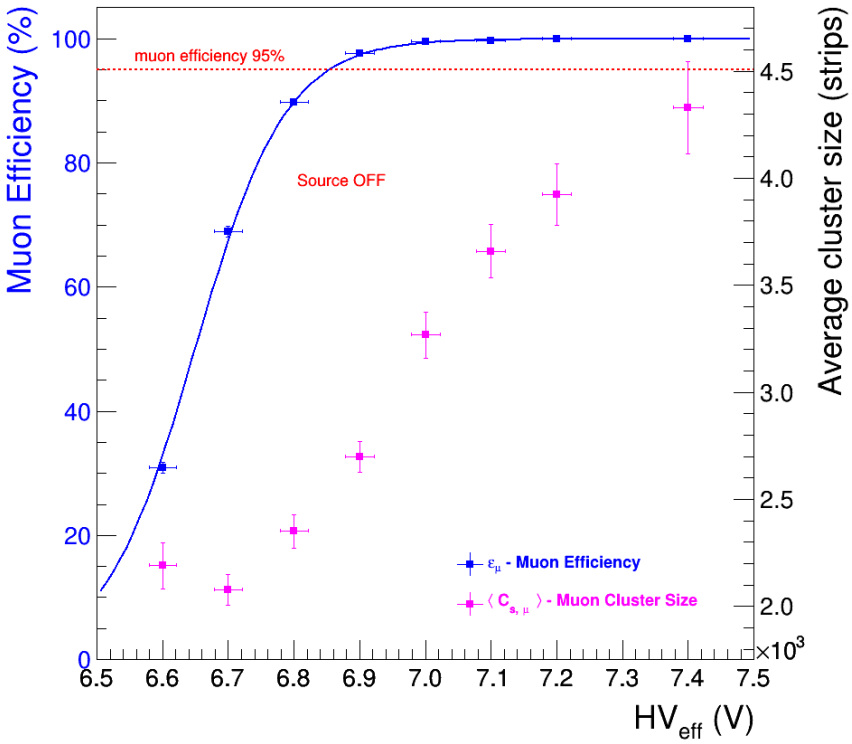

Figure 7.36: Muon detection efficiency and muon cluster size as a function of the high voltage applied to the double-gap iRPC detector prototype without gamma photon flux from the source. The applied high voltage values have been normalized by using the PT correction formula explained in Section 6.2.2.2.

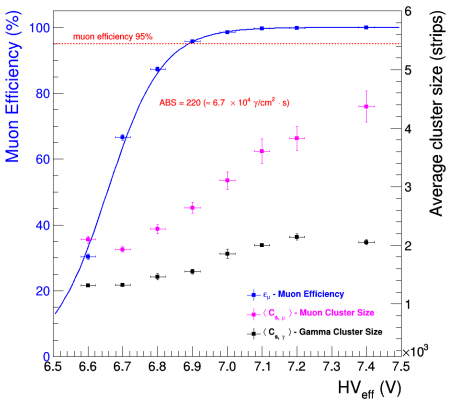

(a) $\phi_\gamma = 6.7 \times 10^4\ \gamma/cm^2 \cdot s$ (ABS 220).

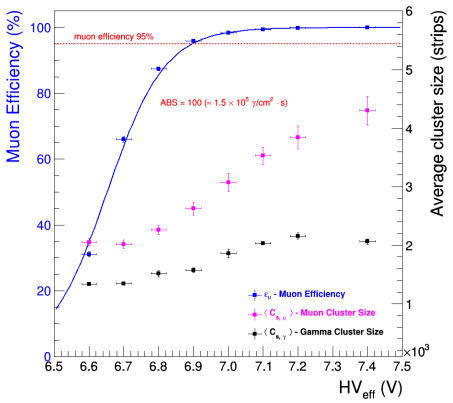

(b) $1.5 \times 10^5\ \gamma/cm^2 \cdot s$ (ABS 100).

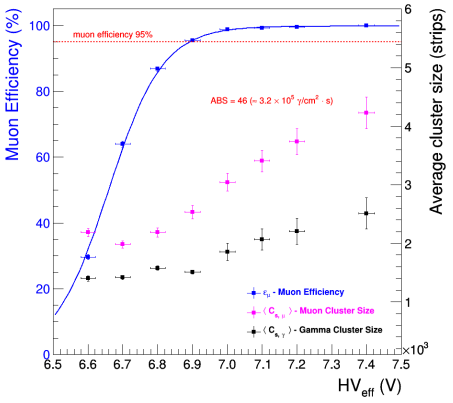

(c) $\phi_\gamma = 3.2 \times 10^5\ \gamma/cm^2 \cdot s$ (ABS 46).

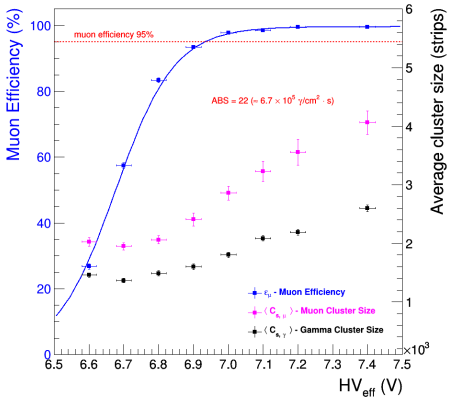

(d) $\phi_\gamma = 6.7 \times 10^5\ \gamma/cm^2 \cdot s$ (ABS 22).

Figure 7.37: Muon detection efficiency, muon and gamma cluster size as a function of the high voltage applied to the double-gap iRPC detector prototype at the different levels of the gamma photon flux from the source (the nominal filter absorption factors are indicated). The applied high voltage values have been normalized by using the PT correction formula explained in Section 6.2.2.2.

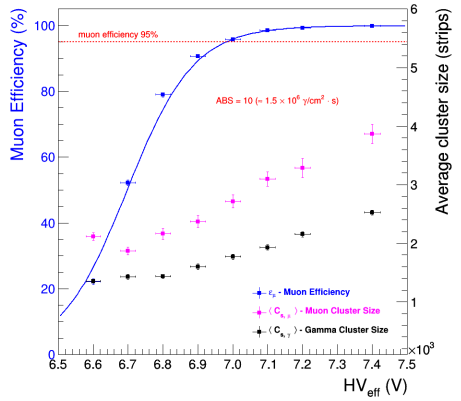

(a) $\phi_\gamma = 1.5 \times 10^6\ \gamma/cm^2 \cdot s$ (ABS 10).

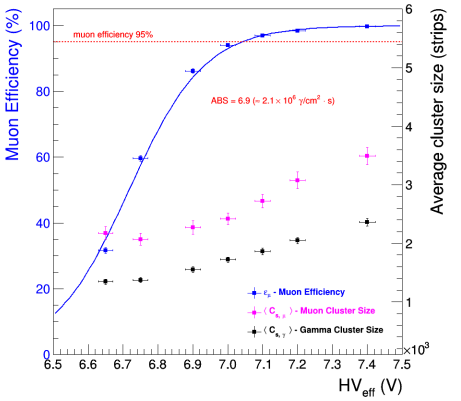

(b) $\phi_\gamma = 2.1 \times 10^6\ \gamma/cm^2 \cdot s$ (ABS 6.9).

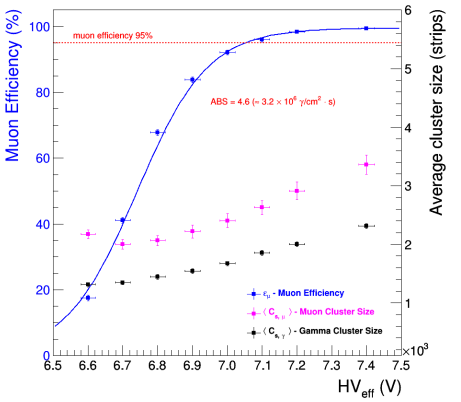

(c) $\phi_\gamma = 3.2 \times 10^6\ \gamma/cm^2 \cdot s$ (ABS 4.6).

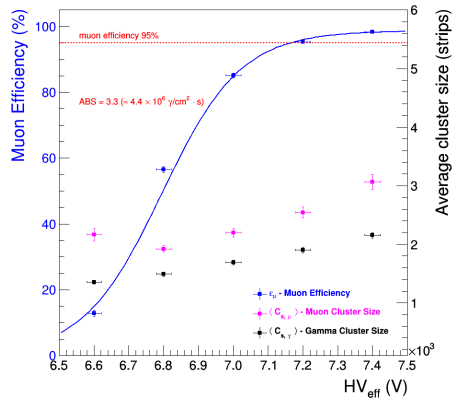

(d) $\phi_\gamma = 4.4 \times 10^6\ \gamma/cm^2 \cdot s$ (ABS 3.3).

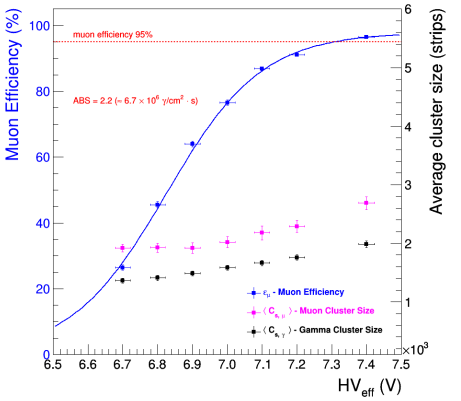

(e) $\phi_\gamma = 6.7 \times 10^6\ \gamma/cm^2 \cdot s$ (ABS 2.2).

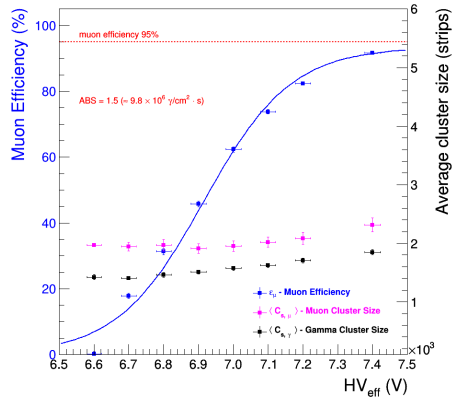

(f) $\phi_\gamma = 9.6 \times 10^6\ \gamma/cm^2 \cdot s$ (ABS 1.5).

Figure 7.38: Muon detection efficiency, muon and gamma cluster size as a function of a high voltage applied to the double-gap iRPC detector prototype at different levels of gamma photon flux from the source (the nominal filter absorption factors are indicated). The applied high voltage values have been normalized by using the PT correction formula explained in Section 6.2.2.2.

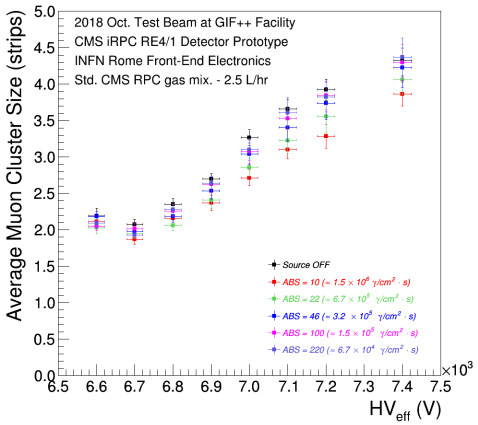

(a) Muon cluster studies at the low background irradiation.

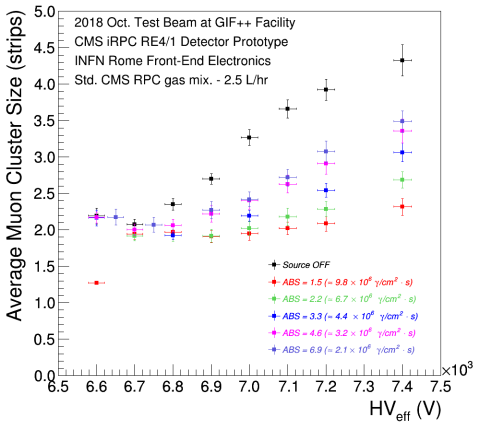

(b) Muon cluster studies at the high background irradiation.

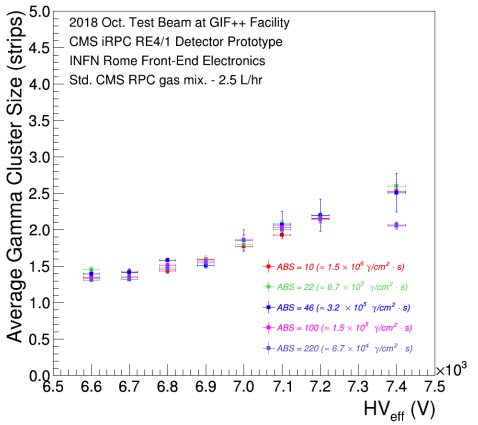

(c) Gamma cluster studies at the low background irradiation.

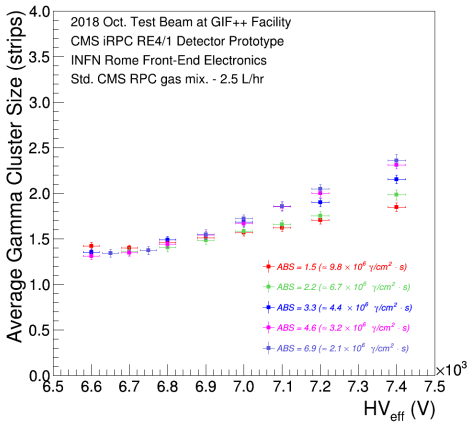

(d) Gamma cluster studies at the high background irradiation.

Figure 7.39: Summary plots of the muon and gamma cluster size as a function of the high voltage applied to the double-gap iRPC detector prototype at the different levels of the gamma photon flux from the source (the nominal filter absorption factors are indicated). The applied high voltage values have been normalized by using the PT correction formula explained in Section 6.2.2.2.

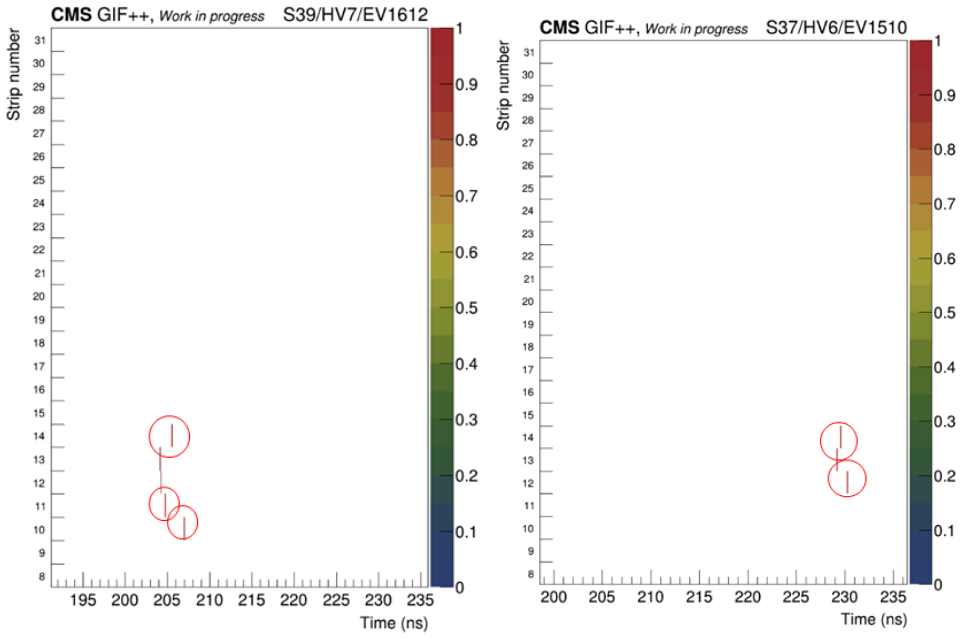

(a) (b)

Figure 7.40: Number of strips as a function of time at the fixed applied high voltage point 7200 V without source and with gamma photon flux of $\phi_\gamma = 6.7 \times 10^6\ \gamma/cm^2 \cdot s$ (ABS 2.2). The cross-talk events are marked with red circles.

7.6 Additional Performence Studies of the iRPC RE4/1 Detector Prototype with INFN Rome FEB at the Cosmic Ray Stand in the CERN CMS-RPC QA/QC facility

The clear understanding of the quality of the electrodes and the readout strip panel are crucial in the study of detection performances of the iRPC detectors. Several factors, such as non-uniformity electrodes thickness or surface, local contamination or presences of defects on the electrodes or on the readout strip panel could affect the uniformity of detection efficiency all over the detector active area. Due to the fact that the detection efficiency determines the detector performances (e.g. working point, cluster size, multiplicity, and spatial resolutions, etc), the study of the detection efficiency uniformity across the entire detector active area is fundamental.

7.6.1 Experimental Setup

After the Test Beam in October 2018, CMS-iRPC Collaboration decided to continue the performance studies of the iRPC RE4/1 detector prototype with

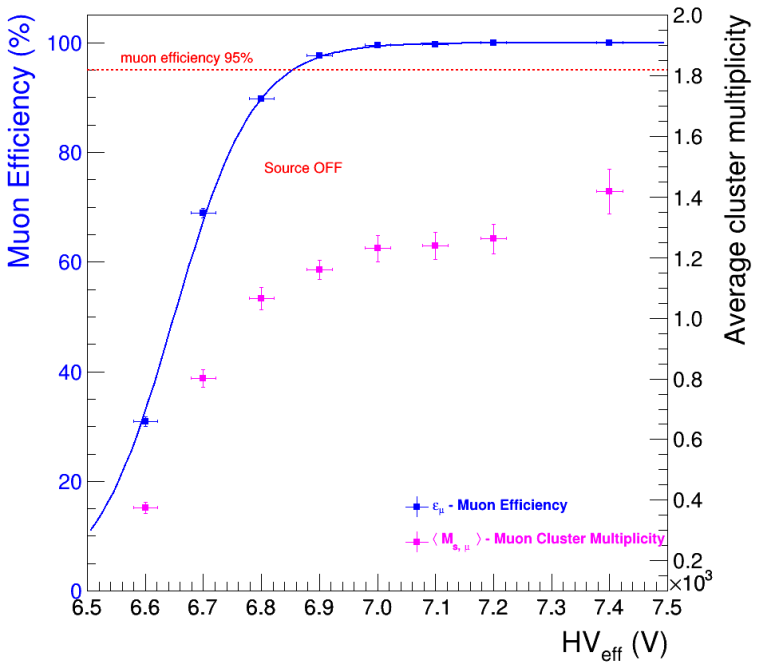

Figure 7.41: Muon detection efficiency and muon cluster multiplicity as a function of the high voltage applied to the double-gap iRPC detector prototype without gamma photon flux from the source. The applied high voltage values have been normalized by using the PT correction formula explained in Section 6.1.2.2.

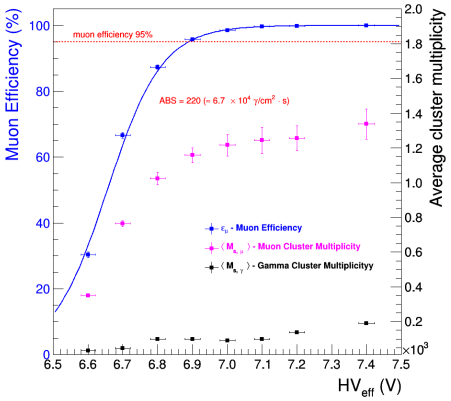

(a) $\phi_\gamma = 6.7 \times 10^4\ \gamma/cm^2 \cdot s$ (ABS 220).

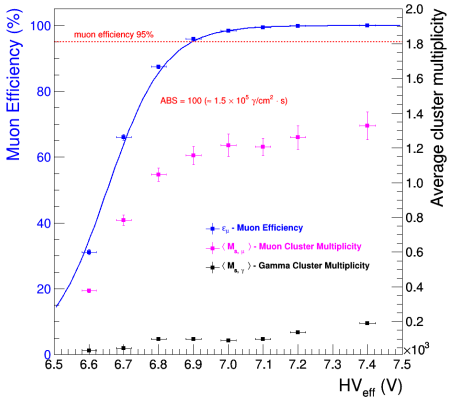

(b) $1.5 \times 10^5\ \gamma/cm^2 \cdot s$ (ABS 100).

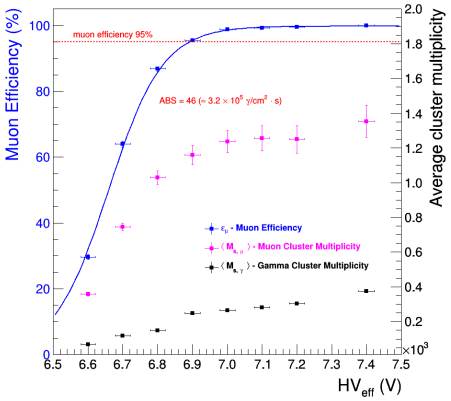

(c) $\phi_\gamma = 3.2 \times 10^5\ \gamma/cm^2 \cdot s$ (ABS 46).

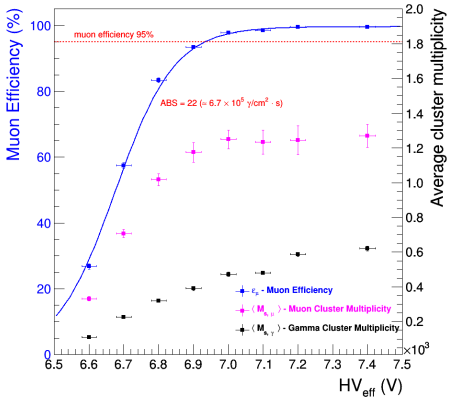

(d) $\phi_\gamma = 6.7 \times 10^5\ \gamma/cm^2 \cdot s$ (ABS 22).

Figure 7.42: Muon detection efficiency, muon and gamma cluster multiplicity as a function of the high voltage applied to the double-gap iRPC detector prototype at the different levels of the gamma photon flux from the source (the nominal filter absorption factors are indicated). The applied high voltage values have been normalized by using the PT correction formula explained in Section 6.2.2.2.

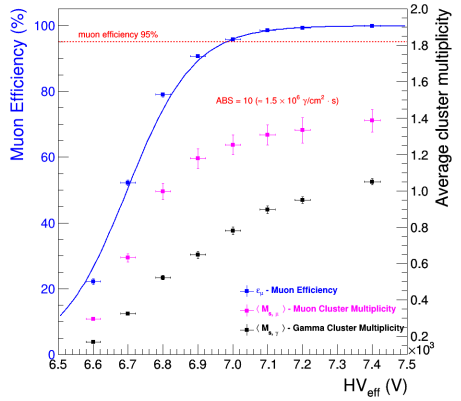

(a) $\phi_\gamma = 1.5 \times 10^6\ \gamma/cm^2 \cdot s$ (ABS 10).

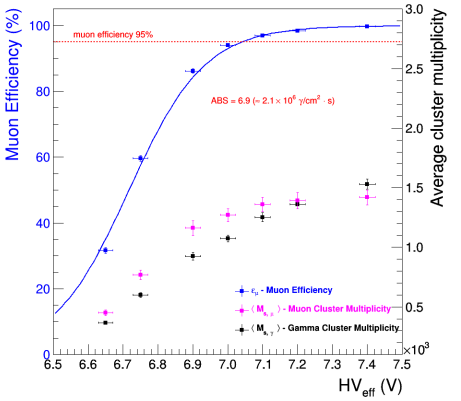

(b) $\phi_\gamma = 2.1 \times 10^6\ \gamma/cm^2 \cdot s$ (ABS 6.9).

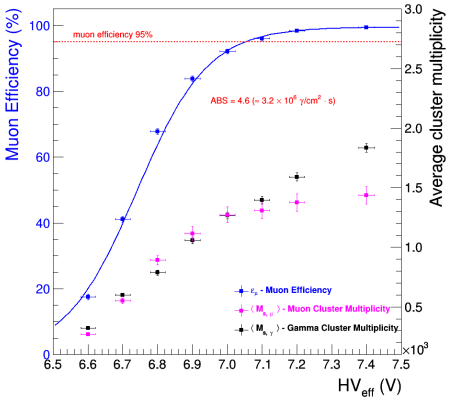

(c) $\phi_\gamma = 3.2 \times 10^6\ \gamma/cm^2 \cdot s$ (ABS 4.6).

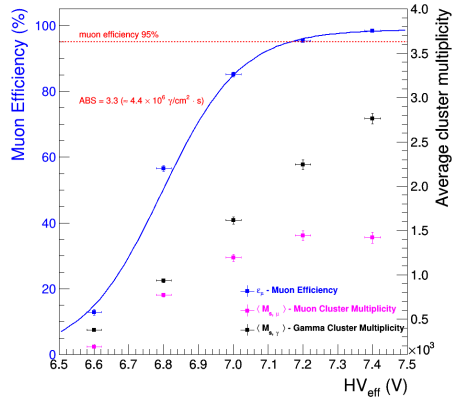

(d) $\phi_\gamma = 4.4 \times 10^6\ \gamma/cm^2 \cdot s$ (ABS 3.3).

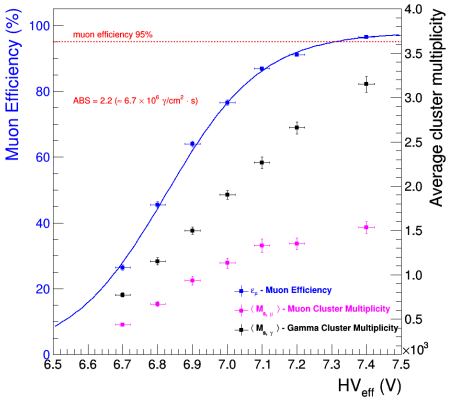

(e) $\phi_\gamma = 6.7 \times 10^6\ \gamma/cm^2 \cdot s$ (ABS 2.2).

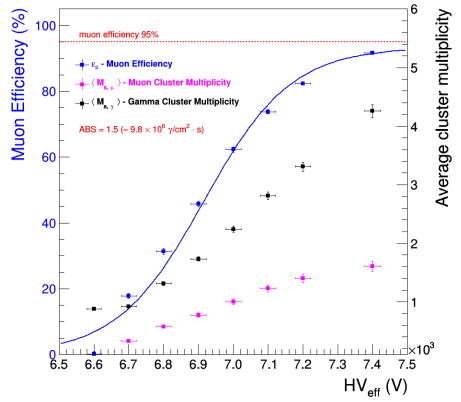

(f) $\phi_\gamma = 9.6 \times 10^6\ \gamma/cm^2 \cdot s$ (ABS 1.5).

Figure 7.43: Muon detection efficiency, muon and gamma cluster multiplicity as a function of the high voltage applied to the double-gap iRPC detector prototype at the different levels of the gamma photon flux from the source (the nominal filter absorption factors are indicated). The applied high voltage values have been normalized by using the PT correction formula explained in Section 6.2.2.2.

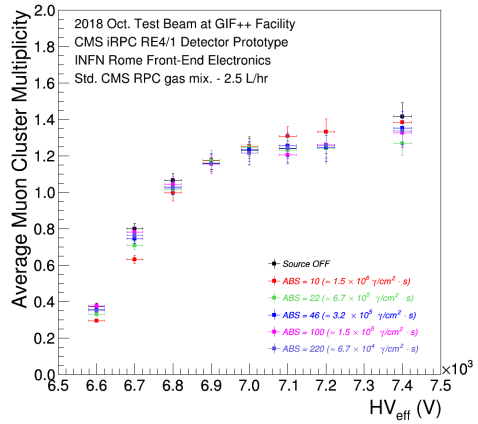

(a) Muon cluster multiplicity studies at the low background irradiation.

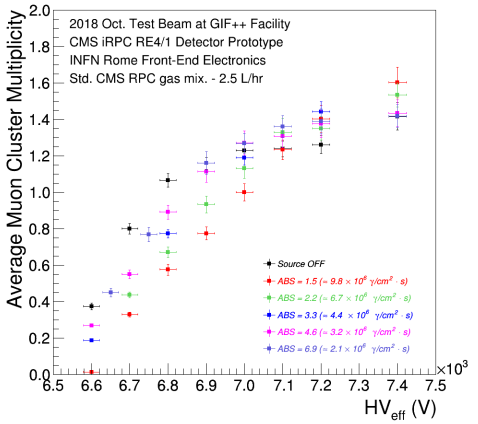

(b) Muon cluster multiplicity studies at the high background irradiation.

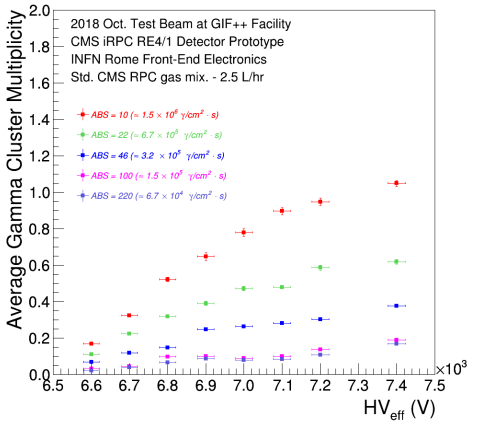

(c) Gamma cluster multiplicity studies at the low background irradiation.

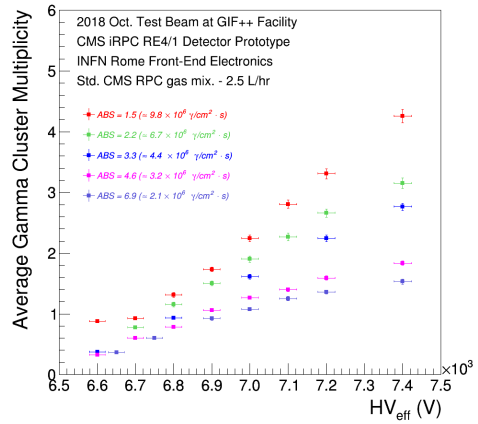

(d) Gamma cluster multiplicity studies at the high background irradiation.

Figure 7.44: Summary plots of the muon and gamma cluster multiplicity as a function of the high voltage applied to the double-gap iRPC detector prototype at the different levels of the gamma photon flux from the source (the nominal filter absorption factors are indicated). The applied high voltage values have been normalized by using the PT correction formula explained in Section 6.2.2.2.

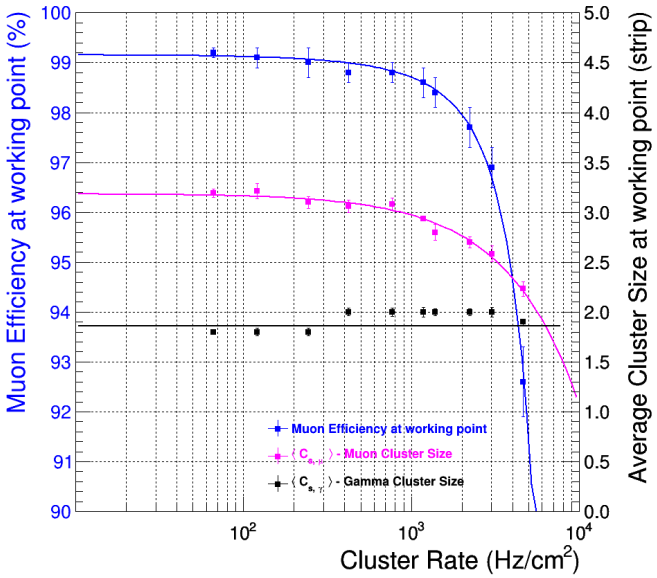

(a)

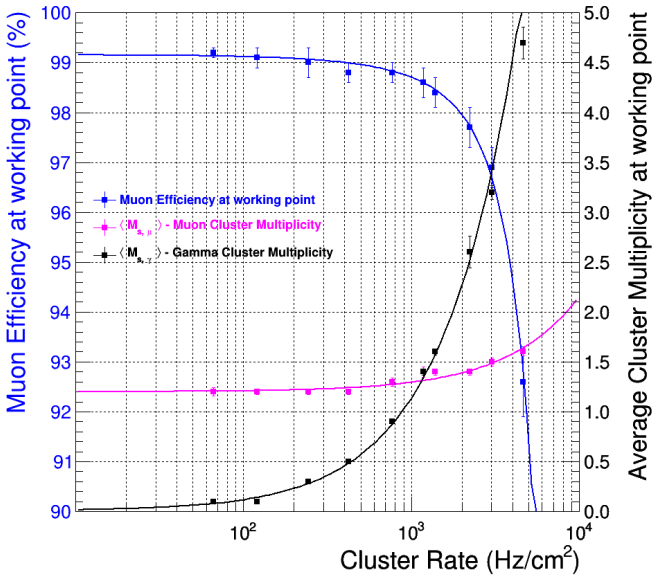

(b)

Figure 7.45: Summary results of the iRPC RE4/1 detector prototype with new INFN Rome Front-end electronics obtained during Test Beam period in October 2018. Muon detection efficiency at the working point as a function of the cluster rate,(a) muon and gamma cluster size at the working point as a function of the cluster rate, (b) muon and gamma cluster multiplicity at the working point as a function the cluster rate.

new INFN Rome electronics at the CERN CMS-RPC QA/QC facility. Particularly, in order to carefully study the uniformity of the detection efficiency, a new cosmic ray muon telescope setup has been developed by using three scintillator paddles marked as S_{bottom}, S_{middle} and S_{top}. These three scintillators paddles had different overall dimensions: S_{bottom}, S_{middle} with dimensions of 15 cm x 30 cm and 16 cm x 20 cm and the S_{top} with overall dimensions of 9 cm x 15 cm. Thus, in order to study the uniformity of the detection efficiency as a function of trigger position on the detector prototype, the final size of the telescope active area had the dimensions of 9 cm x 15 cm.

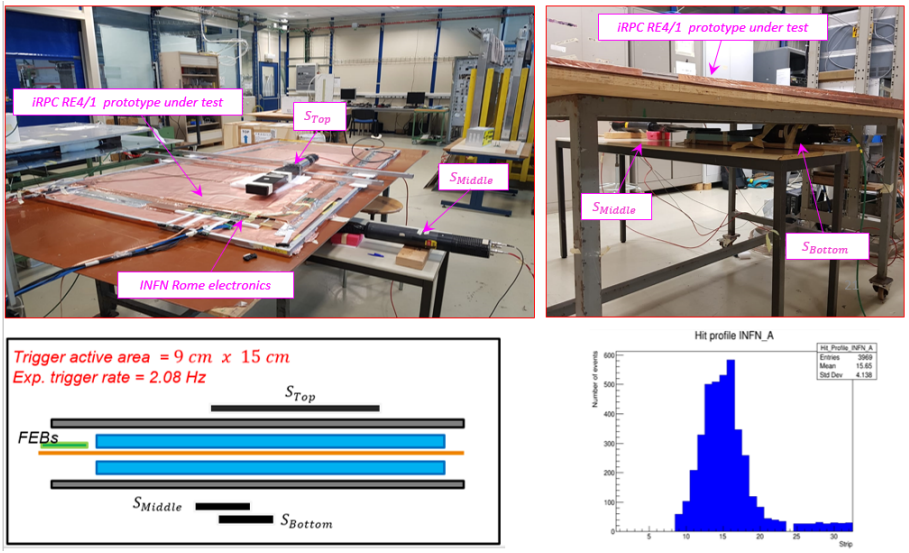

Figure 7.46: Picture of the experimental set-up and the schematic view of a cosmic ray muon telescope stand during the uniformity detection efficiency study campaign.

A discriminated AND (3 - fold coincidence) signal of these three scintillator paddles S_{bottom}, S_{middle} and S_{top} was considered as the master trigger. Master trigger signals were sent to a CAEN V1190A 128-Channel Multihit TDC in order to open the acquisition time window for the Data Acquisition (DAQ) system and to start the recording of the experimental data. Schematic view of the cosmic ray muon telescope stand and the picture of the experimental set-up during the uniformity detection efficiency study campaign are presented in Fig. 7.46. In order to map the efficiency, the measurements have been performed for six different trigger positions along strip direction. A trigger position map for the uniformity efficiency measurements is shown in Fig 7.47. For these studies, the top honeycomb panel of the detector casing was removed to precisely control the trigger position with respect to the strips under test. The efficiency scanning in each position under test has been continuously taken during 12 hours in order to record enough data and to reduce the statistical error.

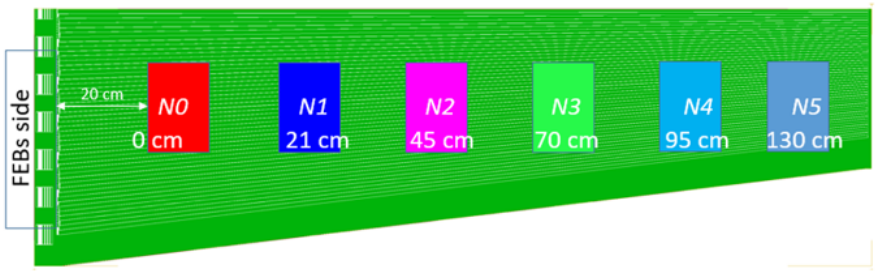

Figure 7.47: A trigger position map for the uniformity efficiency measuremens.

7.6.2 Data Acquisition System

For this additional performance study, a new electronics rack has been installed. On this electronics rack, all electronics needed to operate with prototype such as the NIM crates, VME crate with VME -USB 2.0 Bridge and TDC, High Voltage and Low Voltage power supplies, and the portable computer with WebDCSportable-software, have been mounted. Picture of the electronics rack and principle scheme of DAQ are given in Fig. 7.48.

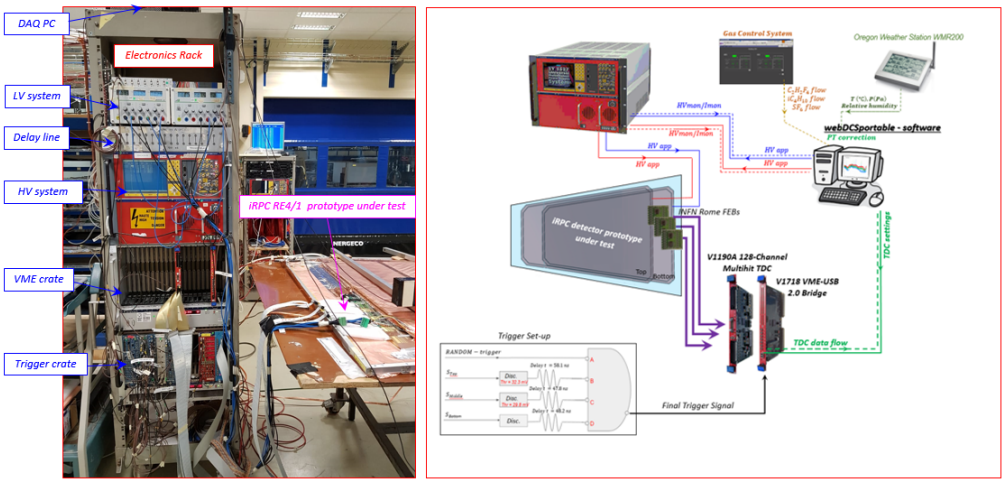

Figure 7.48: Picture of the electronics rack and principle scheme of the Data Acquisition System installed at the CERN CMS-RPC QA/QC facility for the uniformity efficiency studies.

The communication between the PC and the VME crate is made through the CAEN VME USB Bridge. During the measurements, the constant monitoring of all the environmental parameters, gas parameters, temperature, pressure and voltage and current values delivered by the power supplies have been performed and displayed on the WebDCSportable software. More detailed information about the Detector Control System was already described in Section 6.5.2.

7.6.3 Results and Discussions

Electrical test of the gas gaps. After one-week of continuous irradiation with a very high dose of gamma rays during the Test Beam in October 2018, an electrical test of the bottom and top gas gaps has been carried out in order to investigate any possible damages due to the strong irradiation. The results of the high voltage integrity test for the bottom and top gas gaps are presented in Fig. 7.49. No damages after strong irradiation and after subsequent transportation of the detector prototype form CERN GIF++ facility to the CERN CMS-RPC QA/QC facility have been found. The average current value of the bottom and top gas gaps remained consistently low (below 0.035 uA).

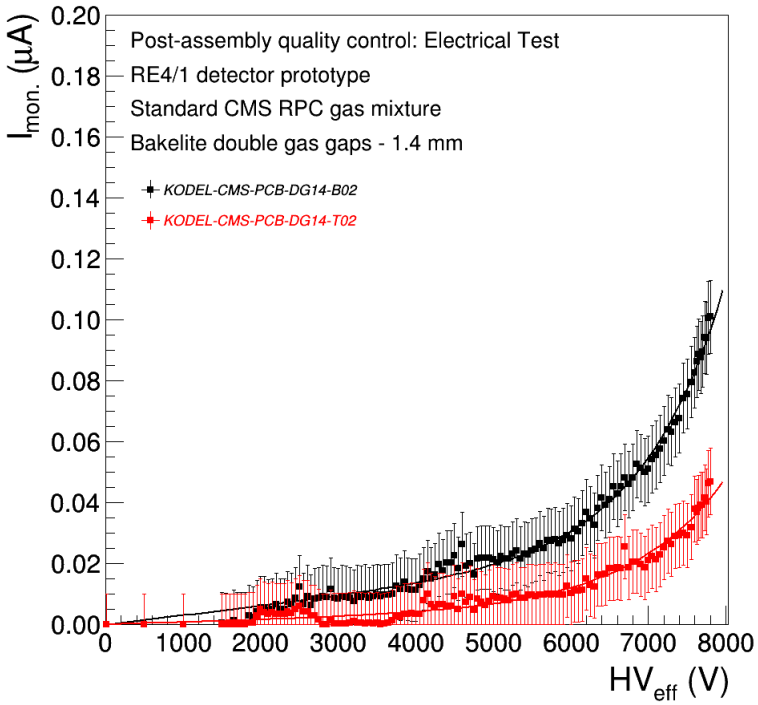

Figure 7.49: Results of the high voltage integrity test for the bottom and top gas gaps installed in the iRPC RE4/1 detector prototype after the Test Beam in October 2018 campaign.

Uniformity studies of muon detection efficiency. During the uniformity campaign, six different trigger positions on the strips longitudinal coordinate have been investigated. For each trigger position, the measurement of the muon detection efficiency has been performed in double, bottom and top gas gaps mode. In particular, for each operation mode at the different trigger position, the experimental data have been interpolated by using a standard sigmoidal fitting curve in order to extract all the interesting parameters. Summary plots of the muon detection efficiency for double and single gap mode

as a function of the applied high voltage point for all scanned trigger position on the active area of the prototype are presented in Fig. 7.50. The electronic threshold value for the uniformity studies was identical to the thresould value used during the Test Beam period (5-10 fC).

By using the fitting results, the working point values for the different trigger positions have been estimated. Fig. 7.51 shows the detector working point as a function of the trigger positions on the detector active area for the double and single gap mode. The efficiency at the working point in the double gas gap mode is quite stable along the strips longitudinal coordinate with small fluctuations within 1-2%, the average value of the working point being 7085.4 V. For the single gap modes the variation is within 2-3%. The average value of the working point is 7348.0 V for the bottom gas gap and 7332.5 V for the top gas gap, respectively. The working point values in the double gap mode are lower with respect to those measured in the single gap mode. It can be explained by assuming that an ionizing particle crossing this detector, when it operates with two gas gaps, produce ion-electron pairs in both gaps and the signals induced by the avalanches in the two gaps are practically simultaneous and add up on the central readout electrodes. It increases the detection efficiency of the detector at the lower voltage values compared to the single gas gap. The last fact is confirmed by the detection efficiency values at the working point for each operational regime: $\varepsilon(7085.4V) = 98.77\%$ for the double gap mode, $\varepsilon(7348.0V) = 96.64\%$ for bottom gas gap and $\varepsilon(7332.5V) = 97.13\%$ for the top gas gap, respectively. The detection efficiency at the working point as a function of a different trigger position is shown in Fig. 7.52: the efficiency values at working point are comparable along the strips longitudinal coordinate with small fluctuations within 2%.

The previous results of the efficiency at working point show that each sector along the strips longitudinal coordinate of the detector has different working point values. Fig. 7.53 shows the detection efficiency as a function of the trigger position for a fixed working point equal to the average values of Fig. 7.51. Measurements refer to the double and single gap modes: the average detection efficiency for the double gap mode is around 98.69 %, while for the bottom and top gas gaps is 96.58% and 97.0%. The efficiency drop at some trigger position could be affected by the presence of the spacers.

Cluster size uniformity studies. In addition, the muon cluster size has been measured at different trigger position and has been computed around the fastest fired strip by counting the number of adjacent strips fired within 10 ns. In Fig. 7.54 the muon cluster size as a function of applied high voltage for the double and single gap mode are presented. The muon cluster size increases with increasing high voltage because of the increasing charge produced in the chamber. Moreover, the increasing signal amplitude could also produce a large amount of cross-talk. Therefore, the measurement of the muon cluster size was affected by the presence of cross-talk among the readout strips.

Fig. 7.55 shows the muon cluster size at the working point as a function of

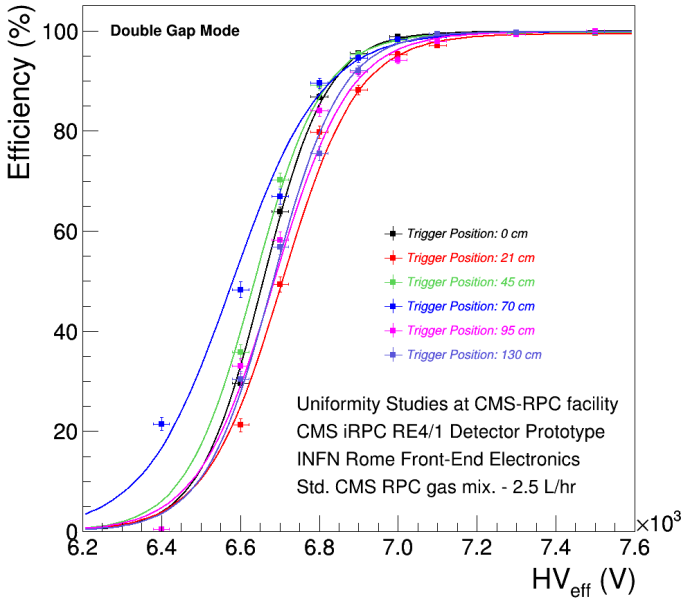

(a) Uniformity of muon efficiency studies for the double gas gap regime.

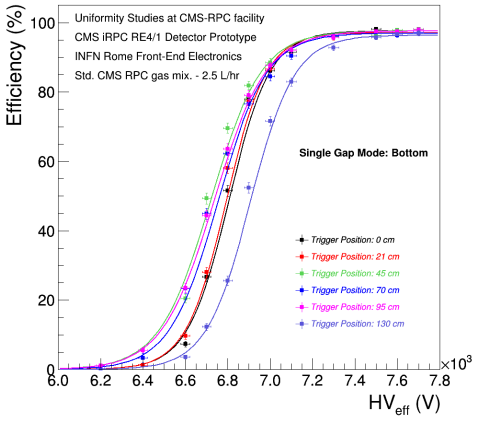

(b) Uniformity of muon efficiency studies for the bottom gas gap regime.

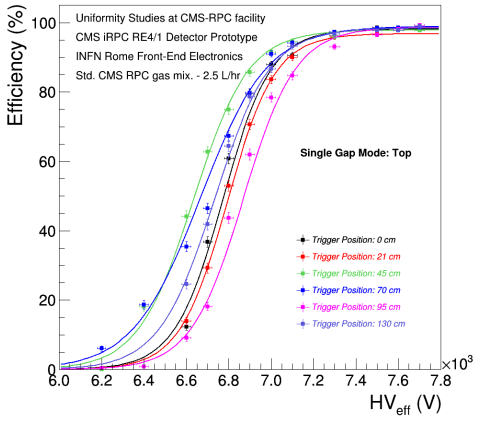

(c) Uniformity of muon efficiency studies for the top gas gap regime.

Figure 7.50: Summary plots of the muon detection efficiency for the double (a), bottom (b) and top (c) gas gaps regimes as a function of the applied high voltage for all scanned trigger position on the active area of the iRPC RE4/1 detector prototype. The applied high voltage values have been normalized by using the PT correction formula explained in Section 6.2.2.2.

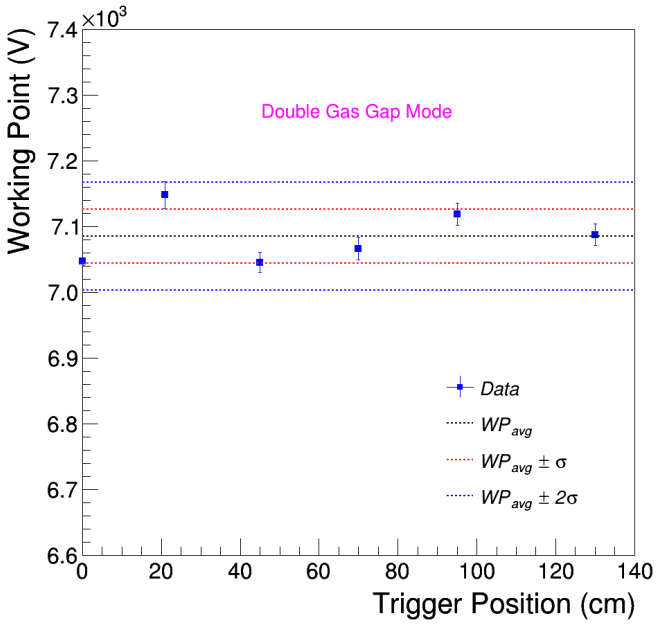

(a) Working point studies for the double gas gap regime.

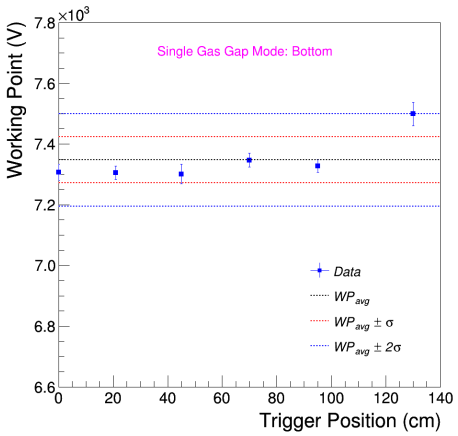

(b) Working point studies for the bottom gas gap regime.

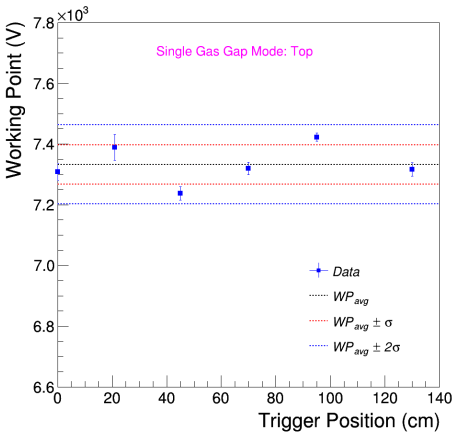

(c) Working point studies for the top gas gap regime.

Figure 7.51: Working point as a function of the trigger position on the detector active area for the double (a), bottom (b) and top (c) gas gaps. The working point values for the double, bottom and top gas gaps are comparable along the strips longitudinal coordinate with a small fluctuations within 3%.

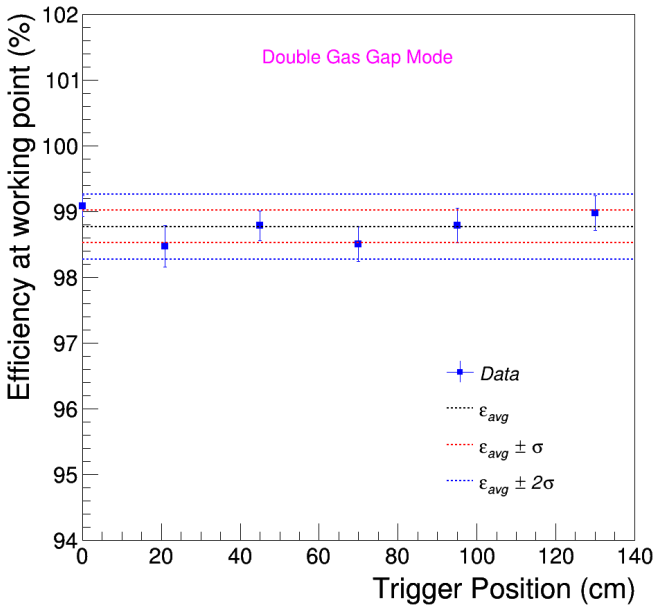

(a) Efficiency at WP studies for the double gas gap regime.

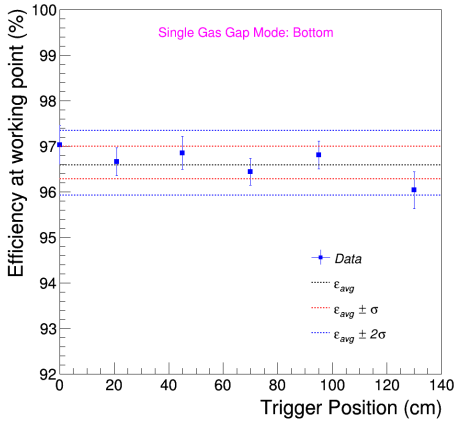

(b) Efficiency at WP studies for the bottom gas gap regime.

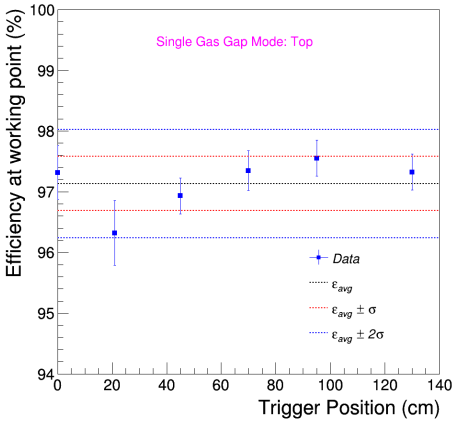

(c) Efficiency at WP studies for the top gas gap regime.

Figure 7.52: Detection efficiency at working point as a function of the trigger position on the detector active area for the double (a), bottom (b) and top (c) gas gaps. The efficiency values at the working point for the double, bottom and top gas gaps are comparable along the strips longitudinal coordinate with a small fluctuations within 2%.

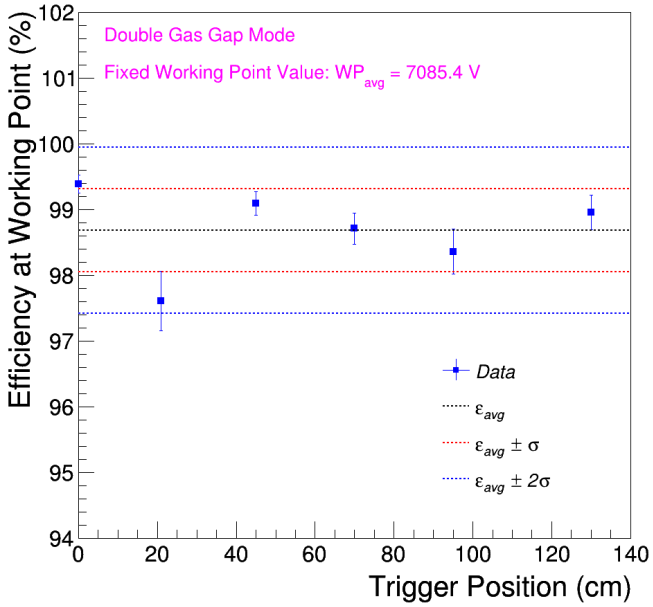

(a) Efficiency at fixed WP studies for the double gas gap regime.

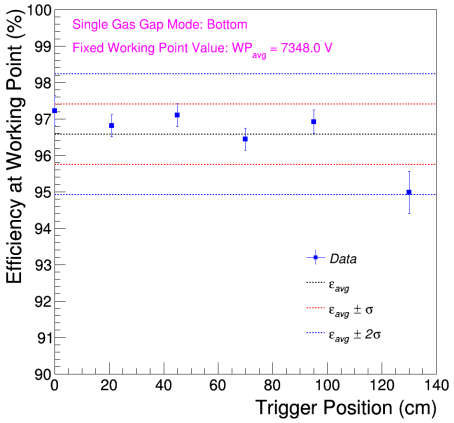

(b) Efficiency at WP studies for the bottom gas gap regime.

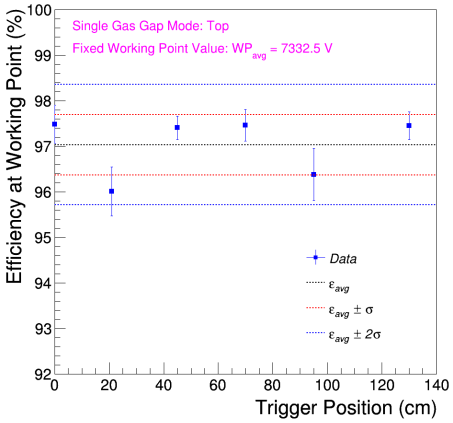

(c) Efficiency at fixed WP studies for the top gas gap regime.

Figure 7.53: Detection efficiency at fixed applied working point value as a function of the trigger position on the detector active area for the double (a), bottom (b) and top (c) gas gaps.

the trigger position on the detector active area. The muon cluster size of the double gas gap is stable within 5%. Concerning the results of the muon cluster size at the working point for the bottom and top gas gaps are comparable along the strips longitudinal coordinate with fluctuation within 10%.

As described previously in the uniformity studies of the muon detection efficiency, the average working point value has been chosen in order to measure the muon cluster size at fixed working point value for each trigger position. In Fig. 7.56 is shown the muon cluster size at the fixed working point value as a function of the trigger position for double and single gas gaps modes, respectively: at the fixed working point value, the average muon cluster size for the double gap, the bottom and top gas gaps is around 3.1. The muon cluster size values are stable along the strips longitudinal coordinate and only fluctuate within 10-15%.

Thus, the studies show that at the fixed working point, the muon cluster size is typically 3.1 proving that the strip cross-talk is not negligible. A second-order contribution to the high value of the muon cluster size is also due to the low electronics threshold 5-10 fC applied during the uniformity studies campaign.

In the last step of the uniformity studies, by following the same structure of measurements, the muon cluster multiplicity for double and single gap mode have been studied (see Fig. 7.57): the muon cluster multiplicity increases with increasing high voltage and reaches a plateau level because the muon detection efficiency reaches closely 100% and the muon particles per trigger is nearly constant (average value about 1.1 for each operation mode). Fig. 7.58 swons the results of the muon cluster multiplicity at the working point for the double gap only: the cluster multiplicity value is comparable along the strips longitudinal coordinate with negligible fluctuations within 2%.

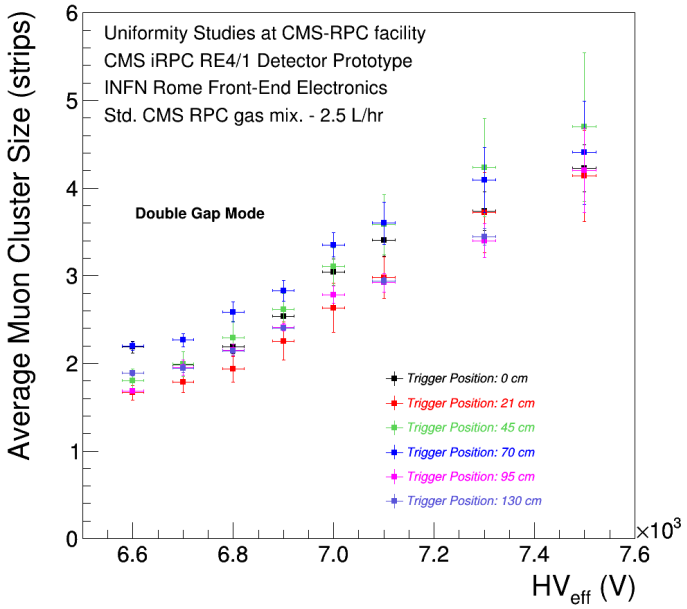

(a) Muon cluster size studies for the double gas gap regime.

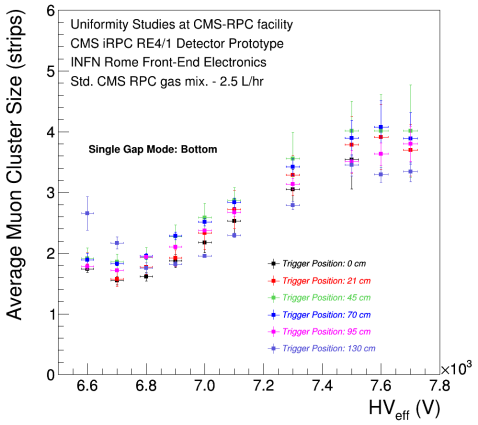

(b) Muon cluster size studies for the bottom gas gap regime.

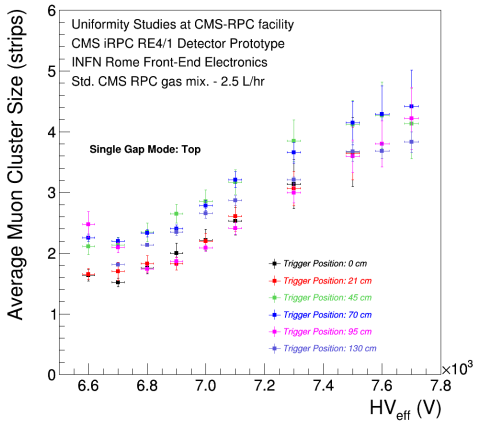

(c) Muon cluster size studies for the top gas gap regime.

Figure 7.54: Muon cluster size as a function of the applied high voltage at the different trigger position on the detector active area for the double (a), bottom (b) and top (c) gas gaps. The applied high voltage values have been normalized by using the PT correction formula explained in Section 6.1.2.2.

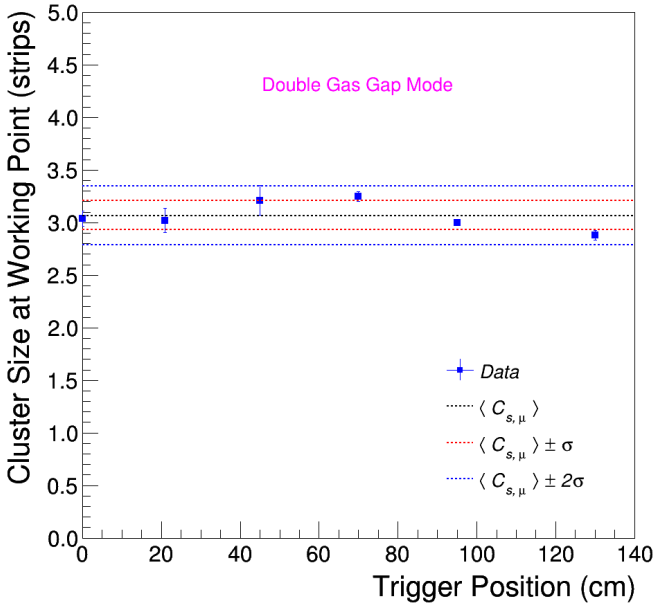

(a) Cluster size at working point studies for double gas gap regime.

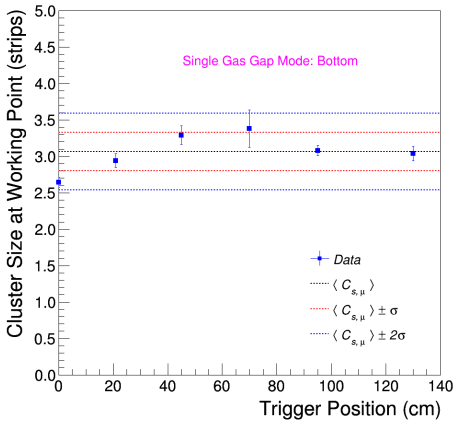

(b) Cluster size at working point studies for bottom gas gap regime.

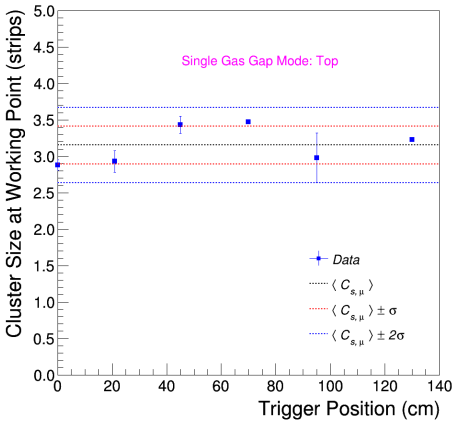

(c) Cluster size at working point studies for top gas gap regime.

Figure 7.55: Cluster size at working point as a function of the trigger position on the detector active area for the double (a), bottom (b) and top (c) gas gaps.

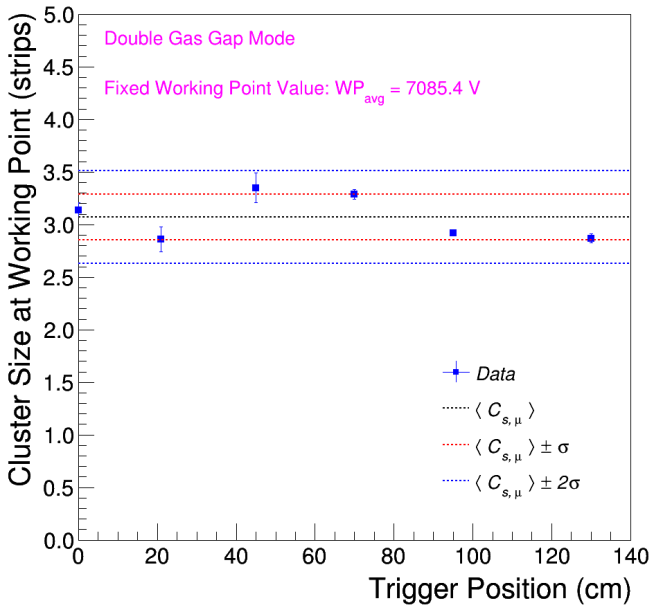

(a) Cluster size at fixed WP for the double gas gap regime.

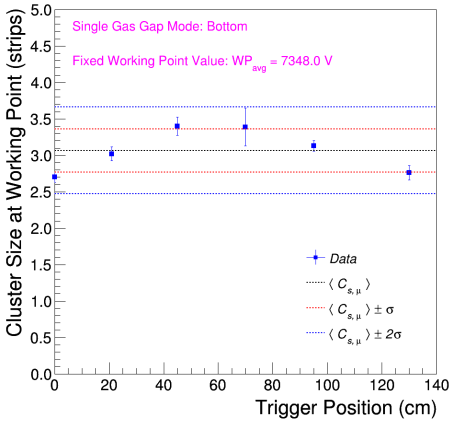

(b) Cluster size at fixed WP for the bottom gas gap regime.

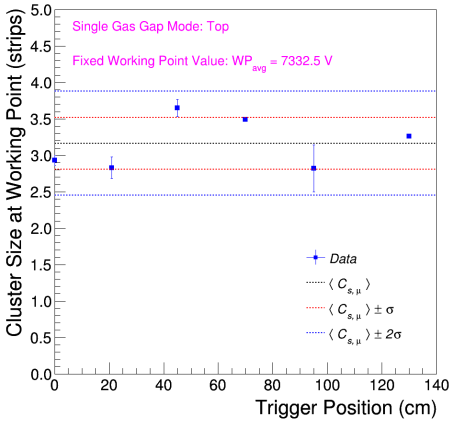

(c) Cluster size at fixed WP for the top gas gap regime.

Figure 7.56: Muon cluster size at the fixed applied working point value as a function of the trigger position on the detector active area for the double (a), bottom (b) and top (c) gas gaps.

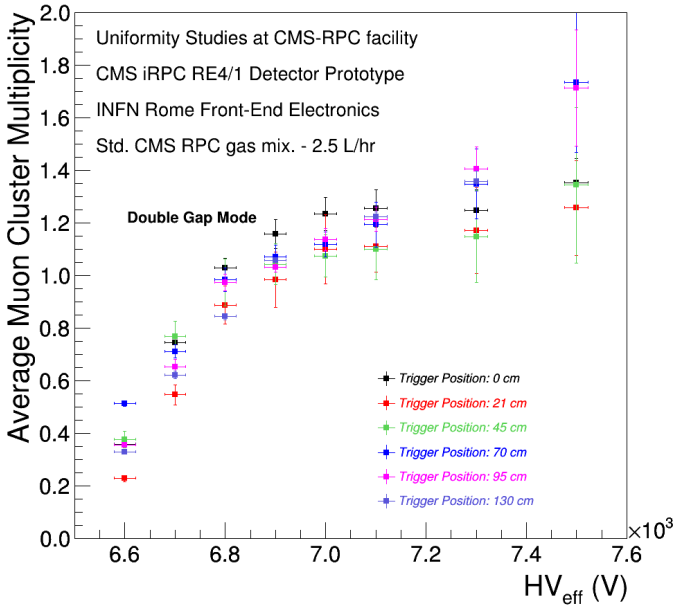

(a) Cluster multiplicity studies for the double gas gap regime.

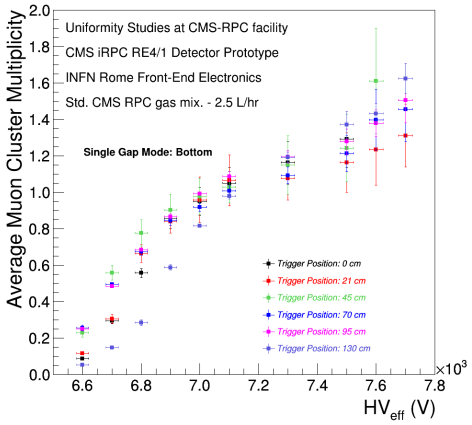

(b) Cluster multiplicity studies for the bottom gas gap regime.

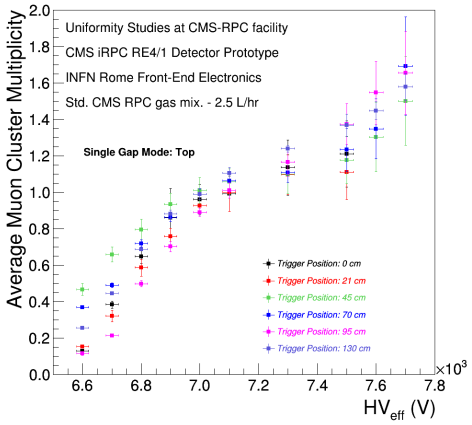

(c) Cluster multiplicity studies for the top gas gap regime.

Figure 7.57: Cluster multiplicity as a function of the applied high voltage at the different trigger position on the detector active area for the double (a), bottom (b) and top (c) gas gaps. The applied high voltage values have been normalized by using the PT correction formula explained in Section 6.2.2.2.

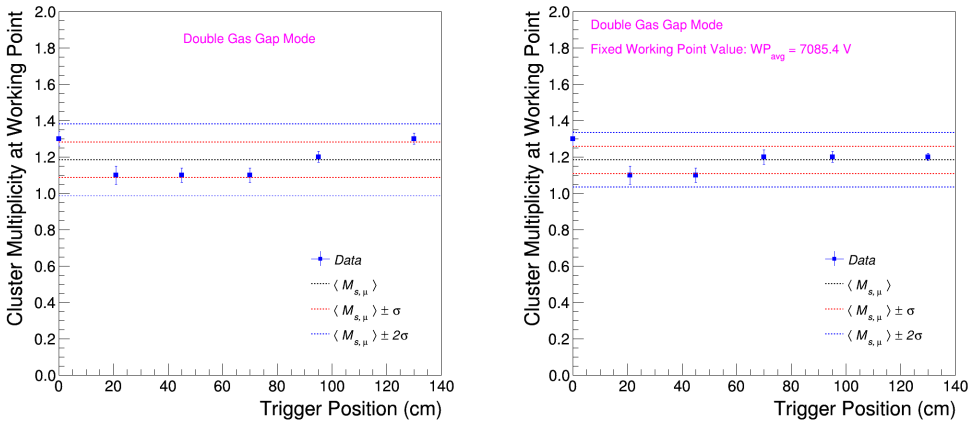

(a) Cluster multiplicity for the double gas gap regime.

(b) Cluster multiplicity at fixed WP for the double gas gap regime.

Figure 7.58: Cluster multiplicity as a function of the trigger position on the detector active area for the double gas gaps.

Chapter 8

General Conclusions

The Compact Muon Solenoid (CMS) is a general purpose experiment measuring proton-proton and heavy-ion collisions at Large Hadron Collider (LHC) at CERN laboratory, in Geneva. The detector has been running successfully at unprecedented proton-proton center-of-mass energies up to 13 TeV, with a luminosity exceeding 10^{34} $cm^{-2}s^{-1}$. The missing key particle of the Standard Model, the Brout-Englert-Higgs boson, was discovered through its two-photon and leptonic decay modes in 2012. To extend the sensitivity for new physics searches, a major upgrade of the LHC has been decided and is being prepared, the High Luminosity LHC (HL-LHC). The center-of-mass energy for proton-proton collisions is expected to be raised from the current 13 TeV up to 14 TeV and the instantaneous luminosity is expected to exceed the nominal value and reach 2.5×10^{34} $cm^{-2}s^{-1}$, after the second Long Shutdown (LS2) in 2019-2020. A further increase is planned during the third Long Shutdown (LS3) in 2024-2026, up to 5×10^{34} $cm^{-2}s^{-1}$, i.e. a yield five times larger than the initial LHC design. The increase of the center-of-mass energy and instantaneous luminosity during the future upgrades of the LHC machine will deeply affect the performance of the CMS detectors as well as their data acquisition system due to the harsh background environment and the high pile-up. To cope with very high operation condition, high pile-up and background environment the CMS experiment and the muon detectors, in particular, need major upgrades.

This Doctoral Thesis has been carried out in the framework of the upgrade of the forward muon spectrometer of the CMS experiment. One of the future major CMS upgrade is the addition of new detector layers in the forward muon spectrometer of CMS experiment. The detector technology chosen by the CMS Collaboration for this upgrade is the new generation of the Resistive Plate Chamber technology, the so-called improved RPC (iRPC). The new set of iRPC detectors will be installed in two inner forward regions of the Muon System of the CMS experiment at $1.8 < \eta < 2.4$, called RE3/1 and RE4/1 stations, during the annual Year-End Technical Stops 2022 & 2023. The RE3/1 and RE4/1 detectors are wedge-shaped RPC detectors, each contains a double

1.4 mm high-pressure laminates plate, making 1.4 mm thick the gas gap. They will cover 20° in RE3/1 and RE4/1 stations, respectively, overlapping in φ just like the corresponding CSC detectors in ME3/1 and ME4/1 stations, complementing them and providing redundancy and enhanced triggering and tracking capabilities in the region which currently suffers from the highest background rates and a non-uniform magnetic field. The iRPC project will add 18 new chambers per muon disk, i.e. 72 chambers in total for the RE3/1 and RE4/1 stations in both muon endcaps in order to ensure the full azimuthal coverage. Each station will provide one single hit for muon reconstruction with precise time information of about 2 ns, spatial resolution in the transverse direction of about 0.3 cm and 2 cm along strip.

During the Ph.D period carried out in the Naples group belonging to the CMS Collaboration, I worked on engineering part and hardware, starting with the engineering design of the new CMS-iRPC RE3/1 and RE4/1 stations. In particular, I focused my work on the integration and installation of new iRPC RE3/1 and RE4/1 chambers in the innermost region of CMS Muon Spectrometer. This activity was crucial for all iRPC project. I organized and performed dedicated survey measurements in order to determine the space actually available for installation of the new iRPC detectors during the Yearly Technical Stops at the end of 2022 and 2023. The surfaces topology and geometry of the Yoke Endcap (YE) ±2 and YE±3 iron disks in the region $1.8<|\eta|<2.4$ have been studied in detail by using different methods such as photography and photogrammetry, theodolite and the infrared proximity sensor. After analyzing the experimental data obtained during the survey measurements, I developed a very precise 3D-model of the mechanical simulation for the installation iRPC RE3/1 and RE4/1 chambers in the innermost region of CMS Muon Spectrometer. I designed the mechanical components to mount chambers here. This first experience allowed me to have a comprehensive view of the RPC detector and was really useful in the second part of my Ph.D.

My second activity consisted of developing and assembling the first real-size iRPC iRE3/1 and RE4/1 detector prototypes at the CMS-RPC QA/QC facility. In August 2017, I developed the first real-size improved RPC RE3/1 and RE4/1 detector prototypes and studied its performence with the first version of the new PETIROC ASIC front-end electronics. I was the key person for both the production and test of all the detector elements, assembling of the new improved CMS-RPC detector prototypes and subsequent testing of the prototypes with new electronics using the muon beam at the CERN Gamma Irradiation Facility (GIF++) in August 2018. By using the unique test area of the CERN GIF++ facility, I have studied the iRPC detector performance at background rates similar to the future CMS conditions during the HL-LHC program. By studying the rate capability of the real-size iRPC detector prototypes I experimentally shown that iRPC technology can effectively operate in the harsh background CMS environment:

- at the expected rates during the Phase-II at HL-LHC of the order of 2

kHz/cm^2, the maximum detection efficiencies of the iRPC RE3/1 and RE4/1 detector prototypes with the first version of the PETIROC ASIC front-end electronics are approximately 97.3 % and 97.1 %, well above the 95% required by the CMS specs;

- the operational high voltage and the efficiency at the working point are 7367 V (7402 V) and 96.1 % (96.4%) for RE4/1 (RE3/1) chambers. The working point of the iRPC detector is substantially reduced with respect to the present RPC detector (around 10 kV);
- the average charge of the gamma background particle is about 6.8 pC when digitized at a threshold 81 fC for RE4/1 detector and 107.8 fC for RE3/1 chambers at the high gamma particle rate. The average charge of iRPC is 3 times less than the present CMS RPC system (21pC). Thus slowing down the aging process of the detection components;
- the observed muon cluster size value of the iRPC is around 2.5 due to the large capacitive cross-talk among the iRPC strips while a value smaller than 2 is required by the specs. Additional studies will be carried out to better understand the effect of the cross-talk on the cluster size.

My last activity was the test of new Front-end electronics developed by INFN Rome on the iRPC detector prototype. The INFN Rome electronics has been proposed as a possible alternative to PETIROC ASIC electronics to significantly reduce the risk of failure associated with a single choice. In September 2018, I developed and assembled the second real-size iRPC RE4/1 detector prototype in the INFN Rome Tor Vergata laboratories in order to study the performance of this detector with the INFN Rome Front-end electronics. As in the previous research activity, I performed the test of the iRPC prototype with the INFN Rome electronics in the last available muon particle beam at the GIF++ facility at CERN before the Long Shutdown-2 period. I studied the detection performance and I have shown that this type of new electronics can effectively replace the PETIROC ASIC electronics:

- at the expected rates of 2 kHz/cm^2, the muximum detection efficiency of the iRPC RE4/1 prototypes with the INFN Rome Front-end electronics is 98 %;
- the operational high voltage and the efficiency at the working point are 7190 V and 98.6%;
- the average charge of the gamma background particle is about 8 pC when digitized at a threshold 5-10 fC at the high gamma particle rate;
- the observed muon cluster size value is around 3. The high value of the muon cluster size can be explained by the sensitivity of the components of the electronics and the low electronics threshold value (5-10 fC) applied to the INFN Rome electronics during the Test Beam in October 2018.

All results obtained in this Ph.D. thesis contributed to the success of the iRPC project and its final approval by CMS Collaboration.

Appendix A

Characterisation of the real-size iRPC RE3/1 Detector Prototypes

Current density J_{mon} and counting rate R_γ are two physical quantities closely related to each other. Indeed, monitoring the current in the individual gas gaps composing a iRPC detector prototype, while knowing the rate, the charge deposition per avalanche q_γ can be computed. The current driven by the gas gap is assumed to be due to the irradiation, i.e. to the avalanches developing in the gas gap due to the gamma photons of the ^{137}Cs source. Moreover, counting rate is supposed to be a measure of the number of gamma photons interacting with the gas gap of the detector prototype. Therefore, the charge deposition per avalanche is expressed like: $q_\gamma = J_{mon} / R_\gamma$, where J_{mon} is the monitored current density and R_γ the measured average background hit rate. In particular, the relation between current density and counting rate is linear as shown in the Fig. A.1 - A.4, where the average current density values are plotted as a function of the average background hit rate at different levels of gamma photon flux from the source both for bottom and top gas gaps of the iRPC RE3/1 detector prototype.

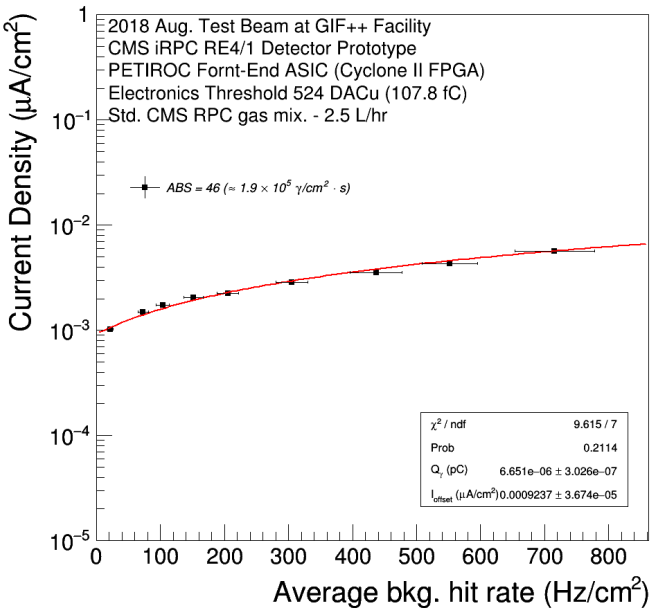

(a) $\phi_\gamma = 3.2 \times 10^5\ \gamma/cm^2 \cdot s$ (ABS 46).

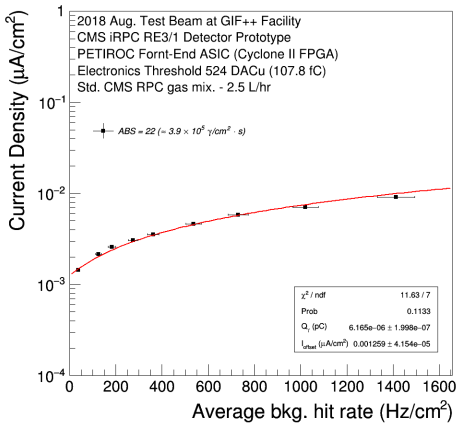

(b) $6.7 \times 10^5\ \gamma/cm^2 \cdot s$ (ABS 22).

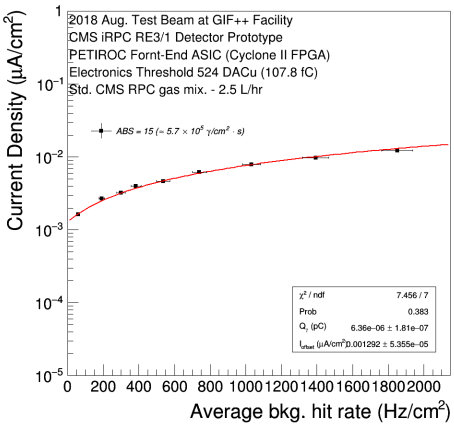

(c) $\phi_\gamma = 9.7 \times 10^5\ \gamma/cm^2 \cdot s$ (ABS 15).

Figure A.1: Average current density as function of average background hit rate for the bottom gas gap of the iRPC RE3/1 detector prototype at different levels of gamma photon flux from the source (*ABS factors*: 46, 22, 15).

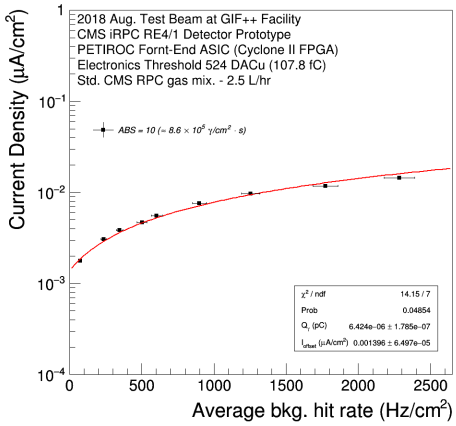

(a) $\phi_\gamma = 1.5 \times 10^6\ \gamma/cm^2 \cdot s$ (ABS 10).

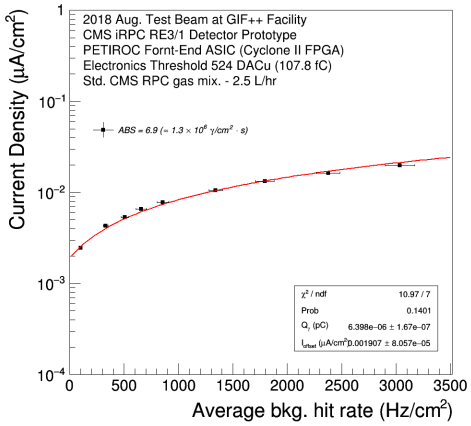

(b) $\phi_\gamma = 2.1 \times 10^6\ \gamma/cm^2 \cdot s$ (ABS 6.9).

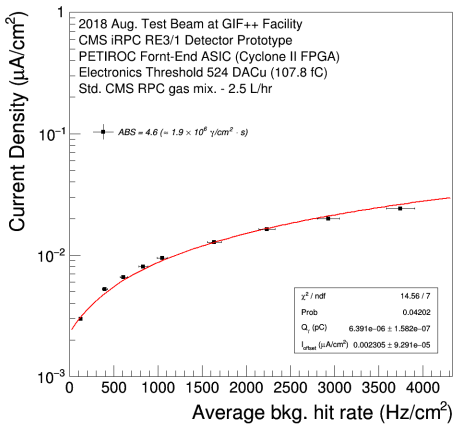

(c) $\phi_\gamma = 3.2 \times 10^6\ \gamma/cm^2 \cdot s$ (ABS 4.6).

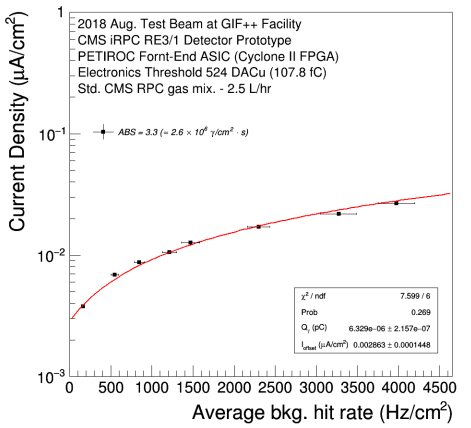

(d) $\phi_\gamma = 4.4 \times 10^6\ \gamma/cm^2 \cdot s$ (ABS 3.3).

Figure A.2: Average current density as function of average background hit rate for the bottom gas gap of the iRPC RE4/1 detector prototype at different levels of gamma photon flux from the source (*ABS factors*: 10, 6.9, 4.6, 3.3).

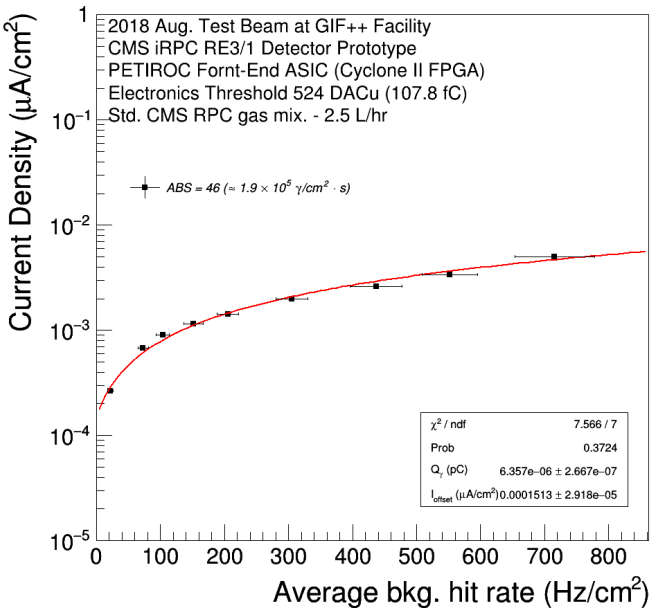

(a) $\phi_\gamma = 3.2 \times 10^5\ \gamma/cm^2 \cdot s$ (ABS 46).

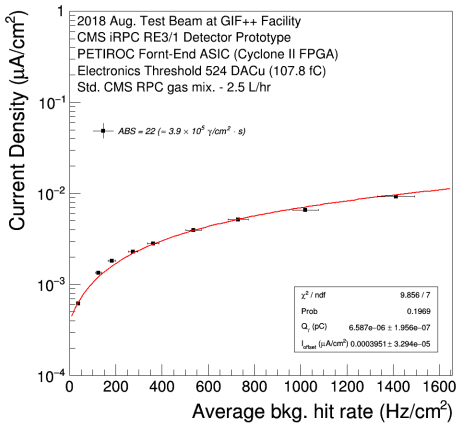

(b) $\phi_\gamma = 6.7 \times 10^5\ \gamma/cm^2 \cdot s$ (ABS 22).

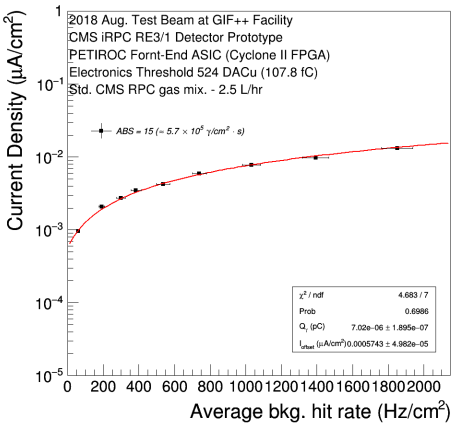

(c) $\phi_\gamma = 9.8 \times 10^5\ \gamma/cm^2 \cdot s$ (ABS 15).

Figure A.3: Average current density as function of average background hit rate for the top gas gap of the iRPC RE3/1 detector prototype at different levels of gamma photon flux from the source (*ABS factors*: 46, 22, 15).

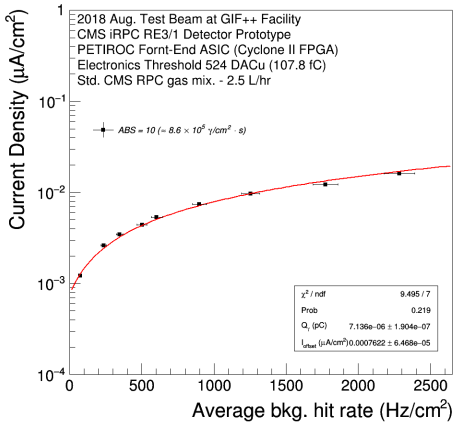

(a) $\phi_\gamma = 1.5 \times 10^6\ \gamma/cm^2 \cdot s$ (ABS 10).

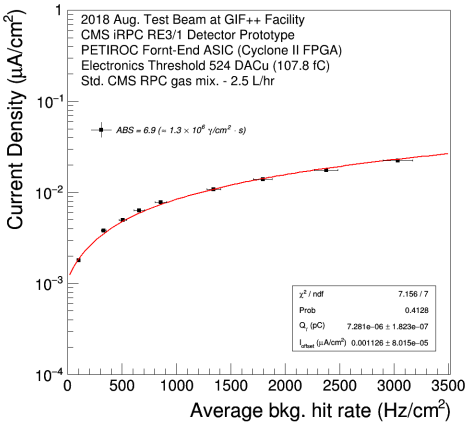

(b) $\phi_\gamma = 2.2 \times 10^6\ \gamma/cm^2 \cdot s$ (ABS 6.9).

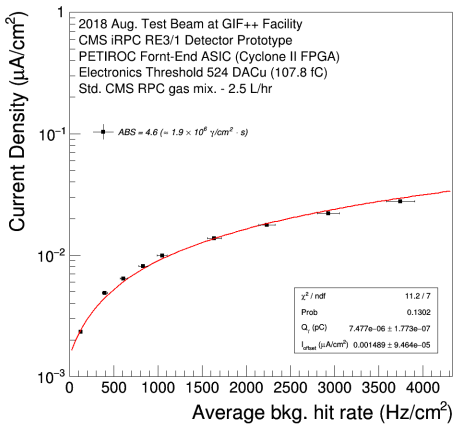

(c) $\phi_\gamma = 3.2 \times 10^6\ \gamma/cm^2 \cdot s$ (ABS 4.6).

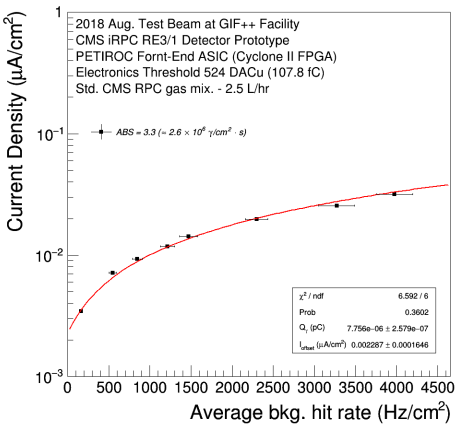

(d) $\phi_\gamma = 4.4 \times 10^6\ \gamma/cm^2 \cdot s$ (ABS 3.3).

Figure A.4: Average current density as function of average background hit rate for the top gas gap of the iRPC RE3/1 detector prototype at different levels of gamma photon flux from the source (*ABS factors*: 10, 6.9, 4.6 and 3.3).

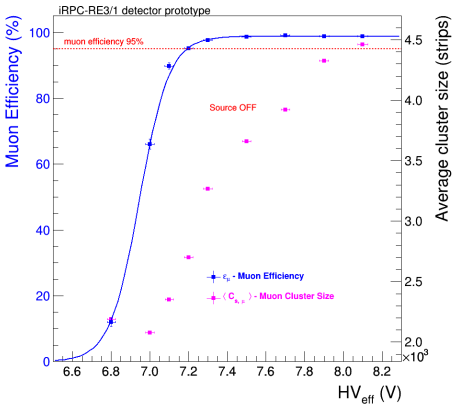

(a) Cluster size studies without gamma photon flux.

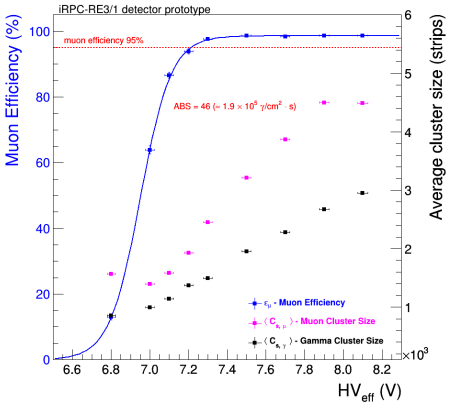

(b) $\phi_\gamma = 1.9 \times 10^5\ \gamma/cm^2 \cdot s$ (ABS 46).

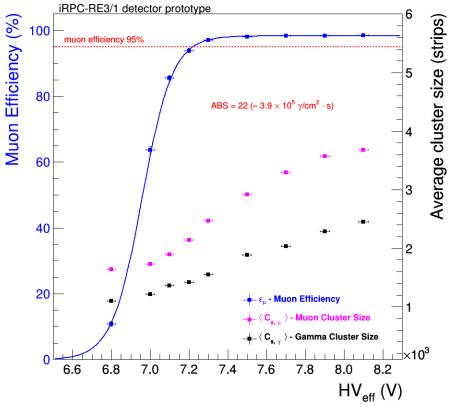

(c) $\phi_\gamma = 3.9 \times 10^5\ \gamma/cm^2 \cdot s$ (ABS 22).

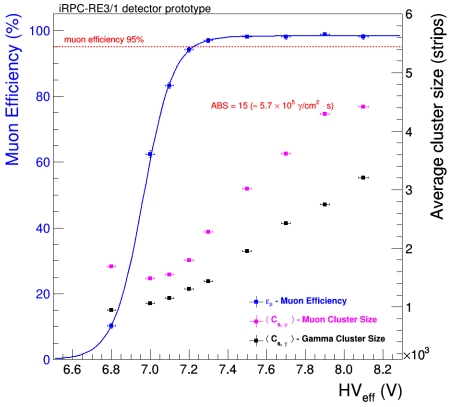

(d) $\phi_\gamma = 5.7 \times 10^5\ \gamma/cm^2 \cdot s$ (ABS 15).

Figure A.5: Muon detection efficiency, muon and gamma cluster size as a function of high voltage applied to the RE3/1 prototype at different levels of gamma photon flux from the source (the nominal filter absorption factors are indicated). The applied high voltage values have been normalized by using the PT correction formula explained in Section 6.2.2.2.

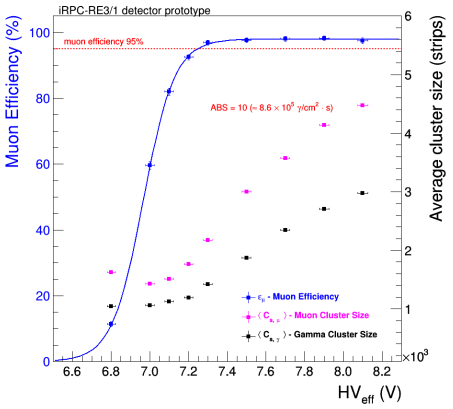

(a) $\phi_\gamma = 8.6 \times 10^5\ \gamma/cm^2 \cdot s$ (ABS 10).

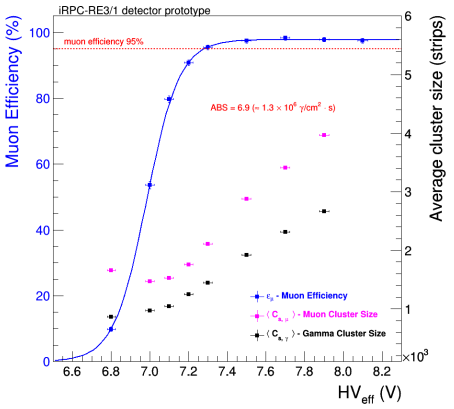

(b) $\phi_\gamma = 1.3 \times 10^6\ \gamma/cm^2 \cdot s$ (ABS 6.9).

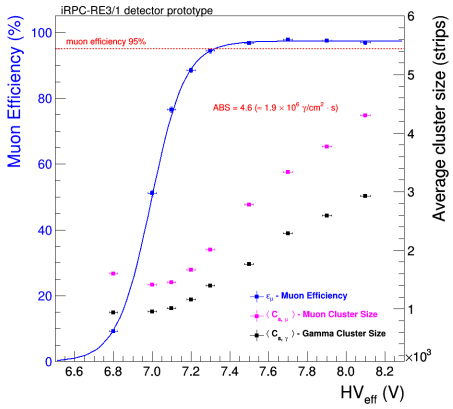

(c) $\phi_\gamma = 1.9 \times 10^6\ \gamma/cm^2 \cdot s$ (ABS 4.6).

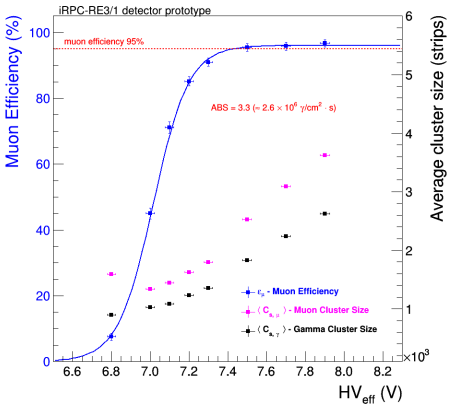

(d) $\phi_\gamma = 2.6 \times 10^6\ \gamma/cm^2 \cdot s$ (ABS 3.3).

Figure A.6: Muon detection efficiency, muon and gamma cluster size as a function of high voltage applied to the RE3/1 prototype at different levels of gamma photon flux from the source (the nominal filter absorption factors are indicated). The applied high voltage values have been normalized by using the PT correction formula explained in Section 6.2.2.2.

Bibliography

[1] CERN, Home Page - https://home.cern/

[2] The LHC Study Group, *The Large Hadron Collider Conceptual Design Report*. CERN/AC 95-05, 1995.

[3] O. S. Brüning, P. Collier, P. Lebrun, S. Myers, R. Ostojic, J. Poole, and P. B. Proudlock, *LHC Design Report Vol. 1: The LHC Main Ring*. CERN-2004-003-V1, 2004.

[4] O. S. Brüning, Poole, P. Collier, and P. B. Proudlock, P. Lebrun, S. Myers, R. Ostojic, J. *LHC Design Report Vol. 2: The LHC Infrastructure and General Services*. CERN-2004-003-V2, 2004.

[5] M. Benedikt, P. Collier, V. Mertens, J. Poole, and K. Schindl, *LHC Design Report Vol. 3: The LHC Injector Chain*. CERN-2004-003-V3, 2004.

[6] Lep Injector Study Group, *LEP Design Report Vol. 1: The LEP Injector Chain*. CERN-LEP-TH-83-29, CERN-PS-DL-83-81, CERN-SPS-83-26, LAL-RT-83-09, 1983.

[7] Lep Injector Study Group, *LEP Design Report Vol. 2: The LEP Main Ring*. CERN-LEP/8-01, 1984.

[8] Lep Injector Study Group, *LEP Design Report Vol. 3: LEP2*. CERN-AC-96-01-LEP2, 1996.

[9] The ATLAS Collaboration, *ATLAS: A Toroidal LHC ApparatuS Technical Proposal*. CERN/LHCC 94-18, LHCC/P1, December, 1994.

[10] CMS Collaboration, *The CMS experiment at LHC*, JINST 08 (2008) 03.

[11] The ALICE Collaboration, *A Large Ion Collider Experiment Technical Proposal Design*. CERN/LHCC 95-71, LHCC/P3, 1995.

[12] The LHCb Collaboration, *A Large Hadron Collider Beauty Experiment for Precision Measurements of CP-Violation and Rare Decays LHCb Technical Proposal*, CERN/LHCC 98-04, LHCC/P4, 1998.

[13] A. W. Chao, K. H. Mess, M. Tigner, F. Zimmermann, *Handbook of Accelerator Physics and Engineering*, ed. World Scientific (2013).

[14] CMS Collaboration, *CMS Luminosity* - Public Results, https://twiki.cern.ch/twiki/bin/view/CMSPublic/LumiPublicResults.

[15] F Halzen and A D Martin. *Quarks and Leptons*. John WILEY and SONS, 1985.

[16] The Review of Particle Physics, Home Page - URL http://pdg.lbl.gov.

[17] K A Olive. *(PDG) Chin. Phys.*, C(38), 2014.

[18] LHC/LC Study Group Collaboration. *Physics Interplay of the LHC and the ILC*. Phys. Rep., 426(hep-ph/0410364. ANL-HEP-PR-2004-108. CERN-PH-TH-2004-214. DCPT-2004-134. DESY-04-206. DESY-2004-206. IFIC-2004-59. IISc-CHEP-2004-13. IPPP-2004-67. SLAC-PUB-10764. UB-ECM-PF-2004-31. UCD-2004-28. UCI-TR-2004-37. 2-6):47–358. 472 p, Oct 2004. URL https://cds.cern.ch/record/800650.

[19] S. Dittmaier et al. *Handbook of LHC Higgs Cross Sections: 1. Inclusive Observables*. CERN, Geneva, 2011. URL https://cds.cern.ch/record/1318996. Comments: 153 pages, 43 figures, to be submitted to CERN Report. Working Group web page: https://twiki.cern.ch/twiki/bin/view/LHCPhysics/CrossSections.

[20] F. Gianotti. *Collider physics: LHC*. (CERN-OPEN-2000-293), 2000. URL https: //cds.cern.ch/record/458489.

[21] *Combination of standard model Higgs boson searches and measurements of the properties of the new boson with a mass near 125 GeV*. Technical Report CMS-PAS-HIG-13-005, CERN, Geneva, 2013. URL https://cds.cern.ch/record/1542387.

[22] ATLAS Collaboration, *The ATLAS Experiment at the CERN Large Hadron Collider*, JINST 3 (2008)

[23] CMS Collaboration, *The CMS experiment at the CERN LHC*, JINST 3 (2008)

[24] ALICE Collaboration, *The ALICE experiment at the CERN LHC*, JINST 3 (2008)

[25] LHCb Collaboration, *The LHCb Detector at the LHC*, JINST 3 (2008)

[26] V. Karimäki, *The CMS tracker system project: Technical Design Report*. Technical Design Report CMS. CERN, Geneva, 1997.

[27] *The CMS tracker: addendum to the Technical Design Report*. Technical Design Report CMS. CERN, Geneva, 2000.

[28] Vardan Khachatryan et al. *CMS Tracking Performance Results from Early LHC Operation*. Eur. Phys. J. C, 70(arXiv:1007.1988. CERN-PH-EP-2010-019. CMS-TRK-10-001):1165. 29 p, Jul 2010. URL https://cds.cern.ch/record/1277738.

[29] *The CMS electromagnetic calorimeter project: Technical Design Report*. Technical Design Report CMS. CERN, Geneva, 1997.

[30] P. Bloch, R. Brown, P. Lecoq, and H. Rykaczewski, *Changes to CMS ECAL electronics: addendum to the Technical Design Report*. Technical Design Report CMS. CERN, Geneva, 2002.

[31] CMS Collaboration, *Energy calibration and resolution of the CMS electromagnetic calorimeter in pp collisions at* $\sqrt{s} = 7\ TeV$, JINST 8 (2013) P09009, arXiv:1306.2016 [hep-ex]

[32] *The CMS hadron calorimeter project: Technical Design Report*. Technical Design Report CMS, CERN-LHCC-97-031. CERN, Geneva, 1997.

[33] *The CMS muon project: Technical Design Report*. Technical Design Report CMS, CERN-LHCC-97-032. CERN, Geneva, 1997.

[34] A. Colaleo et al., CERN-LHCC-2017-012, CMS-TDR-016, 12 September 2017.

[35] *CMS TriDAS project: Technical Design Report; 1, the trigger systems*. Technical Design Report CMS, CERN-LHCC-2000-038. CERN, Geneva, 2000.

[36] CMS Collaboration. *CMS. The TriDAS project. Technical design report, vol. 1: the trigger sistem*. CMS-TDR-6-1, 2000. http://cds.cern.ch/record/706847ln=it.

[37] CMS Collaboration, *CMS: The TriDAS project. Technical design report, Vol. 2: Data acquisition and high-level trigger*, CMS-TDR-6, 2002. http://cds.cern.ch/record/578006l

[38] A. Colaleo et al., *CMS Technical Design Report for the Muon Endcap GEM Upgrade*. Technical Design Report CMS; CERN-LHCC-2015-012; CMS-TDR-013 CERN, Geneva, Sep. 2015. URL https://cds.cern.ch/record/2021453.

[39] CMS Collaboration. *Technical proposal for the upgrade of the CMS detector through 2020*. Technical Report CERN-LHCC-2011-006. LHCC-P-004, CERN, Geneva, Jun 2011. URL https://cds.cern.ch/record/1355706.

[40] CMS Collaboration, *Technical proposal for the phase II upgrade of the Compact Muon Solenoid*, CERN-LHCC-2015-10, CMS-TDR-15-02.

[41] V. Parkhomchuk et al., *A spark counter with large area.* Nucl. Instrum. Methods, 93, 269–270 (1972).

[42] Y. Pestov, *Status and future developments of spark counters with a localized discharge*, Nucl. Instrum. Methods Phys. Res., 196 (1), 45–47 (1979).

[43] H. Schmidt, *Pestov spark counters: work principle and applications*, Nucl. Phys. B (Proc. Suppl.), 78 (1–3), 372–380 (1999).

[44] R. Santonico and R. Cardarelli, *Development of Resistive Plate Counters*, Nucl. Instr. and Meth., vol.187, 377-380 (1981).

[45] T. Ferber, *Experimantal Techniques in High Energy Physics*,Frontiers in Physics Lecture Note Series.

[46] G. Knoll, *Radiation Detection and Measurement*, Wiley (1989).

[47] Marcello Abbrescia, Vladimir Peskov, and Paulo Fonte, *Resistive Gaseous Detectors. Designs, Performance, and Perspectives*, Wiley-VCH (2018).

[48] E. Cerron Zeballos et al., *Avalanche fluctuations within the multigap resistive plate chamber*, Nucl. Instrum. Methods Phys. A 381, 569-572 (1996).

[49] M. Williams, *The development of the multigap resistive plate chamber*, Nuclear Physics B (Proc. Suppl.) 6IB, 250-257 (1998)

[50] M. Abbrescia et.al.,*Effect of the linseed oil surface treatment on the performance of resistive plate chambers*, Nucl. Instrum. Methods Phys.A 394, 13-20 (1997).

[51] L. Changguo, *RPC electrode material study*, Nucl. Instrum. Meth. A , vol. 602, no. 3, 761 – 765 (2009).

[52] M. Abbrescia et al., *Properties of the C2H2F4 based gas mixture for avalanche mode operation of Resistive Plate Chambers*,Tech. Rep. CMS-NOTE-1997-004, CERN, Geneva, Jan 1997.

[53] E. Gorini et al., *Drift velocity measurements in C2H2F4 based mixtures*, in Proceedings of the 4th International Workshop on Resistive Plate Chamber and Related Detectors, Napoli, Italy, 15-16 October 1997.

[54] A. Ranieri, *A New Front-End Board for RPC Detector of CMS*, CERN-CMS-NOTE-1999-047, (1999).

[55] M. Abbrescia et al., *New Developments on Front End Electronics for the CMS Resistive Plate Chambers*, Nucl. Instrum. Meth. A, vol. 456, 143 (2000).

[56] A. Colaleo, A. Safonov, A. Sharma, and M. Tytgat. CMS TECHNICAL DESIGN REPORT FOR THE MUON ENDCAP GEM UPGRADE. Technical Report CERN-LHCC-2015-012. CMS-TDR-013, CERN, Geneva, Jun 2015.

[57] CMS Collaboration, *The Phase-2 Upgrade Of the CMS Muon Detectors. Technical Design Report*, CERN-LHCC-2017-012, CMS-TDR-016, 12 September 2017.

[58] D. Contardo et al., *Technical Proposal for the Phase-II Upgrade of the CMS Detector*, CERN-LHCC-2015-010 ; LHCC-P-008 ; CMS-TDR-15-02.

[59] M.I. Pedraza-Morales et.al. *RPC upgrade project for CMS Phase II.* https://arxiv.org/pdf/1806.11503.pdf.

[60] M. Abbrescia et al., *The upgrade of the Muon System of the CMS experiment*, *JINST* **9** (2014) C12021.

[61] B. Carpinteyro et al., *RPC Radiation Background Simulations for the High Luminosity Phase in the CMS Experiment*,CMS CR-2018-144

[62] E. Voevodina et al., *Improving of RPC for Muon System of CMS experiment*, Journal of Physics: Conference Series, 3rd International Conference on Particle Physics and Astrophysics (ICPPA 2017).

[63] K. S. Lee & S. K. Park, *Thin Double-gap RPCs for the Phase-2 Upgrade of the CMS Muon System*,CERN-CMS-NOTE-2017-005.

[64] A. Fagot et al., *R&D towards the CMS RPC Phase-2 upgrade*, arxiv:1606.04291v1 (2016).

[65] F. Lagarde et al., *High Rate RPC detector for LHC*, https://arxiv.org/abs/1807.05680 (2018).

[66] P. Swallow et al., *Measurement and Recording of Historic Buildings*, Routlege, (2016).

[67] FARO Focus 3D Laser Scanner, https://www.faro.com/en-gb/products/construction-bim-cim/faro-focus/ .

[68] Leica Cyclone 3D Point Cloud Processing Software, https://leica-geosystems.com/products/laser-scanners/software/leica-cyclone

[69] Geomagic Design X software, https://www.3dsystems.com/software/geomagic-design-x

[70] CATIA 3D Design & Engineering Software, Design https://www.3ds.com/products-services/catia/

[71] 3D CAD Design Software SOLIDWORKS, https://www.solidworks.com/

[72] F. Lagarde et al.,*High Rate RPC detector for LHC*, (2018), https://arxiv.org/abs/1807.05680.

[73] Electromagnetic Simulator - Home Page, https://sourceforge.net/projects/mmtl/files/.

[74] A. Fagot et al., *Fast timing measurement for CMS RPC Phase-II upgrade*, JINST, V13 (2018).

[75] WEEROC, Home Page, ASIC products - https://www.weeroc.com/en/products/petiroc-2a.

[76] A. Fagot et al., *R&D towards the CMS RPC Phase-2 upgrade*, arxiv:1606.04291v1 (2016).

[77] Altera Corporation, *Cyclone II Device Handbook*, Volume 1.

[78] CMS Collaboration, *The CMS muon project: Technical Design Report*. Technical Design Report CMS, CERN-LHCC-97-032. CERN, Geneva, 1997.

[79] D. Pfeiffer et al., *The radiation field in the Gamma Irradiation Facility GIF++ at CERN*. Nucl. Instrum. Meth., A 866 (2017), 91-103, arXiv:1611.00299

[80] CERN, Super Proton Synchroton (SPS) Home Page - http://ab-dep-op-sps.web.cern.ch/ab-dep-op-sps/

[81] The H4 Secondary Beam Line of EHN1/SPS: http://sba.web.cern.ch/sba/BeamsAndAreas/H4/

[82] Overview over CERN SPS test beams, Home Page: https://indico.desy.de/indico/event/18050/session/7/ contribution/7/material/slides/

[83] L. M. Pant et al., *Effect of environmental parameters on the performance of resistive plate chambers*, Proceedings of the DAE Symp. on Nucl. Phys., Vol. 55 (2010).

[84] S.H.Ahn et. al., *Temperature and humidity dependence of bulk resistivity of bakelite for resistive plate chambers in CMS*, Nucl. Instrum. Meth., A 451, (2000).

[85] G.Aielli et al., *Large Scale Test and Performances of the RPC Trigger Chambers for the Atlas experiment at LHC*, IEEE04,(2004): http://people.na.infn.it/ pietra/Repository/IEEE04/DellaPietraIEEE04.pdf.

[86] G.Aielli et al., *The ATLAS RPC Test Stand at INFN Roma Tor Vergata*, IEEE06,(2006).

[87] R. Cardarelli et al., *Performance of RPCs and diamond detectors using a new very fast low noise preamplifier*, JINST 8 P01003,(2013).

[88] W. Shockley et al., *The Theory of P-N Junctions in Semiconductors and P-N Junction Transistors*, Bell System Technical Journal Vol. 28, No. 3, (1949).

[89] L. David et al., *Current Status and Future Trends of SiGe BiCMOSTechnology*, IEEE Transactions on Electron Devices, Vol. 48, No. 11, (2001).

[90] L. Pizzimento et al., *Development of a new Front End electronics in Silicon and Silicon-Germanium technology for the Resistive PlateChamber detector for high rate experiments*, JINST, https://arxiv.org/pdf/1806.04113.pdf.

[91] Eltos S.p.A., Home page: https://www.gmc-instruments.de/en/

[92] R. Karnam et al., *Design and Characterization of a 2m x 2m Resistive Plate Chambers (RPCs)*, INO Graduate Training Programme, TIFR.

[93] GOSSEN METRAWATT and CAMILLE BAUER company, Home page: http://www.eltos.com.

[94] M. Abbrescia, V. Peskov and P. Fonte, *Resistive Gaseous Detectors. Design, Performance, and Perspectives*, 2018 Wiley-VCH Verlag GmbH & Co.

[95] E. Voevodina, A. Gelmi et al., *Upgrade program of the RPC system of the CMS Muon Spectrometer*, Poster on the ELBA2018: 14th Pisa meeting on advanced detectors, 27 May-2 Jun 2018, INFN - Sezione di Pisa, Biodola (Italy).

[96] D. Pfeiffer et al., *The radiation field in the Gamma Irradiation Facility GIF++ at CERN*. Nucl. Instrum. Meth. A 866 (2017), 91-103 arXiv:1611.00299.

Acknowledgements

All the work achieved during the Ph.D. program would not have been possible without the great help from many colleagues and friends. I will do my best to give here a clear list of these people and their contributions to what was, without doubts, the most intense years of my life.

I wish to place on record my deep sense of gratitude to my internal guide Prof. Giovanni De Lellis for his initiative, encouragement and determination to help me. Had I not met him, my dream of doing a Ph.D. would have possibly remained just one. My external guide Dr. Gabriella Pugliese for her great support. You gave me the opportunity to work in the most amazing place for particle physics.

Since I began to work on the development of improved Resistive Plate Chambers, I had opportunities to interact with many experts in the field. I wish to particularly thank: Dr. Ian Crotty, Dr. Salvatore Buontempo, Dr. Nicolas Zaganidis, Dr. Salvador Carrillo Moreno, Prof. Iuri Bagaturia, Prof. Kong Kyong Sei Lee, Prof. Roberto Cardarelli, Prof. Paulo Vitulo.

I would like to give a special big thank to Dr. Nicolas Zaganidis and Dr. Salvador Carrillo Moreno for great help during the Test Beam and all activities which were organized at the CERN CMS-RPC QA/QC facility.

I am very thankful to Dr. Jan Eysermans and Alexis Fagot, who helped me in the long process of analyzing experimental data. I would like to thank them for this kind of never-ending support.

Here is the place to thank to all the members of the RPC Community and especially the colleagues I have worked during my Ph.D program. They helped me learn and grow in a stimulating and fun environment.

Finally, nothing could have been possible without the great support of my family and my friends who pushed me to pursue my studies and make my dream come true. A special thank goes to my boyfriend Francesco Fallavollita who believed in me and despite of the stress and sometimes my bad mood, has accepted to become my husband.

Thank you very much to all of you.